Methods for Enhancing the Accuracy, Precision and Spatial Resolution of the Atomic Force Microscope

Ashley D. Slattery

A thesis presented for the degree of
Doctor of Philosophy

Faculty of Science and Engineering
Flinders University
Australia
October 27, 2015

Declaration

I certify that this thesis does not incorporate without acknowledgment any material previously submitted for a degree or diploma in any university; and that to the best of my knowledge and belief it does not contain any material previously published or written by another person except where due reference is made in the text.

Candidate: Ashley D. Slattery

Signature: ....

Date: October 27, 2015

Acknowledgements

I have a great many people to thank for their support and patience during the course of this endeavour, and also for their inadvertent help in making the journey an enjoyable one. I feel that the use of headings and subheadings probably isn't warranted in an acknowledgements section, so I'll try to keep this concise.

My dear Samantha, you get to be first. Considering you're usually the first person I see at the end of many stressful days, I know that you deserve the bulk of my appreciation. Thank you for your unfaltering support over the years, for being amazing, and most importantly, for making me food while I was absorbed in writing this document.

In addition to my lovely wife, I have an amazing family (even bigger now) who have been incredibly supportive over the years. Mum, Dad, Sandie, Tim and Tracy, while it is hard at this moment to comprehend anything other than finishing this PhD, I know that the journey to this point started long ago, and I am so very grateful for the role you all played in putting me on the path to end up here. This wouldn't be complete without thanking my array of siblings for being as awesome as they are, thank you all for everything.

My supervisors, Jamie and Chris, I can't even begin to cover the amount of work and support you have both invested to allow me to become the person I am today. After guiding me through an Honours and PhD thesis, I certainly regard you both as colleagues and friends, and I am immensely grateful for everything you have done for me.

Chris, I could not have asked for a better person to share an office with. Thank you for many interesting discussions (both productive and unproductive) and for being an all-round awesome guy!

Joe, over the course of my PhD I gradually figured out what I really enjoy doing (and I guess that's kinda the idea). Thank you for giving me the opportunity to pursue my love of working with instrumentation, I still enjoy every day of it.

There are a whole bunch of people who have come and gone during the course of my studies, and the experience would not have been the same without them. If I attempt to list all these people, I will inevitably forget someone and I will also run out of paper, so I am hoping you know who you are and I will make the effort to thank each and every one of you personally. From outings at conferences like ICONN, to hilarious conversations in office doorways, I want to thank all of you for an awesome time.

Abstract

Atomic force microscopy (AFM) is an extremely powerful characterisation technique, its versatility has resulted in applications across a broad range of fields from direct visualisation of walking motor proteins to the characterisation of nanoscale semiconductor devices. Since the invention of the AFM in 1986, there has been significant development in the technique and instrumentation; there are now a number of manufacturers which offer a variety of AFMs to suit a range of applications. One of the instruments' greatest strengths is the ability to perform a variety of measurements, however it is the measurement of sample topography and nanoscale forces which are at the heart of the AFM.

This thesis reports the development of these two fundamental aspects; the initial focus is on the challenge of accurate force measurement, whereby a number of different approaches are used to improve the process of AFM cantilever spring constant calibration. The accuracy by which the cantilever spring constant can be determined is directly responsible for uncertainty in AFM force measurement, and as such is an important area of development. Focused ion beam (FIB) milling is a common theme throughout this work, and was used to greatly improve the accuracy with which the cantilevers' spring constant can be determined. The techniques reported here provide excellent accuracy, avoid tip damage and are applicable to a wide variety of the many types of cantilevers available.

The measurement of cantilever deflection sensitivity is another critical aspect of force measurement, and FIB milling was again used to improve this measurement. By inverting the measurement geometry and milling spatial markers on the cantilever, the deflection sensitivity was measured without any damage to the cantilevers' delicate imaging tip, an otherwise unavoidable aspect of this measurement.

The chapter on force calibration concludes with an investigation of the recently commercialised fast-scanning cantilevers; these cantilevers offer video-rate imaging by virtue of their ultra-small size and resonant frequencies in the MHz regime. The vastly different properties of these "next-generation" cantilevers' is expected to have an effect on the measurement of their spring constant, and here the applicability of standard calibration techniques is reported.For the first time, a number of fast-scanning cantilevers were calibrated using a variety of methods and compared to determine their effectiveness.

The later chapters switch focus to the improvement of spatial resolution, by reducing the size of the AFM tip. Carbon nanotubes (CNTs) are attached to AFM probes by a variety of different methods, resulting in an imaging tip which is of high aspect ratio, small diameter and incredibly high wear resistance. CNT attachment using a micromanipulator in a scanning electron microscope (SEM) was found to be an efficient approach which yielded high quality CNT tips, and the final chapter reports two different applications of these specialised probes.

Using the method reported herein, CNTs were attached to fast-scanning cantilevers for the first time, allowing a CNT probe to be scanned with a tip velocity of 109 μms^{-1}. The CNT tips also demonstrated superior wear resistance in comparison to standard silicon tips, which are expected to wear at accelerated rates for fast-scanning probes.

Application of the recently-developed PeakForce tapping (PFT) imaging mode was demonstrated with CNT probes; this mode shows great promise for providing simple, stable imaging with CNT probes which are notoriously difficult to apply. The PFT mode is used to demonstrate high resolution imaging on samples with very small features, and artifacts associated with the technique were investigated. In addition to stable operation, the PFT mode is shown to eliminate the "ringing" artifact which affects CNT probes in tapping mode near large vertical steps. This will allow characterisation of high aspect ratio structures using thin CNT probes, an exercise which has previously been challenging with other imaging modes.

Published Works

Much of the work presented in this thesis has been published, and the details of these publications are included here for reference.

Book Chapters

- Slattery, A. D., Gibson, C. T., & Quinton, J. S. (2013). *Application of Ion Beam Processes to Scanning Probe Microscopy.* In Z. M. Wang (Ed.), FIB Nanostructures (pp. 205–240). Springer International Publishing.

Journal Publications

- Slattery, A. D., Quinton, J. S., & Gibson, C. T. (2012). *Atomic force microscope cantilever calibration using a focused ion beam.* Nanotechnology, 23(28), 285704.
- Slattery, A. D., Blanch, A. J., Quinton, J. S., & Gibson, C. T. (2013). *Calibration of atomic force microscope cantilevers using standard and inverted static methods assisted by FIB-milled spatial markers.* Nanotechnology, 24(1), 015710.
- Slattery, A. D., Blanch, A. J., Quinton, J. S., & Gibson, C. T. (2013). *Efficient attachment of carbon nanotubes to conventional and high-frequency AFM probes enhanced by electron beam processes.* Nanotechnology, 24(23), 235705.
- Slattery, A. D., Blanch, A. J., Quinton, J. S., & Gibson, C. T. (2013). *Accurate measurement of Atomic Force Microscope cantilever deflection excluding tip-surface contact with application to force calibration.* Ultramicroscopy, 131, 46–55.
- Slattery, A. D., Blanch, A. J., Ejov, V., Quinton, J. S., & Gibson, C. T. (2014). *Spring constant calibration techniques for next-generation fast-scanning atomic force microscope cantilevers.* Nanotechnology, 25(33), 335705.

Contents

Chapter 1

Introduction

1.1 The atomic force microscope

The AFM is an instrument used across a broad range of scientific and industrial fields, for imaging surfaces and measuring forces on the nanoscale. Invented by Binnig, Quate and Gerber in 1986 [1]; the AFM has become one of the most versatile instruments available for nanoscale characterisation, force measurement and colloid science. A great advantage of the AFM is its' ability to operate in almost any environmental conditions (including air, liquid and vacuum) and without requiring a conductive sample. This enables samples to be imaged in ambient conditions, which is simple compared to techniques requiring high vacuum. The ability to perform measurements in-situ is a significant advantage for the analysis of biological samples, which often alter their behaviour or degrade when removed from a liquid media.

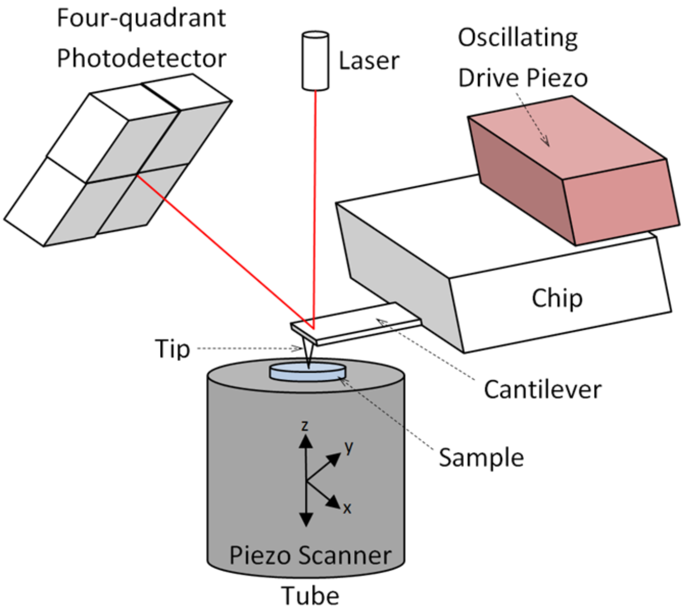

Figure 1.1: A schematic of a basic atomic force microscope

Conceptually, the AFM instrument is quite simple and a schematic of the key components typical of an AFM are shown in figure 1.1. The sample is translatable in three dimensions by a piezoelectric scanner tube, and is brought into contact with the sharp tip mounted at the end of a flexible cantilever. A laser provides light which is focussed onto the back of the cantilever and the reflected light is detected by a position-sensitive four-quadrant photodiode array. The cantilever deflection can then be accurately measured in both normal and lateral directions as the tip interacts with the sample. The sharp tip is then rastered across the sample surface and nano-scale forces interacting with the tip result in deflection of the cantilever. During scanning, typically, the sample height is constantly varied in order to maintain constant interaction force. The motion of the sample thus provides a constant-force map which is interpreted as the sample topography.

1.1.1 The AFM probe

The probe used to make AFM measurements is fundamentally important to the operation of the instrument. The properties of the probe directly affect the performance of the AFM, and a significant portion of the work presented herein is focussed on this aspect of the microscope.

Although the materials and geometry of AFM probes can vary extensively, all have several basic features in common which are introduced here. An AFM probe generally consists of a cantilevered beam clamped at one end, with a sharp tip attached to the other, free end as can be seen in figure 1.2. The cantilever is often fabricated from silicon or silicon nitride and the clamped end is attached to a much larger piece of material referred to as the "chip" which facilitates handling. There are many companies which manufacture AFM probes with Bruker, Mikromasch, Olympus and Nanoworld being the most prominent.

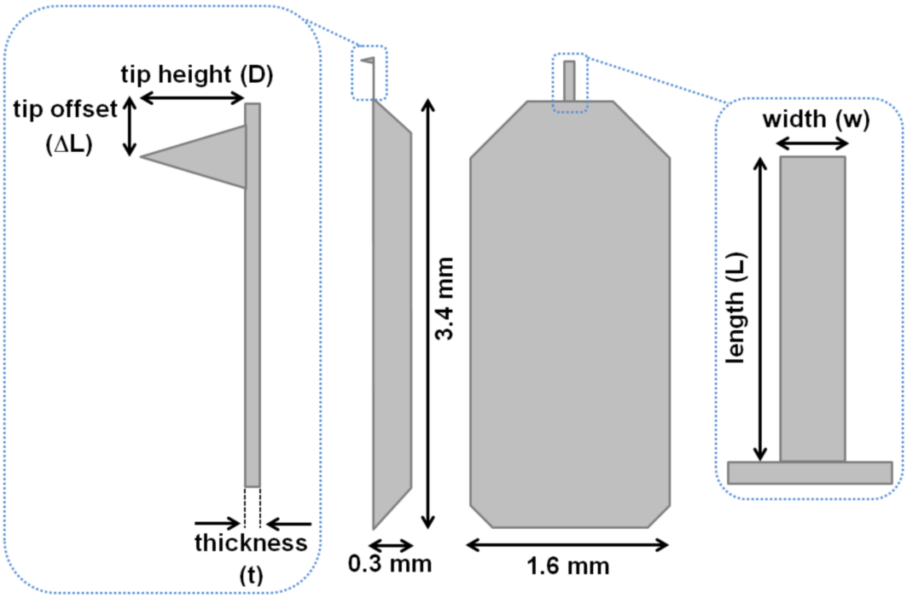

Figure 1.2: A schematic of an AFM probe, showing the cantilever and chip with various important dimensions of the cantilever and tip defined.

1.1.1.1 Geometry

There are two common cantilever geometries which are in widespread use, these are the rectangular beam and V-shaped types. Additionally, low mass cantilevers with trapezoidal plate geometry have been recently introduced for fast-scanning applications.

In general, rectangular cantilevers are manufactured from silicon and are designed to be stiff such that they operate in dynamic imaging modes, while V-shaped cantilevers are made from silicon nitride and are generally softer. V-shaped cantilevers are applied in either static or dynamic modes (ie. contact or tapping mode respectively) in air or fluid.

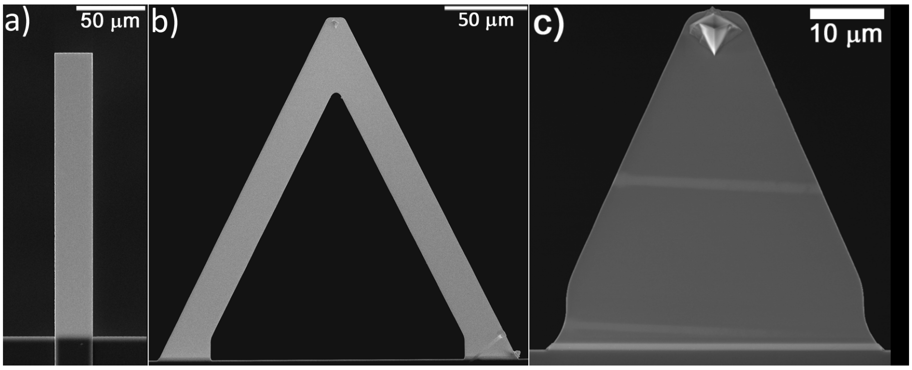

Figure 1.3: SEM images of the different types of cantilever geometries. Reprinted and adapted with permission from [2, 3].

The dimensions of the cantilever play a significant role in defining its' properties and operation, and are used extensively in characterising individual cantilevers. Figure 1.3 shows an example of three common types of AFM cantilever geometry.

1.1.1.2 Composition

Cantilever composition The material properties of the cantilever have a significant influence on its' overall mechanical properties. Both silicon and silicon nitride cantilevers can vary in material properties for different reasons. Single-crystal silicon has a very well-defined density, however it is anisotropic and so the Young's modulus varies substantially depending on the orientation of the crystal planes [4]. Silicon nitride cantilevers are less well-defined as the Si:N stoichiometric ratio varies substantially depending upon the process conditions under which it was grown. Sader et al. reports the density of silicon nitride to range from 2700-3700 kgm^{-3}, while Khan et al. reported the Young's modulus to vary by almost 100% [5, 6].

Metallic coatings Cantilevers' are typically coated with a metallic layer, on the opposite side to the imaging tip in order to improve their reflectivity. Aluminium coatings are reserved for operation in air, whereas gold is predominantly used for fluid applications where chemical stability is important. Metallic films can also be used to impart other properties to the cantilever. For instance, platinum can be applied to the cantilever tip to improve conductivity, whereas a cobalt film enables the cantilever to sense magnetic fields.

The presence of a metal coating can significantly alter the overall density and Young's modulus of the cantilever, and can be difficult to account for if the coating thickness is poorly defined [5].The cantilever density can be an important consideration for spring constant measurement and so it is necessary to correct this value when required, using the following expression from the work of Sader et al. [5].

$$\rho_{lever} = \frac{\rho_c t_c + \rho_f t_f}{t_{lever}} \tag{1.1}$$

Where ρ_{lever} and t_{lever} are the overall density and thickness of the cantilever, ρ_c and t_c are the density and thickness of the cantilever substrate and while ρ_f and t_f are the density and thickness of the metal film.

Metal coatings also alter the effective Young's modulus of the cantilever, and the correction required is slightly more complicated. The effective Young's modulus for metal coated cantilevers can be found using the following equation, which is an approximation developed by Sader et al. [5].

$$E_{lever} = \frac{E_c t_c + E_f t_f}{t_{lever}} \tag{1.2}$$

Where E_{lever} and t_{lever} are the overall Young's modulus and thickness of the cantilever, E_c and t_c are the Young's modulus and thickness of the cantilever substrate and E_f and t_f are the Young's modulus and thickness of the metal film.

1.1.1.3 Important properties

Tip diameter The imaging tip traces the sample topography to produce an image of the surface, and so the lateral spatial resolution of the AFM is often determined by the sharpness of the tip. For this reason, the maximum tip diameter is specified by the manufacturer and is generally ∼10 nm. The improvement of this property is one of the primary aspects of this work, where carbon nanotubes have been applied to reduce the tip size below 5 nm for ultra-high resolution imaging.

Resonant frequency Application of the AFM in dynamic, oscillatory modes often requires the cantilever to be excited at its' resonant frequency. In most applications, the cantilever is mounted on an oscillating drive piezo, and the resonant frequency is determined by sweeping the frequency of oscillation while measuring cantilevers' amplitude. The resultant amplitude versus frequency plot appears as shown in figure 1.4a and allows the resonant frequency to be determined where the amplitude is a maximum. The effect of the tip-surface interaction on the resonant frequency of the cantilever is also shown in figure 1.4b. When the tip is close to the surface, external forces on the cantilever cause a damping of the oscillation which causes the resonant frequency and amplitude to reduce.

Q-factor The Q factor is a dimensionless quantity that is related to the damping properties of the cantilever, and can be observed by the "sharpness" of the resonance peak; it is inversely proportional to the damping coefficient of the oscillating cantilever. This factor describes the number of oscillations which occur before the cantilevers' amplitude decays to $\frac{1}{e}$ of its initial value (when no external forced oscillation is present). In addition to the resonant frequency, the Q factor is used extensively to describe the dynamic properties of the cantilever. Accurate knowledge of the Q factor is important for a number of spring constant calibration methods, which are discussed in detail in the following sections.

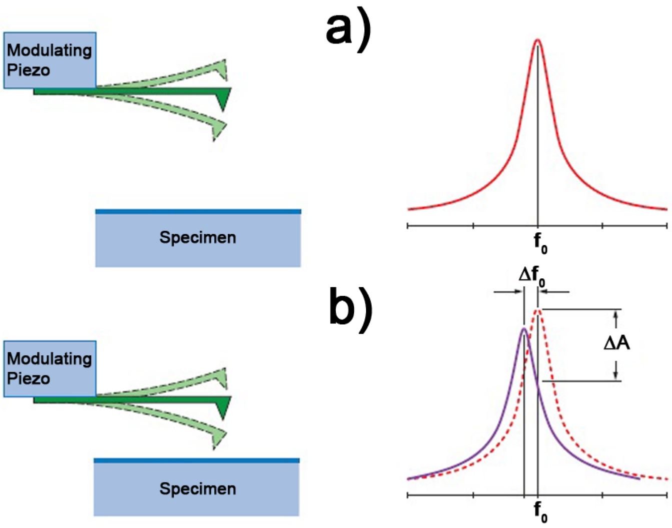

Figure 1.4: Example resonant frequency curve of an AFM cantilever, showing the reduction of resonant frequency due to damping interaction with the surface. Reprinted with permission from Bruker corporation [7].

Spring constant The spring constant (or stiffness) is used to express the rigidity of the cantilever, and is essential for making quantitative force measurements with the AFM. This quantity is determined by the cantilevers' geometric and material properties, which are in most cases, highly variable due to the micro-fabrication process by which cantilevers are fabricated. A primary focus of this work is the accurate determination of the cantilever spring constant, which is commonly referred to as "spring constant calibration" or more simply "cantilever calibration".

Static and dynamic values An often neglected aspect of the cantilevers' spring constant is the difference between the static and dynamic values of this property. The spring constant of a cantilever varies depending on whether the cantilever is undergoing static or dynamic deflection (ie. oscillation), and the relationship between the static and dynamic spring constants is not trivial. For rectangular cantilevers the static spring constant has been shown to be 3% lower than the dynamic spring constant [8, 9], and this effect can be even greater for cantilevers with other geometries [10, 11].

It is important to account for this effect both when performing force measurements and also when calibrating the cantilever. Depending on whether the force measurement is performed in a static or dynamic mode, the spring constant may need to be adjusted accordingly. In addition, one should be mindful of the spring constant provided by a particular calibration method. A spring constant obtained from a dynamic technique such as the thermal method requires correction before use in static force measurements.

Off-end loading Cantilevers are intuitively more flexible at their free end than at their fixed end (base). The variation in the spring constant along the length of the cantilever can be determined using Euler-Bernoulli beam theory, for beam-shaped cantilevers. This relationship is given by equation 1.3, which is commonly called the off-end loading equation.

$$k_{\Delta L} = k_{end}(\frac{L - \Delta L}{L})^3 \tag{1.3}$$

This expression is accurate along the entire length of the cantilever, precluding any effects due to non-uniformity; however this is not the case for cantilevers with non-rectangular geometry. Application of the off-end loading equation to V-shaped cantilevers is possible, at the cost of significant uncertainty [12–14]. The off-end loading correction is of great importance, as the imaging tip is almost always set back some distance from the free end of the cantilever. If the spring constant is determined at the cantilevers' end, as it is in many calibration techniques, then this must be corrected to the location of the imaging tip.

1.1.2 Tip-surface interaction

At the core of the AFM is the interaction between the tip and the sample. When the tip of the AFM probe approaches a surface, the force exerted on the tip is the result of several different interactions. These can be classified as attractive (van der Waals, electrostatic and chemical) and repulsive (hard sphere repulsion, electron-electron coulomb interaction and Pauli-exclusion interaction) types.

For the case of a cantilever approaching a surface in a vacuum, a familiar interaction curve can be observed in figure 1.5, where the long-range attractive and short-range repulsive forces are superimposed and show the force exerted on the AFM tip with distance from the sample.

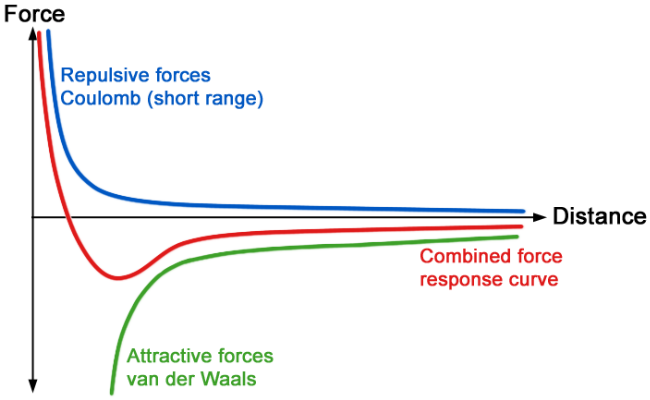

Figure 1.5: Force interaction curve, showing the variation in attractive and repulsive forces with tip-sample separation, and the resultant interaction curve.

The van der Waals interaction force is dependent on the geometry and dielectric properties of the tip and sample. A common geometry in AFM experiments is that of a flat surface (sample) and a sphere (tip), and the van der Waals interaction force (F_{vdW}) in this case is given by equation 1.4, where A_H is the Hamaker constant, R_{sphere} is the radius of the sphere and $D_{sphere\text{-}surface}$ is the sphere-surface distance.

$$F_{vdW} = -\frac{A_H R_{sphere}}{6D^2_{sphere-surface}} \tag{1.4}$$

The repulsive forces are described by a rapidly decaying (exponential) interaction which dominates the total interaction at short range. Behaviour of the system beyond hard contact is described by various models of contact mechanics, which are concerned with either elastic or plastic deformation of the sample; these are discussed in section 1.1.2.1.

The AFM is however, operated under a variety of different conditions such as vacuum and liquid, with the most common being ambient. There are several forces in addition to the fundamental ones introduced above, which are observed under these "realistic" conditions. These include electrostatic and magnetic forces, capillary forces (in ambient conditions) due to an absorbed water layer and DLVO forces in aqueous solutions, amongst others.

1.1.2.1 Force measurement

While there are many ways to measure forces using the AFM; the most common is by recording a force-displacement curve, sometimes referred to as force spectroscopy. This is a plot of the deflection of the cantilever (multiplied by the spring constant), against the vertical extension of the tip onto/into the sample.

The measurement process can be visualised by beginning with the tip away from the surface; the tip is then moved towards the surface and pressed onto it, causing deflection of the cantilever. The tip is subsequently retracted and this results in a force versus displacement curve like the one shown in figure 1.6.

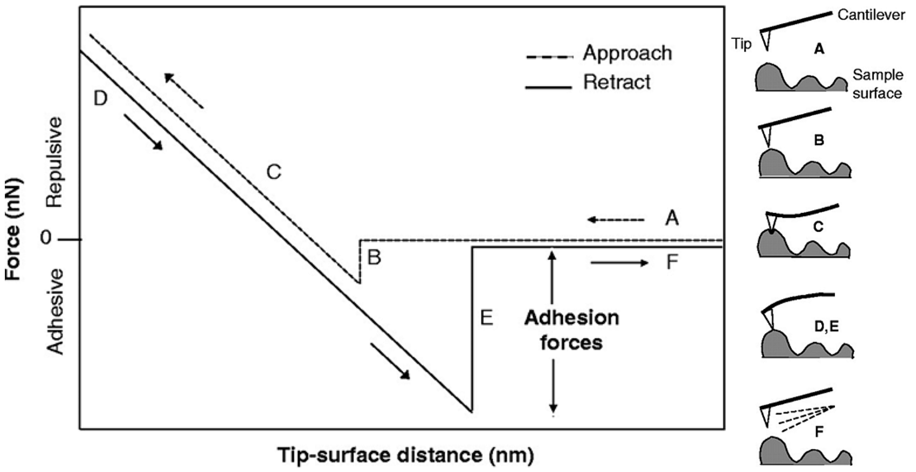

Figure 1.6: Representative static force curve, showing the movement of the AFM probe with respect to the surface at each point. Reprinted and adapted with permission from [15]

The approach (of the tip) to the sample is shown in region A where the cantilever experiences no force. At a distance of several nanometers from the surface, attractive forces (primarily van der Waals) cause the tip to "snap" into contact with the surface at position B, which is observed as an adhesive force. Continued approach to the surface results in deflection of the cantilever back to zero force, and the cantilever then continues to deflect as repulsive contact forces are observed in region C. The tip movement is then reversed at the beginning of region D, and this retraction of the cantilever typically produces a similar slope as was observed in region C. Attractive forces are observed at the end of region D as the tip adheres to the surface, and the cantilever then breaks free of the surface adhesive forces (often dominated by the water capillary). This event is seen in region E as a sharp return to the equilibrium position, whereby the tip is retracted further in region F.

The tip-sample force interaction can provide useful information about the sample, which can be extracted from several features of the force curve. The contact region (C,D) often indicates deformation of the sample by the tip, and can be used to determine the samples' modulus with accurate knowledge of the tip shape. The elastic deformation of the sample is described by several theories, these are the Hertz [16], Johnson-Kendall-Roberts (JKR) [17] and Derjaguin-Muller-Toporov (DMT) [18–20] models. The Hertz model neglects sample adhesion, whereas the JKR and DMT models both account for this factor. Using the latter two models, the work of adhesion can be calculated from the jump-off point (E) if the tip radius is known. Both theories are approximations however; the JKR model is best applied to a large tip with a soft sample and strong adhesion, while the DMT model performs better with sharp tips and a stiff sample with low adhesion [21].

Variation of the sample deformation with different loading/unloading rates can provide information about the viscoelastic properties of the sample. A more recent theory developed by Maugis improves significantly on existing models, and is accepted as the only theory which fully describes the elastic deformation of the sample [22, 23].

Hysteresis There are several different types of hysteresis which can be observed in force-distance curves, which are a result of different physical effects. Hysteresis is commonly observed in the contact region, where the approach/retract slopes are not the same. This is most often due to plastic or viscoelastic deformation of the sample, as described earlier. Friction can also result in hysteresis in this region, which is a result of the tip sliding due to the inherent tilt of the cantilever [24].

Sample adhesion causes hysteresis in the retract curve, where the tip stays in contact with the surface until the cantilever overcomes the total adhesive force (F_{ad}). The work of adhesion (W_{ad}) can be determined by integrating the region of the retraction curve below the zero force line. This is given by equation 1.5, assuming no deformation of the sample and where k is the spring constant.

$$W_{ad} = \frac{F_{ad}^2}{2k} \tag{1.5}$$

Hysteresis is also observed in the jump to contact, seen as the tip approaches the surface and discussed previously. Additionally, a basic form of hysteresis can arise from the Z-piezo. If there is hysteresis in the scanner then it will be observed in the force curve. Scanners should be linearised, and so this effect should not be observed with a system that is correctly calibrated.

1.1.3 Imaging and feedback

There are many different AFM imaging modes which have been developed, however these all require two basic abilities; a mechanism to determine and maintain the distance/force between the tip and the sample, and the ability to raster the tip in two dimensions. The feedback system maintains a fixed interaction between the tip and the sample (setpoint) by analysing the deflection of the cantilever and modulating the height (Z) piezo, while the tip is rastered across the surface by the scanning (X and Y) piezos. By maintaining a constant tip-sample interaction, the tip tracks over the topography of the sample and the extension of the Z-piezo provides an image of the surface topography.

1.1.3.1 Feedback

The tip-surface interaction provides a mechanism to maintain a constant separation between the tip and the sample. In order to obtain surface topography, the tip must scan the surface maintaining this constant separation. As the tip scans, the tip-surface interaction changes as the separation increases or decreases depending on the topography. This change in interaction is measured as a signal (cantilever deflection, amplitude, phase etc...) and the Z-piezo alters the height of the tip to keep this signal constant, thus maintaining constant tip-surface separation. This is the process by which the AFM acquires an image, and there are several terms commonly encountered which are explained briefly below.

Lock-in amplifier The lock-in amplifier is effective at extracting a weak oscillating signal at a specific frequency from a noisy background; this is used in the AFM system to precisely monitor the oscillation or deflection of the AFM cantilever during scanning. Because the cantilever deflection changes rapidly during scanning, the lock-in amplifier is essential for extracting the important deflection signal which is critical for tracking the surface.

Setpoint In order to effectively track the sample surface, a constant tip-sample interaction must be maintained. This corresponds to a constant deflection signal, and the value chosen for this is called the setpoint. For imaging where the cantilever deflection is measured, higher setpoint corresponds to greater force exerted on the sample surface.

Feedback gain As the tip scans, the height piezo must react quickly to changing topography and this is achieved through the use of a PID controller. The PID controller defines the reaction speed of the height piezo to variations in the cantilever deflection, and there are three different gains which determine how rapidly the system reacts. These are the proportional, integral and differential gains and most common AFM systems only use the proportional and integral gains for feedback. Imaging of rough topography or with high speed generally requires high gain values, however gain values that are set too high will result in strong oscillation as the system reacts too quickly.

1.1.3.2 Imaging modes

The AFM has been developed substantially since it was first introduced, and is capable of imaging with a wide variety of modes. This section introduces the most commonly used imaging modes.

Contact mode This is perhaps the simplest of all AFM imaging modes, and was used in the application of the first AFM. In the contact mode, the tip is in static contact with the surface and the cantilever undergoes static deflection by a certain amount, representing the contact force or setpoint. The system maintains constant force as the tip scans across the surface and produces an image. Contact mode has an inherent disadvantage, in that lateral forces are caused by the tip sliding across the surface which can displace loosely-bound sample material and cause a high rate of tip wear. Despite this disadvantage, contact mode remains conceptually and experimentally, the simplest imaging mode available.

Tapping mode Tapping mode is a dynamic imaging technique, whereby the tip is oscillated sinusoidally at its' resonant frequency (often by an additional excitation piezo). The oscillation amplitude generally ranges up to 50 nm and varies with different applications and the type of cantilever. The cantilevers' oscillation is damped by the surrounding medium and also through interaction with the surface. This effect is shown in figure 1.7, which represents the tapping mode equivalent of a force-distance curve.

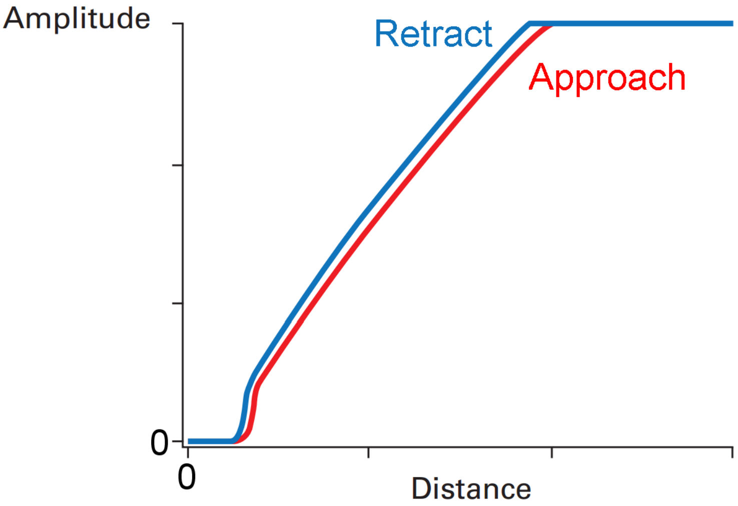

Figure 1.7: Schematic showing the damping of an oscillating cantilevers' amplitude as a result of tip-sample interaction. Reprinted with permission from Bruker corporation [7].

The amplitude of the cantilever is used as the feedback signal, and the feedback system maintains constant amplitude while the tip "taps" the surface. The movement of the height piezo during scanning produces a map of the sample topography in a similar manner to contact mode. Tapping mode addresses the primary shortcoming identified in contact mode, as lateral forces are effectively eliminated. With careful application, tapping mode allows soft/loosely-bound features to be imaged, and also reduces the rate of tip wear.

It is important to understand the forces that are measured by the probe in tapping mode operation, as the interaction between the tip and the surface is not measured directly. During an oscillation cycle the tip moves through the same attractive and repulsive regimes discussed previously, but on a very short timescale. Damping of the cantilevers' oscillation is thus, a function of several different forces including long-range attractive and short-range repulsive forces. The signal monitored in tapping mode is hence an average over the entire oscillation cycle.

Non-Contact mode Non-contact mode is similar to tapping mode in that the cantilever is oscillated at resonance; the difference lies in the feedback mechanism used. While tapping mode utilises damping of the cantilevers' amplitude due to repulsive forces experienced when the tip "taps" the surface, non-contact mode senses attractive forces and never contacts the surface. The cantilever is oscillated with very small amplitude (less than 10 nm), and operated in the regime of attractive van der Waals and other forces which extend up to 10 nm from the sample surface.

These attractive forces experienced by the tip cause the amplitude to reduce, and also result in a shift of the resonant frequency. Most applications of non-contact mode utilise the shift in resonant frequency as the feedback mechanism, as this proves to be the most sensitive measure of tip-sample distance. Non-contact mode often requires very stiff cantilevers and rapid Z-feedback in order to avoid the snap-in feature due to strong attractive forces, and is regularly performed in high vacuum to eliminate the meniscus force.

PeakForce tapping mode PeakForce tapping (PFT) is a relatively new imaging mode, available on Bruker AFM systems as of 2005. There are several companies which offer similar imaging techniques; these include the QI mode developed by JPK instruments and the Pulsed Force mode developed by Witec, which is in some ways an early form of PFT. The work presented herein focuses on the PFT imaging mode, due to its availability during the study, however the basic understanding and applications can be transferred to the other modes.

The motion of the cantilever in PFT mode is actually very similar to tapping mode; the cantilever is oscillated and the tip taps the surface, but at a fixed frequency which is well below the cantilevers' resonance (0.5-8 kHz). Unlike tapping mode, the cantilevers' amplitude is not monitored, but the deflection of the cantilever is recorded instead. As the cantilever repeatedly taps the surface, a force-distance curve is observed with each impact. This results in the observation of thousands of force-distance curves per second, at the same rate as the tapping frequency. The peak force of these force curves is used as the feedback signal.

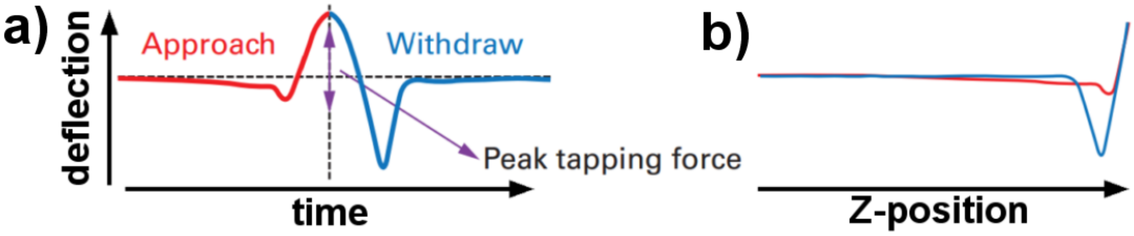

Figure 1.8: Representation of the cantilever deflection signal observed when using PeakForce tapping mode. While undergoing a sinusoidal approach-retract cycle to the surface, the cantilever deflection is shown against a) time and b) tip-sample separation (or Z-position). Reprinted and adapted with permission from Bruker corporation [7].

The deflection signal observed during PFT operation results in curves similar to those shown in figure 1.8. The signal is directly measured as deflection varying with time, and results in the curve seen in figure 1.8a, which is referred to as the "heartbeat" curve by Bruker. After analysis of this deflection signal, the control software identifies the peak force and converts the curve into a deflection vs height signal as seen in figure 1.8b; this results in the familiar shape observed for static force-distance curves.

The advantage of recording and analysing the force curve produced at each tap, is that useful information can be extracted from the signal in a similar manner to static force curves. Simple properties such as deflection sensitivity can be obtained, and with accurate knowledge of the spring constant and tip diameter, further analysis of the force curve can yield information such as adhesion, modulus, energy dissipation and deformation of the sample. Bruker calls this imaging mode PeakForce quantitative nano-mechanical mapping (PF-QNM), and figure 1.9 shows the various regions of the curve fitted to obtain these properties.

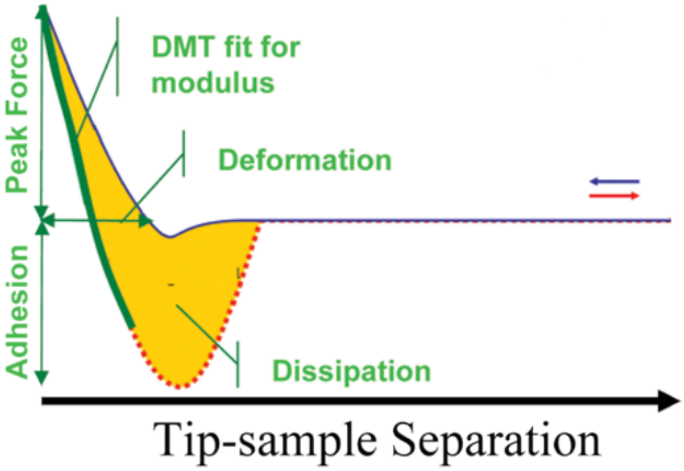

Figure 1.9: An example PFT curve showing regions fitted to extract the various properties of the tip-sample interaction. Reprinted with permission from Bruker corporation [25].

PF-QNM produces quantitative maps of mechanical properties and tip-sample interactions, in addition to the sample topography. Analysis of this type has existed for some time using the force-volume imaging mode, which performs static force-distance curves in an array over the surface of interest. The disadvantage of the force-volume technique is that even with a comparatively small number of measurements (64x64), the acquisition time is prohibitively long. Typical force curves are obtained on a timescale of 0.1-1 s, which results in a total acquisition time of 6-60 min for a 64x64 grid of measurements. The high tapping rate of PF-QNM allows nano-mechanical data to be obtained at the same rate and resolution as standard imaging, with a typical 512x512 point PF-QNM image obtained in ~8 minutes. This represents a significant improvement in both image resolution and acquisition time.

It should be noted that there are certain technical issues associated with quantitative analysis of the PF-QNM signal, reported by the Haviland group at KTH, Sweden [26]. These are associated with filtering of the deflection signal, and it was observed that evaluation of data obtained from soft PDMS layers was challenging with PF-QNM [27].

1.2 AFM cantilever calibration

Calibration of AFM cantilevers generally refers to the measurement of two different properties, whose knowledge facilitate accurate measurement of force. These properties are the spring constant (k) which has already been introduced, and the cantilevers' deflection sensitivity (S) which will be introduced in detail in the following section. The accurate measurement of these values is a highly active field of research, and this section introduces some of the many techniques developed for this purpose.

1.2.1 Assessing calibration techniques

There are a great number of techniques available for cantilever calibration, particularly for determination of the cantilevers' spring constant. In addition to this, the techniques developed vary considerably, covering different areas of physics; as a result, selecting the appropriate technique for a particular cantilever or application can be a challenging task in itself. An overview of the prominent calibration methods is given in the following two sections, however here we aim to introduce the primary considerations for assessing and selecting a particular calibration technique.

Uncertainty Possibly the most important attribute of a calibration method is the degree of uncertainty. Calibration methods are available with varying levels of uncertainty, which arises from the varying sources inherent within each method. In general, calibration methods with low uncertainty (below $\sim$10%) are desirable, however other factors may preclude their application.

Destructiveness Calibration techniques can be separated into two categories, based on whether they are destructive (or potentially destructive) to the cantilever, or not. The term "destructive" is somewhat ambiguous however, as this could range from minor damage to the tip to complete destruction/removal of the entire cantilever. The degree of damage depends on the technique itself, and also on the skill of the operator. In contrast there are calibration methods which offer no potential damage to the cantilever, these are often theoretical methods which are based on dimensional and material properties.

Ease-of-use The "ease of use" is an important consideration for a calibration method to become routine. Techniques which are simple to apply have several advantages in that they promote rapid and widespread adoption, and that simple application often reduces the probability of damaging the cantilever or applying the technique incorrectly.

Applicability Many calibration methods are limited to certain types of cantilevers. For example, techniques which determine the spring constant based on material properties of the cantilever are poorly suited to cantilevers composed of silicon nitride. Uncertainty in the Young's modulus of the silicon nitride causes significant uncertainty in the spring constant if these methods are used. There are also several geometric techniques which are derived from beam theory for rectangular cantilevers.

Application of these methods to other geometries (ie. V-shaped, triangular, trapezoidal) often results in significant uncertainty. It is important that a technique can be applied to a wide range of cantilevers, given the many different types in use.

Cantilever uniformity Following on from the consideration of technique applicability, this is often dependent on the geometry of the cantilever. An important factor to consider is that many theoretical methods rely on beam theory, and assume that the cantilever has an ideal beam shape. Non-uniformity is regularly observed for practical cantilevers, and certain methods are impacted by this to a greater degree than others.

Calibration techniques which are based on geometric modelling tend to be highly affected, whereas methods which measure the spring constant directly tend to be affected to a lesser extent or not at all. This is an aspect which should be considered on the basis of each technique, and is discussed in detail in the following section. Here, the non-uniformities most commonly observed are introduced.

One of the most common forms of non-ideal geometry is the presence of a trapezoidal cross-section, this can be observed in figure 1.10 and is a result of dynamic etching processes used by manufacturers to achieve high-aspect ratio tips [28]. Trapezoidal beam geometry represents a controlled deviation from ideal dimensions, however cantilevers often exhibit non-uniformity in many other areas. Variation in both the thickness and width can often be observed along the length of the cantilever.

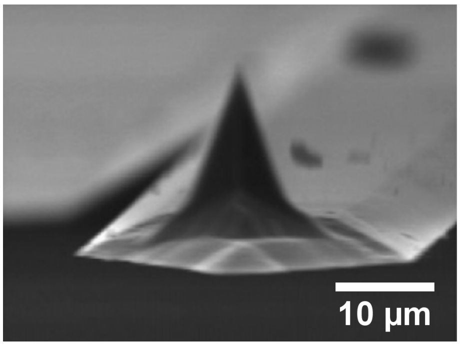

Figure 1.10: SEM image of a Veeco FESP type cantilever, showing the trapezoidal geometry of the cantilevers' cross-section. Reprinted with permission from [28]. Copyright 2015 American Chemical Society.

Cantilevers fabricated with "perfect" geometry are commercially available, which are specifically designed with precise dimensions for spring constant calibration (ie. Bruker tipless CLFC-NOBO type), however these are too expensive to be used for practical applications and don't include an imaging tip.

1.2.2 Deflection sensitivity calibration

In most commercial AFMs, the deflection of the cantilever is measured using the optical lever or beam bounce technique, a schematic of this type of detection system is shown in figure 1.11. The laser is focused onto the back of the cantilever, and deflection of the cantilever causes the reflected laser spot to move on the photodiode, which is measured as an electrical signal. Quantities such as deflection, setpoint and oscillation amplitude are, hence, measured in units such as volts which is ambiguous. To determine the actual deflection of the cantilever in nanometers, the deflection sensitivity must be determined. This quantity relates the actual deflection of the cantilever (in nanometers) to the displacement of the laser spot on the photodiode (in Volts), and generally has units of nmV^{-1}.

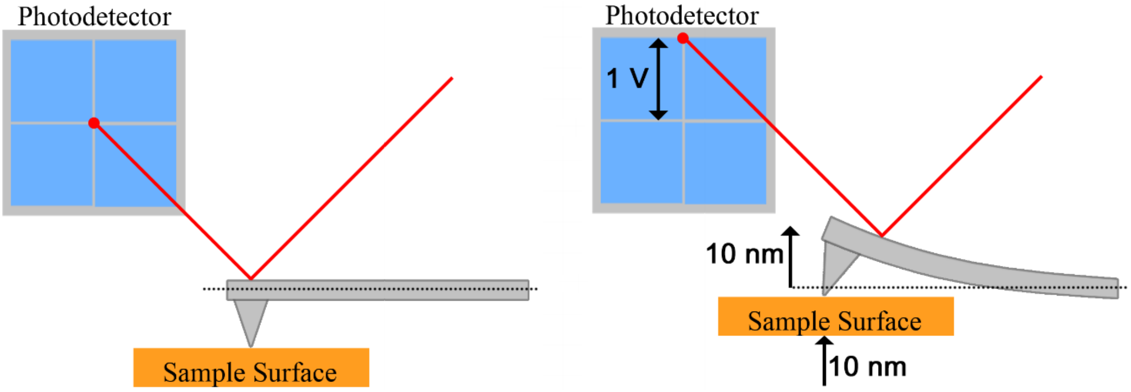

Figure 1.11: Schematic of the optical lever detection system used in most AFMs, showing a cantilever with deflection sensitivity of 10 nmV^{-1}.

The deflection sensitivity depends on a number of factors including the dimensions of the cantilever, the location of the cantilever in the beam path and the size and location of the laser spot on the cantilever. These factors almost always change between individual cantilevers, and also each time the same cantilever is re-mounted inside the AFM; as a result, calibration of the deflection sensitivity is common practice in AFM operation.

The simplest method to determine the deflection sensitivity is by performing a static force-distance curve on a surface which has negligible deformation. After contact with the surface, the deflection of the cantilever is assumed to be equal to the extension of the Z-piezo and the corresponding deflection of the laser spot on the photodiode is recorded. The deflection sensitivity is then determined by taking the slope of the force-distance curve in the contact regime.

In practice, for silicon and silicon nitride probes, a single crystal silicon surface provides a reasonably incompressible surface for cantilevers with soft to medium spring constant. For cantilevers with high spring constant (i.e. nano-indentation probes), a sample with very high modulus is desirable (ie. sapphire). These surfaces also need to be flat and clean so as to minimise the effect of surface roughness or contaminants on the measured deflection sensitivity.

1.2.2.1 Sources of uncertainty

This method of sensitivity calibration (referred to here as the “hard surface contact” method) has many advantages, in particular that it is simple and can be performed in-situ. Although the method is simple to implement, there are several potential sources of uncertainty which must be minimised.

Piezo calibration Calibration of the AFM Z-piezo is a direct source of uncertainty, which can significantly affect the deflection sensitivity. This is not typically a serious limitation, as long as accurate calibration standards are used periodically to maintain instrument calibration.

Laser position and heating Laser spot positioning on the cantilever is very important, since movement of the laser spot will alter the deflection sensitivity. Cumpson et al. have reported laser spot movement on the order of microns due to cantilever heating, which causes significant cantilever deflection [29]. While AFM cantilevers are very small and rapidly dissipate heat, many are metal-coated to improve laser reflectivity. This causes the cantilever to behave as a bimetallic strip, and so coated cantilevers can be very sensitive to temperature variation.

In addition to laser heating, resistive heating from the AFM electronics can also increase the temperature of the cantilever. Te Riet et al. measured the temperature of contact mode cantilevers and noted a 6°C increase compared to the ambient room temperature [30]. This heating effect will be particularly significant for metal-coated cantilevers with low spring constant, such as those typically employed for force measurement. This effect can be minimized by aligning the cantilever and then allowing time (30 minutes or more) for the system to equilibrate thermally with its' environment.

Hysteresis There are a number of factors introduced in section 1.1.2.1 which can cause hysteresis in the contact region of the force curve, affecting the sensitivity measurement. Recent work by Pratt et al. has shown that simply averaging the approach and retract slopes provides a good approximation which can account for these effects [31]. Therefore, when using the hard surface contact technique it is important to take an average of the approach and retract slopes for each sensitivity measurement.

Tip Damage Whilst it is important to use a hard sample for sensitivity calibration, applying the standard calibration method in this manner can result in significant tip damage [32–34]. The tip of most new AFM probes ranges in sharpness (end radius) from 5-20 nm. The application of seemingly small forces to such a sharp tip can result in extremely high pressure due to the nanoscale interaction area.

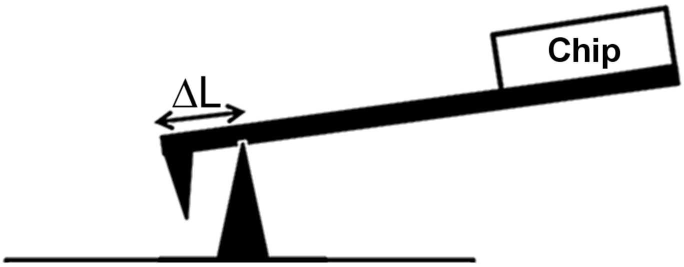

Figure 1.12: Non-destructive measurement of the deflection sensitivity using an inverted sharp tip. Reprinted and adapted with permission from [35]

This is of particular concern for delicate tips which have been functionalised with molecules or biological species [36] and those with carbon nanotube [37] or ultra-sharp silicon tips [33]. In order to reduce the destructiveness of sensitivity calibration, there have been several approaches developed which eliminate tip-sample contact, these are introduced in section 3.3 along with advances reported in this work.

1.2.3 Spring constant calibration

There are many different methods available to measure the spring constant of a micro-cantilever. New methods and variations on existing methods are regularly reported in the literature, driven by the goal to improve many of the aspects covered at the beginning of this section. Provided here is an overview of well-established calibration methods, which are of particular relevance to this work.

1.2.3.1 Euler beam method

The Euler-Bernoulli beam equation is used extensively in engineering applications to model the displacement behaviour of beams, and has been successfully applied to determine the mechanical properties of microcantilevers in AFM and MEMS (microelectromechanical systems). This equation is widely used in the field of AFM, and warrants a detailed derivation which is presented here.

The Euler beam equation arises from several components of beam theory, which are introduced briefly in the following paragraphs. The derivation assumes a simple beam fixed at one end, with rectangular cross section and axes defined as shown in figure 1.13. The force on the cantilever (p) is defined per unit length and in the direction of the y-axis.

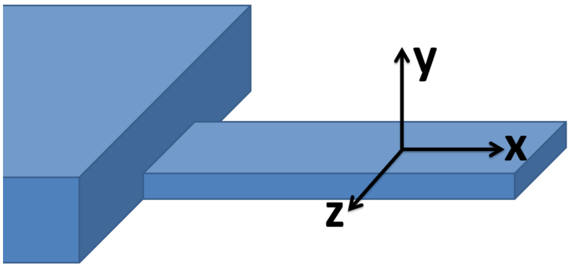

Figure 1.13: Schematic showing the cantilever and axes assumed for the derivation of the Euler-Bernoulli beam equation.

Constitutive The direct stress and strain within the beam are described by the constitutive equation, for which Hookes law for continuous media is used. This relates the stress (σ) and strain (ϵ) over the cross section of the beam, where E is the elastic modulus of the material. Note that the expressions for stress and strain used in this derivation are those for the uniaxial case only.

$$\sigma(x, y) = E \cdot \epsilon(x, y) \tag{1.6}$$

Kinematics Motion of the beam is described by equation 1.10, which ultimately relates the beams' displacement from the neutral position (w) to its bending deflection (χ). The deflection is measured as the angular variation of a normal to the surface of the beam, and is equal in magnitude but opposite in sign to the angular deflection along the long axis of the beam as shown in figure 1.14.

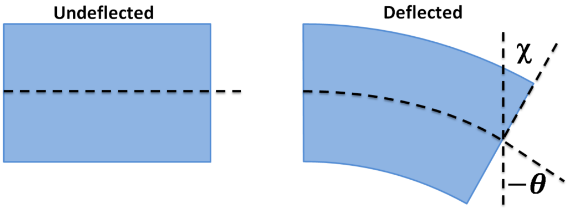

Figure 1.14: Schematic showing the angular deflection of a small portion of the beam.

The direct strain in the beam can be represented as follows, knowing the displacement in the x direction across the beam cross section:

$$\epsilon = \frac{du}{dx} \tag{1.7}$$

This derivation is governed by several assumptions however (Kirchoff assumptions), which relate to lines normal to the beams' neutral axis plane (plane including the x and z axes). The assumptions are that the normal lines are always straight, do not stretch and are always normal to the neutral axis. These assumptions allow negligible strain in the y direction to be assumed, and the following expression can be written where the x and y dependence in $u(x, y)$ is explicit:

$$u(x, y) = \chi(x) \cdot y \tag{1.8}$$

Using the expression above, the direct uniaxial strain in the beam can now be written as:

$$\epsilon(x, y) = \frac{d\chi}{dx} \cdot y \tag{1.9}$$

Additionally, the assumptions relating to the normals within the beam allow the following expression to be written for the beams' displacement, where x is the displacement in the x-axis through the cross section, and w is the beams' displacement in the y-axis.

$$\chi = -\theta = -\frac{dw}{dx} \tag{1.10}$$

Resultants It is convenient to describe the uniaxial stresses within the beam in terms of a single variable, and this can be accomplished through the use of resultants. Two resultants are obtained by summing the contribution of the individual moments and shear stresses over the cross section of the beam. The expressions for the total bending moment ($M(x)$) and total shear stresses ($V(x)$) are shown below.

$$M(x) = \int \int y \cdot \sigma(x, y) \cdot dy \cdot dz, \qquad V(x) = \int \int \sigma(x, y) \cdot dy \cdot dz \tag{1.11}$$

Equilibrium External load on the beam results in internal stresses, which reach an equilibrium as the beam reaches a steady state. Equilibrium of the shear stress and moment are both considered, and resultants are again used due to their simplicity. These equilibriums are described in the equations below.

$$\frac{dM}{dx} = V, \qquad \frac{dV}{dx} = -p \tag{1.12}$$

Euler-Bernoulli beam equation Combination of the above expressions allows us to arrive at the familiar Euler-Bernoulli beam equation. Combining the equilibrium equations eliminates the shear stress term.

$$\frac{d^2M}{dx^2} = -p \tag{1.13}$$

Substituting the expression for the total bending moment then provides:

$$\frac{d^2}{dx^2}\int\int y \cdot \sigma(x,y) \cdot dy \cdot dz = -p \tag{1.14}$$

The constitutive relation is then used to write this expression in terms of strain:

$$\frac{d^2}{dx^2}E\int\int y \cdot \epsilon(x,y) \cdot dy \cdot dz = -p \tag{1.15}$$

To arrive at a measurable quantity, the strain is then converted to the bending angle χ using equation 1.9.

$$\frac{d^2}{dx^2}\left[E\frac{d\chi}{dx}\int\int y^2 \cdot \sigma(x,y) \cdot dy \cdot dz\right] = -p \tag{1.16}$$

The kinematics expressions are again used by substituting equation 1.10, to arrive with an expression containing the displacement of the cantilever.

$$\frac{d^2}{dx^2}\left[E\frac{d^2w}{dx^2}\int\int y^2 \cdot \sigma(x,y) \cdot dy \cdot dz\right] = p \tag{1.17}$$

By recognising that $\int\int y^2 dydz$ is the beams' moment of inertia, and assuming that the Young's modulus and moment of inertia do not vary along the length of the beam, the Euler-Bernoulli beam equation can be written in its familiar general form shown below.

$$EI\frac{d^4w}{dx^4} = p \tag{1.18}$$

In the case considered here, that of an AFM cantilever with rectangular cross section and point loading at the free end of the beam, $p = 0$ and repeated integration of equation 1.18 yields:

$$w(x) = \frac{1}{6}c_1x^3 + \frac{1}{2}c_2x^2 + c_3x + c_4 \tag{1.19}$$

The following boundary conditions are then applied, which allow the constants to be determined as shown in equations 1.21

$$w(0) = \theta(0) = 0, \qquad EI\frac{d^2w(L)}{dx^2} = 0, \qquad EI\frac{d^3w(L)}{dx^3} = -F \tag{1.20}$$

$$c_3 = c_4 = 0, \qquad c_1 = -\frac{F}{EI}, \qquad c_2 = -\frac{FL}{EI}, \tag{1.21}$$

Substituting these back into equation 1.19, we arrive at the following expression:

$$w(L) = \delta = \frac{FL^3}{3EI}, \qquad F = \frac{3EI}{L^3}\delta \tag{1.22}$$

Considering that $F = k\delta$, and that the moment of inertia for the beam is $I = \frac{wt^3}{12}$, the following expression for the normal spring constant can be written.

$$k = \frac{Et^3w}{4L^3} \tag{1.23}$$

The spring constant can be determined simply by knowing the physical dimensions of the cantilever and its composition, using equation 1.23.

The Euler-Bernoulli beam method is applicable to rectangular cantilevers, and can be highly accurate when the cantilever has perfect rectangular shape and well-defined material properties (ie. single crystal silicon). Application of this method to V-shaped cantilevers is also possible through corrections reported in the literature, although at the cost of additional uncertainty [12, 13].

Uncertainty in the method is generally dominated by non-uniformity in the cantilever dimensions, or by inaccurate knowledge of the cantilevers' Young's modulus (ie. silicon nitride cantilevers and those with metal coatings). Poggi et al. reported a correction to the method for cantilevers with trapezoidal cross-section, which allows this method to be applied with improved accuracy to a wider range of cantilevers [28]. Of course uncertainty in measurement of the cantilevers' dimensions also contributes to the overall uncertainty. Accurate measurement of the cantilevers' thickness can be particularly difficult since this is usually on the order of 0.5-5 μm, which adds significant uncertainty due to this term being cubed.

1.2.3.2 Cleveland formula

The Cleveland formula is a resonance method which eliminates the requirement to determine the cantilevers' thickness, by combining equations 1.23 and 1.29 [38].

$$k = 2\left(\pi\nu L\right)^3\sqrt{\frac{\rho^3_{lever}}{E}} \tag{1.24}$$

This method is best suited to silicon cantilevers with known crystal orientation and beam-shaped geometry. Uncertainty arises due to metal coatings affecting the cantilever density, air damping of the resonant frequency and the mass of the tip if it is a significant fraction of the cantilever mass.

1.2.3.3 Cleveland added mass method

The Cleveland added mass method determines the dynamic spring constant of an oscillating cantilever, by observing the reduction in resonant frequency as a result of damping by an added mass [38]. Treating the cantilever as a simple harmonic oscillator, a simple relationship between loading mass and resonant frequency can be determined.

$$M = k(2\pi\nu)^{-2} - m^* \tag{1.25}$$

Equation 1.25 shows that if mass is incrementally added to the cantilever, the relationship with $(2\pi\nu)^{-2}$ should be linear in nature. A plot of these terms should be linear with the slope being equal to the spring constant and the y-intercept equal to the cantilevers' effective mass. Cleveland et al. showed that this relationship is indeed linear and thus the spring constant and effective mass can be determined by measuring the resonance shift due to a single added mass (M_{sphere}). The expression for determining the spring constant in this manner is given by equation 1.26 and represents one of the first spring constant calibration methods developed.

$$k = \frac{4\pi^2 M_{sphere}}{\nu_1^{-2} - \nu_0^{-2}} \tag{1.26}$$

The added mass method is traditionally performed by affixing a microsphere (tungsten or gold) with mass significantly greater than the mass of the cantilever, to the end of the cantilever using a micromanipulator and adhesive [5]. This highlights one disadvantage of the method, in that the attachment of the microsphere is a delicate and potentially destructive process. The presence of the microsphere can also interfere with measurements made after calibration, as can be seen in figure 1.15.

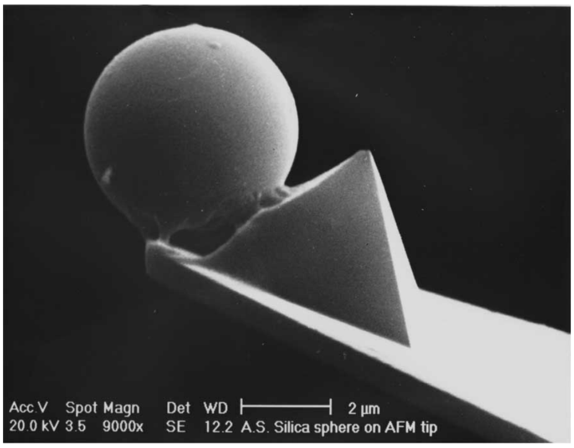

Figure 1.15: SEM image of an AFM cantilever with a silica microsphere attached for colloidal force measurement, showing the glue used for attachment. Reprinted with permission from [39].

A significant portion of the uncertainty in this method arises from determining the mass of the added microsphere, as these are not necessarily spherical and in many cases, optical microscopy is often used to determine the volume. The additional mass of the adhesive is also difficult to quantify and further adds to the uncertainty. There have been several adaptations to simplify the loading procedure and reduce uncertainty in the method. One such example is coating the entire cantilever with a gold layer of well defined thickness, by sputter deposition [40, 41].

1.2.3.4 Sader hydrodynamic method

Developed by Sader et al., the Sader hydrodynamic method determines the cantilevers' spring constant according to its' resonant frequency (ν), plan view dimensions (L and w), density (ρ), Q factor (Q) and the imaginary component of the Reynolds number (Γ) [42]. A web tool is available on the internet at `http://www.ampc.ms.unimelb.edu.au/afm/calibration.html` for simple application of the technique, which determines the spring constant using equation 1.27.

$$k = 0.1906 L w^2 \rho_f Q_f \Gamma_i (2\pi\nu)^2 \tag{1.27}$$

The Sader hydrodynamic method has been widely adopted, owing to its ease of use and non-destructive nature. There are several potential sources of uncertainty, which include non beam-shaped cantilever geometry, measurement of the Q-factor and variation in the density of the surrounding medium. The technique requires the cantilever to have a length/width ratio which is greater than 3, unfortunately there are certain short tapping mode cantilevers for which this is not the case.

Sader hydrodynamic (arb. shapes) The Sader hydrodynamic method is based on fluid dynamics, and was initially only applicable to beam-shaped cantilevers [42]. The technique has recently been extended to cantilevers of arbitrary shapes, where the spring constant of an accurately calibrated "standard" cantilever can be transferred to other cantilevers of the same geometry [43]. The equation for calibrating cantilevers of arbitrary shape is as follows:

$$k_{tip} = k_{standard} \frac{Q_{test}}{Q_{standard}} \left(\frac{\nu_{test}}{\nu_{standard}} \right)^{1.3} \left(\frac{L_{tiptest}}{L_{tipstandard}} \right)^{3} \tag{1.28}$$

Where k, Q and ν are the spring constant, Q-factor and resonant frequency for the test or standard cantilever respectively. The term $\left(\frac{L_{tiptest}}{L_{tipstandard}} \right)^{3}$ is a correction required if the tip location on the test cantilever is different to that for the standard.

The method is simple to apply and scales the spring constant based on the ratio of the Q-factor and resonant frequency of the two cantilevers. Uncertainty in the method depends upon the error on the standard cantilever, the geometric similarity between the standard and the test cantilever, and any inherent uncertainty in the method. Sader and Friend recently validated this technique [44, 45], while Ergincan et al. performed further validation by applying the method to conventional cantilevers with nanostructured surfaces [46].

1.2.3.5 Sader resonance

The Sader resonance method determines the spring constant by scaling from the resonant frequency, relying on the effective mass of the cantilever [5].

$$k_{end} = nAt\rho_{lever} \left(2\pi\nu_0 \right)^2 \tag{1.29}$$

Here, A and ρ_{lever} are the cantilevers' plan view surface area and density respectively. The effective mass is related to the actual mass by the correction factor n, which depends on the cantilevers' geometry. For beam-shaped geometry n=0.242, while for V-shaped geometry n is determined using tables supplied by Sader et al. [5]. Similarly to the Euler beam equation, the measurement of cantilever thickness and high density metal coatings can introduce uncertainty. A distinct advantage is that this method has a linear dependence on the cantilever thickness, reducing this dimensional uncertainty compared to the Euler beam method.

1.2.3.6 Thermal method

The thermal method was developed by Hutter and Bechhoefer, and uses the equipartition theorem to relate the cantilevers' spring constant to the mean square of its thermally-excited vibrational amplitude [47]. The spring constant can be determined using equation 1.30.

$$k = \frac{k_B T}{\langle d_c^2 \rangle} \tag{1.30}$$

This method has been widely implemented and is available as a feature on many commercial AFM systems, as it is simple to apply, can be performed in-situ by the AFM prior to measurements and is applicable to a wide range of cantilevers. Once the deflection sensitivity of the cantilever is known, the oscillation of the cantilever can be measured accurately by the AFM, and the spring constant determined. The thermal method is reported to be applicable only to "soft" cantilevers with a spring constant below 1 Nm^{-1}, which is regarded as a limitation of the technique [48].

The thermal noise spectrum is typically observed to have Lorentzian shape, and is fitted to extract the various useful parameters (such as resonant frequency, Q factor and spring constant). This fitting process is carried out automatically in most cases, however there can be significant uncertainty associated with this often overlooked aspect of the method. Sader et al. recently investigated the uncertainty associated with the various fitting parameters and reported formulas which enable estimation of these uncertainties [49].

There are a number of corrections which must be applied to the thermal method, these account for the tip height and cantilever tilt [47], dynamic-static spring constant conversion [50], sensitivity correction [48] and laser spot position [51]. These corrections are often grouped into a single value known as the Chi factor [52, 53]. The thermal noise method has an inverse square relationship with this Chi value, and for beam-shaped cantilevers the recommended value is 1.106, whereas 1.144 is generally used for V-shaped cantilevers [52].

The Chi factor for V-shaped cantilevers has been derived from finite element analysis by Stark et al., but was determined for a specific V-shaped geometry [54]. Only recently has a study been conducted to verify whether this correction is appropriate for the wide variety of V-shaped cantilever geometries available. Sader et al. measured this correction for a range of rectangular and V-shaped geometries [55]. It was found that the sensitivity ratio varied considerably, resulting in errors of over 100% if the incorrect value was used.

1.2.3.7 Reference cantilever method

The reference cantilever method determines the spring constant of an uncalibrated "test" cantilever using an accurately calibrated reference cantilever [56–60]. Transfer of the calibration is achieved by measuring the deflection sensitivity of the test cantilever, and then pressing the test cantilever against the reference cantilever as shown in figure 1.16.

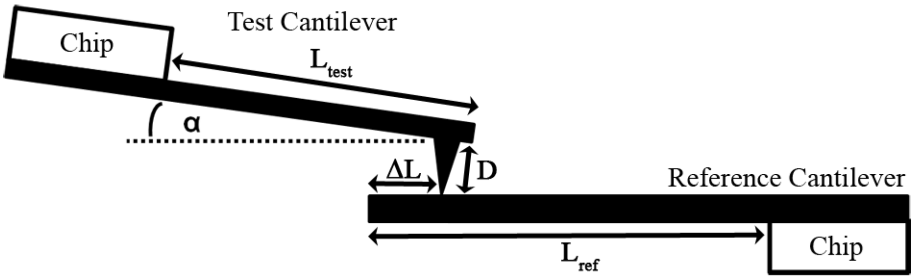

Figure 1.16: Schematic showing the application of the reference cantilever method. Reprinted with permission from [2].

Once the slope of the force curve has been measured for a hard surface and on the reference cantilever, the spring constant of the test cantilever can be determined using equation 1.31. The $\cos^2\alpha$ term accounts for the approach angle of the cantilever which is necessary since most AFM systems impart a 10^o tilt to ensure the imaging tip contacts the surface first.

$$k_{test} = k_{ref}\left(\frac{S_C}{S_H} - 1\right)\cos^2\alpha\left(\frac{L - \Delta L}{L}\right)^3 \tag{1.31}$$

The off-end loading correction term is used here because the reference spring constant used (k_{ref}) must be accurate for the contact position of the test cantilever. Figure 1.31 shows that this is not necessarily the end of the cantilever (where the spring constant is often specified), and so this value must be corrected. Determination of the contact position (ΔL) is generally achieved using the AFM's inbuilt optical microscope, and generates significant uncertainty.

The off-end loading correction is derived for a perfect rectangular beam, however in practice it can be applied as an approximation to V-shaped cantilevers. It should be noted that previous research has demonstrated that significant uncertainty can be introduced when $\frac{\Delta L}{L} > 0.20$ [12–14].

An additional correction may be required when the height of the tip is comparable to the length of the cantilever. This correction is shown in equation 1.32 and accounts for the torque produced due to the height of the tip [58, 61]. For the majority of probes, this term is equal to 1 since D is much smaller than L_{test}. However, for certain types of probes (e.g. Mikromasch NSC15), this will be significant and can reduce the measured spring constant by up to 4%

$$1 - \tan(\alpha)\frac{3D}{2L_{test}} \tag{1.32}$$

It is important that the deflection in the test and reference cantilevers is similar during the measurement. If one cantilever has a significantly greater spring constant, then only the softer cantilever will exhibit a measurable deflection. This introduces significant uncertainty and Gibson et al. suggest that the spring constants of the two cantilevers should be within $0.3 < \frac{k_{test}}{k_{ref}} < 3$ to keep uncertainty at an acceptable level [56]. The range of the reference cantilever method may be larger than this, however, as suggested in recent work by Pratt et al. and Clifford et al. [31, 58]. Many probe manufacturers offer tip-less cantilevers specifically designed as reference cantilevers, which have an array of different spring constants with ideal geometry such that they may be calibrated with high accuracy by various theoretical methods.

1.3 Advanced AFM

1.3.1 Carbon nanotube probes

Carbon nanotubes (CNTs) have been recognised as the ultimate probe for use in many AFM applications, due to their small diameter, high aspect ratio and wear resistance [62–64]. Many different methods to fabricate CNT AFM probes have been reported, however often these techniques have utilised multi-walled carbon nanotubes (MWCNTs) in contrast to smaller diameter single-walled carbon nanotubes (SWCNTs). This is in-part due to the difficulty in fabricating these probes and although SWCNT AFM probes are commercially available, they command a price up to 55 times that of standard silicon AFM probes [65]. This high cost is largely due to the attachment procedure and processing required by the manufacturer to inspect individual probes and further modification to stabilise the attached CNT.

Strategies for CNT attachment have included direct growth of the CNT on the silicon AFM tip by chemical vapour deposition (CVD) [66, 67], manual attachment using optical or electron microscopy [62, 68–71], random pick-up from CNT-covered surfaces [72–74] and dielectrophoresis [75, 76] among others [77]. A review by Wilson et al provides an excellent overview of the many fabrication methods and applications of CNT probes [78].

A long-standing goal in the field of AFM has been the batch-production of CNT probes for commercial fabrication, which would allow probes with extremely high resolution to be made at an affordable cost. There have been several reports of progress in this area, where CVD processes have been used to grow CNTs on arrays of AFM probes [67, 79–81]. Although CVD processes are able to produce CNT probes in batches, there is little control over the length and orientation of the protruding nanotube which, in addition, is often not rigidly attached to the tip. Parameters such as length, orientation, diameter and stability of the nanotube are all of high importance [82]. These factors makes mass production of high-quality CNT probes very difficult, as the probes are not suitable for imaging without extensive and individual processing. For these reasons, CNT probes remain very expensive and highly specialised.

1.3.1.1 CNT probe fabrication methods

Drawing similarities with the variety of spring constant calibration methods available, there have been many different approaches reported for the fabrication of CNT AFM probes. An overview of the common fabrication approaches is provided here.

Manual assembly The very first CNT probes were fabricated by Dai et al., who used a micromanipulator to attach large MWCNTs under an optical microscope [62]. This method has since been used to produce robust MWCNT probes, which do not necessarily possess the small tip diameter of SWCNTs, but are well-suited to functionalisation, indentation and other applications where SWCNTs may be damaged or unstable [83, 84]. A logical step to improve the resolution of this technique is to shift the process into a micromanipulator-equipped SEM, allowing smaller CNTs to be manipulated with greater precision. Nishijima et al. were the first to achieve this with MWCNTs, using electron beam-induced deposition (EBID) to fix the CNT to the tip with carbon [85]. While manual attachment is by no means a batch fabrication process, the superior control over fabrication produces functional probes with high yield and very high quality.

There have since been several reports of SEM-assisted manual attachment [68–70, 85] and the general process used in addition to the challenges encountered will be discussed here in detail. Bringing the CNT into contact with the AFM probe is the first step in the attachment process, and this can usually be achieved using the SEM focus to determine the relative distance between the two objects. When the CNT is near to the AFM tip, attachment of the CNT is quite evident as attractive electrostatic and Van Der Waals forces often cause the nanotube to snap into contact with the tip.

For CNT probes fabricated using the CVD process, it is these attractive Van der Waals forces which keep the CNT attached. While these forces are relatively strong (particularly for long CNTs with large contact areas), the forces experienced during AFM imaging can be comparable, especially during initial tip engagement on the sample. This force can cause the nanotube to shift, which results in an unstable probe, or even detach entirely. In order to ensure firm attachment of the CNT to the AFM tip, EBID is often used to deposit materials such as carbon or platinum at the nanotube-tip contact area [69, 70, 85].

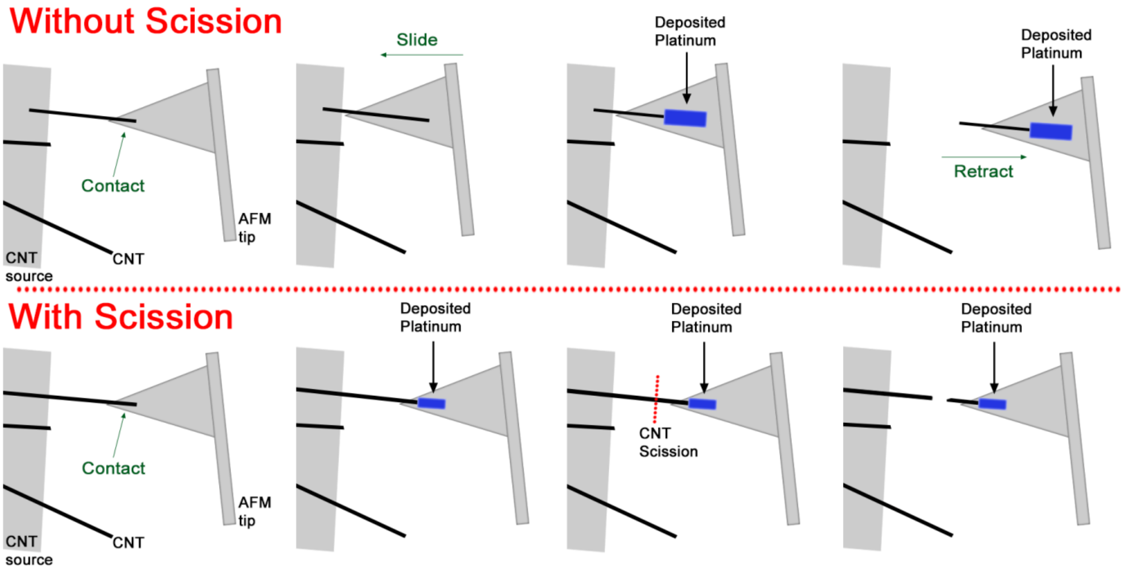

Figure 1.17: Schematic showing two possible methods of manual CNT attachment, one with and one without a technique to cut the nanotube. Reprinted with permission from [86].

The length of the CNT protruding from the probe is an important factor for stable imaging, and once the nanotube bridges the CNT source and the AFM probe, the length must be adjusted. Prior to fixing with material from EBID, it is possible to slide the CNT along the probe until the desired length is achieved. The nanotube is then affixed using material from EBID and the tip is retracted with the nanotube attached. This process is only effective for rigid CNTs (often thick MWCNTs) as thin CNTs are very flexible. Once contact is achieved, the adhesive forces cause flexible CNTs to bend rather than slide along the probe surface. In addition, the minimum length attainable is limited by the total length of the nanotube and the length of the nanotube attached to the CNT source. As a result, unless the nanotube is rigid, has a small portion attached to the CNT source and is not strongly affixed to the source, some form of scission will be required to adjust the nanotubes' length as shown in figure 1.17.

There are several methods which have been employed to adjust the length of CNTs; one of the simplest is to pass a current through the nanotube, causing it to heat locally at a defect site along the tube and sever at this random location, highlighting the main disadvantage of this method [87, 88]. A more direct approach was developed by Wei et al., who used a carbon nanotube "nanoknife" to cut and sharpen CNTs inside a SEM [89]. By applying a bias to a short CNT mounted on the end of a tungsten manipulator needle, the nanotube could be used to cut and sharpen other nanotubes with ease.

Carbon nanotubes can be cut rapidly using a focused ion beam, which has also been used to alter the alignment of the nanotube [70, 90]. Chang-Soon et al. reported that MWCNT fibers attached to AFM probes straightened and aligned in the direction of the ion beam, and used this to improve the imaging stability of their fibers [90]. While ion beam irradiation results in a highly aligned CNT, the damage caused to the nanotube at the point of cutting is substantial. Raghuveer et al compared transmission electron microscopy (TEM) images of MWCNTs before and after ion beam irradiation and observed that the resulting structure is effectively a carbon nanorod as can be seen in figure 1.18 [91].

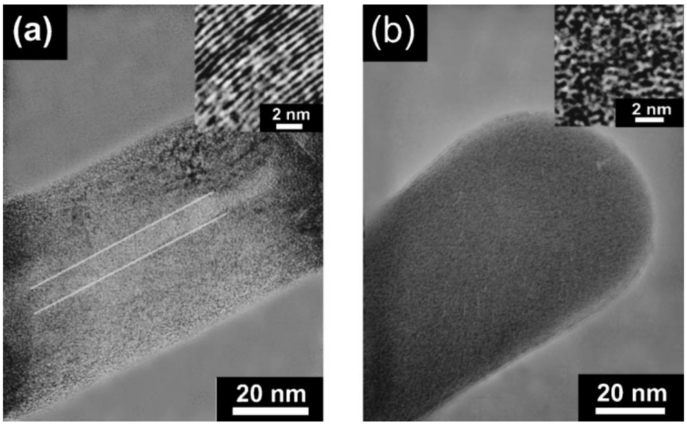

Figure 1.18: TEM images of a MWCNT before a) and after b) exposure to 10^{-17} cm^{-2} of 30kV Ga^{+} ions. Reprinted with permission from [91]

Rather than imaging and cutting with a highly destructive ion beam, damage to the CNTs can be minimized by cutting with an electron beam. Yuzvinsky et al. reported the cutting of MWCNTs with a low-energy electron beam in a SEM [92]. Water vapour was introduced into the chamber during the cutting process, which was observed to result in cutting rates increased by up to ten times. Scanning the electron beam perpendicularly to the CNT resulted in a precise cut which was 40 nm wide, using a beam diameter of 3 nm. TEM imaging of the region before and after the cutting process showed that damage to the surrounding CNT was minimal, making this an ideal process for cutting CNTs within a SEM.

Shortly after, Martinez et al. reported the attachment of MWCNTs to AFM probes in a SEM using a micromanipulator, affixing them with carbon deposited by EBID and subsequently cutting the CNTs to the desired length using the electron beam [69]. Their cutting process was reported to take ~2 minutes before the carbon bonds started to break, and under an applied potential difference of 2 V (DC) the MWCNTs could be sharpened at their end to a diameter comparable to a SWCNT.

Chemical vapour deposition CVD is one of the primary methods by which CNTs are commercially maufactured in bulk quantities. The CNTs grow from catalytic nanoparticles (ie. iron) at high temperature in the presence of a carbon containing species (ie. acetylene). By decorating an AFM tip with catalytic nanoparticles, CNTs can be grown directly onto the tip and used for imaging.

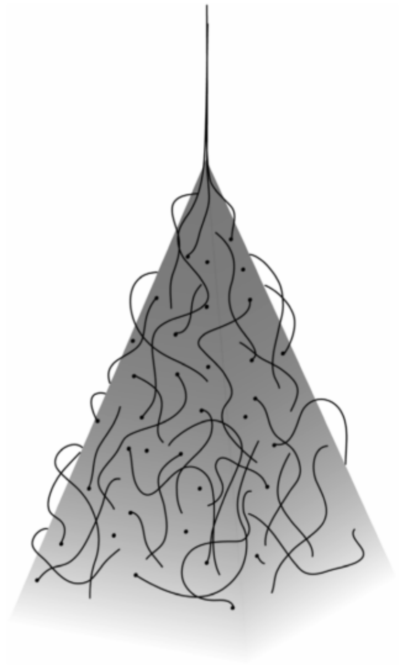

Figure 1.19: Schematic of CNT growth on the surface of an AFM tip, as a result of CVD growth [67]. © IOP Publishing. Reproduced with permission. All rights reserved.

This method is capable of producing very sharp AFM tips with narrow single-walled CNTs, however there are also a number of disadvantages to the method. Primarily, the control over the nanotube length and alignment is quite poor. Figure 1.19 illustrates the manner in which CNTs grow on an AFM tip, and illustrates the random manner by which the alignment occurs. A benefit of the CVD technique is that batch fabrication is possible, and a detailed study by Edgeworth et al. investigated the optimum parameters to obtain a high proportion of “good quality” CNT probes. Under the optimum fabrication conditions, 80% of 97 tips exhibited straight CNT structures [67]. This optimisation enables much higher fabrication efficiency and moves closer to batch fabrication, however there remains the issue of length control and attachment stability as discussed previously.

Dielectrophoresis When a polarisable particle immersed in a medium is subjected to a non-uniform electric field, the particle becomes polarised and experiences a force. This is known as a dielectrophoretic (DEP) force and causes the particle to align either with or against the field lines, depending on the particles’ permittivity. The DEP force is dependant on a number of factors including dielectric properties of the particle and medium, the size and shape of the particle and the frequency of the applied electric field. DEP has found extensive applications in nanotechnology, as it offers the ability to selectively align and assemble nano and micro-particles based on their size, shape and electrical properties. Excellent reviews by Pethig and Zhang et al. cover the theory of DEP and a range of applications to which this effect has been applied [93, 94].

While the simplest application of DEP is for spherical particles, interesting effects are observed for particles with high aspect ratios. Rod-like particles such as nanowires or CNTs are found to orientate with the electric field lines, which enables alignment and deposition onto electrodes in solution [95, 96]. The sharp AFM tip provides a convenient electrode with which to form a non-uniform electric field, and several groups have used DEP to attach CNTs onto AFM tips in solution and studied the effect of parameters such as electric field frequency on the attachment efficiency [75, 97–100].

Langmuir-Blodgett films Deposition of CNTs onto an AFM tip requires alignment of the nanotubes, and another method of aligning CNTs in solution is by the use of capillary forces. Lee et al. reported a simple and rapid technique for attaching CNTs, by forming an aligned CNT monolayer at an air-water interface in a Langmuir-Blodgett (LB) film [77]. Dipping and subsequent retraction of the AFM probe from this monolayer resulted in the deposition of a small, aligned SWNT bundle at the tip apex. Lee et al. showed that these probes were robust, and capable of high resolution imaging. Munz et al. successfully used these LB probes to investigate their effectiveness in measuring nanoscale roughness [34].

1.3.2 Fast-scanning

A significant drawback of atomic force microscopy is the slow scan rate of most commercial instruments. Depending on the number of points and scan size, AFM images are generally obtained with scan rates below 3 Hz. This results in acquisition times in excess of 10 minutes per image and the inability to image dynamic processes occurring on short time-scales.

Such limitations have recently been overcome, following significant research into improving the scan rate of these instruments [101–103]. The fastest imaging rate achieved thus far has been demonstrated with a tuning fork scanner, and is capable of imaging at 1330 images per second, which is equivalent to a tip velocity of 13 cms^{-1} [102, 104]. This research has driven development of commercial AFM systems, which are now available with line-scan rates of up to 100 Hz. This technology represents a significant advancement, improving sample throughput and allowing dynamic processes to be visualized on previously unachievable time-scales [105, 106].

In addition to the commercial instruments described earlier, a specialised video-rate AFM developed by Ando and sold by the research institute of biomolecule metrology (Japan) offers extremely high scan rates. This instrument can produce an image every 50 ms (approximately 5000 Hz for an image with 256 lines), with a maximum scan area of 600x600 nm and z-piezo range of 100 nm [107]. Although these specialised AFMs reach very high scan rates, they are often limited in other aspects; including the maximum size of the sample (1.5 mm diameter), scan area and sample roughness. As mentioned previously, there are several companies (Bruker, Asylum Research and AIST-NT among others) producing commercial AFMs capable of scanning at up to 100 Hz, depending on the sample topography. These AFMs are capable of scanning much larger areas (approximately 30x30 μm with z-piezo range of 3 μm), but are not able to image at the extremely high scan rates of specialised instruments.

Fast-scanning cantilevers Commercial fast-scanning AFMs operate in tapping mode (or intermittent contact mode) due to the requirement of rapid feedback response, and reduced lateral forces compared to contact mode. For tapping mode imaging at high scan rates, the bandwidth of the probe is very important [108]. Cantilevers with high bandwidth are capable of rapidly sensing changes in tip-sample distance, which increases the rate with which the feedback system can respond to changes in topography.

In order to image at high speed, specially-designed fast-scanning probes are now produced by various manufacturers (Olympus, Bruker, Nanosensors, AppNano). These probes feature very high resonant frequencies in the MHz range which serves to increase the bandwidth, allowing effective feedback to be maintained at high scan rates. High resonant frequencies are achieved by reducing the length of the cantilever, which requires the thickness to also be reduced in order to maintain a low spring constant. A fast-scanning cantilever is shown in figure 1.20 compared to a standard contact mode cantilever, demonstrating the significantly reduced dimensions.

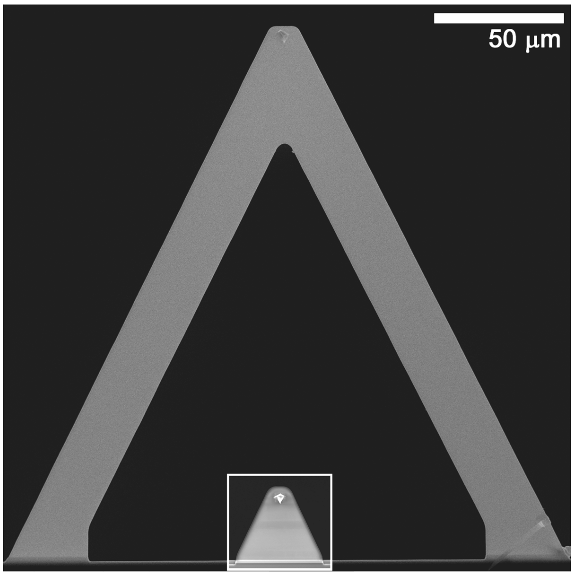

Figure 1.20: SEM image comparing the size of a Bruker FastScan A cantilever (inset in white border) and standard silicon nitride Bruker SNL contact mode cantilever. Reprinted with permission from [3]

Fast-scanning applications There have been many exciting applications of high-speed AFM in recent years, one example in particular is the realtime observation of the myosin V protein, walking on an actin filament by Kodera et al. [105]. The myosin V protein takes steps of 36 nm along the actin filament, which were imaged at 7 fps using the high-speed AFM developed by the group of Ando. An excellent overview of high-speed AFM and its applications, particularly to dynamic biological processes, is given in the following review articles [106, 109].

1.4 Summary

The following chapters report several developments in the field of atomic force microscopy, with the aim of improving the accuracy, precision and imaging resolution of the microscope. Chapter 3 focuses on the measurement of force and deflection, and presents several novel approaches to improve measurement of the cantilevers' spring constant and deflection sensitivity. Chapter 2 provides experimental details for the thesis, while chapters 4 and 5 focus on the field of carbon nanotube probes for enhancement of imaging resolution and wear, by reporting methods for their fabrication and the application of these probes respectively.

Bibliography - Chapter 1

[1] G. Binnig, C. F. Quate, and Ch Gerber. *Physical Review Letters* 56.9 (1986), pp. 930–933. DOI: `10.1103/PhysRevLett.56.930`.

[2] Ashley D Slattery et al. *Nanotechnology* 24.1 (2013), p. 015710. DOI: `10.1088/0957-4484/24/1/015710`.

[3] Ashley D. Slattery et al. *Nanotechnology* 25.33 (2014), p. 335705. DOI: `10.1088/0957-4484/25/33/335705`.

[4] Matthew a. Hopcroft, William D. Nix, and Thomas W. Kenny. *Journal of Microelectromechanical Systems* 19.2 (2010), pp. 229–238. DOI: `10.1109/JMEMS.2009.2039697`.

[5] John E. Sader et al. *Review of Scientific Instruments* 66.7 (1995), p. 3789. DOI: `10.1063/1.1145439`.

[6] A. Khan. *Journal of Applied Physics* 95.4 (2004), p. 1667. DOI: `10.1063/1.1638886`.

[7] Stefan B. Kaemmer. Tech. rep. 2011, pp. 1–12.

[8] J. Sidles et al. *Reviews of Modern Physics* 67.1 (1995), pp. 249–265. DOI: `10.1103/RevModPhys.67.249`.

[9] J. Kokavecz and a. Mechler. *Physical Review B* 78.17 (2008), pp. 1–4. DOI: `10.1103/PhysRevB.78.172101`.

[10] Georg Hähner. *Ultramicroscopy* 110.7 (2010), pp. 801–6. DOI: `10.1016/j.ultramic.2010.02.008`.

[11] Richard S Gates, William A Osborn, and Jon R Pratt. *Nanotechnology* 24.25 (2013), p. 255706. DOI: `10.1088/0957-4484/24/25/255706`.

[12] Charles a Clifford and Martin P Seah. *Nanotechnology* 16.9 (2005), pp. 1666–1680. DOI: `10.1088/0957-4484/16/9/044`.

[13] John Elie Sader. *Review of Scientific Instruments* 66.9 (1995), pp. 4583–4587. DOI: `10.1063/1.1145292`.

[14] Ivan U Vakarelski et al. *Langmuir : the ACS journal of surfaces and colloids* 23.22 (2007), pp. 10893–6. DOI: `10.1021/la701878n`.

[15] Victor Shahin et al. *Journal of cell science* 118.13 (2005), pp. 2881–9. DOI: `10.1242/jcs.02429`.

[16] H Hertz. *Journal für die reine und angewandte Mathematik* 92 (1882), pp. 156–171.

[17] K. L. Johnson, K. Kendall, and A. D. Roberts. *Proceedings of the Royal Society A: Mathematical, Physical and Engineering Sciences* 324.1558 (1971), pp. 301–313. DOI: 10.1098/rspa.1971.0141.

[18] B.V Derjaguin, V.M Muller, and Yu.P Toporov. *Journal of Colloid and Interface Science* 53.2 (1975), pp. 314–326. DOI: 10.1016/0021-9797(75)90018-1.

[19] V.M Muller, V.S Yushchenko, and B.V Derjaguin. *Journal of Colloid and Interface Science* 77.1 (1980), pp. 91–101. DOI: 10.1016/0021-9797(80)90419-1.

[20] V.M. Muller, B.V. Derjaguin, and Yu.P. Toporov. *Colloids and Surfaces* 7.3 (1983), pp. 251–259. DOI: 10.1016/0166-6622(83)80051-1.

[21] H Butt, B Cappella, and M Kappl. *Surface Science Reports* 59.1-6 (2005), pp. 1–152. DOI: 10.1016/j.surfrep.2005.08.003.

[22] Daniel Maugis. *Journal of Colloid and Interface Science* 150.1 (1992), pp. 243–269. DOI: 10.1016/0021-9797(92)90285-T.

[23] M. A. Lantz et al. *Physical Review B* 55.16 (1997), pp. 10776–10785. DOI: 10.1103/PhysRevB.55.10776.

[24] Jan H. Hoh and Andreas Engel. *Langmuir* 9.11 (1993), pp. 3310–3312. DOI: 10.1021/la00035a089.

[25] Bede Pittenger, Natalia Erina, and Chanmin Su. Tech. rep. Bruker corporation, 2012, p. 12.

[26] Daniel Platz et al. *Nanotechnology* 23.26 (2012), p. 265705. DOI: 10.1088/0957-4484/23/26/265705.

[27] Hui Huang et al. PhD thesis. KTH, 2015.

[28] Mark a Poggi et al. *Analytical Chemistry* 77.4 (2005), pp. 1192–1195. DOI: 10.1021/ac048828h.

[29] Peter J Cumpson et al. *Applied Scanning Probe Methods VIII.* 2008, pp. 289–314. DOI: 10.1007/978-3-540-74080-3{_}8.

[30] Joost te Riet et al. *Ultramicroscopy* 111.12 (2011), pp. 1659–69. DOI: 10.1016/j.ultramic.2011.09.012.

[31] Jon R. Pratt et al. *Journal of Applied Physics* 107.4 (2010), p. 044305. DOI: 10.1063/1.3284957.

[32] Ferdinand Walther, Wolfgang M. Heckl, and Robert W. Stark. *Applied Surface Science* 254.22 (2008), pp. 7290–7295. DOI: 10.1016/j.apsusc.2008.05.323.

[33] J Liu et al. *Small (Weinheim an der Bergstrasse, Germany)* 6.10 (2010), pp. 1140–9. DOI: 10.1002/smll.200901673.

[34] Martin Munz et al. *Surface and Interface Analysis* 43.11 (2011), pp. 1382–1391. DOI: 10.1002/sia.3727.

[35] Ashley D. Slattery et al. *Ultramicroscopy* 131 (2013), pp. 46–55. DOI: 10.1016/j.ultramic.2013.03.009.

[36] Mrinal Mahapatro et al. *Ultramicroscopy* 97.1-4 (2003), pp. 297–301. DOI: 10.1016/S0304-3991(03)00055-X.

[37] Christopher T Gibson, Stewart Carnally, and Clive J Roberts. *Ultramicroscopy* 107.10-11 (2007), pp. 1118–22. DOI: `10.1016/j.ultramic.2007.02.045`.

[38] J. P. Cleveland et al. *Review of Scientific Instruments* 64.2 (1993), p. 403. DOI: `10.1063/1.1144209`.

[39] Hans J. Griesser et al. *Proc. SPIE 4590, BioMEMS and Smart Nanostructures.* 2001, pp. 45–56. DOI: `10.1117/12.454587`.

[40] Christopher T. Gibson et al. *Review of Scientific Instruments* 72.5 (2001), p. 2340. DOI: `10.1063/1.1361080`.

[41] Ashley D. Slattery, Christopher. T. Gibson, and Jamie. S. Quinton. *2010 International Conference on Nanoscience and Nanotechnology.* 2010, pp. 407–410. DOI: `10.1109/ICONN.2010.6045265`.

[42] John E Sader, James W M Chon, and Paul Mulvaney. *Review of Scientific Instruments* 70.10 (1999), pp. 3967–3969. DOI: `10.1063/1.1150021`.

[43] John E Sader et al. *The Review of scientific instruments* 83.10 (2012), p. 103705. DOI: `10.1063/1.4757398`.

[44] John E. Sader and James R. Friend. *Review of Scientific Instruments* 85.11 (2014), p. 116101. DOI: `10.1063/1.4901227`.

[45] John E. Sader and James R. Friend. *Review of Scientific Instruments* 86.5 (2015), p. 056106. DOI: `10.1063/1.4921192`.

[46] O Ergincan, G Palasantzas, and B J Kooi. *The Review of scientific instruments* 85.2 (2014), p. 026118. DOI: `10.1063/1.4864195`.

[47] Jeffrey L. Hutter and John Bechhoefer. *Review of Scientific Instruments* 64.7 (1993), p. 1868. DOI: `10.1063/1.1143970`.

[48] S M Cook et al. *Nanotechnology* 17.9 (2006), pp. 2135–2145. DOI: `10.1088/0957-4484/17/9/010`.

[49] John E. Sader, Morteza Yousefi, and James R. Friend. *Review of Scientific Instruments* 85.2 (2014), pp. 1–5. DOI: `10.1063/1.4864086`.

[50] H J Butt and M Jaschke. *Nanotechnology* 6.1 (1999), pp. 1–7. DOI: `10.1088/0957-4484/6/1/001`.

[51] R Proksch et al. *Nanotechnology* 15.9 (2004), pp. 1344–1350. DOI: `10.1088/0957-4484/15/9/039`.

[52] Benjamin Ohler. Tech. rep. Bruker, 2007, pp. 1–12.

[53] Richard S Gates et al. *Journal of Research of the National Institute of Standards and Technology* 116.4 (2011), p. 703. DOI: `10.6028/jres.116.015`.

[54] Robert W. Stark, Tanja Drobek, and Wolfgang M. Heckl. *Ultramicroscopy* 86.1-2 (2001), pp. 207–215. DOI: `10.1016/S0304-3991(00)00077-2`.

[55] John E. Sader, Jianing Lu, and Paul Mulvaney. *Review of Scientific Instruments* 85.11 (2014), p. 113702. DOI: `10.1063/1.4900864`.

[56] Christopher T Gibson, Gregory S Watson, and Sverre Myhra. *Nanotechnology* 7.3 (1999), pp. 259–262. DOI: `10.1088/0957-4484/7/3/014`.

[57] Christopher T. C.T. Gibson et al. *Review of Scientific Instruments* 75.2 (2004), p. 565. DOI: `10.1063/1.1642750`.

[58] Charles A Clifford and Martin P Seah. *Measurement Science and Technology* 20.12 (2009), p. 125501. DOI: `10.1088/0957-0233/20/12/125501`.

[59] Richard S Gates and Jon R Pratt. *Measurement Science and Technology* 17.10 (2006), pp. 2852–2860. DOI: `10.1088/0957-0233/17/10/041`.

[60] Richard S Gates and Mark G Reitsma. *The Review of scientific instruments* 78.8 (2007), p. 086101. DOI: `10.1063/1.2764372`.

[61] Jeffrey L Hutter. *Langmuir* 21.6 (2005), pp. 2630–2632. DOI: `10.1021/la047670t`.

[62] Hongjie Dai et al. *Nature* 384.6605 (1996), pp. 147–150. DOI: `10.1038/384147a0`.

[63] S. S. Wong et al. *Journal of the American Chemical Society* 120.33 (1998), pp. 8557–8558. DOI: `10.1021/ja9817803`.

[64] T. Larsen et al. *Applied Physics Letters* 80.11 (2002), p. 1996. DOI: `10.1063/1.1452782`.

[65] Bruker AXS. *Bruker AFM Probes.* URL: `www.brukerafmprobes.com/c-193-fib.aspx` (visited on 01/14/2013).

[66] Jason H. Hafner, Chin Li Cheung, and Charles M. Lieber. *Journal of the American Chemical Society* 121.41 (1999), pp. 9750–9751. DOI: `10.1021/ja992761b`.

[67] J P Edgeworth et al. *Nanotechnology* 21.10 (2010), p. 105605. DOI: `10.1088/0957-4484/21/10/105605`.

[68] Shu-Cheng Chin, Yuan-Chih Chang, and Chia-Seng Chang. *Nanotechnology* 20.28 (2009), p. 285307. DOI: `10.1088/0957-4484/20/28/285307`.

[69] J Martinez et al. *Nanotechnology* 16.11 (2005), pp. 2493–2496. DOI: `10.1088/0957-4484/16/11/004`.

[70] F.Z. Fang et al. *CIRP Annals - Manufacturing Technology* 58.1 (2009), pp. 455–458. DOI: `10.1016/j.cirp.2009.03.088`.

[71] Ramsey M Stevens, Cattien V Nguyen, and M Meyyappan. *IEEE Transactions on Nanobioscience* 3.1 (2004), pp. 56–60. DOI: `10.1109/TNB.2004.824275`.

[72] Lawrence a. Wade et al. *Nano Letters* 4.4 (2004), pp. 725–731. DOI: `10.1021/nl049976q`.

[73] Jason H. Hafner et al. *The Journal of Physical Chemistry B* 105.4 (2001), pp. 743–746. DOI: `10.1021/jp003948o`.

[74] C T Gibson et al. *Environmental Science and Technology* 41.4 (2007), pp. 1339–1344. DOI: `10.1021/es061726j`.

[75] Yang Wei et al. *Diamond and Related Materials* 17.11 (2008), pp. 1877–1880. DOI: `10.1016/j.diamond.2008.04.001`.

[76] Hee-Jin Jeong, Yoong-Ho Jung, and Deug-Woo Lee. *Transactions of Nonferrous Metals Society of China* 19.1 (2009), s280–s283. DOI: `10.1016/S1003-6326(10)60285-3`.

[77] JH Lee et al. *Ultramicroscopy* 108.10 (2008), pp. 1163–1167. DOI: `10.1016/j.ultramic.2008.04.073`.

[78] Neil R Wilson and Julie V Macpherson. *Nature nanotechnology* 4.8 (2009), pp. 483–91. DOI: `10.1038/nnano.2009.154`.

[79] Kazuhiko Takagahara et al. *2008 IEEE 21st International Conference on Micro Electro Mechanical Systems*. 2008, pp. 713–716. DOI: `10.1109/MEMSYS.2008.4443756`.

[80] K Takagahara et al. *2007 IEEE 20th International Conference on Micro Electro Mechanical Systems (MEMS)*. January. 2007, pp. 855–858. DOI: `10.1109/MEMSYS.2007.4433180`.

[81] Erhan Yenilmez et al. *Applied Physics Letters* 80.12 (2002), p. 2225. DOI: `10.1063/1.1464227`.

[82] M C Strus et al. *Nanotechnology* 16.11 (2005), pp. 2482–2492. DOI: `10.1088/0957-4484/16/11/003`.

[83] S Wong. *Chemical Physics Letters* 306.5-6 (1999), pp. 219–225. DOI: `10.1016/S0009-2614(99)00488-1`.

[84] N. a. Kouklin et al. *Applied Physics Letters* 87.17 (2005), p. 173901. DOI: `10.1063/1.2112183`.

[85] Hidehiro Nishijima et al. *Applied Physics Letters* 74.26 (1999), p. 4061. DOI: `10.1063/1.123261`.

[86] Ashley D Slattery et al. *Nanotechnology* 24.23 (2013), p. 235705. DOI: `10.1088/0957-4484/24/23/235705`.

[87] Seiji Akita and Yoshikazu Nakayama. *Japanese Journal of Applied Physics* 41.Part 1, No. 7B (2002), pp. 4887–4889. DOI: `10.1143/JJAP.41.4887`.

[88] Niels de Jonge, Yann Lamy, and Monja Kaiser. *Nano Letters* 3.12 (2003), pp. 1621–1624. DOI: `10.1021/nl034792h`.

[89] XianLong Wei et al. *Nanotechnology* 18.18 (2007), p. 185503. DOI: `10.1088/0957-4484/18/18/185503`.

[90] Chang-Soo Han, Young-Hyun Shin, and Yu-Hwan Yoon. *2nd IEEE International Conference on Nano/Micro Engineered and Molecular Systems*. 2007, pp. 290–293. DOI: `10.1109/NEMS.2007.352029`.

[91] M. S. Raghuveer et al. *Applied Physics Letters* 84.22 (2004), p. 4484. DOI: `10.1063/1.1756191`.

[92] T. D. Yuzvinsky et al. *Applied Physics Letters* 86.5 (2005), p. 053109. DOI: `10.1063/1.1857081`.

[93] Ronald Pethig. *Biomicrofluidics* 4.2 (2010), p. 022811. DOI: `10.1063/1.3456626`.

[94] C Zhang et al. *Analytical and bioanalytical chemistry* 396.1 (2010), pp. 401–20. DOI: `10.1007/s00216-009-2922-6`.

[95] J. Tang et al. *Advanced Materials* 15.16 (2003), pp. 1352–1355. DOI: `10.1002/adma.200305086`.

[96] J. Zhang et al. *Advanced Materials* 16.14 (2004), pp. 1219–1222. DOI: `10.1002/adma.200400124`.

[97] Jie Tang et al. *Nano letters* 5.1 (2005), pp. 11–4. DOI: `10.1021/nl048803y`.

[98] Ji-Eun Kim and Chang-Soo Han. *Nanotechnology* 16.10 (2005), pp. 2245–50. DOI: `10.1088/0957-4484/16/10/046`.

[99] Ji-Eun Kim, June-Ki Park, and Chang-Soo Han. *Nanotechnology* 17.12 (2006), pp. 2937–2941. DOI: `10.1088/0957-4484/17/12/019`.

[100] Haoyan Wei et al. *Nanotechnology* 19.45 (2008), p. 455303. DOI: `10.1088/0957-4484/19/45/455303`.

[101] Georg Schitter et al. *IEEE Transactions on Control Systems Technology* 15.5 (2007), pp. 906–915. DOI: `10.1109/TCST.2007.902953`.

[102] L M Picco et al. *Nanotechnology* 18.4 (2007), p. 044030. DOI: `10.1088/0957-4484/18/4/044030`.

[103] A J Fleming, B J Kenton, and K K Leang. *Ultramicroscopy* 110.9 (2010), pp. 1205–14. DOI: `10.1016/j.ultramic.2010.04.016`.

[104] T Ando. *2011 IEEE 24th International Conference on Micro Electro Mechanical Systems*. 2011, pp. 57–62. DOI: `10.1109/MEMSYS.2011.5734361`.

[105] Noriyuki Kodera et al. *Nature* 468.7320 (2010), pp. 72–6. DOI: `10.1038/nature09450`.

[106] Toshio Ando, Takayuki Uchihashi, and Noriyuki Kodera. *Annual review of biophysics* 42 (2013), pp. 393–414. DOI: `10.1146/annurev-biophys-083012-130324`.

[107] Toshio Ando. *High Speed Atomic Force Microscope - Ando Model*. URL: `www.ribm.co.jp/equipment/sub%7B%5C_%7Dnex.html`.

[108] Georg E Fantner et al. *Ultramicroscopy* 106.8-9 (2006), pp. 881–7. DOI: `10.1016/j.ultramic.2006.01.015`.

[109] Arivazhagan Rajendran, Masayuki Endo, and Hiroshi Sugiyama. *Chemical reviews* 114.2 (2014), pp. 1493–520. DOI: `10.1021/cr300253x`.

Chapter 2

Materials and Methods

Materials used and measurement procedures are detailed in this chapter, for the work presented throughout the thesis. Many measurements were performed in a similar manner across different areas of the thesis (ie. AFM force curve acquisition), and these general measurement procedures are provided in section 2.1. Materials and methods specific to each chapter are provided in the following sections, in the order that they are presented throughout the thesis.

2.1 General experimental details

Instrument calibration AFM scanners were regularly calibrated in x, y and z directions using silicon calibration grids (Bruker model numbers PG: 1 μm pitch, 110 nm depth and VGRP: 10 μm pitch, 180 nm depth). When cantilever dimensions were measured, SEM instruments were also calibrated in x and y dimensions, at the appropriate working distance and magnification using the aforementioned calibration grids.

AFM imaging AFM images were acquired in either contact, tapping or PeakForce tapping modes with all parameters including set-point, scan rate and feedback gains adjusted to optimize image quality and minimise imaging force where desired.

Material properties In this work the density for silicon nitride is taken to be 3300 kgm^{-3} (as quoted by probe manufacturers) and the density of silicon used is 2329 kgm^{-3}, which is widely established in the literature [1]. The densities used for aluminium and gold are the bulk values, which are known to be 2700 kgm^{-3} and 19300 kgm^{-3} respectively.

The Young's modulus of silicon nitride is quoted by the manufacturer (Bruker) as 200 GPa, whereas that for silicon is 169 GPa in the $< 110 >$ direction. The Young's modulus for aluminium and gold metal films are taken to be the bulk values of 70 GPa and 79 GPa respectively.

2.1.1 Spring constant correction

Off-end loading A number of methods provide the spring constant in a location other than the imaging tip, and correction in these cases is achieved using the off-end loading formula (equation 1.3). For results presented in this work, the spring constant is always reported at the cantilevers' imaging tip, while for tip-less cantilevers the spring constant is reported at the cantilevers' free end.

Intrinsic spring constants Spring constants reported in this work are static and intrinsic. This means that where appropriate, the spring constant has been corrected using the available dynamic to static correction ratio and also corrected for the cantilever tilt when mounted in the AFM [2–4]. These correction factors are discussed in more detail in section 1.1.1.3 of the introduction.

Torque effect Where appropriate, the spring constant has been corrected for the torque effect discussed in section 1.2.3.7, using equation 1.32. This is only required for cantilevers where the tip is of comparable size to the cantilevers' length (ie. Mirkromasch NSC15 and FastScan A).

2.1.2 Spring constant calibration procedures

Thermal noise and resonant properties The cantilevers' thermal noise spectrum was measured using the thermal tune option available in the Nanoscope AFM software, from which the spring constant, resonant frequency and Q factor were extracted using a simple harmonic oscillator fit. These values are (unless otherwise specified) an average of at least 5-10 individual measurements with the quoted uncertainty being one standard deviation. Resonant frequencies for rectangular and V-shaped cantilevers were corrected for fluid damping in air by using their corresponding correction term, except for use in the Sader hydrodynamic method [5, 6].

Force curve acquisition Prior to any force measurements, the AFM system was left for 30 minutes after probe loading and laser alignment, to avoid uncertainty arising from heating (either by the laser spot or instrument electronics). Any movement in the laser spot or photodiode drift over this duration was corrected at this point.

Force distance curves were acquired using a cantilever deflection of 100 nm and a z scanner total ramp size of 300 nm, unless specified otherwise. The slope, or sensitivity, for each force curve is an average of the approach and retract cycle, and where reported, uncertainties represent one standard deviation. Recent work by Pratt et al. has demonstrated that this is a good approximation to account for any friction or sliding effects of the AFM tip during force curve measurements on surfaces or during reference lever calibration [7]. Sensitivity values for contact regions of the force curves are an average of at least 5-10 individual force curves, unless specified otherwise.

When calibrating the deflection sensitivity of cantilevers, measurements were made on either a flat silicon or sapphire surface at a minimum of three separate locations unless specified otherwise. For reference cantilever measurements, the cantilever sensitivity was measured at the beginning and end of the experiment to ensure there is no drift. The variation in sensitivity measurements before and after reference cantilever experiments was found to be on the order of ±1% and represents the typical uncertainty on averaged sensitivity values.

2.2 Cantilever calibration

2.2.1 FIB mass removal

Cantilevers were milled using a FEI Helios D433 Dualbeam FIB microscope with 30 kV accelerating voltage and an ion current of approximately 25 pA. The initial holes were milled within 10-20 minutes, after which they were subsequently enlarged which was generally completed in less than 5 minutes. All AFM measurements were acquired using a Bruker Multimode AFM with Nanoscope V controller. SEM measurements of cantilever dimensions were acquired using either the electron microscope on the FEI Helios D433 Dualbeam or a CamScan MX2500 SEM. Uncertainty in instrument calibration is included in the uncertainty quoted for dimensional measurements by SEM.

2.2.2 Reference cantilever

Spatial markers were milled into the cantilevers using a FEI Helios D433 Dualbeam FIB microscope, with an accelerating voltage of 30 kV and an ion current of approximately 2 pA. Milling of the markers was completed in less than 2 minutes. The diameter of each circular marker varied but was always between 1-2 μm, with each marker approximately 100-200 nm in depth. In general, two to three of these markers were milled into the test cantilevers, while a maximum of four markers were created for any single cantilever.

Reference cantilever chips and test cantilever chips for the inverted technique were mounted on circular steel pucks 11 mm in diameter and affixed using double-sided tape, with the cantilevers oriented as per figures 3.13a and 3.15a. Mounting the cantilever chips with this orientation was simple to execute and allowed the sensitivity measurements on the hard surface to be performed on the silicon cantilever chips. Moving from these measurements to the cantilever sensitivity measurements was also much simpler with this configuration. All force distance curves were acquired using a cantilever deflection of 100-200 nm and a z scanner ramp size of 300-800 nm.

SEM measurements of cantilever dimensions were acquired using either the electron microscope on the FEI Helios D433 Dualbeam or a CamScan MX2500 SEM. Uncertainty in instrument calibration is included in the uncertainty quoted for dimensional measurements by SEM.

2.2.3 Deflection sensitivity

Spatial markers were milled into the cantilevers using a FEI Helios D433 Dualbeam FIB microscope with an accelerating voltage of 30 kV and a milling current of approximately 2 pA. Milling of the markers was completed in less than 2 minutes per cantilever. The diameter of each circular marker varied but was always between 1-2 μm, with each marker approximately 100-200 nm in depth. SEM measurements of cantilevers were acquired using either the electron microscope on the FEI Helios D433 Dualbeam or a CamScan MX2500 SEM.

Force distance curves were acquired using a cantilever deflection of 100 to 200 nm and a z scanner ramp size of 300 to 2000 nm. Substantially larger ramp sizes were required to complete the approach and retract cycles with soft cantilevers (e.g. cantilever ^{3}V2). The scanner used was a Bruker type J scanner with maximum xy range of 100 μm and z range of 5 μm. The rigid cantilever chip was mounted on a circular steel puck 11 mm in diameter and was stuck down using double-sided tape with the cantilevers' tip orientated vertically upwards.

The resonant frequency and Q factor were measured before and after FIB milling for cantilevers ^{3}V1 and ^{3}F1, with very small changes noted for both parameters (less than 1% for Q factors and 0.25% for resonant frequencies). The small changes in these properties were within experimental error, and are a result of the very small quantity of mass removed from the cantilevers, and the location that the spatial markers were milled.

The cantilever used as the lower rigid cantilever was a NSC15 silicon tapping mode probe (Mikromasch). The same reference cantilever was used for calibration of each test cantilever. These types of probes have a nominal tip diameter of 20 nm and the cantilever spring constant was determined using both the Sader hydrodynamic method and the thermal noise technique. The spring constant of this cantilever is estimated to be $k_{rigid} = 77.4 \pm 7.7$ Nm^{-1}. The other advantage of this type of probe is that the tip height is typically greater than 15 μm, further ensuring that the test cantilever tip will not contact any surface when performing the sensitivity measurements.

2.2.3.1 Measurement procedure

The procedure for the sensitivity calibration is as follows. The first step is to align the laser spot such that it is as close to the end of the cantilever as possible. This is achieved by moving the spot along the cantilever towards its free end until the signal just begins to drop from its maximum value, indicating that the spot is at the free end of the cantilever. It is important for inexperienced operators to ensure the laser is aligned correctly, ie. not on the arm of V-shaped cantilevers which will introduce significant errors.

The system should then be left to equilibrate for at least 30 minutes before performing measurements in order to minimize laser spot drift. The test cantilever should then be positioned above the rigid cantilever tip using the AFM optics as depicted in figure 2.1, depending on whether using a tip-less cantilever 2.1a, using a cantilever with a spatial marker 2.1b or reverse imaging the V-arm intersection 2.1c.

The cantilever should then be brought into feedback with the deflection set-point at 0 V, which will correspond to the centre of the photodiode. The operator should then commence imaging the test cantilever surface and adjust the scan size and image centre position (offset) until either the end of the cantilever, a spatial marker or the arm intersection is located. Images can then be acquired until any drift in the scanner is minimized, which will result in images similar to those in figure 2.1d, e and f respectively. It is then a simple task to perform force curves at the desired location within the images.

Depending on the geometry of the cantilever and the ratio of the spring constants for the test and rigid cantilever, either equations 3.18, 3.22 or 3.23 can subsequently be used to determine the corrected cantilever sensitivity. For tip-less cantilevers, no corrections will be required provided the sensitivity is measured very close to the end of the test cantilever and $k_{test} \ll k_{rigid}$.

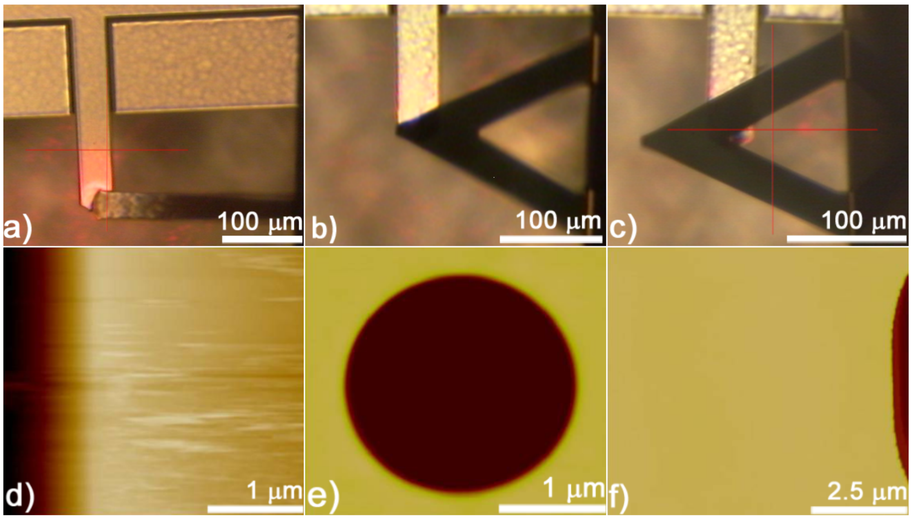

Figure 2.1: Optical images of a) tipless and V-shaped cantilevers imaging b) FIB-milled marker and c) the V-intersection. Corresponding AFM images are shown in d), e) and f). Reprinted with permission from [8].

2.2.4 Fast-scanning cantilevers

AFM measurements were acquired using a Bruker Dimension FastScan AFM with Nanoscope V controller and Nanoscope control software; AFM images were acquired using PeakForce tapping mode. The laser spot position was measured optically, such that the appropriate corrections could be applied for the thermal noise method.

SEM imaging and FIB milling was performed with a FEI Helios D433 Dualbeam FIB microscope; milling was performed using an accelerating voltage of 30 kV and an ion current of approximately 25 pA. Pilot holes were initially milled within 10-20 minutes, and were subsequently enlarged to the final hole size in less than 5 minutes. In the case of milling a pyramidal section, the process was performed in a single step.

Dimensional measurements were performed using the high-resolution immersion mode SEM feature. A high-resolution SEM was critical for measuring small dimensions such as the thickness of the cantilever and metal films.

Calculation of removed volume, centre of mass and uncertainty The removed volume and centre of mass was determined mathematically using SEM measurements and numerical integration.

For the case where a hole was milled through the AFM tip, the volume was found to have the shape of a cone, truncated at each end by a plane representing the faces of the AFM tip. This shape was modeled by considering that the volume of the milled section is the difference between the original cone truncated only at its' base, and the smaller cone truncated from the narrow end of the original cone. A schematic showing the general dimensions of the removed volume is provided in figure 2.2a, and the various parameters used to describe the truncated cone are indicated on the ^{4}FSB1 cantilever in figure 2.2b.

General equations describing the cone and the planes, due to the symmetries of the cone, can be written in normal forms in equation 2.1 and 2.2, respectively.

$$m^2(y^2 + z^2) = x^2 \tag{2.1}$$

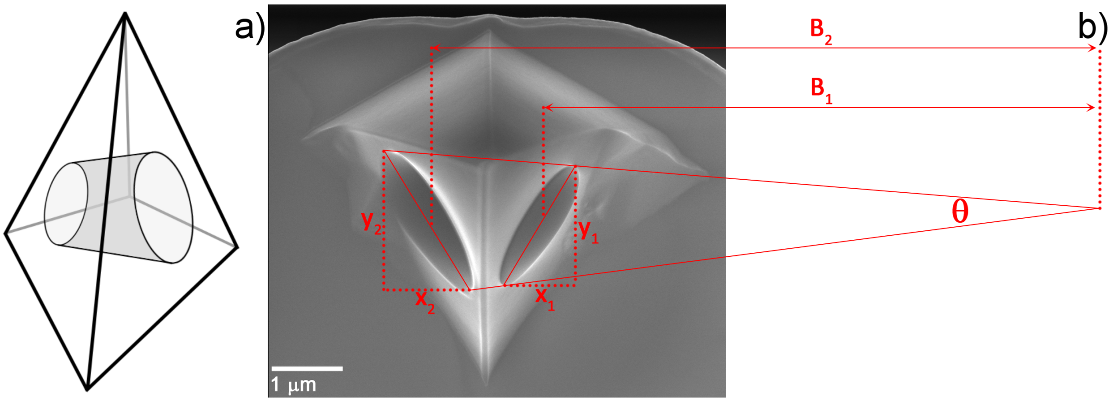

Figure 2.2: Schematic of the cone/plane geometry and an SEM image of a milled FastScan tip with measured values indicated. Reprinted with permission from [9].

$$x = kz + b \tag{2.2}$$

$$k = \frac{x}{y} \tag{2.3}$$

The removed volume and its centre of mass were analytically expressed in an integral form and then computed by numerical integration using Mathematica. The uncertainty on the volumes were estimated by inputting the maximum and minimum values for the different variables and assuming the uncertainty is equal to the upper and lower volumes calculated. This yielded uncertainties from 10-15% for cantilevers ^{4}FSA1, ^{4}FSB1, ^{4}FSB2, ^{4}FSC1 and ^{4}FSC2. The volume removed for cantilever ^{4}FSA3 was simpler to determine since it was a pyramid. The error on the volume removed for this cantilever is estimated to be approximately 10%.

2.3 CNT probe fabrication

2.3.1 Chemical vapour deposition

Growth of MWCNTs was achieved by sputtering 10 nm aluminium (Proscitech, 99.99%) and 5 nm iron (Goodfellow, 99.5%) sequentially onto a bare silicon surface (Siltronix). The sample is then placed into the CVD system, under a flow of 1500 sccm argon (99.997%, BOC) and 500 sccm hydrogen (99.98%, BOC) and then raised to 750 °C and left for 10 minutes once the temperature is reached. CNT growth begins by adding 200 sccm acetylene (98%, BOC) and introducing water vapour with a 2500 sccm argon flow through a water bubbler. The growth is stopped after 10 minutes by stopping the acetylene, hydrogen, and water vapour flow in the order listed, and the system is cooled under the original 1500 sccm flow of argon.

Iron nanoparticle formation was achieved using the method reported by Choi et al. [10]. Silicon (Siltronix) (cut into 1x1 cm pieces) or AFM probes were oxidised by heating the sample to 1000 °C for 13 hours in the CVD tube, with a flow of compressed air passing through a bubbler containing water. The oxidised silicon was then cleaned by rinsing with acetone, ethanol and then water, and dried with pure nitrogen. Iron nanoparticles were formed by immersing the sample in a vial containing 10 mL water and 10 μL iron chloride (APS Specialty Chemicals) solution (10 mM), and then adding 100 μL hydroxylamine hydrochloride (Sigma-Aldrich, 99%) solution (40 mM) under stirring. The reaction was allowed to proceed for approximately 20 seconds before the sample was removed and rinsed with water, acetone, ethanol and then dried with pure nitrogen.

SWCNT growth was performed using the following process. Samples were placed in the furnace under a flow of 600 sccm argon and 450 sccm hydrogen, heated to 900 °C and held for 5 minutes. Growth was initiated by redirecting the 600 sccm flow of argon through a bubbler containing ethanol (95% with 5% water impurity, ChemSupply). Growth proceeded for 5-10 minutes, at which point the flow was switched to 1000 sccm argon and the system cooled.

AFM analysis in this section was performed using an NTMDT Ntegra and Bruker Multimode 8 AFM.

2.3.2 Solution-based methods

The SWCNT solution used in this section was prepared as reported elsewhere [11]; briefly, 10 mg of SWCNTs (P3, Carbon Solutions) and 0.13 g tetraoctylammonium bromide (TOAB) (Sigma-Aldrich, 98%) were dissolved in 25 mL tetrahydrofuran (THF) (Sigma-Aldrich, 99.9%) by sonication for 30 minutes. After centrifugation of the resultant solution at 10 000 rpm for 10 minutes, the supernatant was discarded and the precipitate was re-dispersed in THF by sonication and this process repeated to remove unbound TOAB. Characterisation in this section was performed using a CamScan MX2500 SEM and a Bruker Multimode 8 AFM.

2.3.2.1 Dielectrophoresis

AFM cantilevers used in this work were Veeco OTR8 and Mikromasch NSC15 types. Dielectrophoresis was performed by bringing the AFM tip close to a silicon surface (within 20 μm) using a micromanipulator. A droplet of the THF CNT solution described above was placed onto the silicon surface, such that a meniscus formed, bridging the gap between the tip and the surface. An alternating current (1 MHz) electrical bias was then applied across the gap, this was 25 V in the case of the OTR8 probe and 2.5 V for the silicon probes.

2.3.2.2 Solvent evaporation

Tungsten tips were fabricated by etching 0.25 mm tungsten wire in a 1 M sodium hydroxide (ChemSupply, 98%) solution, these tips were rinsed with water and then dried in a stream of nitrogen. For both the tungsten tips and the AFM probes, the tip was brought close to the surface and then a 5 μL droplet of the SWCNT solution was applied. When drawing very long fibres a 5 μL droplet of the SWCNT solution was applied to the silicon surface and the tip was immersed in the droplet using a translator. The tip was then slowly removed from the droplet and a thin black fibre was drawn out of the solution, attached to the apex of the tip.

2.3.2.3 Fibre processing

Fibre straightening was performed with the cantilever tuned to 500 mV amplitude (~20 nm) and then this value reduced iteratively while scanning the surface until stable operation was achieved. The amplitude was then returned to a stable value near the free amplitude, and imaging continued as normal. The sample imaged by these CNT probes after straightening was MWCNTs dispersed on silicon.

2.3.3 Manual attachment

For the majority of the results presented in this section, buckypaper was used as the CNT source. Buckypaper was fabricated using a procedure described by Blanch et al., from a dispersion of arc-discharge produced SWCNTs (AP-SWNT, Carbon Solutions) in 0.5 wt% sodium dodecylbenzenesulfonate (SDBS) surfactant (Sigma-Aldrich, technical grade) [12]. The dispersion was purified by ultracentrifugation at 40000 g for one hour before extraction of the upper ~75 % of the supernatant. After purification, buckypaper was created through vacuum filtration of the supernatant solution over a 0.22 μm polytetrafluoroethylene (PTFE) membrane (Millipore) using acetone to flocculate the nanotubes, followed by excessive washing with water to remove residual surfactant.

A piece of the buckypaper was affixed to the end of a micromanipulator needle using cyanoacrylate adhesive and a small section was then torn in the direction away from the needle which produced a straight edge with aligned SWCNTs.

In earlier work, prior to using buckypaper, CNTs grown directly onto a surface by thermal CVD were used as the nanotube source. An iron film 0.5 nm in thickness was sputtered onto oxidized silicon, this sample was then heated to 900 °C in a quartz tube under a flow of 1000 sccm argon. Upon reaching 900 °C, the flow was changed to 600 sccm argon, 400 sccm hydrogen and left for 10 minutes, at which point the argon flow was redirected through a bubbler containing 95 % ethanol and 5 % water for 10 minutes while the CNTs grew. The flow was then switched back to 1000 sccm argon and the furnace was cooled.

The example CNT source prepared using dielectrophoresis (DEP) was made by aligning the sharp edges of two razor blades within 200 μm of each other, and a droplet of SWCNT solution applied to the gap between them. The SWCNT solution was prepared as follows. SWCNTs (NTP, SWNT-1) were purified by refluxing the SWCNT powder at a concentration of 1 mgmL^{-1} in a 4:1 solution of ultrapure water and concentrated nitric acid, at 80 °C for 8 hours. The solution was then cooled and filtered through a 0.4 μm HTTP filter using a Millipore filter system; the filtered material was rinsed with excess ultrapure water, and dried at 100 °C. The purified SWNTs were then dispersed by sonication in a 1:1 solution of isopropyl alcohol and ultrapure water. A 2.5 V AC potential difference was applied between the razor blades, with a frequency of 1 kHz, this was maintained until the solution evaporated which occurred within 5 minutes.

A FEI Helios D433 Dualbeam FIB microscope was used to image the attachment process and cut the CNTs. This system was equipped with a gas injection system (GIS), which was capable of introducing platinum precursor (Trimethyl [(1, 2, 3, 4 , 5-ETA)- 1 Methyl 2, 4 Cyclopentadien-1-YL] Platinum) and water vapour (Magnesium Sulphate Heptahydrate) onto the sample through needles located approximately 200 μm from the electron beam. Most imaging, deposition and cutting was performed at a beam energy of 1 kV. The micromanipulator used to position the CNTs on the AFM probes is a MM3A model (Kleindiek).

2.4 CNT probe application

The CNT probes used in this chapter were obtained by the manual fabrication process reported in section 4.3 of the preceding chapter.

2.4.1 Fast-scanning CNT probes

AFM imaging was performed using a Dimension FastScan system (Bruker). The AFM samples imaged were the Tipcheck and Nioprobe tip characterization samples (Aurora nanotechnology), and a TGZ01 scanner calibration sample (Mikromasch) which was used for the ringing artifact investigation.

2.4.2 PeakForce tapping application of CNT AFM probes

Probe engage procedure AFM engage parameters were set such that the force experience by the CNT tip was minimised. The "PeakForce Engage Setpoint" is the main parameter which must be controlled, and was set at its minimum value such that false engages were avoided but that the engage contact force was minimised. This parameter was initially set to 0.02 V (∼1 nm), and then increased incrementally until a successful engage was obtained.

Gold nanoparticle sample preparation The gold nanoparticles were prepared using a similar approach to that of Flavel et al., the procedure for which is briefly reported here [13]. Prior to the reaction, glassware was cleaned in a solution of 3:1 v/v hydrochloric acid (36%, RCI Labscan) and nitric acid (70%, RCI Labscan). 1 mL of 1% aqueous gold (III) chloride solution (99.9985%, Proscitech) was then added to 100 mL water under stirring and allowed 1 minute to disperse. 1 mL of 1% aqueous sodium citrate (99%, Sigma-Aldrich) solution was then added and stirring continued for 1 minute. Following this, 1 mL of sodium borohydride (0.075% wt. dissolved in 1% aq. Sodium Citrate) (99%, Sigma-Aldrich) was added and stirred for 5 minutes. The solution was stored at 4°C away from light prior to further use.

Silicon was cut into 1x1 cm pieces and cleaned by immersing in a 1:3 v/v solution of hydrogen peroxide (30%, ChemSupply) and sulfuric acid (98%, RCI Labscan) at 80°C for 15 minutes. The silicon was then removed, rinsed with water and dried with nitrogen. The silicon was then immersed in a 8.3 mM solution of 3-aminopropyltriethoxysilane (3-APTES) (99%, Sigma-Aldrich) in methanol (99.8%, Optigen) for 24 hours. The silicon pieces were then sonicated in methanol to remove any unbound silane, rinsed with methanol and dried with nitrogen.

A droplet of gold nanoparticle solution was then placed onto the silanised silicon surface and allowed to sit for 20 minutes, after which it was rinsed with water and dried gently with nitrogen.

The gold nanoparticle sample on bare silicon was prepared simply by placing a droplet of the gold nanoparticle solution on clean silicon and allowing it to dry.

Bibliography - Chapter 2

[1] Kenichi Fujii, Atsushi Waseda, and Naoki Kuramoto. *Technology* 12 (2001), pp. 2031–2038. DOI: `10.1088/0957-0233/12/12/302`.

[2] Joost te Riet et al. *Ultramicroscopy* 111.12 (2011), pp. 1659–69. DOI: `10.1016/j.ultramic.2011.09.012`.

[3] Benjamin Ohler. Tech. rep. Bruker, 2007, pp. 1–12.

[4] Richard S Gates et al. *Journal of Research of the National Institute of Standards and Technology* 116.4 (2011), p. 703. DOI: `10.6028/jres.116.015`.

[5] John Elie Sader. *Journal of Applied Physics* 84.1 (1998), p. 64. DOI: `10.1063/1.368002`.

[6] James W. M. Chon, Paul Mulvaney, and John E. Sader. *Journal of Applied Physics* 87.8 (2000), p. 3978. DOI: `10.1063/1.372455`.

[7] Jon R. Pratt et al. *Journal of Applied Physics* 107.4 (2010), p. 044305. DOI: `10.1063/1.3284957`.

[8] Ashley D. Slattery et al. *Ultramicroscopy* 131 (2013), pp. 46–55. DOI: `10.1016/j.ultramic.2013.03.009`.

[9] Ashley D. Slattery et al. *Nanotechnology* 25.33 (2014), p. 335705. DOI: `10.1088/0957-4484/25/33/335705`.

[10] Hee Cheul Choi et al. *Nano Letters* 3.2 (2003), pp. 157–161. DOI: `10.1021/nl025876d`.

[11] Prashant V Kamat et al. *Journal of the American Chemical Society* 126.34 (2004), pp. 10757–62. DOI: `10.1021/ja0479888`.

[12] Adam J. Blanch, Claire E. Lenehan, and Jamie S. Quinton. *Carbon* 49.15 (2011), pp. 5213–5228. DOI: `10.1016/j.carbon.2011.07.039`.

[13] Benjamin S. Flavel et al. *Journal of Nanoparticle Research* 11.8 (2009), pp. 2013–2022. DOI: `10.1007/s11051-008-9562-1`.

Chapter 3

Cantilever Calibration by Focused Ion Beam Milling

Chapter 1 introduced the fundamental importance of accurate spring constant and sensitivity calibration for quantitative AFM measurements. Due to the difficulty of spring constant calibration, a variety of calibration methods have been developed; in comparison, sensitivity calibration techniques have remained comparatively simple and have not received as much attention.

Spring constant calibration techniques can be categorized as either static methods (loading the cantilever with a known force) [1–11], dynamic methods which require knowledge of the cantilever resonance behaviour [12–22], methods based on Euler-Bernoulli beam equations [23, 24] and those which are a combination [25]. Each of the different categories possess advantages and disadvantages with some being more appropriate for certain types of AFM cantilevers depending on stiffness, composition and geometry. The wide range of cantilever types is shown in figure 3.1, which contains a number of the cantilever types used in this work.

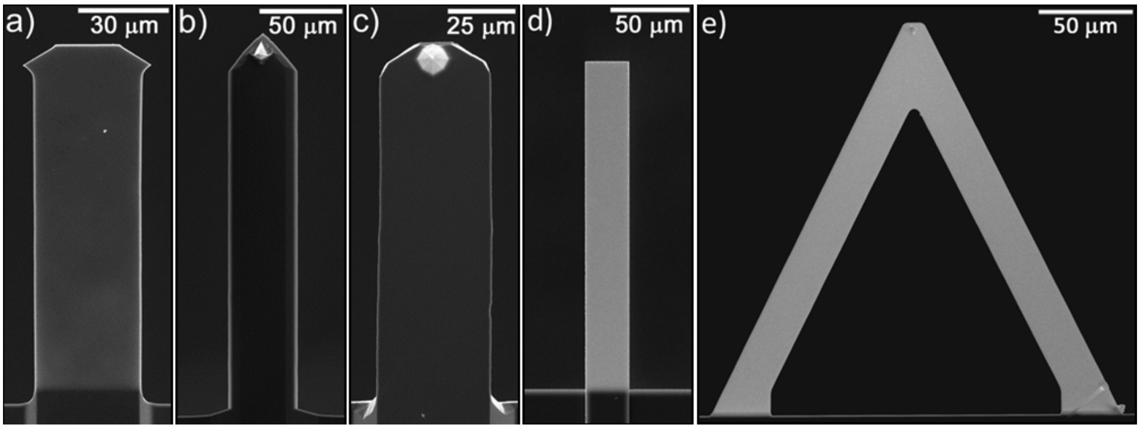

Figure 3.1: SEM images of the various types of cantilevers used throughout this work; these are Mikromasch CSC12 a)Bruker FMV b), Mikromasch NSC15 c), Bruker CLFC d), and a V-shaped Bruker SNL cantilever e) which is representative of the various types of V-shaped cantilevers used. Reprinted with permission from [26].

This chapter reports the development of techniques to improve the calibration of cantilever spring constants [22, 26, 27] and deflection sensitivity [28]. The application of focused ion beam (FIB) milling is a common theme throughout these methods, which presents itself as an enabling technology for high accuracy cantilever calibration. In concluding this chapter, section 3.4 reports the recent calibration of fast-scanning cantilevers, providing a first-look at the applicability of existing calibration methods to the next generation of AFM probes.

3.1 FIB mass removal method

3.1.1 Introduction

Although there are many spring constant calibration methods available, there is no single technique which simultaneously offers extremely low uncertainty (below 5%), wide applicability, ease-of-use and avoids functionally altering the cantilever. The Cleveland added mass technique is in fact, very sound, but suffers from several disadvantages which were introduced in section 1.2.3 and are discussed below. Possible approaches to reduce the uncertainty of this method were considered, and local access to a FIB microscope allowed a mass removal method to be used as an alternative. Instead of adding mass in the form of a microsphere, a section of mass can be removed from the cantilever using ion beam milling.The major sources of uncertainty in the Cleveland added mass method are as follows, along with the possible improvements afforded by FIB milling.

The location and size of the attached sphere introduce significant uncertainty. Microspheres used for this method are generally not perfectly spherical, and thus determination of the added mass is difficult. Optical microscopy is often used to determine the size of the sphere and its location on the cantilever, which introduces further uncertainty. FIB milling allows removal of a well-defined region of the cantilever, and dimensional measurement using electron microscopy significantly reduces the uncertainty in both the size and location of the removed section. Accurate knowledge of the density of the cantilever material allows accurate determination of the removed mass.

Addition of a microsphere to the cantilever is achieved using a micromanipulator and an adhesive, which is potentially very destructive. Physically contacting the cantilever (even with the use of a precise micromanipulator) presents the risk of damaging the tip or the cantilever itself, and the adhesive further increases the uncertainty in the added mass. Even if no visible damage to the cantilever is observed, high stress during loading could result in fractures which may be difficult to detect and would certainly affect the mechanical properties of the cantilever. Mass removal using FIB milling reduces the risk of damage as the cantilever is not physically contacted, and no adhesive is required.

A schematic of the FIB milling process is shown in figure 3.2, where the cantilever is aligned normal to the ion beam during milling and there is an angle of 52^o between the two beams.

The spring constant of the cantilever can be determined in a similar manner to the Cleveland added mass method, whereby:

$$k_{\Delta L} = \frac{4\pi^2 M_1}{\nu_1^{-2} - \nu_0^{-2}} \tag{3.1}$$

This expression provides the spring constant at the centre of the removed mass (a distance ΔL from the cantilevers' end), however it is necessary to know the spring

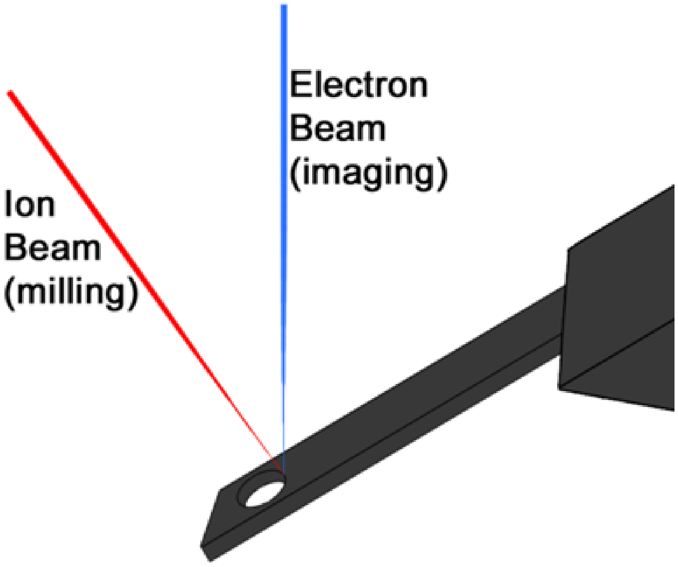

Figure 3.2: Schematic showing the geometry with which the incident electron and ion beams impinge on the cantilever during the milling process.

constant at the tip for practical application. The spring constant at the tip can be calculated relative to that at the centre of the removed mass using the off-end loading expression.

$$k_{\Delta L} = k_{end}\left(\frac{L-\Delta L}{L}\right)^3 \tag{3.2}$$

The offset due to the mass location can also be corrected by considering an effective mass, which is represented in equation 3.3:

$$M_{effective} = M\left(\frac{L-\Delta L}{L}\right)^3 \tag{3.3}$$

Substituting this correction into the original equation, the following expression for the spring constant is obtained:

$$k_{\Delta L} = \frac{4\pi^2 M_1}{\nu_1^{-2}-\nu_0^{-2}}\left(\frac{L-\Delta L}{L}\right)^3 \tag{3.4}$$

FIB-milled cantilevers are shown in figure 3.3 for both standard and tip-less types, and the ΔL offset is shown in each case. For standard cantilevers the spring constant is corrected to the apex of the imaging tip, while for tip-less cantilevers it is stated at the free end.

There have been several reports in the literature of using FIB milling to determine the mechanical properties of AFM cantilevers. These cover areas which are somewhat different to the application described here, as they are used to calibrate cantilevers in the field of mass-sensing.

Friedli et al. used FIB milling to remove a small rectangular volume ($\sim 1\mu m^3$) from a piezoresistive mass-sensing silicon cantilever, in order to calibrate its spring constant [29]. The hole was milled partly through the cantilevers' thickness, and so the mass data was corrected for ion implantation. This value was then used to determine, in-situ, additional mass removed by the FIB or deposited by an electron

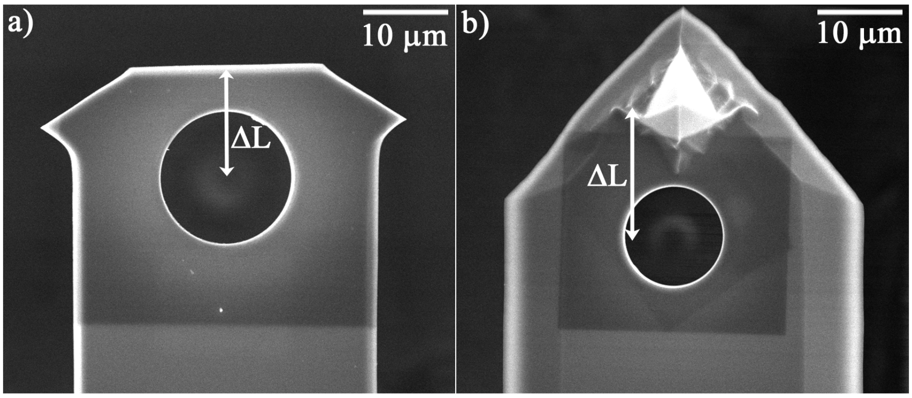

Figure 3.3: SEM images showing the free end of a) tip-less and b) standard cantilevers, with the spring constant correction distance shown. Reprinted with permission from [22].

beam. Woszczyna et al. used the same method to determine the spring constant of a piezoresistive AFM cantilever similar to the mass sensor used by Friedli et al. The mass removed in this case was the entire AFM tip [30].

Chuang et al. used FIB mass removal to determine the thickness and Young's modulus of silicon nitride thin films which were manufactured into T-shaped cantilevers [31]. Circular shaped masses of increasing diameter were removed from the end of the T shaped cantilever and a plot of mass milled versus $1/L^3\nu^2$ were generated. The plots displayed the expected linear relationship, and after fitting a linear regression to the data, the slope of the fit provided the Young's modulus while the y-intercept gave the thickness of the silicon nitride film.

In the research discussed above, FIB milling was used to determine properties of large mass-sensing cantilevers (over 500 μm long in some cases; primarily for measuring the milling and deposition rates of FIB processes. These papers were not concerned with achieving spring constant calibration with high accuracy, nor did they seek to test and validate the method itself by comparing the results to other techniques. The cantilevers studied by Friedli and Woszczyna were also not used to acquire any AFM data after the milling process.

The calibration method reported here represents a significant development on these previous approaches, and is applied in an unprecedented manner to the calibration of AFM cantilevers with very low uncertainty. In addition, the method is supported with rigorous validation and practical guidelines for implementation.

3.1.2 Results and discussion

The FIB method was applied to a wide variety of cantilevers, in order to demonstrate the scope of the technique. The 4 different types of cantilevers used are shown in figure 3.1a-d) and vary in material, geometry, dimensions and presence of an imaging tip. The cantilevers studied are also listed in table 3.1 for reference. A comprehensive overview of each type is provided, including its properties and the designation for each.

Cantilever	Composition	Geometry	Coating	Manufacturer and model	Nominal spring constant range (Nm^{-1})	Length (μm)	Width (μm)
^{1}M1	Si	Beam	Al	Mikromasch NSC15	20 - 75	120	39
^{1}C1			Au/Cr	Mikromasch CSC12	0.15-1.5	133	34.5
^{1}C2					0.25-2.5	112.4	33.5
^{1}C3					0.45-5.0	94.1	34.7
^{1}C4					0.15-1.5	135.6	34.5
^{1}C5					0.25-2.5	114.6	34.5
^{1}C6					0.45-5.0	94.2	34.2
^{1}C7					0.15-1.5	138	34
^{1}C8					0.45-5.0	97.5	34.1
^{1}R1			None	Bruker CLFC	0.157	390	25.3
^{1}R2					1.3	193	25.3
^{1}R3					10.4	91	25.3
^{1}R4					1.3	193	25
^{1}R5					10.4	93.2	25
^{1}F1^a				Bruker FMV	1.1-5	215	33
^{1}F2^a					1.1-5	209	41.5
^{1}V1	Si_3N_4	V shaped	Au/Ti	Bruker OTR8	0.57	97	15

[a] These cantilevers have a trapezoidal cross section.

Table 3.1: Properties and types of the different cantilevers used.

Single-point calibration FIB milling was used to remove circular sections from four different cantilevers, three tip-less types ^{1}R1-3 (CLFC, Mikromasch) and a standard tapping mode type ^{1}M1 (NSC15, Mikromasch). This approach is referred to as a “single-point” measurement as a single mass removal step was used along with equation 3.4 to determine the spring constant. In each case the hole was milled large enough such that the resonance shift was easily detectable. As a percentage of the cantilevers' width, the hole was 50% and 35% for the tip-less and tapping mode cantilevers respectively. The results are compared to several established calibration methods in table 3.2.

For cantilevers ^{1}R1-3, it is expected that the established methods will have low uncertainty as these CLFC type cantilevers are designed as reference cantilevers for spring constant calibration, possessing almost perfect beam geometry. Although the uncertainties quoted in table 3.2 are very low, this is expected to be the case for cantilevers ^{1}R1-3 only. Cantilever ^{1}M1 is a tapping mode type which better represents standard cantilevers in use, and deviates from ideal geometry. The uncertainty for this cantilever is expected to be much higher, and the results for ^{1}M1 indeed show a greater variance than the tip-less types.

Multiple-point calibration In addition to the standard, single-point calibration, a multiple-point method was also used. This is primarily performed to demonstrate validity of the FIB method itself, and this is discussed thoroughly in section 3.1.3. It is, however, useful to compare these results with existing methods in the same manner as the single-point technique.

The multiple-point measurement method is essentially a series of single-point measurements on an individual cantilever, but where the hole size is initially small and then gradually enlarged. Observing equation 3.5, if the mass removed is plotted against the frequency term, then a linear expression results from which the spring constant of the cantilever can be extracted.

$$M = k\,(2\pi\nu)^{-2} - m^* \tag{3.5}$$

This approach increases measurement time, but provides greater accuracy in the final result. Multiple-point measurement results are presented in table 3.3 and are discussed in the following section along with the results of the single-point measurements.

Cantilever	Spring Constant (Nm^{-1})					
	FIB (7-10%)	Thermal (10-20%)	Sader hydrodynamic (5-10%)	Sader resonance (5-10%)	Cleveland dimensional (5-10%)	Euler beam (10%)
^{1}R1	0.0950 ±0.021	-	0.0842	0.0811	0.082	0.086
^{1}R2	0.746 ±0.060	-	0.727	0.69	0.701	0.726
^{1}R3	6.40 ±0.45	-	6.51	6.22	6.22	6.77
^{1}M1[a]	44.3 ±2.8	42.1	46.8	44.1	36.7	42.3

[a] The non-ideal geometry of this cantilever results greater uncertainty than that reported for ^{1}R1-3, in the case of the established methods.

Table 3.2: Spring constant of cantilevers determined using the single-point FIB method, compared to established techniques.

Cantilever	Spring Constant (Nm^{-1})							
	FIB (±7-10%)	Thermal (±10-20%)	Sader hydrodynamic (±5-15%)	Sader resonance (±10-20%)	Cleveland dimensional (±10-15%)	Euler beam (±10-20%)	Reference lever pre-milling (±10-20 %)	Reference lever post-milling (±10-20 %)
^{1}C1	1.36±0.15	-	1.41	1.29	1.29	1.52	1.45	1.45[a]
^{1}F1	2.53±0.18	2.5	2.5	2.55	2.5	2.67	-	2.40[a]
^{1}F2	3.40±0.25	3.11	3.27	3.07	2.91	3.4	-	3.37[a]

[a] Measurements were made when D/W=0.44, 0.50 and 0.50 for levers ^{1}C1, ^{1}F1 and ^{1}F2. ^{1}C1 was calibrated using ^{1}V1 and ^{1}F1, ^{1}F2 was calibrated using ^{1}R4.

Table 3.3: Spring constant of cantilevers determined using the multiple-point FIB method, compared to established techniques.

3.1.2.1 Comparison with existing methods

For most cantilevers, the FIB method is observed to compare very well to existing techniques, with variation between the methods of less than 8%. This is not the case for the single-point measurement of cantilever ^{1}R1, where the spring constant appears to be overestimated by 10-15%, indicating a limitation of the method. Cantilever ^{1}R1 has a very low spring constant, and as a result the shift in resonant frequency upon mass removal is significantly reduced. Cantilevers ^{1}R1-3 exhibit resonance shifts of 22.63 kHz, 2.735 kHz and 323 Hz respectively; reduction of the resonance shift results in significant uncertainty. As a result the total uncertainty for cantilever ^{1}R1 is very high at 22%, in comparison to an uncertainty of 7% for cantilevers' ^{1}R2-3. This effect is clearly observed in the uncertainty analysis, which is provided in section 3.1.3.3.

In this regard, short cantilevers with high resonant frequency and spring constant have an advantage using the FIB method, since they will produce large resonant frequency shifts (greater than 2 kHz) for small diameter holes. However for cantilevers with thickness below 1 μm and/or spring constants below 0.700 Nm^{-1} exhibiting a low resonant frequency shift, the FIB method can be applied, but at the cost of increased uncertainty.

This seems to potentially exclude a large number of cantilever types, however there are many applications for cantilevers with high spring constant in determining adhesion and material properties of surfaces and structures [32–36], as well as micro-mechanical sensor research [29–31]. For cantilevers with spring constants greater than 0.7 Nm^{-1} and thickness greater than 1 μm, the percentage of the cantilever mass which should be removed in order to generate a 2 kHz resonance shift is estimated to be between 1-5%.

Percentage uncertainties and their ranges are quoted for each method in tables 3.2 and 3.3. Each value is estimated from the propagation of measurement uncertainty for the parameters in each technique, as well as from review articles and detailed technique comparisons reported in the literature [17, 37–40].

Thermal noise The general agreement with the thermal method is quite good, despite previous research suggesting that this technique should not be applied to cantilevers with spring constant greater than 1 Nm^{-1} [40]. This is particularly tested by cantilever ^{1}M1, which has a spring constant of $\sim$45Nm^{-1} and yet still shows good agreement. The reason for this improvement is most likely due to the low noise detection system of the Multimode 8 instrument used and the increased sampling rate of the newer Nanoscope V controller. The sampling rate used is 200 kHz, and is a significant improvement over previous controllers which have sampling rates of 62.5 kHz.

Application of the thermal method was restricted to cantilevers with imaging tips and as such, there are no thermal results for both C and R type cantilevers. This is due to very high adhesion on tip-less cantilevers which prohibits sensitivity measurements, prior to the thermal calibration.

Sader hydrodynamic The Sader hydrodynamic method compares well with the FIB method for all cantilevers. Previous research claims that this method varies significantly for cantilevers with trapezoidal geometry (ie. ^{1}F1-2). The reason for this deviation is how the width or length of the cantilever is defined with regard to the trapezoidal geometry. The width used should be the larger of the two, since the Sader hydrodynamic method relies on modelling the hydrodynamic drag on the cantilever. The length should be measured from the base of the cantilever to the tip apex, excluding the tapered section after the tip.

Poggi et al. used the entire length of the cantilever when comparing the Sader hydrodynamic method and Euler beam theory [24]. Using this approach, any overestimation of the length will exaggerate the difference between these two methods. The Sader hydrodynamic method will overestimate while Euler beam theory will significantly underestimate the spring constant.

The investigation by Poggi et al. showed that the Sader hydrodynamic method was 20-40% larger than the corrected Euler beam theory technique they developed. If the length of the cantilever is reduced by 5-10% (which is the typical tip offset percentage for these cantilevers) then the Sader hydrodynamic method will reduce by 5-10% and the beam theory result will increase by 15-30%. This improves the comparison of all the results presented by Poggi et al. For cantilevers with trapezoidal cross-section, the Sader hydrodynamic technique can be improved by at least 5-10% by correctly defining cantilever dimensions, indicating that this method is more robust than previously reported.

However, given that the Sader hydrodynamic method is modelled on the cantilever possessing a perfect beam shape, the uncertainty for application to these types of cantilevers is estimated to be between 10-15%. Recent work extending the Sader hydrodynamic method to cantilevers of arbitrary shape would reduce the uncertainty of this technique substantially, provided an accurate reference measurement is available [41]. With regard to the combination of ease of use and low uncertainty, the Sader hydrodynamic method is an excellent technique when applied correctly.

For high accuracy measurements, the FIB technique is particularly relevant, since cantilevers such as ^{1}F1 and ^{1}F2 are composed of single crystal silicon with no metal coatings and have relatively high resonant frequencies (i.e. greater than 50 kHz), making these types of probes excellent candidates for the FIB method.

In the case of cantilever ^{1}M1, the geometry of this cantilever more closely approximates the shape of a beam at the end section than cantilevers' ^{1}F1 or ^{1}F2. Therefore the length was measured from the base to the very end of the cantilever and the spring constant was corrected for ΔL. Using this approach cantilever ^{1}M1 shows good agreement between the Sader hydrodynamic and FIB methods.

It should also be noted that the point where the length measurement should begin is not necessarily a trivial matter [2]. A plan view image of cantilever ^{1}M1 shows that the base could be taken at the point where the beam meets the chip in figure 3.4a), approximately 6 μm below the dotted line. When the cantilever is imaged from behind in figure 3.4b), or from the side in figure 3.4c), it is obvious that the effective length of the lever is much shorter. The actual clamped point of the cantilever is shown in figure 3.4a) and 3.4b) by the dotted white line, meaning that the length of the cantilever could be overestimated by approximately 6 μm.

Correct measurement of the cantilever length will affect each calibration method, depending on how the spring constant in each technique varies with regard to the length of the cantilever. For the Sader hydrodynamic method, for example, the dependence of spring constant on cantilever length is linear so the above example would result in an overestimation of the spring constant by approximately 5%. For the Euler-Bernoulli beam equation the spring constant is inversely proportional to

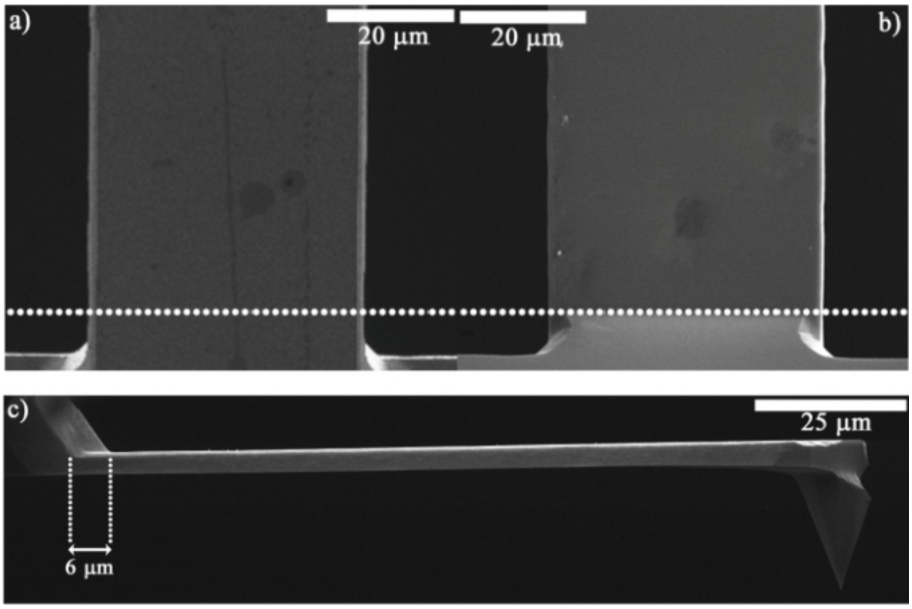

Figure 3.4: SEM images of cantilever ^{1}M1 where (a) and (b) are plan views from the tip side and back of the cantilever respectively while (c) is a side view. Reprinted with permission from [22].

the length cubed of the cantilever and therefore the effect is more significant. If the above length correction were not accounted for in the Euler-Bernoulli beam method, then the spring constant would be underestimated by 15%.

Sader resonance For this method it is necessary to include the mass of the AFM tip for cantilevers ^{1}F1-2 and ^{1}M1. The tip height for these probes is on the order of 13-25 μm and contributes significantly to the cantilever mass (~5-10%). Recent work also supports this requirement for particular types of AFM probes [42]. Depending on the complexity of the tip shape, this will add additional uncertainty to the method.

Cleveland dimensional The Cleveland dimensional method compares well to the FIB method for most cantilevers, with a tendency to underestimate the spring constant. This is not the case for cantilever ^{1}M1 however, where the spring constant is significantly underestimated while the discrepancy is less for cantilevers ^{1}F1-2. This is not surprising as the tip volume for this cantilever accounts for a significant proportion of the total volume (refer to figure 3.4c) and the Cleveland dimensional method does not take tip mass into account.

Euler beam Comparison between the Euler beam and FIB methods is generally quite good, considering the high uncertainty associated with the technique. This is likely due to accurate measurement of cantilever dimensions, and appropriate specification of the cantilevers' length and width.

Reference cantilever method The reference lever method was applied to cantilever ^{1}M1 before and after milling (using reference lever ^{1}R5), and the spring constant was found to be 46.0 Nm^{-1} before milling and 45.2 Nm^{-1} after milling. This is only a 1.7% change and is within the uncertainty of the measurement. These results suggest that the holes milled produce negligible changes in the cantilever spring constant, however this is investigated in further detail in the following section.

3.1.3 Validation of the FIB method

Although the FIB method is based on the well-established Cleveland method, modifications made to the technique necessitate careful validation. The aim to provide a highly accurate technique also demands careful testing of assumptions, if claims of low uncertainty are to be made. There are a number of potential sources of uncertainty introduced, which are discussed extensively. Several aspects of the original Cleveland method are also investigated in greater detail.

3.1.3.1 Validation of the Cleveland formula

Application with small masses The Cleveland added mass method is often performed with gold or tungsten spheres, whose mass is larger than that of the cantilever. Sader et al. have reported that application of the off-end loading correction to this method is reliant on the assumption that the mass added (or removed in the case of the FIB method) is greater than that of the cantilever [13].

In the case of the FIB method, the mass removed is certainly less than the cantilevers' total mass and so this aspect was investigated thoroughly. There are numerous examples in literature where the Cleveland method is applied with masses lighter than the cantilever (such as polystyrene spheres), but the actual uncertainty introduced is yet to be investigated [25, 38, 43–47].

An analysis of a publication by Xie et al. is performed below, where a polystyrene sphere was moved incrementally along the length of a silicon microcantilever and the resonant frequency measured at each point [47]. The total mass of the polystyrene sphere was measured to be less than 2% of the cantilevers' mass, which violates this assumption inherent in the off-end loading correction.

Analysis of the data from figure 4b in the paper by Xie et al. yields the resonant frequency of the cantilever at each sphere position. Calculation of the effective mass of the sphere at each position using the off-end loading correction and the resonant frequency factor $(2\pi\nu)^{-2}$, produces a linear relationship as shown in figure 3.5.

This satisfies equation 3.6 which is the familiar expression used by Cleveland et al. and introduced previously [25]; where k is the spring constant of the cantilever, ν is the loaded resonance frequency, $m*$ is the effective mass of the cantilever and M is the mass of the sphere (corrected for position on the cantilever using equation 3.3).

$$M = k\,(2\pi\nu)^{-2} - m* \tag{3.6}$$

The relationship in figure 3.5 is highly linear, and the spring constant can be read directly from the slope as 20.44 Nm^{-1}, which is in excellent agreement with the value of 20.15 Nm^{-1} obtained by Xie et al.

If the spring constant is determined at each sphere position on the cantilever and not corrected for off-end loading, the variation in spring constant along the cantilevers' length can be observed. Comparing this data to the off-end loading relationship (using k = 20.15 Nm^{-1}) allows the spring constant measured by the Cleveland method with a light mass to be compared against the theoretical variation along the length of the cantilever. This resembles the analysis performed by Sader

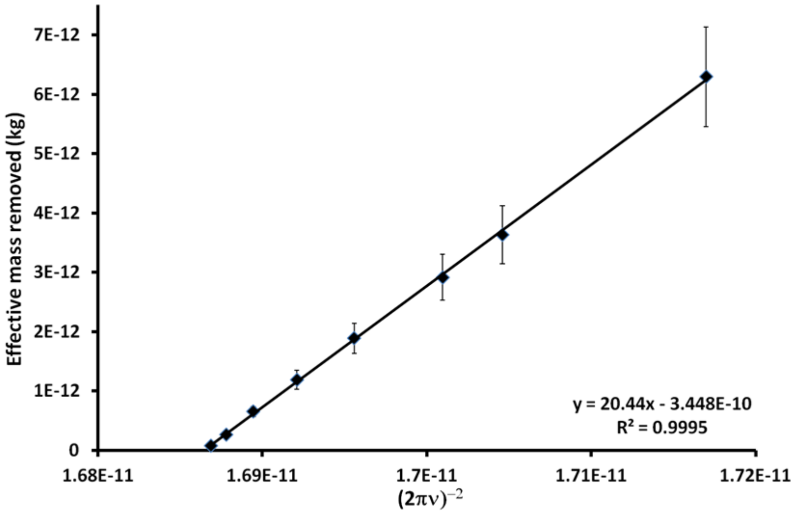

Figure 3.5: Plot of effective mass versus $(2\pi\nu)^{-2}$ for the polystyrene sphere at different positions on the silicon cantilever. Reprinted and adapted with permission from [47].

et al. for a V-shaped cantilever with a heavy tungsten sphere, to verify the off-end loading relationship for V-shaped cantilevers [13].

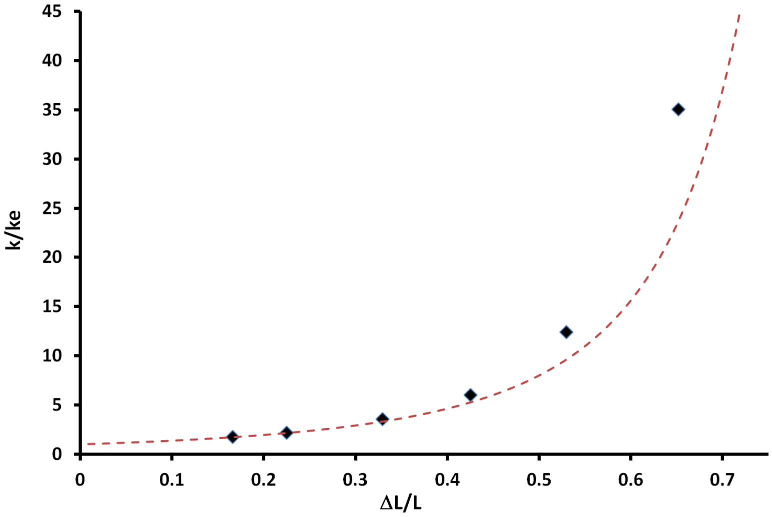

Figure 3.6: Comparison between theory (dashed line) and experimental data (diamonds) of the variation of the spring constant along the length of a cantilever. The ratio k/k_e represents the spring constant relative to that at the free end of the cantilever. Reprinted and adapted with permission from [47].

This result is shown in figure 3.6 using the same data from Xie et al. which was presented in figure 3.5. For loading positions near the free end of the cantilever (within approximately 35%), the agreement between theory and experiment is good. As the sphere is placed closer towards the fixed end of the cantilever, there is substantial deviation between the two (over 30 % for the final data point). This suggests that application of the Cleveland method with masses much smaller than that of the cantilever is valid as long as the mass is placed as close to the free end as possible.

Multiple-point measurement validation In accordance with equation 1.25, a plot of the resonant frequency with removal of successively greater masses should yield a linear relationship where the slope corresponds to the cantilevers' spring constant [25]. This test was performed by Cleveland et al. in their original publication and it is useful to perform this analysis again here. In addition to providing validation of the Cleveland formula, a multiple-point measurement also affords greater accuracy (albeit at the cost of greater measurement time).

Cleveland et al. made these measurements by attaching spheres of increasing mass; in contrast, here this is achieved by sequentially milling holes of increasingly diameter. The resonant frequency was measured after each step and the results of this analysis for several cantilevers are shown in figure 3.7. From the slope of the linear regression fits, the spring constants were determined in addition to the correlation coefficients. The data shows the expected linear response, with correlation coefficients greater than 0.997 indicating a high degree of linearity.

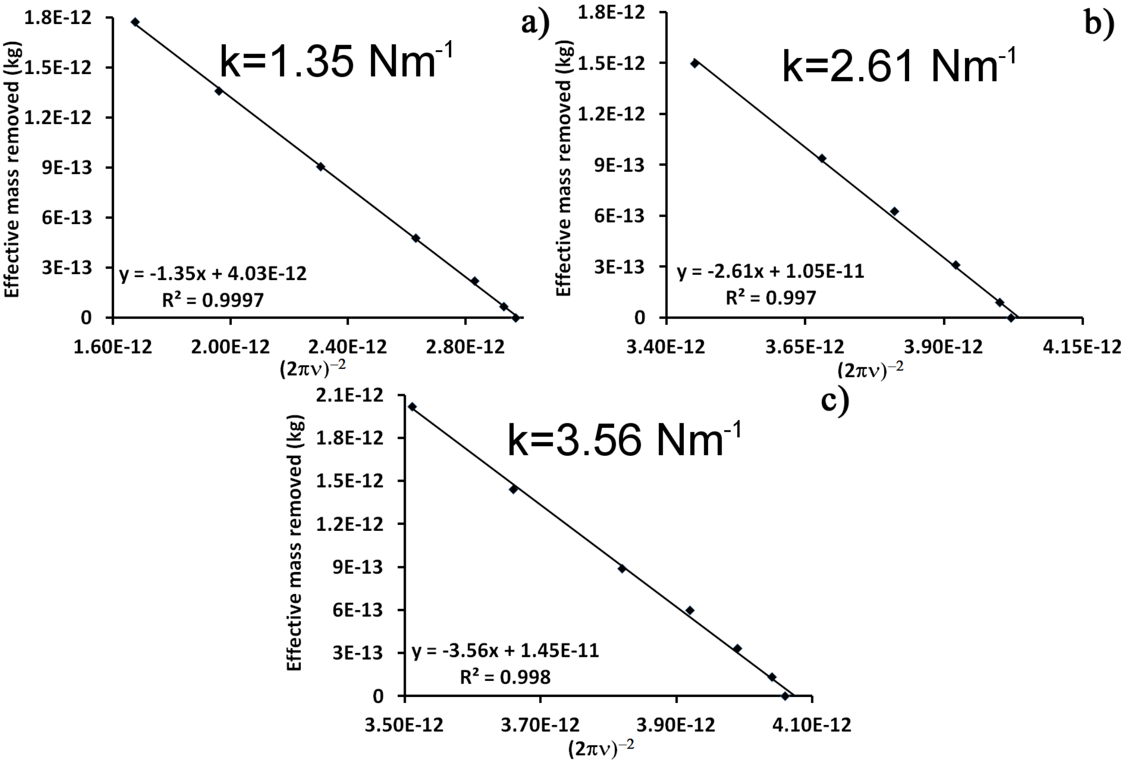

Figure 3.7: Effective mass removed versus $(2\pi\nu)^{-2}$ for cantilevers (a) ^{1}C1 (b) ^{1}F1 and (c) ^{1}F2. Simple linear regression fits were applied to the data; the equation and correlation coefficient for each fit is displayed on the corresponding graph. The slope of the linear fit gives the spring constant for each cantilever. Reprinted with permission from [22].

3.1.3.2 Effect of milling on cantilever properties

Perhaps the most obvious source of uncertainty in the mass removal method arises from modification of the cantilevers' structure – the removal of a complete section near the free end. Extensive testing was performed to detect any variation in the mechanical properties of the cantilever as a result of the milling process, the results of which are presented here.

Resonant frequency comparison In order to determine if the spring constant of the cantilever changes as a result of milling, the resonant frequency shift due to mass removal was predicted theoretically. This derivation is shown below, and requires the following assumptions:

- The cantilever must have perfect rectangular geometry, with uniform cross section and material properties.
- The spring constant is unchanged by the mass removal.

Comparison between the theoretically predicted resonant frequency and the measured values allows these assumptions to be tested, which enables variation of the spring constant to be detected. The latter assumption allows the following expression to be written, using the familiar relationship $k = mv^2$.

$$m_0\nu_0^2 = m_1\nu_1^2 \tag{3.7}$$

The resonant frequency and cantilever mass are given by m and ν, where the subscripts 0 and 1 denotes pre- and post-milling respectively. The mass of the milled cantilever can be written as $m_1 = m_0 - m*$, where $m*$ is the mass removed. Combining this expression with the formula for effective cantilever mass $m_0 = 0.24\rho\ wtL$ [25], and assuming removal of a cylindrical volume (of radius r) allows the removed mass ($m*$) to be written as:

$$m* = \pi r^2 \rho t \left(\frac{L - \Delta L}{L}\right)^3 \tag{3.8}$$

Here, t and ρ are the thickness and density of the cantilever respectively; the off-end loading correction is also used to account for the location of the removed mass. Substitution of these expressions and rearranging to obtain ν_1 as the subject of the equation, the following formula is obtained for the predicted resonant frequency of the cantilever after milling.

$$\nu_1 = \nu_0 \sqrt{\frac{0.24WL}{0.24WL - 0.5\pi D^2\left(\frac{L-\Delta L}{L}\right)}} \tag{3.9}$$

Equation 3.9 was applied to cantilever ^{1}C1, which has ideal geometry and cross section. The theoretical and measured frequencies were plotted against the ratio of the milled hole diameter to cantilever width (D/W), and the result is shown in figure 3.8.

Figure 3.8 shows good agreement between theory and experiment, which is within the range of experimental uncertainty for the entire range of holes milled. The uncertainty on the experimental values is estimated to be ±50 Hz, while the uncertainty on the theoretical values is less than 5% and is dominated by uncertainty in the diameter of each hole (1-3%). According to equation 3.9, the uncertainty for the theoretical values will increase as the diameter of the milled hole increases. Even so, the difference between theory and experiment is less than 1%; therefore these measurements do not indicate any significant change in the cantilevers' dynamic spring constant as the hole size increases. The increase in resonant frequency is, thus, expected to be due entirely to a decrease in the cantilevers' effective mass. This also supports the use of equation 3.3 in correcting the mass removed.

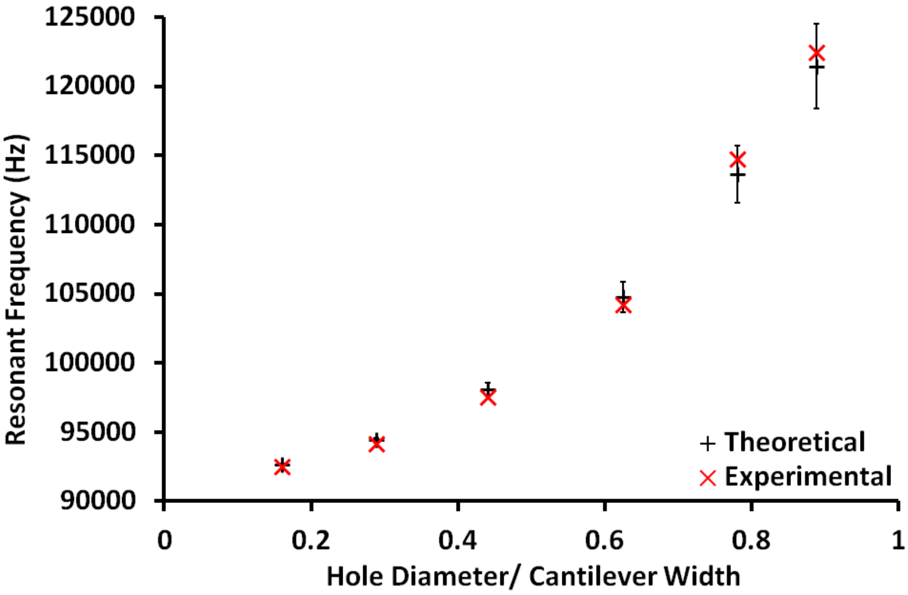

Figure 3.8: Theoretically derived and experimentally measured resonant frequencies versus D/W for cantilever ^{1}C1. Reprinted with permission from [22].

Holes of $D/W = 0.70$ were also milled near the ends of two other cantilevers (^{1}C2, ^{1}C3) and equation 3.9 again used to predict their resonant frequencies after FIB milling. For cantilever ^{1}C2 ν_{theory}= 148.608 kHz while $\nu_{experimental}$= 148.410 kHz. For cantilever ^{1}C3 ν_{theory}= 222.729 kHz while $\nu_{experimental}$= 224.522 kHz. Both cantilevers display a difference of less than 1% between theory and experiment, which further supports the claims made above.

Relative reference cantilever method In order to further understand and confirm the effect of mass removal on the cantilevers' mechanical properties, the reference cantilever method was used to monitor variation in the spring constant of a test cantilever as a result of FIB milling.

Effect of hole size In order to directly measure variation of the static spring constant due to the milling process, the effect of increasing hole size on the spring constant of cantilever ^{1}C1 was investigated using the reference cantilever method [1, 10]. While the validation up until now is useful in testing underlying assumptions of the technique, the reference cantilever method allows direct determination of the static spring constant at a precise location between the milled hole and the very end of the cantilever. One might expect that as the size of the hole increases, the cantilever could weaken and a flexible hinge may form. This would reduce the overall spring constant of the cantilever, and this analysis is performed specifically to test this effect.

The reference cantilever technique was used to determine the ratio of spring constants between a reference cantilever (^{1}V1 from table 3.1) and cantilever ^{1}C1 as the hole size was increased. The spring constant of the reference cantilever is assumed to be constant, so the post-milling spring constant ratios can be divided by the pre-milled spring constant ratio to obtain a change in the spring constant for cantilever ^{1}C1. The spring constant of the reference cantilever was measured before and after each application using the thermal method, to ensure that it remained the same [16]. The reference spring constant ($k_{thermal}$) remained at 0.680 ±0.07 Nm^{-1}, with a ±7% variation over the experimental period (~8 months).

This variation is unlikely to be due to any actual change in the cantilever, but rather the repeatability of the thermal method. To reduce uncertainty in the loading position, the reference cantilever (^{1}V1) was used to image the end of the test cantilever (^{1}C1) prior to measurement. This allowed precise positioning and meant that ΔL could be determined with an uncertainty of well below 1%. Figure 3.9 shows an AFM and corresponding SEM image of cantilever ^{1}C1, these images were acquired after the first hole had been milled.

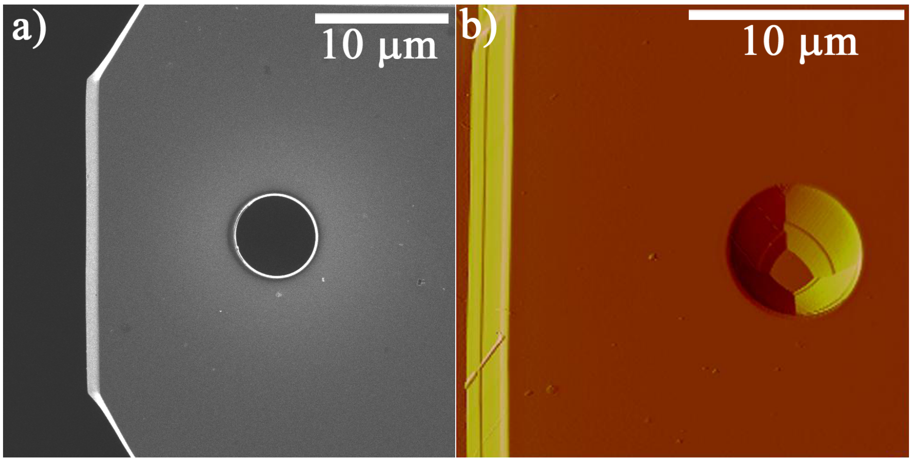

Figure 3.9: SEM image (a) and AFM image (b) of cantilever ^{1}C1 after the first hole was milled. Reprinted with permission from [22].

Figure 3.10 shows the ratio of $k_{\text{post-mill}}/k_{\text{pre-mill}}$ determined using the reference lever method versus D/W at each stage of mass removal for cantilever ^{1}C1 (except for $D/W = 0.35$, this point was not measured). The data shows that the static spring constant of ^{1}C1 is essentially constant and within experimental uncertainty until D/W reaches 0.64, 0.78 and 0.88, at which point the spring constant is observed to decrease by 6%, 9.5% and 10% respectively.

This appears to be inconsistent with the data in figure 3.8, which suggests that the dynamic spring constant of the cantilever is essentially unchanged. The change in the static spring constant for cantilevers ^{1}C2 and ^{1}C3 was also measured after FIB milling and a similar decrease (approximately 8-11%) was also observed. This apparent inconsistency may be due to variation in the relationship between the static and dynamic spring constant as the hole size increases, and the cantilever shape changes.

The static spring constant (k_s) is not equal to the dynamic spring constant (k_d) for the first resonance mode [48, 49], and these values are individually measured by the reference cantilever and frequency shift validation techniques respectively. For a rectangular cantilever, the difference is only a few percent and is given by k_d/k_s= 1.03. Recent work by Melcher et al. [50] and Hahner et al. [51] has demonstrated that cantilevers with non-rectangular geometries may have a dynamic spring constant which is significantly greater than the static spring constant. For a picket or dagger shaped cantilever (these cantilevers have the end corners removed) they derived k_d/k_s = 1.07 and for a V shaped geometry k_d/k_s = 1.09k$_s$. Recent research by Sader et al.

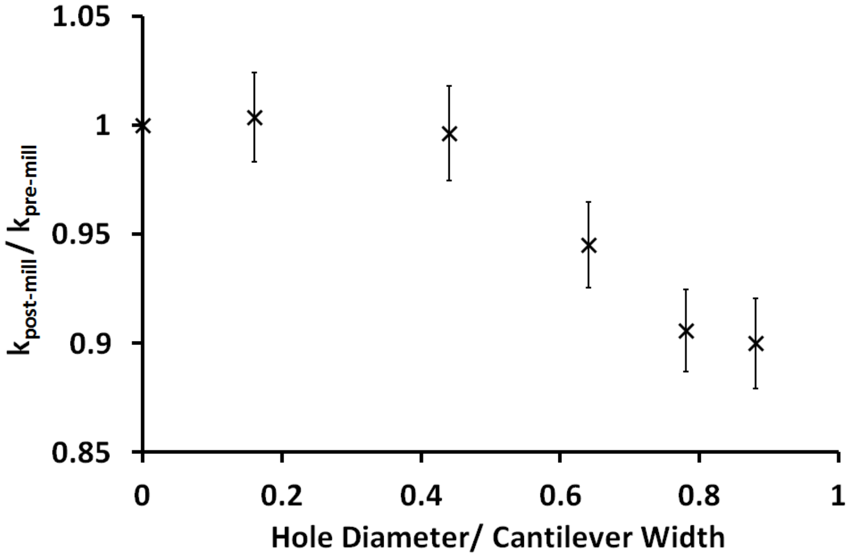

Figure 3.10: Variation in the spring constant of cantilever ^{1}C1 before and after milling ($k_{post-mill}/k_{pre-mill}$) versus D/W. Reprinted with permission from [22].

has shown that this value can be even greater [41].

It is likely that milling of the cantilever affects the k_d/k_s ratio, which would vary as the size of the hole changes. An increase in k_d/k_s for cantilever ^{1}C1 could compensate for the reduction of $\mathrm{k_s}$ and therefore little or no change in k_d would be observed. This is a likely explanation for the discrepancy observed, and suggests that the assumptions inherent in equation 3.9 remain valid.

In figure 3.10 the static spring constant does not decrease until $D/W = 0.64$, so k_d/k_s will be valid for a rectangular cantilever until this point. Given these results, it would be wise to restrict the hole diameters to ~50% or less of the total cantilever width. In order to avoid this effect and obtain a more precise measurement of the spring constants determined in figure 3.7, points 5-7 were removed from figure 3.7a (cantilever ^{1}C1) and point 7 removed from figure 3.7c (cantilever ^{1}F2). Recalculating the linear fits after removing these points gives a new spring constant value of 1.36 $\mathrm{Nm^{-1}}$ for cantilever ^{1}C1 and 3.40 $\mathrm{Nm^{-1}}$ for cantilever ^{1}F2; recalculation for cantilever ^{1}F1 was not necessary as D/W was less than 0.5 for all measurements.

Effect of hole location In addition to hole size, the effect of hole position on the spring constant was also investigated by milling large holes ($D/W = 0.7$) at varying positions on cantilevers across three chips. Cantilevers ^{1}C1-3 had a hole located close to their free end, ^{1}C4-6 had a hole located at the centre of the cantilever, while for ^{1}C7 and ^{1}C8 the hole was positioned close to the fixed end. The reference cantilever technique was again used to measure variation of the static spring constant due to milling, employing the same reference cantilever (^{1}V1).

The ratio of the cantilevers' resonant frequency before and after milling was also determined, and the effective mass ratio for each lever was calculated using the relationship $k = m\,(2\pi\nu)^2$. For cantilevers ^{1}C1-3, $\mathrm{k_d}$ is assumed to be constant, whereas k_d and k_s are both expected to vary for cantilevers ^{1}C4-8. Variation of k_d and k_s is not likely to be equal, and thus the k_d/k_s ratio is expected to vary for cantilevers ^{1}C4-8. This comparison is still useful, however, as it provides a qualitative estimate for variation of cantilever effective mass due to milling. Table 3.4 displays this data.

Cantilever	$\left(\frac{L-\Delta L}{L}\right)$	$\frac{D}{W}$	$\frac{D}{L}$	$\frac{k_{post-mill}}{k_{pre-mill}}$	$\left(\frac{\nu_{post-mill}}{\nu_{pre-mill}}\right)^2$	$\frac{m_{post-mill}}{m_{pre-mill}}$
^{1}C1	0.9	0.78	0.2	0.92	1.56	0.64
^{1}C2	0.85	0.7	0.22	0.89	1.41	0.71
^{1}C3	0.8	0.7	0.27	0.92	1.48	0.68
^{1}C4	0.5	0.7	0.18	0.8	0.83	0.96
^{1}C5	0.5	0.7	0.22	0.75	0.78	0.96
^{1}C6	0.5	0.7	0.27	0.82	0.75	1.09
^{1}C7	0.14	0.7	0.27	0.32	0.36	0.89
^{1}C8	0.1	0.7	0.18	0.42	0.41	1.02

Although the perfectly rectangular ^{1}R1-5 cantilevers are better suited to these measurements than ^{1}C1-8, these levers were not acquired until the majority of the milling experiments were completed and were hence used for other purposes.

Table 3.4: Properties of cantilevers ^{1}C1-8, showing the effect of hole position along the length of the cantilever.

The data in table 3.4 clearly shows that the position of the hole has a significant effect on the cantilevers' spring constant. When the hole is positioned at the free end the change in stiffness is minimal, while holes positioned at the middle and fixed end of the cantilever reduce the static spring constant by approximately 20-25% and 60-65% respectively. This effect is not surprising since the cantilevers' fixed end is where the bulk of the cantilever strain occurs. Any removal of material from this region is expected to have substantial effects on the cantilevers' mechanical properties. This effect will decrease as holes are milled further from the fixed end.

Variation in the resonant frequency reflects the changes observed in the spring constant. Holes milled at the free end of the cantilever result in an increase in resonant frequency, indicating that the hole is simply behaving as a removed mass; while for holes milled closer to the cantilevers' fixed end, the resonant frequency decreases significantly, indicating that the hole is significantly affecting both the dynamic and static spring constant of the cantilever.

These results suggest that removal of mass at the free end of the cantilever has a substantial effect on the cantilevers' effective mass, resulting in a reduction of approximately 40%; while holes positioned closer to the base of the cantilever result in a much smaller change to the effective mass. These results are supported by Wilkinson et al., who measured and calculated changes in stiffness and effective mass for beam shaped cantilevers after milling square holes of varying width and length located at the base of each cantilever [52]. Their experimental and theoretical results indicated that holes milled at the base of the cantilever significantly reduce the spring constant and resonant frequency with small change to the effective mass. Depending on the size and geometry of the hole, in some instances a minor increase of the effective mass was expected and observed experimentally.

These results are useful in determining the most effective way to apply the FIB calibration method, such that the assumptions made are valid and that the uncertainty associated with the method is minimised. In order to achieve this, the diameter of the hole milled should be approximately 50% of the cantilevers' width and be positioned as close to the free end as possible. This allows the hole to act only as a removed mass and reduces any effect that the milling process has on modifying the static spring constant of the cantilever. The other advantage of reducing the hole size, is limiting the reduction of laser signal from the back of the cantilever. For cantilever ^{1}C1, the $D/W = 0.88$ hole resulted in a ~50% reduction of the laser signal, whereas a reduction of ~15% was observed for $D/W = 0.44$.

Operational quality of FIB cantilevers The ability of each practical cantilever to acquire data was verified through AFM imaging. The maximum reduction in laser signal was 30-40% for cantilevers ^{1}F1-2, and 5% for cantilever ^{1}M1. Each probe was tested by imaging a CNT-covered silicon surface. Figure 3.11 is an AFM image acquired using cantilever ^{1}F1, the image was acquired after the final milling step had been completed.

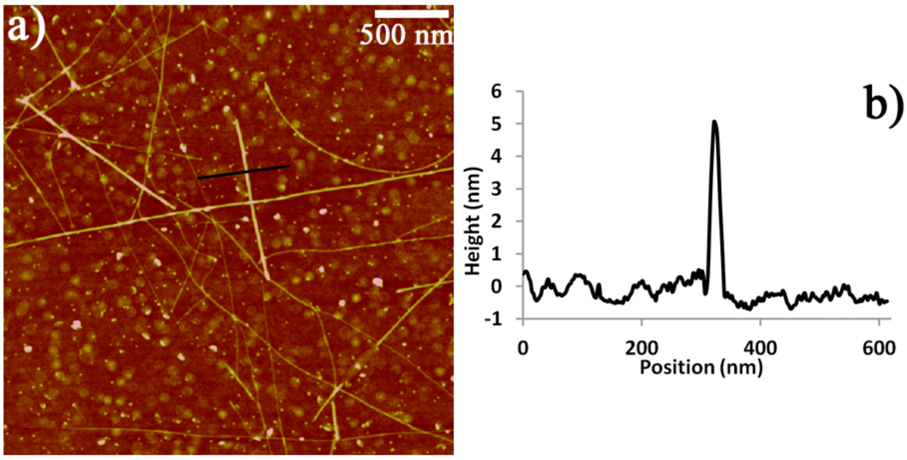

Figure 3.11: Tapping mode AFM image of a carbon nanotube covered silicon surface, acquired using cantilever ^{1}F1 after the final milling step and (b) a cross section located along the black line. Reprinted with permission from [22].

It is important to note that the quality of the image is excellent, considering the operational lifetime of the probe (approximately 8 months) and no degradation in cantilever performance due to mass removal is observed. Similar quality data was obtained for all probes that were FIB processed, in fact Hodges et al. claim that removing mass from AFM cantilevers can potentially improve their performance by increasing their resonant frequency and reducing their thermal noise profile [53].

A cross-section of a carbon nanotube is shown in figure 3.11b. Using the technique described by Wang et al., the diameter of the imaging tip can be estimated as ~34 nm [54]. The nominal diameter, quoted by the manufacturer, for the ^{1}F2 probe used to acquire this image is 20-24 nm. This indicates an increase in tip diameter compared to the nominal values, which is not surprising. However, the observed tip diameter is occasionally outside this range for as-received probes, which is likely due to damage of the delicate tip upon engaging on the surface. These cantilevers are also ideally suited to dynamic imaging modes such as force modulation and tapping mode and therefore can be blunted very easily when applied in static modes of operation which were necessary for contact mode imaging, reference cantilever and deflection sensitivity measurements. Since the FIB method does not require tip to surface contact, the advantage of eliminating damage to delicate tips is clear.

3.1.3.3 Uncertainty in the FIB method

The uncertainty associated with application of the FIB method is determined according to the ISO guide to the expression of uncertainty in measurement [55]. A Taylor series based law of propogation of uncertainty was used to determine the combined standard uncertainty, as shown in equation 3.10.

$$u_c^2(y) = \sum_{i=1}^{N} (\frac{df}{dx_i}) u^2(x_i) \tag{3.10}$$

In this case, f is taken to be $k_{\Delta L}$ as defined in equation 3.4, which is simplified to "k" here. This results in the following expression for the combined standard uncertainty in the spring constant, with additional thickness terms for cantilevers incorporating metal coatings as shown:

$$\begin{split} dk^2 = (\frac{\delta k}{\delta r} dr)^2 + (\frac{\delta k}{\delta t_{Si}} dt_{Si})^2 + (\frac{\delta k}{\delta t_{film}} dt_{film})^2 + (\frac{\delta k}{\delta \nu_0} d\nu_0)^2 + \\ (\frac{\delta k}{\delta \nu_1} d\nu_1)^2 + (\frac{\delta k}{\delta L} dL)^2 + (\frac{\delta k}{\delta \Delta L} d\Delta L)^2 \end{split} \tag{3.11}$$

A detailed error budget is provided in table 3.5, which shows the standard uncertainty assigned to each of the measured quantities used to determine the spring constant for cantilever ^{1}R3. Included are the sensitivity coefficients associated with each of these variables and their contribution to the total uncertainty in the spring constant. For all measurements the standard uncertainties are quoted with complete confidence in their range, and as such the number of degrees of freedom is effectively infinite. All uncertainties reported in table 3.5 are expected to have a normal distribution.

The uncertainty budget in table 3.5 shows that a large portion of the uncertainty arises from measurement of the removed mass, where the uncertainty in measurement of hole diameter and cantilever thickness are both potentially dominated by non-uniform geometry rather than the resolution of the SEM. Uniformity of the cantilever is dependent on the fabrication process tolerances employed by the manufacturer, while the non-uniform hole diameter is a result of the ion beam creating a rounded edge on the hole and occasionally distorting the hole shape. These effects can be reduced by investing more time in the milling process; however for the results presented here the milling time was kept well below 30 minutes for each cantilever.

In addition to the dimensions of the milled hole, if the density of the removed material is not well known then additional uncertainty will be introduced. Most of the cantilevers presented in this work are fabricated from single crystal silicon, of which the density is known to be 2329 kgm^{-3} with very high accuracy, and so the uncertainty contribution to these types of cantilever is negligible [56].

In order to increase reflectivity, many cantilevers are coated with a metallic film (such as the ^{1}M1 and ^{1}C-type cantilevers). This introduces additional uncertainty as the thickness of the film often carries an uncertainty of 50%. This has a significant effect for films with high density (such as gold and chromium), whereas for films

Variable (x)	Description	Value	Standard Uncertainty	Sensitivity $\left(\frac{\delta k}{\delta x}\right)$	Variance Contribution (Nm^{-1})
r	hole diameter	12.78 mm	3%	2.06 $\frac{Nm^{-1}}{\mu m}$	0.3958 (59%)
t_{si}	cantilever thickness	1.71 mm	50 nm	3.86 $\frac{Nm^{-1}}{\mu m}$	0.1929 (29%)
L	cantilever length	92.3 mm	5%	0.0300 $\frac{Nm^{-1}}{\mu m}$	0.1385 (21%)
ν_0	initial res. frequency	269.04 kHz	0.050 kHz	0.328 $\frac{Nm^{-1}}{Hz}$	0.01641 (2.4%)
ν_1	final res. frequency	291.72 kHz	0.050 kHz	-0.257 $\frac{Nm^{-1}}{Hz}$	-0.01287 (1.9%)
δL	hole offset	11.33 mm	2%	-0.244 $\frac{Nm^{-1}}{\mu m}$	-0.05539 (8.2%)
				Spring constant	Uncertainty (Nm^{-1})
				6.400 Nm^{-1}	0.4514 (7.1%)

Table 3.5: Uncertainty budget for cantilever ^{1}R3

with density similar to silicon (such as aluminium), the additional uncertainty is significantly reduced. The thickness of metal films for coated cantilevers was included in the spring constant calculations, and the uncertainty in film thickness was also included in the uncertainty analysis. This is evident for cantilever ^{1}C1 shown in table 3.3, where the uncertainty is approximately 4% higher than that of the uncoated cantilevers ^{1}F1 and ^{1}F2.

Cantilevers composed of silicon nitride pose a problem for any method which requires the mass of the cantilever, as the density and modulus of silicon nitride can vary substantially [13, 57]. Sader et al. have reported several methods by which the density of silicon nitride can be determined, however these are quite cumbersome and will introduce additional uncertainty [13]. Application of the FIB method to cantilevers composed of silicon nitride, thus introduces substantial uncertainty, and so the method is suited to cantilevers composed of materials with well-known density such as silicon.

Another potential source of uncertainty is debris on the cantilever, resulting in overestimation of the spring constant. Gates et al. noted this potential source of error for resonance methods, and attributed it to small pieces of the chip attaching to the cantilever [38]. Of course any source of small debris could potentially contaminate the cantilever, including fragments of the milled section as shown in figure 3.12. Cantilevers were thoroughly cleaned using ethanol and dry nitrogen, and stored in clean, dust-free containers to prevent particle attachment. Inspection using an optical microscope or SEM is recommended to ensure that cantilevers are free of particles.

The uncertainty reported in table 3.5 accounts only for propagated uncertainty resulting from measurements, and does not account for systematic sources of uncertainty and assumptions in the method. The purpose of the validation performed is to support the assumptions made in applying the FIB method, and justify the claim of low uncertainty in the range of 7-10%.

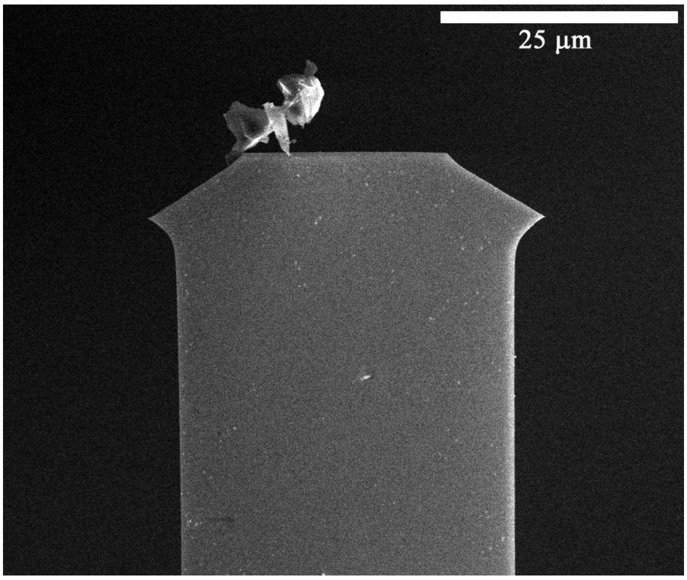

Figure 3.12: SEM image showing debris attached to an AFM cantilever. Reprinted with permission from [22].

With all measurements made as carefully as possible and the FIB milling process implemented slowly so as to produce highly-circular and uniform holes, an uncertainty in dimensional measurement (excluding cantilever thickness) of 1% should be achievable. This being the case, the FIB method may be capable of achieving uncertainty below 5%. The technique could also be further improved and extended to softer cantilevers, if cantilevers were supplied with a well-defined silicon section at the very end of the lever, extending past the imaging tip. The only requirement would be that this extra section of cantilever would have to possess sufficient mass to produce a significant shift (greater than 2 kHz) in resonant frequency once milled.

3.1.4 Summary

Accurate knowledge of micro-cantilever spring constants is critical, not only to AFM force measurements, but for many other applications such as high performance sensor devices. Here, a method has been presented for calibrating the spring constant of AFM cantilevers with uncertainty of 7-10% and with possible reduction to less than 5%.

The FIB method is best applied to tapping mode silicon probes but can be applied to silicon nitride contact mode levers at the cost of additional uncertainty. Milling cantilevers using a FIB allows careful control over the amount and location of cantilever material removed, allowing accurate application of the technique.

FIB-milled cantilevers were shown to function after milling, producing high quality images of a CNT covered silicon surface. In the process of testing and validating the FIB method, important practical insights were offered on correctly measuring cantilever dimensions and implementing other previously developed methods which will allow more accurate application of these techniques. The effects of FIB milling at different locations on the cantilever was also investigated, and the removal of mass was found to affect the static to dynamic spring constant ratio and the effective mass of the cantilever.

3.2 Modified reference cantilever method

Static methods to determine the spring constant of AFM cantilevers have been widely used in the scientific community since the importance of such calibration techniques was established nearly 20 years ago. Commonly used static techniques involve loading a test cantilever with a known force by pressing it against a pre-calibrated standard or reference cantilever.

Reference cantilever methods have several sources of uncertainty, including the measured spring constant of the reference cantilever, the exact position of the loading point on the reference cantilever and how closely the spring constant of the test and reference cantilever match. A detailed introduction to the application of the reference cantilever method is provided in section 1.2.3.

3.2.1 Introduction

In this work, spatial markers are milled into reference cantilevers using a FIB, in order to reduce uncertainty in the reference cantilever method. Additionally, accurate calibration of AFM cantilevers is achieved without the tip of the test (unknown) cantilever contacting a surface, by combining the FIB spatial markers with an inverted reference cantilever method.

This work also demonstrates that for V-shaped cantilevers, it is possible to determine the precise loading position by AFM imaging the intersection of the two arms. Removing tip-to-surface contact in both the reference cantilever method and sensitivity calibration is a significant improvement, since this is an important consideration for AFM users who require the imaging tip to remain in pristine condition before commencing measurements. Uncertainties of between 5-10 % are routinely achievable with these methods.

Modified reference cantilever method A FIB was used to mill small holes in commercially available beam-shaped silicon reference cantilevers, these holes are used as positional markers and can be AFM imaged by the test cantilever. A schematic of the experimental set up is shown in figure 3.13a, figure 3.13b is an optical image from the AFM showing a V-shaped test cantilever positioned over the FIB milled reference cantilever and figure 3.13c is an SEM image of the same reference cantilever. The spatial markers produced by FIB milling are easily observed using the optics integrated into most commercial AFMs, and the distances of these holes from the end of the reference cantilever can be measured precisely with an SEM.

The spring constant at each spatial marker can then be determined using equation 3.2, and the unique value at each marker means that a single reference cantilever can provide a range of spring constants, instead of using multiple reference cantilevers. A test cantilever can then be calibrated using a multiple point technique similar to those developed by Clifford et al. and Gates et al. [2, 9].

The technique reported herein is similar to the method employed by Gates et al., but has the advantage of requiring only a single reference cantilever instead of several, which each require individual calibration. The technique developed by Gates et al. also has the disadvantage of not knowing the precise contact point of the test probe on the reference cantilever. This is eliminated in the current method by imaging the spatial markers.

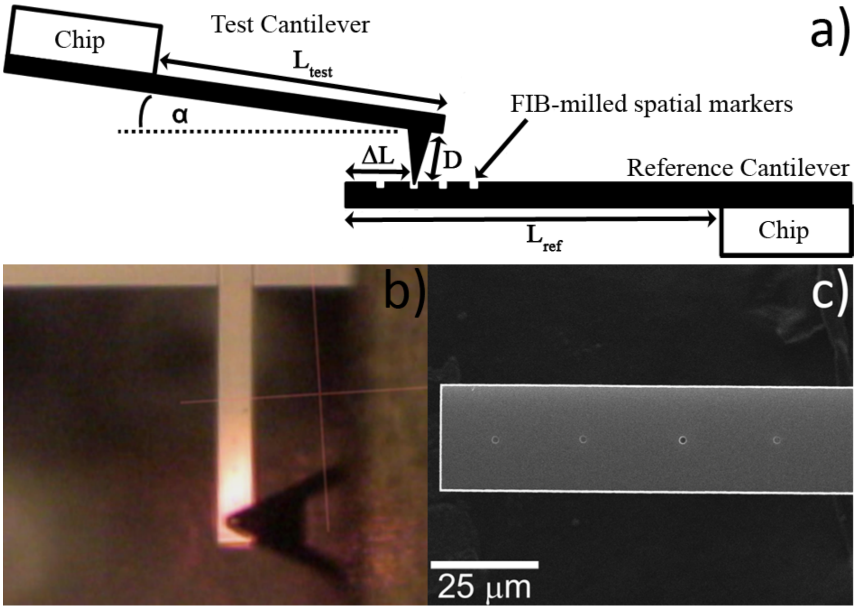

Figure 3.13: Schematic of the reference cantilever method using FIB-milled positional markers, b) an optical view of the measurement being performed and an SEM image of the FIB-milled cantilever is shown in c). Reprinted with permission from [26].

A single point calibration can also be employed with close matching of the spring constant between the test cantilever and the appropriate spatial marker on the reference cantilever, by using the nominal spring constant value as a guide for the test cantilever. This method can be applied to any type of reference cantilever, and the calibration is performed using the reference lever equation from section 1.2.3, which is provided here again for convenience.

$$k_{test} = k_{ref}\left(\frac{S_C}{S_H} - 1\right)\cos^2\alpha\left(1 - \tan(\alpha)\frac{3D}{2L_{test}}\right)\left(\frac{L_{ref} - \Delta L}{L_{ref}}\right)^3 \tag{3.12}$$

It should be noted that the torque correction factor term is included where necessary, although only probes such as the Mikromasch NSC15 with a very large tip show significant variation due to torque effects [58, 59].

Modified inverted reference cantilever method A disadvantage of static methods is that the tip of the AFM probe must be pressed against a hard surface to calibrate the deflection sensitivity. It is obviously beneficial for the tip to be in pristine condition before actual measurements take place. A number of groups have demonstrated that tip damage can easily occur through imaging and/or force spectroscopy [60–63].

Figure 3.14 shows a Bruker FMV silicon cantilever which has undergone significant wear at the tip apex due to contact mode imaging and acquisition of static force curves. Probes such as the Bruker FMV with relatively high spring constant (k = 2.8 Nm^{-1}) and small tip radius (10 nm) are not ideally suited for static measurements since the pressure on the tip during static force measurements can be very high, potentially damaging the tip. Calibration techniques that require static force curves such as thermal noise methods and standard reference cantilever methods can therefore be problematic for these types of probes if maintaining tip quality is essential.

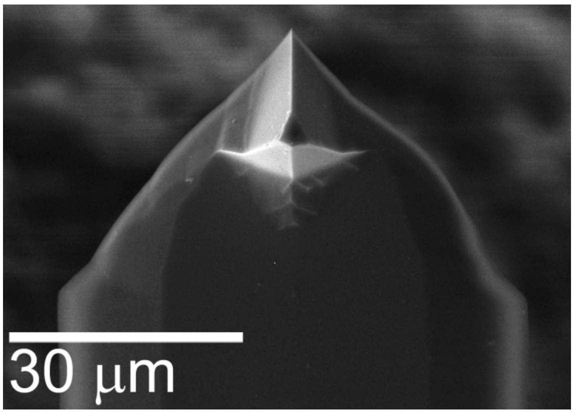

Figure 3.14: SEM image of a worn tip apex on a Bruker FMV silicon probe. Reprinted with permission from [26].

In an effort to eliminate potential tip damage, the reference cantilever technique was modified further. The new methodology inverts the reference cantilever method and uses a precisely-calibrated reference cantilever with an imaging tip in place of the tip-less variant used for the standard approach. The test cantilever is now the lower cantilever and the reference cantilever the upper one. For this technique, equation 3.12 can be expressed as:

$$k_{test} = k_{ref} \left[\left(\frac{S_C}{S_H} - 1 \right) \cos^2\alpha \left(1 - \tan(\alpha) \frac{3D_{ref}}{2L_{ref}} \right) \right]^{-1} \left(\frac{L_{test} - \Delta L}{L_{test}} \right)^3 \qquad (3.13)$$

L_{test} is now the length of the test cantilever and ΔL is the distance from the loading point of the reference cantilever-tip to the test cantilever-tip. D_{ref} is the height of the reference cantilever tip and L_{ref} is the length of the reference cantilever.The FIB was used once again to produce positional markers, but this time on the test cantilever, and ΔL was determined using AFM imaging.

Figure 3.15a shows a schematic of the experimental set-up, while figure 3.15b is an optical image from the AFM of such a calibration measurement and figure 3.15c is an SEM image of the test cantilever (the lower cantilever) with the first spatial marker visible.

Similar to the standard reference cantilever method, a multiple or single point calibration may be used to determine the spring constant of the test cantilever. From figure 3.15c it is evident that the imaging tip is either contaminated and/or blunted. This occurred since the probe had also been calibrated using the standard reference cantilever method and the thermal noise technique. Both of these methods require static force curves and imaging which require the tip to contact a hard surface.

This further demonstrates the type of damage that can occur to AFM probes, which is eliminated by using the inverted reference cantilever technique. Inverting the reference cantilever technique has other applications, for example, it can be used to determine the stiffness of structures such as polymer actuators and wool fibres [33, 35].

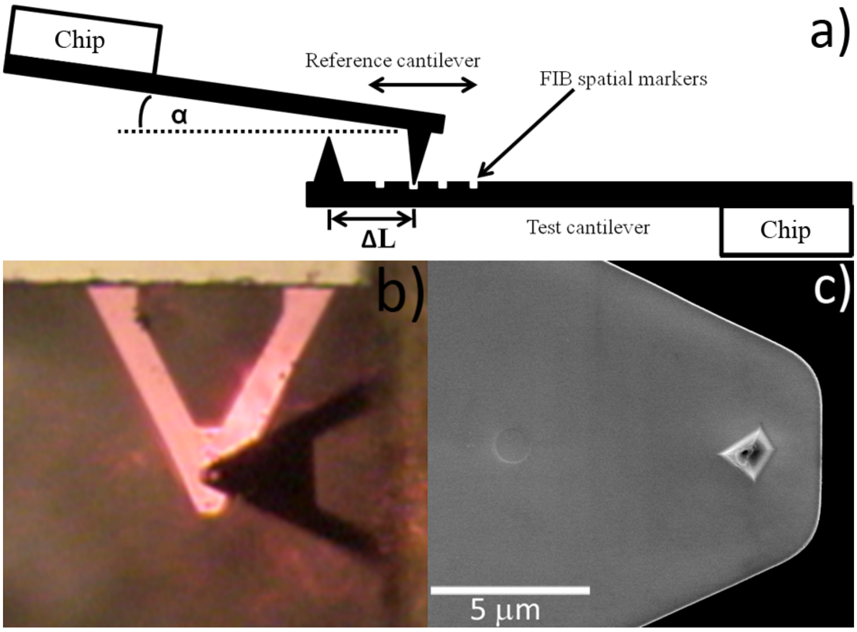

Figure 3.15: a) Schematic of the inverted reference cantilever method using FIB-milled positional markers and b) an optical view of the measurement being performed. An SEM image of a FIB-milled test cantilever for inverted reference lever measurements is shown in c). Reprinted with permission from [26].

3.2.1.1 Cantilever details and established calibration methods

The modified reference cantilever method was applied to a wide range of cantilevers. These cantilevers are listed in table 3.6, along with their model, geometry and composition and nominal spring constant.

A number of established calibration techniques were employed to provide comparative values for the modified reference cantilever method, which provides perspective as to the accuracy and applicability of this method. An overview of the methods applied to the various cantilevers is provided in table 3.7.

It is evident from table 3.7 that not all calibration methods were applied to all cantilevers and there are several reasons for this. Metal coatings such as chromium and gold can significantly increase the average density of an AFM cantilever and manufacturers do not typically provide the precise thickness of the coatings. Therefore, any technique that relies on accurate knowledge of the cantilever density often cannot be accurately applied to cantilevers with chromium and/or gold coatings (e.g. ^{2}V1-V7, ^{2}R4). The variable material properties of silicon nitride cantilevers also pose problems to some techniques, and so methods which rely on the material properties of the cantilever weren't applied to silicon nitride cantilevers such as ^{2}V1-7.

Several techniques assume that the cantilever possess an ideal beam shape. Cantilevers such as ^{2}M1-2 and ^{2}F1-2 may not have uniform thickness, and tip may comprise a significant proportion of the cantilevers' mass. This complicates calibration using these methods [42].

The thermal noise method can be applied to nearly all types of cantilevers except the tip-less type (^{2}R1-4). The large contact area between the cantilever and the surface prevented measurement of the deflection sensitivity. Application of the thermal noise method to these types of cantilevers was, unfortunately not possible.

Cantilever name	Geometry	Composition	Coating	Model & manufacturer	Nominal spring constant (Nm^{-1})
$^{2}\mathrm{V1}_{\mathrm{t}}$	V	Silicon Nitride	Ti/Au	SNL Bruker	0.06
$^{2}\mathrm{V2}_{\mathrm{r,t}}$					0.12
$^{2}\mathrm{V3}_{\mathrm{r,t}}$					0.12
$^{2}\mathrm{V4}_{\mathrm{t}}$					0.12
$^{2}\mathrm{V5}_{\mathrm{r,t}}$					0.35
$^{2}\mathrm{V6}_{\mathrm{r,t}}$				OTR8 Bruker	0.57
$^{2}\mathrm{V7}_{\mathrm{r,t}}$					0.57
$^{2}\mathrm{F1}_{\mathrm{r,t}}$	Beam	Silicon	None	FMV Bruker	2.8
$^{2}\mathrm{F2}_{\mathrm{t}}$					2.8
$^{2}\mathrm{R1}_{\mathrm{r}}$				CLFC Bruker	0.16
$^{2}\mathrm{R2}_{\mathrm{r}}$					1.3
$^{2}\mathrm{R3}_{\mathrm{r}}$					10.4
$^{2}\mathrm{R4}_{\mathrm{r}}$			Cr/Au	CSC12 Mikromasch	0.95
$^{2}\mathrm{M1}_{\mathrm{t}}$			Al	NSC15 Mikromasch	50
$^{2}\mathrm{M2}_{\mathrm{t}}$					50

$^{\mathrm{r}}$ Used as a reference cantilever.
$^{\mathrm{t}}$ Used as a test cantilever.

Table 3.6: Details of all cantilevers involved in this study including their manufacturer, geometry, composition, coating composition and nominal spring constant quoted by the manufacturer.

Cantilever	Sader hydrodynamic	Euler beam	Sader resonance	Cleveland dimensional	Thermal noise
^{2}V1	-	-	-	-	√
^{2}V2	-	-	-	-	√
^{2}V3	-	-	-	-	√
^{2}V4	-	-	-	-	√
^{2}V5	-	-	-	-	√
^{2}V6	-	-	-	-	√
^{2}V7	-	-	-	-	√
^{2}F1	√	-	-	√	√
^{2}F2	√	-	-	√	√
^{2}M1	√	-	-	-	√
^{2}M2	√	-	-	-	√
^{2}R1	√	√	√	√	-
^{2}R2	√	√	√	√	-
^{2}R3	√	√	√	√	-
^{2}R4	√	-	-	-	-

Table 3.7: Details of which established calibration methods were applied to each cantilever.

The reference cantilever method is widely applicable. With an accurately calibrated reference and appropriate procedure, these techniques allow users to routinely calibrate cantilevers with uncertainty below 10% and can be applied to nearly all cantilever geometries.

One of the major drawbacks of reference cantilever methods in comparison to many dynamic techniques, is that tip sample contact is required which potentially damages the tip. With the development of the inverted reference cantilever technique, static methods can be applied to calibrating cantilever spring constants without the need to contact the imaging tip to the sample surface. It is also important to note from table 3.7 that of all the cantilever types studied in this work, V-shaped, gold coated, silicon nitride cantilevers are generally the most difficult to calibrate with low uncertainty.

3.2.2 Results and discussion

The reference cantilever techniques developed in this work were applied to 6 types of AFM cantilevers with different properties and geometries; SEM images of these cantilever geometries can be found in figure 3.1 at the beginning of the chapter.

3.2.2.1 Calibration of reference cantilevers

Spatial markers were milled along the length of cantilevers ^{2}R1-4.Three markers were milled into cantilever ^{2}R4, while four markers were milled into cantilevers ^{2}R1-3. Figure 3.13c shows an example of a reference cantilever (^{2}R2) with small spatial markers milled along its length.

It was assumed that these markers produce no significant change in the cantilever spring constant.The Q factor and resonant frequency for each test cantilever was also measured before and after FIB milling with negligible change for either parameter(less than ±1% for Q factors and ±0.5% for resonant frequencies), indicating that these positional markers do not change the mechanical properties of the test cantilevers.

It was demonstrated in the previous chapter, that a substantial amount of mass positioned between the middle and the end, must be removed from an AFM cantilever to alter the mechanical properties. The spring constant for cantilevers ^{2}R1-4 were measured using various established techniques and the values obtained are shown in table 3.8 with the associated uncertainty.

Percentage uncertainties and their ranges are quoted for each method in table 3.8 and are estimated from the propagation of measurement uncertainty for the parameters in each technique (e.g. cantilever dimensions, resonant frequency and density of single crystal silicon for the Sader resonance method), as well as from review articles and detailed technique comparisons reported in the literature [17, 37–40].

The lower limit for the uncertainty for each method tends to be for tip-less cantilevers with ideal beam shapes, uniform dimensions and uniform cantilever composition; while the upper limit tends to be for more complex geometries [13, 37, 38, 40, 58, 64].

Given the good agreement between different techniques, the uncertainty on each method and the statistical spread in the average spring constants, the uncertainty on the average spring constant for cantilevers ^{2}R1-R3 is estimated to be 3-5%. For cantilever ^{2}R4, the Sader hydrodynamic method was the only approach deemed applicable. Given the error in individual parameters (e.g. cantilever width, Reynolds

Cantilever	Spring Constant (Nm^{-1}) Sader hydrodynamic (±5-7%)	Euler beam (±10%)	Sader resonance (±3-5%)	Cleveland dimensional (±3-5%)	Average
^{2}R1	0.091	0.094	0.093	0.093	0.093 ±0.005
^{2}R2	0.79	0.82	0.81	0.8	0.805 ±0.040
^{2}R3	7.43	7.44	7.41	7.51	7.45 ±0.373
^{2}R4	0.5	-	-	-	0.500 ±0.035

Table 3.8: Spring constant of cantilevers ^{2}R1-4 determined using various calibration methods.

number and Q factor), the uncertainty for this cantilever is estimated to increase by 2%. The spring constant was then calculated at each spatial marker for the cantilevers ^{2}R1-4 using the off-end loading correction, and these results are shown in table 3.9.

Reference cantilever	Spring constant along cantilever length (Nm^{-1}) Cantilever end	Marker 1	Marker 2	Marker 3	Marker 4	Cantilevers calibrated
^{2}R1	0.093 ± 0.005	0.107	0.126	0.162	0.187	^{2}V1-V5
^{2}R2	0.804 ± 0.040	0.969	1.38	2.21	3.71	^{2}V5-6, ^{2}F1-2
^{2}R3	7.45 ± 0.373	10.47	14.77	21.09	30.2	^{2}M1-2
^{2}R4	0.500 ± 0.035	1.43	2.42	4.07	-	^{2}V7

Table 3.9: Spring constant of ^{2}R1-4 calculated along the cantilevers' length at each spatial maker position.

3.2.2.2 Standard calibration

The reference cantilevers ^{2}R1-4 were subsequently used to calibrate a number of test cantilevers using single and multiple point methods, with the results shown in table 3.10. Calibration performed with single or multiple point measurements are denoted with subscripts *s* or *m* respectively. For single point calibration, the reference cantilever and marker that were AFM imaged to determine the location of the loading force are also provided.

Single point calibration was performed by applying equation 3.12. For multiple point calibration, a minimum of four measurements were used and the method of

Gates et al. was applied [9]. The following expressions are plotted against each other, which results in a linear relationship.

$$k_{ref}\left(\frac{L_{ref}}{L_{ref}-\Delta L}\right)^3 \tag{3.14}$$

$$\left[\left(\frac{S_C}{S_H}-1\right)\cos^2\alpha\left(1-\tan\alpha\frac{3D}{2L_{test}}\right)\right]^{-1} \tag{3.15}$$

The spring constant of the test cantilever is equal to the value of equation 3.14 when equation 3.15 is equal to 1. This analysis is shown in figure 3.16 for cantilever ^{2}F1 calibrated against reference cantilever ^{2}R2.

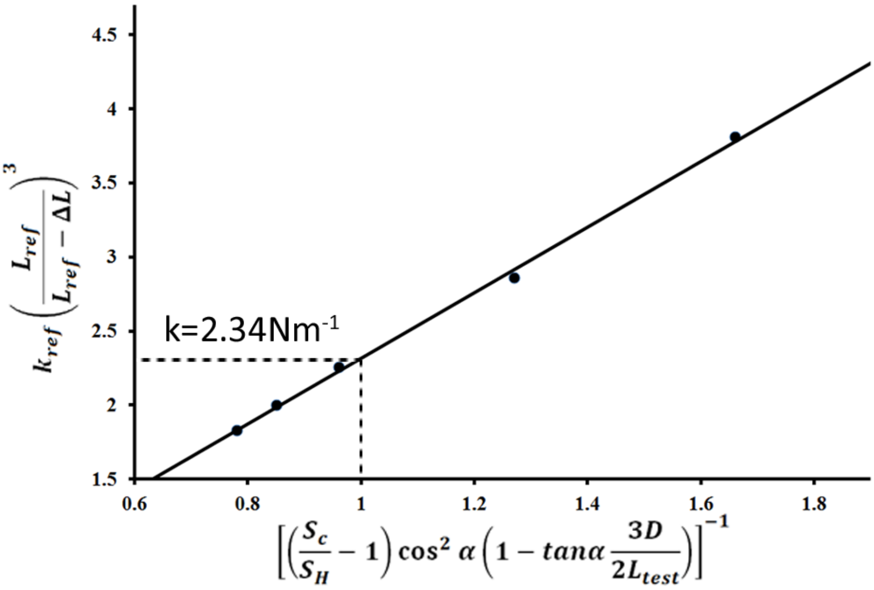

Figure 3.16: The standard, multiple-point reference lever method applied to cantilever ^{2}F1. Reprinted with permission from [26].

The results in table 3.10 show good agreement between all methods, demonstrating that with careful application of the appropriate calibration techniques, AFM cantilever spring constants can be accurately determined. Notably, these methods also cover distinctly different areas of physics including beam, statistical and fluid mechanics. The standard reference cantilever method using spatial markers appears to obtain good agreement with all of the established methods. Uncertainty for the reference cantilever method is between 6-10%. A detailed uncertainty budget for single point calibration is provided in section 3.2.2.4.

Cantilever	Spring constant (Nm^{-1})			
	Standard reference lever (spatial markers)	Thermal noise (10-20%)	Sader hydrodynamic (10-15%)	Cleveland (10-15%)
^{2}V1	$0.088_m \pm 0.005$	0.086 ± 0.013	-	-
^{2}V2	$0.114_m \pm 0.006$	0.109 ± 0.016	-	-
^{2}V3	$0.167_s \pm 0.012$ ^{2}R1[3], 0.157 ± 0.012 ^{2}R1[4]	0.150 ± 0.023, 0.155 ± 0.023	-	-
^{2}V4	$0.176_s \pm 0.011$ ^{2}R1[4]		-	-
^{2}V5	$0.298_s \pm 0.019$ ^{2}R1[4], $0.312_s \pm 0.024$ ^{2}R2[1]	0.292 ± 0.044	-	-
^{2}V6	$0.625_s \pm 0.039$ ^{2}R2[1], 0.633 ± 0.043 ^{2}R2[2]	0.600 ± 0.090	-	-
^{2}V7	$0.680_m \pm 0.052$ ^{2}R4	0.635 ± 0.010	-	-
^{2}F1	$2.34_m \pm 0.13$ ^{2}R2	2.33 ± 0.23	2.48 ± 0.31	2.30 ± 0.29
^{2}F2	2.42 ± 0.14 ^{2}R2[3]	2.38 ± 0.24	2.53 ± 0.32	2.33 ± 0.29
^{2}M1	$37.4_s \pm 2.3$ ^{2}R3[4]	37.5 ± 4.7	37.5 ± 4.7	-
^{2}M2	$40.7_s \pm 2.5$ ^{2}R3[4]	44.6 ± 6.7	42 ± 6.3	-

$_s$ denotes a spring constant determined using a single point calibration.
$_m$ denotes a spring constant determined using a multiple point calibration.
The cantilever and marker used for calibration is defined as “cantilever[marker number]”.

Table 3.10: Spring constants of several cantilevers determined using the reference cantilever method with spatial markers, compared with other established calibration methods.

Cantilevers ^{2}V3 and ^{2}V6 were calibrated twice using the single point method at different marker positions on the same reference cantilever while cantilever ^{2}V5 was calibrated on two different reference cantilevers. These results are in agreement with each other and the uncertainty for the measurements overlaps. The results in table 3.10 also demonstrate that by using spatial markers, single point calibrations can provide uncertainty comparable to the multiple point technique developed by Gates et al. [9].

It is interesting to note that the thermal noise method is consistently lower (1.2-11.9%) for V-shaped cantilevers when compared to the reference cantilever results. This may be due to variation of the Chi factor as a result of the geometry of the V-shaped cantilevers, and possibly the laser spot position. A combination of these factors could account for the consistent discrepancy between thermal noise measurements and the reference cantilever results. Despite these potential errors, the thermal noise method is still an excellent technique especially when considering a combination of ease of use and applicability. However, at this time the uncertainty is estimated to be ~10% for practical beam shaped cantilevers and 10-20 % for V-shaped cantilevers. Recent work by Sader et al. has yielded greater understanding of the relationship between the Chi factor and cantilever geometry [65]. Using the correct Chi factor for the particular cantilever geometry would allow the uncertainty for these cantilevers to be reduced.

3.2.2.3 Inverted calibration

The reference cantilevers used with the inverted technique were commercial cantilevers which first require accurate calibration. For cantilevers ^{2}V4-7 and ^{2}F2 the spring constant value k_{ref}, used to further calibrate other practical cantilevers, was the value determined using the reference cantilever method shown in table 3.10.

Table 3.11 shows data for five cantilevers with FIB spatial markers milled into them. This table gives the $\Delta L/L$ fraction for each marker and the reference cantilever that calibrated them using the inverted reference method. Cantilever ^{2}V1 was not milled, the loading point was instead precisely determined by AFM imaging the internal apex of the V intersection.

Cantilever	$\Delta L/L$ Marker 1	$\Delta L/L$ Marker 2	$\Delta L/L$ Marker 3	Reference Cantilever
$^2\mathrm{V1_s}$	-	-	-	^{2}V4,V7
$^2\mathrm{V2_m}$	0.19	0.27	0.35	^{2}V7
$^2\mathrm{V3_m}$	0.08	0.11	-	^{2}V5
$^2\mathrm{V5_s}$	0.12	0.23	0.32	^{2}V6
$^2\mathrm{F2_m}$	0.1	0.15	0.2	^{2}F1

Table 3.11: $\Delta L/L$ for each spatial maker position for cantilevers ^{2}V1-3, ^{2}V5 and ^{2}F2.

Figure 3.17 demonstrates that it is possible to accurately determine the position of force loading on V-shaped cantilevers without the need to use FIB milling. The advantage of using spatial markers is they allow multiple point measurements to be applied with greater ease. Spatial markers can provide a simple method of aligning force measurements directly along the center of the cantilever axis and reduce the possibility of applying load off-axis.

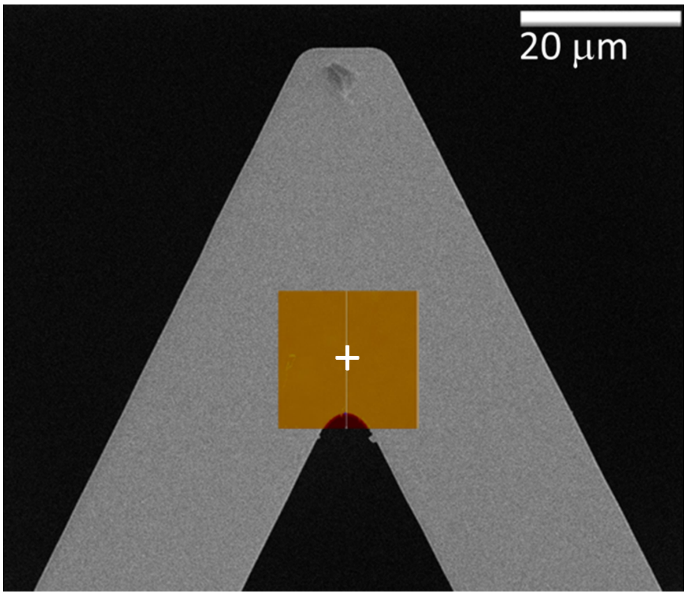

Figure 3.17: An SEM image of the V-intersection of cantilever ^{2}V1, with an overlaid AFM image obtained using cantilever ^{2}V5. The location of the force measurements is denoted by the white +. Reprinted with permission from [26].

Cantilevers ^{2}F2, ^{2}V2 and ^{2}V3 were calibrated using the inverted, multiple point method. In this case, the following expressions are plotted against each other in the same manner as the "standard" multiple point method.

$$k_{ref}\left(\frac{L_{test}}{L_{test}-\Delta L}\right)^{-3} \tag{3.16}$$

$$\left[\frac{S_C}{S_H-1}\cos^2\alpha\left(1-\tan\alpha\frac{3D_{ref}}{2L_{ref}}\right)\right] \tag{3.17}$$

Again, the spring constant is determined by taking the value of equation 3.16 when equation 3.17 is equal to 1. For the V-shaped cantilevers ^{2}V2-3, some loading positions were determined by AFM imaging FIB milled spatial markers and others by imaging the internal apex of the V intersection. The inverted, multiple-point data for these three cantilevers is provided in figure 3.18. The linear fits to the data are excellent, with high correlation coefficients, which suggest that method is effective when inverted.

Table 3.12 shows the results for a number of cantilevers calibrated using the inverted reference cantilever method. These results are again compared to other established techniques and also the corresponding standard reference cantilever method data from table 3.10. The measured spring constants for each cantilever compare well with the values obtained by other methods. Within the data set presented, good agreement is once again observed between the established techniques and the FIB-milled spatial marker technique.

For cantilever ^{2}V2-3, the off-end loading approximation was used where several of the loading points had $\Delta L/L > 0.20$. Figure 3.18a and b shows this data for

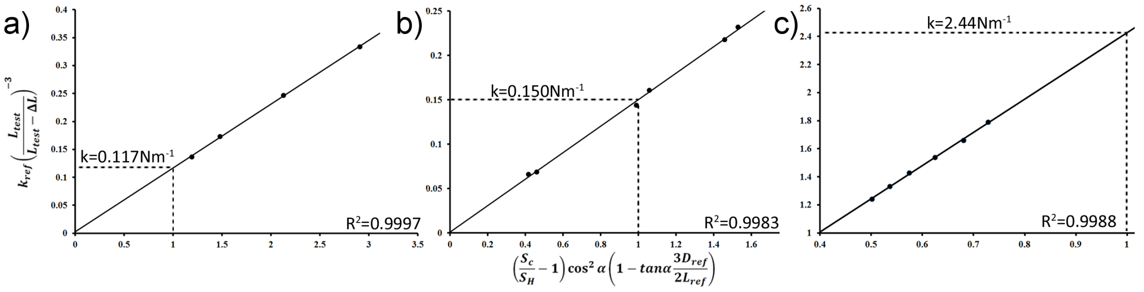

Figure 3.18: Multiple-point inverted reference cantilever results for cantilevers ^{2}V2, ^{2}V3 and ^{2}F2 respectively. Reprinted with permission from [26].

cantilevers ^{2}V2-3. There is a strong linear correlation for all of the data (R^2 above 0.998), which demonstrates that the off-end loading equation holds well for certain types of V-shaped cantilevers despite some loading locations being greater than $\Delta L/L = 0.20$. These results also indicate that for single point calibrations, the off-end loading equation is effective for $\Delta L/L < 0.20$ which supports previous work [2, 13, 15, 23, 66].

However, for completeness, the same ΔL offset correction derived by Vakarelski et al. was applied to cantilever ^{2}V4 [66] and the results show closer agreement between the standard and inverted reference cantilever methods. While this work shows that the off-end loading approximation can be applied to V-shaped cantilevers (especially for certain geometries such as ^{2}V2-3); for single point measurements the ΔL relationships derived by Vakarelski et al or Clifford et al. can be employed, potentially yielding more accurate results [15, 66].

Cantilever	Spring constant (Nm^{-1})				
	Inverted reference lever	Thermal noise (±10-20%)	Standard reference lever$^{\mathrm{d}}$	Sader hydrodynamic (±10-15%)	Cleveland formula (±10-15%)
^{2}V1 (^{2}V4 reference)	$0.084^a_s \pm 0.006$ ($\Delta L/L = 0.19$) $0.088^b \pm 0.006$	0.086 ± 0.013	0.088 ± 0.006	-	-
^{2}V1 (^{2}V7 reference)	$0.085^a_s \pm 0.008$ ($\Delta L/L = 0.17$) $0.089^b \pm 0.008$	0.086 ± 0.013	0.088 ± 0.006	-	-
^{2}V2	$0.117_m \pm 0.010$	0.109 ± 0.016	0.114 ± 0.006	-	-
^{2}V3	$0.150^m \pm 0.013$	0.150 ± 0.023	0.162 ± 0.012^c	-	-
^{2}V5	$0.281^s \pm 0.020$ ($\Delta L/L = 0.12$)	0.292 ± 0.044	$0.305^c \pm 0.024$	-	-
^{2}F2	$2.44_m \pm 0.15$	2.38 ± 0.24	2.42 ± 0.14	2.53 ± 0.32	2.33 ± 0.29

[a] denotes spring constant values corrected using the $\left(\frac{L}{L-\Delta L}\right)^3$ approximation.

[b] denotes spring constant values corrected using the expression derived by Vakarelski et al.

[c] these spring constants are an average of the two single point calibrations reported in table 3.10.

[d] this data is obtained from table 3.10.

Single and multi-point measurements are denoted by s and m respectively.

Table 3.12: Comparison of spring constants determined using the inverted reference cantilever method with other established methods.

3.2.2.4 Uncertainty and analysis

Single point calibration For a single point calibration, equations 3.12 or 3.13 were used, depending on whether the standard or inverted reference method was implemented. Uncertainty for the single point calibration depends primarily on how well the test and reference cantilever spring constants are matched, as well as uncertainty in the slope of the force curves S_H and S_C. For the data presented in this work the uncertainty on the sensitivity is typically 1%; hence for a single point calibration using the current methodology, the total uncertainty can be as low as 1-3%, excluding the error on the reference cantilever. A detailed uncertainty budget for cantilever ^{2}F2 calibrated using the single point method is provided in table 3.13.

Variable (x)	Description	Value	Standard Uncertainty	Sensitivity $\left(\frac{\delta k}{\delta x}\right)$	Variance Contribution (Nm^{-1})
k_{ref}	spring constant (ref. cantilever)	0.804 Nm^{-1}	0.04 Nm^{-1}	3.010	0.1204 (54%)
S_{C}	sensitivity (ref. cantilever)	109 nmV^{-1}	1%	0.04224	0.04604 (21%)
S_{H}	sensitivity (hard surface)	51.8 nmV^{-1}	1%	-0.08897	-0.04609 (21%)
D	tip height	12.5 μm	2.5 μm	-3097	-0.007743 (3.5%)
L_{test}	test cantilever length	191 μm	0.5%	-1589	-0.001517 (0.68%)
ΔL	loading position	56.3 μm	0.5%	5391	0.001518 (0.68%)
L$_{\text{ref}}$	ref. cantilever tip offset	210 μm	0.5%	184.4	0.0001940 (0.087%)
				Spring constant	Uncertainty
				2.420 Nm^{-1}	0.1388 Nm^{-1} (5.74%)

The uncertainty due to α was considered negligible, and as such has been omitted from the uncertainty budget.

Table 3.13: Uncertainty budget for the standard reference cantilever method applied to cantilever ^{2}F2.

Multiple point calibration The method used here is based on the same approach of Gates et al., who estimated an uncertainty of only 2%, excluding the error on the reference cantilever. Clifford et al. determined that the uncertainty on the multiple point technique could be as low 0.6% [2, 9]. Given the significant reduction in the uncertainty of the loading position on the reference cantilever, 0.6% is likely to be a reasonable uncertainty estimate for this technique.

3.2.3 Summary

The reference cantilever method was implemented with high accuracy by FIB milling positional markers into reference cantilevers. AFM imaging of these markers allowed precise positioning and accurate multi or single-point spring constant calibration through a static dual-lever interaction. Furthermore, the reference cantilever method was inverted, which allowed the spring constant to be accurately determined while eliminating tip-surface contact.

FIB may be used to produce spatial markers on both beam-shaped and V-shaped cantilevers; however accurate positioning was demonstrated by imaging the arm intersection on V-shaped cantilevers. The application of FIB for creating markers allows excellent control over position and size, however it is important to note that other techniques may be used to produce similar markers. These markers do not necessarily need to be shallow holes but could instead be small protrusions. Several research groups have demonstrated methods of producing small deposits on silicon surfaces through e-beam deposition techniques [67–69]. Access to FIB microscopy may not be readily available for all research groups throughout the scientific community, however these other methods will be just as suitable.

Ideally, manufacturers could supply reference cantilevers with intrinsic spatial markers. Practical beam and V-shaped cantilevers could also be supplied with spatial markers, allowing simple application of the inverted reference cantilever method developed in this work. Although it may not be entirely necessary for V-shaped cantilevers. These techniques will be of practical use to all users of micro-mechanical cantilevers, including force spectroscopy and sensor research.

3.3 Non-destructive sensitivity measurement

The calibration of AFM cantilever spring constants has received considerable attention over the past 20 years. Techniques which avoid tip-sample contact are considered advantageous, since the imaging tip is not at risk of being damaged. Far less attention has been directed toward measuring the cantilever deflection or sensitivity, despite the fact that the primary means of determining this factor relies on the AFM tip being pressed against a hard surface (silicon or sapphire), which has the potential to significantly damage the tip. Measurement of deflection sensitivity is essential before force measurement, and so removing the possibility of tip damage from this procedure is desirable.

In this work, the deflection sensitivity of the cantilever is measured using an underlying AFM probe with a spring constant much larger than the test cantilever, essentially a rigid cantilever. In a similar approach to that of the previous section, the exact position of loading on the test cantilever can be determined by reverse AFM imaging small spatial markers which are FIB milled into the test cantilever. For V-shaped cantilevers it is possible to reverse image the arm intersection to determine the exact loading point, without requiring spatial markers. The technique is applied to tip-less, beam-shaped and V-shaped cantilevers and compared to the standard (hard surface contact) technique.

3.3.1 Introduction

To measure deflection sensitivity, the conventional approach is to perform force-distance curves on a surface which is essentially incompressible [70]. This “hard surface contact” method is widely used since it is very simple to implement, but places the imaging tip at risk of being damaged as a number of research groups have demonstrated [60, 61, 71]. This is particularly true for ultra-sharp silicon tips [71], carbon nanotube probes [72] and functionalised tips [73].

Some methods have been developed to avoid tip damage, but tend to suffer from poor accuracy and/or large uncertainties. Another advantage of cantilever sensitivity calibration without tip-surface contact is that the thermal noise method can then be applied to determine the spring constant. This offers another route to complete force calibration of the AFM cantilever without damage to the tip. A brief description of the hard surface contact method and alternative techniques is provided in following section, along with a summary of each methods’ potential errors and uncertainties.

3.3.1.1 Sensitivity calibration methods

Hard surface contact The standard hard surface contact technique was introduced in section 1.2.2 and allows the deflection sensitivity to be measured by pressing the tip against an incompressible surface. This measurement method is primarily used with practical AFM probes, but has also been applied to tip-less cantilevers. This can be problematic however, as the large contact area between the end of the tip-less cantilever and the surface produces significant adhesion. This can prevent force curve acquisition, as observed previously for a number of tip-less cantilevers in section 3.1.

Indirect calibration methods While the standard method for sensitivity calibration can provide high accuracy when applied carefully, the potential for tip damage is unavoidable. This is particularly prevalent for cantilevers with high spring constant and those with extremely delicate tips. In order to avoid tip damage, a number of indirect sensitivity calibration methods have been developed, which are briefly reviewed here.

Inverted tip One method of avoiding tip-sample contact during sensitivity calibration is to use an inverted sharp tip to contact the cantilever rather than the imaging tip contacting the surface, this is shown in figure 1.12 of the introduction. Several research groups have reported this by using the tip of an etched tungsten wire, and an array of silicon spikes. Tourek et al. developed a method that involves deflecting the cantilever with the contact point a known distance from the imaging tip using a sharpened tungsten wire [74]. Beam theory is then used to correct the sensitivity at the tungsten wire contact point, back to the AFM tip position.

Sources of uncertainty in this technique include the position of the contact point on the test cantilever and the slope of the sensitivity measurements. The beam theory equations derived by Tourek et al. also require accurate knowledge of the laser spot position on the test cantilever. In their study, these distances were measured by optical microscopy, which will introduce a significant degree of uncertainty, and the error quoted by Tourek et al. reached as high as 12% in some instances [74]. The estimated diameter of the tungsten wire used in this study was 10 μm, which will result in a large contact area between the wire tip and cantilever depending on the sharpness of the wire tip. This could potentially cause difficulties in acquiring force curves. Tip sample adhesion can cause instability in force measurements and therefore increases the error on cantilever sensitivity measurements, as was noted by Tortonese et al. [75].

A similar method for sensitivity calibration was also performed by Ohler using a calibration sample which consists of a series of sharp silicon spikes [64]. These samples are commonly used to characterize the sharpness of AFM tips using reverse imaging (TGT1, NT-MDT). Accurate knowledge of the exact loading point on the cantilever is hard to determine since the spikes are difficult to resolve with AFM optics. This may not be critical for long cantilevers but can cause significant error for shorter cantilevers (i.e. 100 μm or less). The technique was effective for tip-less cantilevers and avoids the complication of large adhesive forces between the end of the tip-less cantilever and the hard surface, since the diameter of the tip calibration spikes is less than 10 nm. However, given the relatively small height of the spikes (200-500 nm) this type of sample would not be effective for practical cantilevers given that the typical tip height for AFM probes is 5-15 μm.

Thermal noise Higgins et al. developed a method for determining the sensitivity for AFM cantilevers without tip-surface contact, which is based on knowing the spring constant and measuring the cantilevers' thermal noise [76]. In their study, the Sader hydrodynamic method was used to calibrate the spring constant of the test cantilevers and sensitivity measurements were performed for beam-shaped cantilevers only [14].

Higgins et al. demonstrate accuracy within 20% when their sensitivity values were compared to the conventional hard surface contact method. The uncertainty observed is likely attributed to the manner in which the Sader hydrodynamic method was applied, which is discussed in greater detail in the results section. The thermal noise measurements will also introduce uncertainty, however recent work by Sader et al. should allow this contribution to be reduced [77]. Uncertainty in cantilever spring constant calibration is typically between 10-30% depending on the method implemented, although this error will be halved when applying the Higgins method.

This method can be applied by directly inputting measured values into the equation derived by Higgins et al. Gates and Pratt also recently suggested performing a thermal noise calibration, and obtaining the optical lever sensitivity through iteration; by having the calculated spring constant eventually match the previously determined spring constant value [78].

Calibration curves D'Costa and Hoh demonstrated that a change in the photodiode voltage as a function of a certain photodiode displacement correlates linearly to the measured optical lever sensitivity, and may therefore be used as a calibration method [79]. This result was obtained by using the hard surface contact method to measure the cantilever sensitivity with a maximized sum signal. Subsequent measurements of the photodiode voltage change for a fixed displacement of the photodiode were made by moving the laser spot parallel to the base of the cantilever beam. A plot of the photodiode shift versus the sensitivity values then provides a linear calibration curve for a cantilever of given length, where the slope may be used to determine the sensitivity for a different cantilever of the same length if the photodiode shift is known.

Uncertainty for this method will be the same as for the hard surface contact technique. While this method can be performed without the tip touching the sample and is suitable for all cantilever geometries, it relies on having to obtain a calibration curve for each cantilever of a given length and is dependent on the configuration of the AFM instrument. It also depends on the instrument operator to align the laser correctly every time and may be problematic for inexperienced users.

3.3.1.2 Proposed method

A method is presented here, for determining deflection sensitivity using an AFM cantilever with a very high spring constant (effectively rigid), instead of the sharpened tungsten wire used by Tourek et al. [74]. Simple beam theory is then used to correct the sensitivity to the imaging tip location. The point of contact was determined precisely using small spatial markers FIB milled into the test cantilevers. These were reverse AFM imaged by the underlying high spring constant probe tip, allowing accurate positioning of sensitivity measurements. For V-shaped cantilevers it is possible to reverse-image the arm intersection, which allowed the point of contact to be determined precisely without necessarily requiring spatial markers.

The measurement process is shown in figure 3.19 and described in section 2.2.3.1 of the materials and methods chapter. It is also shown that even if the test cantilevers' spring constant is a significant proportion of the rigid, lower cantilever (i.e. 20%); then the test cantilever sensitivity can still be accurately determined by using the reference cantilever technique (which is usually applied to determining cantilever spring constants). The results from these methods are compared to the Higgins technique and the conventional hard surface contact method.

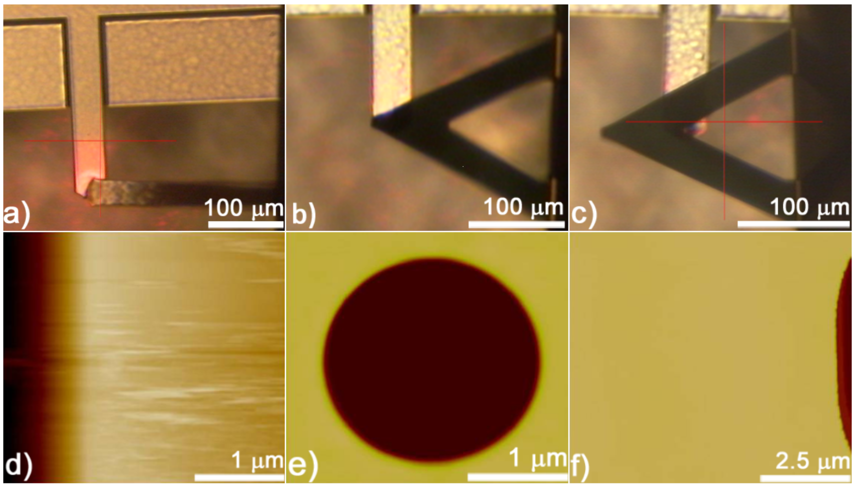

Figure 3.19: Optical images of tipless a) and V-shaped b) cantilevers imaging FIB-milled markers and a V-shaped cantilever imaging the V-intersection c). Corresponding AFM images are shown in d), e) and f). Reprinted with permission from [28].

Figure 3.20 shows a schematic of the experimental set-up for calibration of the deflection sensitivity using an inverted AFM probe. The inverted probe must have a cantilever spring constant significantly greater than the test cantilever for the calibration to be accurate. The upper (test) cantilever is loaded a known distance ΔL from the imaging tip (figure 3.20a), or end of the cantilever in the case of tip-less cantilevers (figure 3.20b).

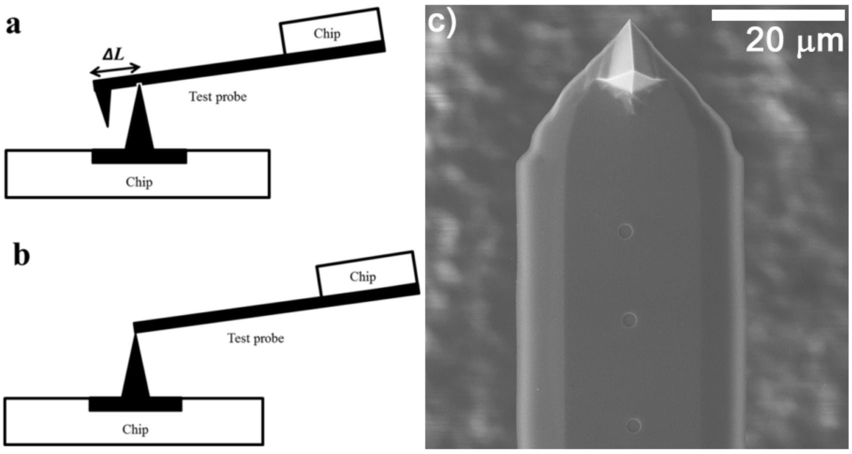

Figure 3.20: Schematic of experimental setup for a) practical test cantilever and b) tipless test cantilever, while c) is an SEM image of cantilever ^{3}F1 with FIB-milled spatial markers. Reprinted with permission from [28].

The distance ΔL can be determined accurately by reverse AFM imaging a marker on the test cantilever surface, and thus the measurement location is defined precisely. As stated in the previous section, other methods are available to produce markers on the cantilever, such as electron-beam deposition [67–69]. The advantage of electron beam techniques is that they can be performed with a standard SEM and therefore are more accessible than a FIB.

Figure 3.20c shows a SEM image of an AFM cantilever with FIB-milled spatial markers. For tip-less cantilevers it is possible to reverse AFM image the very end of the cantilever as shown in figure 3.19, therefore spatial markers are not necessary for these types of cantilevers [22].

Tourek et al. derived, using beam theory, equations for correcting sensitivity measurements made some distance on the cantilever away from the imaging tip. These equations require accurate knowledge of the loading and laser spot position on the test cantilever. However, Valereski et al. used a much simpler equation which considers only the loading position [70, 74, 80]. This is given in equation 3.18, where S_{tip} is the sensitivity at the cantilever tip, $S_{\Delta L}$ is the sensitivity of the cantilever at some position ΔL from the tip and L is the length of the cantilever.

$$S_{tip} = S_{\Delta L}\left(\frac{L}{L-\Delta L}\right) \tag{3.18}$$

Following the guidelines in section 2.2.3, the uncertainty on sensitivity measurements was minimised and so the statistical variation on $\mathrm{S}_{\Delta L}$ measured in this work is typically $\pm 1\%$. Vakarelski et al. measured the spring constant and cantilever deflection sensitivity as the position of loading on a V-shaped cantilever was varied, by incrementally moving an 85 μm diameter latex sphere from the very end of the cantilever to a position approximately 35% along its length. The above expression was derived to determine the cantilever sensitivity at a known distance from the tip for a V-shaped cantilever and excellent agreement was observed between their theoretical and experimental values.

Despite equation 3.18 being suited to beam-shaped cantilevers, Vakarelski et al. observed that the equation performed well, provided that $\Delta L/L < 0.30$. However when the point of loading approaches $\Delta L/L = 0.35$, the difference between the experimental values and those determined using equation 3.18 increases to approximately 4%. Therefore when applying equation 3.18 to V-shaped cantilevers with $\Delta L/L \sim 0.40$ (as for cantilever ^{3}V1 in table 3.16) an additional 10% error is included as a conservative estimate. This case can be avoided quite easily however, by using FIB-milled markers or simply imaging a large area which includes the V-intersection, before making measurements. This allows sensitivity measurements to be made away from the V-intersection and within the $\Delta L/L < 0.30$ range.

It is also important to note that when applying equation 3.18, it is assumed that the laser spot is located close to the free end of the cantilever. Tourek et al. derived equations to correct sensitivity values when the point of loading is a known distance from the imaging tip [74]. If the laser is aligned close to the end of the cantilever, the following equation can be used to correct the sensitivity values where L_{spot} is the distance from the base of the cantilever to the centre of the laser spot.

$$S_{tip} = S_{\Delta L}\left[\frac{L^3}{(L-\Delta L)\left(2L-L_{spot}\right)^2}\right] \tag{3.19}$$

From equation 3.19 it can be seen that as L_{spot} approaches L, then S_{tip} approaches original form in equation 3.18. The proximity with which the laser spot can be aligned to the end of the cantilever depends on the size of the spot and how easy it is to visualise with the AFM optics. Proksch et al. noted that the laser spot on most commercial AFM systems is between 10-50 μm in diameter and developed a technique for positioning the laser spot on the cantilever, using the signal from the photodiode. This technique also accounts for the finite size of the laser spot relative to the cantilever length.

Using the AFM optics and a laser spot diameter of 20 μm; which is typical for the AFM used in this study [53], it was possible to align the laser spot to approximately $0.90L$ for each test cantilever. This will introduce minor uncertainty of approximately 1% on the measurements, using equation 3.18. It should be noted that many newer AFM systems (eg. Bruker FastScan) feature laser spot sizes in the 2-5 μm diameter range, making the laser spot easy to align at the very end of the cantilever.

Recent work by Sader et al. demonstrated that the laser spot position has a significant effect on the static-dynamic spring constant ratio [65]. Good agreement with their hypothesis was observed when the laser spot was placed at the free end of the cantilever, however this was at the expense of laser signal. When the laser signal was optimised, the static-dynamic ratio was observed to decrease significantly. Sader et al. recommended the use of a very small laser spot to maximise laser signal while maintaining an accurate static-dynamic spring constant ratio.

Despite the potential uncertainties; to simplify the analysis in this work, equation 3.18 will be used to correct the sensitivity along the test cantilevers. Much like the hard surface contact method, the underlying cantilever is assumed to be essentially rigid. It is important to note that if there is some small deflection of the underlying cantilever, an accurate deflection sensitivity can still be determined by using the reference cantilever method.

For the standard reference cantilever method, the equation relating the spring constant of the two cantilevers depicted in figure 3.20 is given below [1, 10].

$$k_{test}\left(\frac{L}{L-\Delta L}\right)^3 = k_{rigid}\left(\frac{S_{\Delta L}}{S_H}-1\right)\cos^2\alpha \tag{3.20}$$

Here, S_H is the deflection sensitivity of the test cantilever on an incompressible surface. This is the quantity to be measured, and so if S_H is made the subject of the equation, then the following expression is obtained.

$$S_H = S_{\Delta L}\left[\frac{k_{test}}{k_{rigid}}\left(\frac{L}{L-\Delta L}\right)^3\sec^2\alpha+1\right]^{-1} \tag{3.21}$$

Incorporating the "off-end sensitivity" correction from equation 3.18, this can be expressed further as:

$$S_{tip} = S_{\Delta L}\frac{L}{L-\Delta L}\left[\frac{k_{test}}{k_{rigid}}\left(\frac{L}{L-\Delta L}\right)^3\sec^2\alpha+1\right]^{-1} \tag{3.22}$$

For equation 3.22, it can be seen that if $k_{test}\left(\frac{L}{L-\Delta L}\right)^3 \ll k_{rigid}$ then the lower cantilever is essentially rigid and equation 3.22 simplifies to equation 3.18. Given the structure of the denominator of equation 3.21, precise knowledge of $\frac{k_{test}}{k_{rigid}}\left(\frac{L}{L-\Delta L}\right)^3 \ll k_{rigid}$ is not essential as long as this term is less than 0.2. This fraction is somewhat arbitrary, but it can be shown with simple error analysis that if $\frac{k_{test}}{k_{rigid}} > 0.2$, then either more accurate knowledge of the cantilever spring constants will be required or significant uncertainty (greater than 5%) will result. Alternatively, if $\frac{k_{test}}{k_{rigid}} > 0.2$ then a stiffer lower cantilever could be used.

If a tip-less cantilever is being used as the test probe and reverse imaging is used to position the point of loading very close to the end of the cantilever then equation 3.21 can be simplified to:

$$S_{tip-less} = S_{end}\left[\frac{k_{test}}{k_{rigid}}\sec^2\alpha + 1\right]^{-1} \tag{3.23}$$

where S_{end} is the sensitivity measured at the very end of the tip-less cantilever when pressed against the rigid tip. Therefore, the uncertainty on a particular measurement using the current method will depend upon a number of factors including the cantilever shape, distance from the loading point to the imaging tip and the ratio of the effective spring constant of the test cantilever to the underlying rigid cantilever.

3.3.2 Results and discussion

The sensitivity calibration technique developed in this work was applied to several AFM cantilevers with varying geometry, and a detailed measurement procedure is provided in section 2.2.3.1. Examples of the types of cantilevers used are shown in figure 3.1a,b,d,e), with a complete list of cantilevers and their properties provided in table 3.14.

Cantilever name	Geometry	Composition	Coating	Cantilever type	Nominal spring constant (Nm^{-1})
^{3}V1	V	Silicon nitride	Ti/Au	SNL Bruker	0.12
^{3}V2				Microlever Bruker	0.01
^{3}F1	Beam	Silicon	None	FMV Bruker	2.8
^{3}R1				CLFC Bruker	0.16
^{3}R2					1.3
^{3}R3					10.4
^{3}R4					0.16
^{3}R5					1.3
^{3}R6					10.4
^{3}R7			Cr/Au	Mikromasch CSC12	0.08

Table 3.14: Details of all cantilevers involved in this study including their manufacturer, geometry, composition, coating composition and nominal spring constant quoted by the manufacturer.

3.3.2.1 Sensitivity (tip-less cantilevers)

Data was first collected on tip-less cantilevers, and table 3.15 shows the sensitivity values experimentally determined for the beam shaped cantilevers ^{3}R1-R7. These sensitivity measurements were performed as close to the end of the cantilever as possible, using reverse AFM imaging.

The spring constant measured for cantilevers ^{3}R1-R6 is also given in table 3.15, this value is an average of four different calibration techniques. The methods used were the Euler beam equation, Cleveland formula [25], Sader resonance [23] and Sader hydrodynamic methods [14]. Given the ideal shape of cantilevers ^{3}R1-6, uncertainty on the spring constant is estimated to be ±3-5%.

Cantilever ^{3}R7 is coated with chromium and gold, which can introduce substantial uncertainty where the density or Young's modulus are required [23]. In order to reduce uncertainty, only the Sader hydrodynamic method was applied to this particular cantilever. The uncertainty on cantilever ^{3}R7 is estimated to be approximately ±7%, a value slightly larger than for the other tip-less cantilevers given the non-ideal shape.

Cantilevers ^{3}R1, ^{3}R2, ^{3}R4, ^{3}R5 and ^{3}R7 had spring constants sufficiently low in comparison to k_{rigid} and measurements were made close enough to the end of the cantilever such that no correction to the sensitivity was necessary. The spring constants of cantilevers ^{3}R3 and ^{3}R6 were comparable to k_{rigid} however, so equation 3.23 was used to correct the measured sensitivity values.

Cantilever	Spring constant (Nm^{-1})	Sensitivity (present method) (nmV^{-1})	Sensitivity (Higgins method) (nmV^{-1})
^{3}R1	0.087±0.004	92.2±1.8	88.4±4.4
^{3}R2	0.739±0.037	45.8±1	44.6±2.2
^{3}R3	6.66±0.33	25.0^a±0.5, 23.0^b±0.6	23.8±1.2
^{3}R4	0.091±0.005	83.4±1.6	84.3±4.2
^{3}R5	0.780±0.039	42.4±0.8	42.6±2.1
^{3}R6	6.92±0.346	24.9^a±0.5, 22.8^b±0.6	21.9±1.1
^{3}R7	0.086±0.006	65.7±1.4	65.7±5.3

[a] denotes the initial sensitivity (S_{end}) measured.

[b] denotes the corrected sensitivity ($S_{tip\text{-}less}$) using equation 3.23.

Table 3.15: Spring constant of the tip-less cantilevers ^{3}R1-7, and sensitivity determined using the current method compared to the sensitivity determined using the Higgins technique.

The sensitivity measurements obtained using this method were compared to those obtained using the Higgins thermal noise technique, and the results are shown in table 3.15. Good agreement is observed between the method presented here and the Higgins approach, demonstrating that this technique works well for cases where $k_{test} \ll k_{rigid}$ or when $k_{test} < 0.2_{rigid}$. Uncertainty on the Higgins method is estimated to be between 5-8% for the tip-less cantilevers, due to uncertainty on the spring constant values and errors inherent in the thermal noise measurements. Uncertainty budgets for cantilever ^{3}V1, ^{3}F1 and ^{3}R3 are provided in section 3.3.2.3. The uncertainty for cantilevers ^{3}R1, ^{3}R2, ^{3}R4, ^{3}5 and ^{3}R7 is determined from the standard deviation of 15 measurements and is approximately 2%, in addition to minor contribution due to the laser position. The total uncertainty for cantilever ^{3}R6 will be similar to that of cantilever ^{3}R3 (∼2.5%), which is a combination of propagated error in measurement and uncertainty from the laser position.

3.3.2.2 Sensitivity (practical cantilevers)

Table 3.16 shows data for cantilevers ^{3}V1, ^{3}V2 and ^{3}F1, including sensitivity values, the $\Delta L/L$ value for each measurement and the effective spring constant at each location. The spring constant for cantilever ^{3}F1 was measured using the Sader hydrodynamic method and the Cleveland formula [25]; the uncertainty on this value is estimated to be ±10%. The spring constant of cantilever ^{3}V1 was measured using the inverted reference cantilever technique reported in section 3.2, which excludes tip-sample contact and provides an uncertainty of ±10%.

For cantilever ^{3}V2, the extremely low spring constant means that there are few methods available to calibrate the spring constant which exclude tip-surface contact. However, since a beam shaped cantilever is also on the same chip, indirect techniques can be applied. These are the indirect Gibson and Sader methods [23, 81]. Both techniques assume that the thickness and material properties of cantilevers on the same chip are identical. The uncertainty on the spring constant for cantilever ^{3}V2 is estimated to be 10-15%.

The spring constants of cantilevers ^{3}V1-2 were sufficiently low in comparison to k_{rigid} that the measured sensitivity was only corrected for position using equation 3.18. For cantilever ^{3}F1, the effective spring constant at each spatial marker was large enough in comparison to k_{rigid} that equation 3.22 was required to correct the measured sensitivity values.

Cantilever	Higgins thermal (nmV^{-1})	Hard contact (nmV^{-1})	Sensitivity (nmV^{-1})	$\frac{\Delta L}{L}$	Spring constant (Nm^{-1})	Corrected sensitivity (nmV^{-1})
^{3}V1	49.2±5.0	50.4±0.5	47.6±0.5	0.08	0.191±0.020	51.6±1.5
			45.9±0.5	0.11	0.211±0.020	51.5±1.5
^{3}V1	55.0±5.5	57.4±0.6	34.0±0.3	0.41	0.722±0.072	57.5±6.9
			34.4±0.3	0.42	0.753±0.075	56.4±6.8
^{3}V2	64.8±6.5	62.4±0.6	44.3±0.4	0.26	0.035±0.004	59.9±3.0
^{3}F1	46.2±4.0	46.9±0.5	41.7±0.4	0.15	3.90±0.40	46.6±1.2
			41.0±0.4	0.19	4.56±0.46	48.0±1.2
			40.6±0.4	0.22	5.01±0.50	48.6±1.2
			38.0±0.4	0.28	6.30±0.63	48.4±1.2

Multiple sensitivity values for ^{3}V1-2 represent measurements made on separate occasions.

Table 3.16: Sensitivity values for all practical cantilevers. The sensitivity for cantilevers ^{3}V1-2 were corrected using equation 3.18 while the sensitivity values for cantilever ^{3}F1 were corrected using equation 3.22.

For these practical cantilevers, the sensitivity measurements obtained by the spatial marker method were compared to the Higgins thermal noise technique and the standard hard surface contact method. Once again, good agreement is observed between the two methods and the hard surface contact technique, demonstrating that the technique presented herein is applicable to practical cantilevers where $k_{test}\left(\frac{L}{L-\Delta L}\right)^{3} \ll k_{rigid}$ or when $k_{test}\left(\frac{L}{L-\Delta L}\right)^{3} < 0.2k_{rigid}$. The uncertainty stated here is a combination of the propagation of error in measurement and the estimated uncertainty inherent in the assumptions made. For V-shaped cantilevers; there is significant additional uncertainty introduced when performing measurements with $\frac{\Delta L}{L} > 0.35$ as discussed in section 3.3.1.2, and this is included in the uncertainty of these results.

Uncertainty associated with the Higgins method for sensitivities in table 3.16 will be approximately 8-10%. The increased uncertainty for V-shaped cantilevers in table 3.15 is due to greater uncertainty on their spring constant as well as greater uncertainty in correction factors used for thermal noise measurements. Despite this increased uncertainty for V-shaped geometry, good agreement is observed in table 3.20. Higgins et al. only reported data for beam-shaped cantilevers but did state that the technique had potential to be applied to other geometries. These results indicate that this is the case, as long as accurate spring constant techniques can be applied to the test cantilevers which do not require tip-surface contact (ie. laser doppler vibrometry).

The overall agreement for all test cantilevers, between the Higgins method and the hard surface contact method is much closer than that originally reported by Higgins et al.; this may be due to a more accurate and rigorous calibration of the spring constant. Higgins et al. used the Sader hydrodynamic method which, while excellent for beam shaped cantilevers, encounters difficulties when the ratio between the cantilevers' length and width is less than 3. This was the case for several of the cantilevers that were studied.

Rather than directly measuring the dimensions of each cantilever using optical or electron microscopy, dimensions provided by the manufacturer were used by Higgins et al., which have a tolerance of 5-10%. In a recent publication by Sader et al., where the hydrodynamic method is extended to cantilevers of arbitrary shape, the effects of uncertainty on plan view dimensions are reported to scale by the power of 1.5 [41]. Therefore, combining the uncertainty in the manufacturers quoted dimensions with the inherent limits of the technique (i.e. $\frac{L}{w} < 3$ in some cases), it is perhaps not surprising that discrepancies of up to 20% were reported between their results and the hard surface contact method.

The agreement between the spatial marker and hard surface contact methods is on average, superior to that demonstrated by the technique reported by Tourek et al. This is in part due to the reasons outlined above and also the use of reverse AFM imaging to accurately determine the loading position. Tourek et al. used optical microscopy to determine the loading position on the test cantilever, which has much greater uncertainty then AFM and SEM. The spatial marker technique is also applicable to V-shaped cantilevers while Tourek et al. applied their method only to beam-shaped cantilevers. The data indicates that increasing the distance of loading from the imaging tip does not necessarily affect the agreement with other techniques (e.g. cantilever ^{3}V1). However if spatial markers are used, $\frac{\Delta L}{L} < 0.30$ should be used in order to minimize the uncertainty.

Aside from avoiding tip-sample contact, there are other advantages to the spatial marker method. For V-shaped cantilevers with extremely low spring constant, such as ^{3}V2, the acquisition of force-distance curves is very difficult. The cantilever experiences very large deflection due to adhesion when measuring deflection sensitivity by the hard surface contact method. TeRiet et al. reported that some users were unable to acquire force curves using these cantilevers, since the Z range of the scanner was insufficient and once in feedback the cantilevers could not detach from the surface [37].

Using the inverted spatial marker method, the cantilever can be loaded some distance from the tip and so the spring constant is effectively much greater. This reduces deflection of the cantilever due to adhesion and allows force curves to be acquired over a much smaller Z range. Another advantage is that the rigid tip diameter can be chosen to be as sharp as possible (on the order of 20 nm or less). This further reduces adhesion between the rigid tip and the test cantilever surface, in cases where the imaging tip is very blunt.

These effects can be easily seen with cantilever ^{3}V2 which has a spring constant of 0.015 Nm^{-1} and a nominal tip diameter of 40 nm. Figure 3.21a shows a force curve on silicon using cantilever ^{3}V2 with the hard surface contact method. The adhesion of the cantilever is large enough that the lower portion of the curve is cut-off, as the deflection exceeds the range of the photodiode. Figure 3.21b shows a force curve where the load was applied ~80μm from the imaging tip, against a rigid reference cantilever with nominal tip diameter less than the imaging tip of ^{3}V2.

The Z-range for figure 3.21b is much less than for figure 3.21a, primarily due to the increase in effective spring constant for the test cantilever. This is important since the Z-range in which sensitivity calibration measurements are performed should, if possible, be similar to those used in the actual force experiments [38].

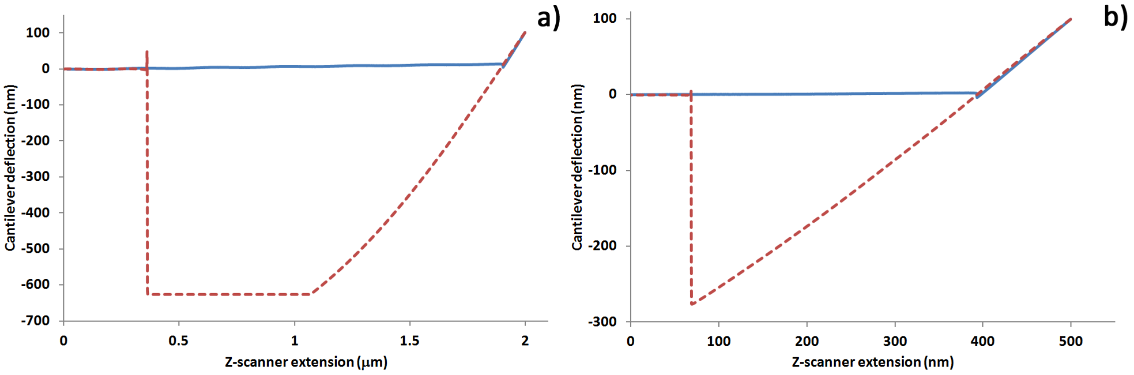

Figure 3.21: Force curves performed using probe ^{3}V2 on (a) a silicon surface and (b) on a rigid cantilever tip approximately 80 μm from the imaging tip of ^{3}V2. Solid line shows the approach cycle while the dashed line shows the retract cycle. Reprinted with permission from [28].

3.3.2.3 Uncertainty analysis

The uncertainty in S_{tip} due to the propagation of measurement error for various cantilevers was determined, and is presented with detailed uncertainty budgets here. As in previous cases, the uncertainty was determined in accordance with the ISO guide to the expression of uncertainty in measurement [55], using equation 3.24 .

$$u_c^2(y) = \sum_{i=1}^{N}(\frac{df}{dx_i})u^2(x_i) \tag{3.24}$$

When this is applied to equation 3.22, the following expression is obtained for the uncertainty in S_{tip}, when summed in quadrature:

$$\begin{aligned} dS_{tip}^2 = (\frac{\delta S_{tip}}{\delta k_{rigid}}dk_{rigid})^2 + (\frac{\delta S_{tip}}{\delta k_{test}}dk_{test})^2 + (\frac{\delta S_{tip}}{\delta S_{\Delta L}}dS_{\Delta L})^2 \\ +(\frac{\delta S_{tip}}{\delta L}dL)^2 + (\frac{\delta S_{tip}}{\delta \Delta L}d\Delta L)^2 \end{aligned} \tag{3.25}$$

This analysis was performed for sensitivity calculation of each of the three different types of cantilevers (^{3}V1, ^{3}F1 and ^{3}R3). The associated uncertainty budgets are presented in the following tables.

Variable (x)	Description	Value	Standard uncertainty	Sensitivity $\left(\frac{\delta S_{tip}}{\delta x}\right)$	Variance contribution (nmV^{-1})
k_{rigid}	spring constant (test cantilever)	77.4 Nm^{-1}	7.7 Nm^{-1}	0.0356378	0.274 (19.0%)
k_{test}	sensitivity (rigid cantilever)	0.753 Nm^{-1}	0.075 Nm^{-1}	-3.66316	-0.275 (19.2%)
$S_{\Delta L}$	sensitivity (position ΔL)	34.4 nmV^{-1}	0.3 nmV^{-1}	1.63983	0.492 (61.3%)
L	test cantilever length	195 μm	0.1 μm	-178751	-0.0179 (0.0811%)
ΔL	loading position	81.9 μm	0.1 μm	425598	0.0426 (0.460%)
				Sensitivity	Uncertainty
				56.4 Nm^{-1}	0.628 nmV^{-1} (1.11%)

Table 3.17: Uncertainty budget for the standard reference cantilever method applied to cantilever ^{3}V1 at $\frac{\Delta L}{L} = 0.42$.

Variable (x)	Description	Value	Standard uncertainty	Sensitivity $\left(\frac{\delta S_{tip}}{\delta x}\right)$	Variance contribution (nmV^{-1})
k_{rigid}	spring constant (test cantilever)	77.4 Nm^{-1}	7.7 Nm^{-1}	0.0484154	0.373 (27.0%)
k_{test}	sensitivity (rigid cantilever)	2.39 Nm^{-1}	0.24 Nm^{-1}	-1.56793	-0.376 (27.4%)
$S_{\Delta L}$	sensitivity (position ΔL)	0.38 nmV^{-1}	0.3 nmV^{-1}	1.27425	0.484 (45.5%)
L	test cantilever length	210.9 μm	0.1 μm	-67191.1	-0.00672 (0.00876%)
ΔL	loading position	58.2 μm	0.1 μm	243481	0.0243 (0.115%)
				Sensitivity	Uncertainty
				48.4 Nm^{-1}	0.718 nmV^{-1} (1.48%)

Table 3.18: Uncertainty budget for the standard reference cantilever method applied to cantilever ^{3}F1 at $\frac{\Delta L}{L} = 0.28$.

For tip-less cantilevers, measurements can be performed at the very end of the cantilever which removes the ΔL and L terms from equation 3.22, resulting in equation 3.23.

This means that in cases where the test tip-less cantilever is very soft compared to the underlying cantilever, the sensitivity can be directly measured and the uncertainty is simply the standard deviation of repeated measurements. For cases when the spring constant of the cantilevers are similar, equation 3.24 is applied to equation 3.23, and the uncertainty analysis for cantilever ^{3}R3 in this case is presented below.

Variable (x)	Description	Value	Standard uncertainty	Sensitivity $\left(\frac{\delta S_{tip}}{\delta x}\right)$	Variance contribution (nmV^{-1})
k_{rigid}	spring constant (test cantilever)	77.4 Nm^{-1}	7.7 Nm^{-1}	0.0241766	0.186 (28%)
k_{test}	sensitivity (rigid cantilever)	6.66 Nm^{-1}	0.33 Nm^{-1}	-0.280972	-0.0927 (7.2%)
S	sensitivity at end	25.0 nmV^{-1}	0.3 nmV^{-1}	0.918508	0.276 (64%)
				Sensitivity	Uncertainty
				23.0 Nm^{-1}	0.345 nmV^{-1} (1.50%)

Table 3.19: Uncertainty budget for the standard reference cantilever method applied to cantilever ^{3}R3 at the very end of the cantilever.

The total uncertainties reported are a combination of that determined here, and uncertainty due to assumptions inherent in the technique.

3.3.2.4 Spring constant calibration

Given that the reported method is able to accurately determine deflection sensitivity without tip-sample contact, it can therefore also be used to determine the spring constant of the test cantilever using the thermal noise technique. This is best applied to test cantilevers with spring constants much less than the rigid cantilever such as ^{3}R1, ^{3}R2, ^{3}R4, ^{3}R5, ^{3}V1 and ^{3}V2; as cantilevers such as ^{3}R3, ^{3}R6 and ^{3}F1 (where k_{test} is a significant fraction of k_{rigid}) require prior knowledge of the spring constant (refer to equation 3.22). If the thermal noise method is applied to ^{3}V1 and ^{3}V2, using sensitivities measured by both the spatial marker and hard surface contact method, the spring constant obtained can be compared. These results are reported in table 3.20.

Cantilever	Hard surface contact method		Non-contact method	
	Sensitivity (nmV^{-1})	$k_{thermal}$ (Nm^{-1})	Sensitivity (nmV^{-1})	$k_{thermal}$ (Nm^{-1})
^{3}V1	50.4±0.5	0.138±0.21	51.6±1.5	0.132±0.026
			51.5±1.5	0.132±0.026
	57.4±0.6	0.141±0.21	57.5±6.9	0.140±0.028
			56.4±6.8	0.146±0.027
^{3}V2	62.4±0.6	0.015±0.003	59.9±3.0	0.016±0.004

Table 3.20: Spring constants for cantilevers ^{3}V1-2 determined using the thermal noise method; comparing between sensitivities measured using the current method and the hard surface contact method.

Good agreement between the two methods suggests that the sensitivity values determined using the spatial marker method can also be used to calibrate the spring constant using the thermal noise method. Uncertainty on the sensitivity values and the errors inherent in the thermal noise technique leads to an uncertainty estimate of ∼15-25% for these spring constants. Obviously, this calibration approach cannot be used in conjunction with the Higgins method, since the thermal noise method is inherent in the Higgins technique.

3.3.3 Summary

Accurate deflection sensitivity calibration was demonstrated on a wide range of cantilever types, while completely avoiding tip-sample contact. The technique uses a rigid, inverted cantilever to load the test cantilever a known distance from its' imaging tip. Reverse AFM imaging was used to accurately determine the loading position on the test cantilever. This was achieved by reverse imaging the very end of the cantilever in the case of tip-less, whereas FIB milled spatial markers or the V-arm intersection were used for cantilevers with an imaging tip or V-shaped geometry.

Deflection of the underlying rigid cantilever was assumed to be negligible, however the reference cantilever method can be adjusted to provide the deflection sensitivity where this is not the case, provided that the spring constant of the test cantilever is less than 20% of the rigid cantilevers'.

For beam shaped cantilevers with an imaging tip, spatial markers are necessary, however these don't necessarily need to be FIB milled. Widely accessible techniques are capable of producing small protrusions on silicon surfaces using electron beam methods. These would be just as effective as FIB-milling and may be more accessible to many research groups. Manufacturers of AFM cantilevers could also modify the cantilever manufacturing process to include spatial markers on AFM cantilevers, which would further simplify the method.

Cantilevers with very high spring constants (k=200 Nm^{-1}), such as the Bruker Tap 525, which would allow a wider range of test cantilevers to be calibrated where correction due to similar spring constants would not be required.

The results obtained were compared to the Higgins method and the hard surface contact technique, where good agreement was demonstrated for all cantilever geometries. The accuracy of the Higgins thermal noise method was improved and applied to non-rectangular beam-shaped geometry. This was achieved by applying accurate spring constant calibration techniques that also avoid tip-sample contact.

Application of the current method to measure the cantilevers' spring constant using the thermal noise method was also demonstrated, provided that $k_{test} \ll k_{rigid}$. Using this simple, inexpensive technique allows users to accurately determine cantilever deflection and perform force calibration without tip sample contact. The current methodology can also be applied to micromechanical sensors which use cantilever deflection to measure stress and strain due to molecules binding to functionalised cantilever surfaces [82].

3.4 Fast-scanning cantilever calibration

3.4.1 Introduction

While conventional cantilevers are now easier to calibrate when compared to the early stages of AFM development, they can still pose experimental challenges primarily due to their small size, particularly in terms of thickness which is often sub-micron. With the advent of commercially available fast-scanning probes, which are an order of magnitude smaller than conventional probes, spring constant calibration becomes even more challenging.

In addition, high speed quantitative imaging techniques such as dynamic force spectroscopy, phase imaging and ultrasonic force microscopy (UFM) have been developed, where mechanical properties and surface forces are mapped at fast-scanning speeds [83, 84]. Recent work by Braunsmann et al. has demonstrated superior performance of ultra-small cantilevers for force measurement in fluid, due to reduction of the cantilevers' hydrodynamic drag [85]. With the development of these new operational modes and cantilever architectures with reduced dimensions, the accurate determination of spring constants has never been more important.

In this work, a range of commercial fast-scanning cantilevers are calibrated using a variety of established methods. The results presented here demonstrate the increased difficulty in calibrating fast-scanning cantilevers. However, it is also shown that by using a combination of techniques, the entire spring constant range for these cantilevers can be calibrated with low to high uncertainty (ranging from 10-45%), depending on the technique used.

Certain established methods are modified to improve their applicability to fast-scanning cantilevers, in particular the mass-removal technique reported in section 3.1. Limitations to these techniques are identified, and the future directions for fast-scanning cantilever calibration are discussed.

Due to the same factors as conventional cantilevers, the dimensions of ultra-small cantilevers can vary between probes, resulting in a wide range of values for the spring constant and resonant frequency. If manufacturing tolerances remain the same, the reduced dimensions of these cantilevers would result in even greater variation of cantilever properties.

Walters et al. reported the fabrication of short cantilevers with resonant frequencies of 500-600 kHz and spring constants of 1-2 Nm^{-1} [86]. These cantilevers were calibrated using the thermal noise and added mass methods [16, 25]. While the two methods agreed to within ±20%, the destructive nature of the added mass method meant that each method was applied to physically different cantilevers of the same type.

Richter et al. developed AFM probes even further reduced in size to length scales of less than 2.5 μm, however these probes are at the limit of conventional optical detection methods [87]. Spring constant calibration for each type of probe was performed using a single technique, which was either the thermal noise method (using a LDV) or a geometric method similar to the approach described by Cleveland et al. [25]. A detailed comparison of techniques was not investigated and therefore it is difficult to determine the accuracy of the spring constants reported, as well as which methods are more appropriate for these cantilevers.

Due to the significantly reduced dimensions of fast-scanning cantilevers, it is reasonable to suggest that certain calibration techniques may have limitations and may require modification. Until this work, no detailed analysis has been performed to validate the application of conventional calibration methods to fast-scanning cantilevers, or to determine which techniques are most appropriate.

3.4.1.1 Commercially available cantilevers

Bruker The cantilevers studied here are manufactured by Bruker and include FastScan A, B and C types. These are metal coated silicon nitride cantilevers incorporating a silicon tip, and have resonant frequencies ranging from 200 kHz (FastScan C) to 2.0 MHz (FastScan A). Details of these cantilevers are provided in table 3.21 and plan view SEM images of these cantilevers are shown in figure 3.22.

Cantilever type	Imaging tip material	Cantilever material	Metal coating	Length/ width/ thickness (μm)	Resonant frequency (kHz)	Spring constant (Nm^{-1})
Fastscan A	Silicon	Silicon Nitride	Al (100nm)	27/32/0.6	1400	18
Fastscan B			Ti/Au (5/60 nm)	30/32/0.3	400	4
Fastscan C				40/40/0.3	300	0.8

Table 3.21: Nominal properties of three FastScan cantilevers manufactured by Bruker, used in this work.

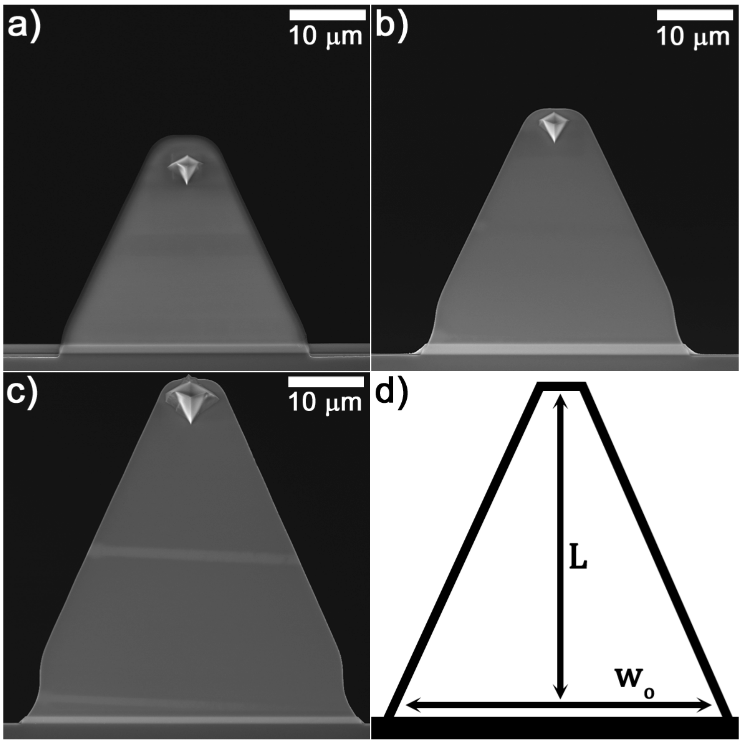

Figure 3.22: SEM images of the FastScan A (^{4}FSA-3) (a), B (^{4}FSB-2) (b) and C (^{4}FSC-2) (c) cantilevers used in this work; the dimensions used to describe the trapezoidal plate cantilever geometry are also shown in (d). Reprinted with permission from [27].

While conventional AFM cantilevers exist in a variety of shapes, the primary geometries are rectangular and V-shaped. Figure 3.22 clearly shows that Bruker FastScan probes deviate from this standard geometry and are shaped like a trapezoidal plate. This cantilever geometry was selected by Bruker to provide high-performance fast-scanning probes, as it reduces the cantilever settling time and allows for faster scanning [88, 89].

FastScan cantilevers feature significantly reduced dimensions in comparison to conventional cantilevers, particularly in their length and thickness. This achieves a lower cantilever mass, which results in a higher resonant frequency and reduces the cantilevers' thermal noise [90]. There are several other types of fast-scanning cantilevers currently available from different manufacturers which include Olympus, Nanoworld and Applied Nanotechnology. Although these cantilevers aren't studied in this work, a brief overview is provided here for completeness.

Olympus Olympus produce fast-scanning probes for imaging in air and fluid, these are the OmegaLever (ν= 1600 kHz, k=85 Nm^{-1}) and the BioLever Fast (ν= 1500 kHz, k=0.1 Nm^{-1}). The BioLever Fast is a small rectangular cantilever, whereas the OmegaLever is comprised of a short rectangular section terminating in a trapezoidal plate [91].

NanoWorld NanoWorld produce the Arrow UHF probe (ν= 1500 kHz, k=not available) which has similar geometry to the FSA probe manufactured by Bruker. A significant difference is that the Arrow UHF cantilever is composed of single-crystal silicon, whereas the Bruker cantilevers are silicon nitride. NanoWorld have also recently commercialised ultra-short cantilevers (USC) with a wide range of properties, including probes with resonant frequency of up to 25 MHz. These cantilevers are semi-rectangular and are comprised of silicon, silicon nitride or an unidentified "quartz-like" material [92].

Applied Nanotechnology Applied Nanotechnology produce the Access-UHF fast-scanning probes (ν= 1.1 MHz, k=115 Nm^{-1}) which are rectangular silicon cantilevers 55 μm in length [93]. These cantilevers feature an extended tip with triangular pyramid geometry, which allows the tip apex to be visualised during imaging.

3.4.1.2 Properties

Designing AFM probes capable of high speed scanning is a matter of balancing the dynamic properties of the cantilever, its dimensions and spring constant, all of which affect each other [94, 95]. The significant departure from standard geometry and properties potentially poses a number of challenges for many of the current state-of-the-art calibration techniques, including:

Size For techniques that require accurate knowledge of all cantilever dimensions, the thickness in particular can be difficult to measure accurately [13, 25]. The thickness of FastScan A probes is comparable to conventional contact mode cantilevers, however type B and C cantilevers are only a few hundred nanometers thick. To measure cantilever thickness accurately via electron microscopy requires careful edge-on imaging which necessitates a high-resolution SEM and an experienced operator, where the angle of image acquisition must be well-aligned.

Geometry Trapezoidal plate geometry is not typical for AFM cantilevers, so there has been minimal research into calibrating cantilevers with this geometry [96]. Recent research found the trapezoidal plate geometry to be ideal for fast-scanning applications [97], resulting in cantilevers with high resonant frequency, high Q factor, low spring constant and a large region for the laser spot. It stands to reason that many next generation AFM cantilevers will likely possess this geometry and as such, certain calibration methods will require some adaptation. The cantilevers studied in this work are supplied by Bruker, however Olympus also produce a trapezoidal cantilever for fast-scanning applications. For calibration methods which require shape correction factors [13], no such data currently exists for this geometry.

Composition The FastScan cantilevers studied in this work are composed of silicon nitride, as are most other types of fast-scanning cantilevers. It is well-established that the material properties of silicon nitride can vary significantly. The density of the silicon nitride FastScan cantilevers was provided by the manufacturer as 3300 kgm^{-3}, but without an estimated uncertainty. Given the possible range of densities reported by Sader et al., an uncertainty of approximately 20% was assumed [13]. Ohler also uses an approximate uncertainty for the density of silicon nitride of 20% [58].

For cantilevers composed of silicon nitride, calibration methods which require these material properties suffer increased uncertainty as a result. Hybrid cantilevers have recently been developed which consist of a silicon nitride cantilever with a single-crystal silicon tip, which combines the high sensitivity of a silicon nitride cantilever with the sharpness of a silicon tip.

Fast-scanning cantilevers are generally very thin and require metallic coatings for reflectivity, this necessitates application of the density and Youngs' modulus corrections introduced in section 1.1.1.2. Gold coated cantilevers such as Fastscan B and C probes have much greater error on the average cantilever density since gold has approximately six times the density of silicon nitride. Precise knowledge of the gold coating thickness is required and this is difficult to achieve since it is typically less than 100 nm. The density of aluminium is much closer to the density of silicon nitride (2700 kgm^{-3} for aluminium compared to 3300 kgm^{-3} for silicon nitride) and therefore will not contribute as much error to the average density of Fastscan A cantilevers.

As fast-scanning cantilevers reduce in size, the thickness of the cantilever must also be reduced to maintain a low spring constant; the thinner the cantilever substrate, the more significant the effect of metal coatings. Figure 3.23 shows a side-on SEM image of an aluminium-coated FastScan A cantilever. Without accurate measurement of the film thickness, this can introduce significant uncertainty for methods which require either density or the Young's modulus of the cantilever. If cantilever thickness continues to reduce, the metal film will have a greater impact as it will constitute a larger proportion of the cantilevers' material.

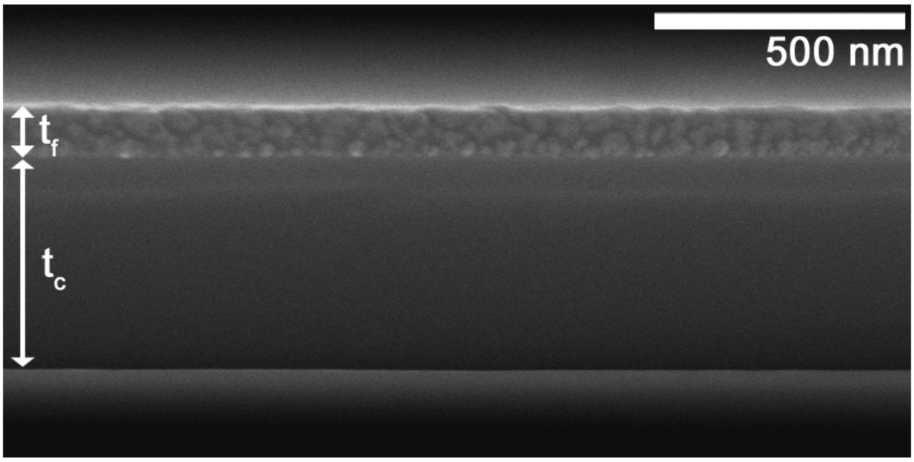

Figure 3.23: Side-on SEM image of a silicon nitride FastScan A cantilever, showing the measurement of cantilever (t_c) and aluminium film (t_f) thickness. Reprinted with permission from [27].

3.4.1.3 Spring constant calibration

The application of established calibration techniques to fast-scanning cantilevers has yet to be evaluated for uncertainty and applicability. Certain calibration techniques may require no modification, however it would be expected that with the factors described previously, many methods will need to be modified . A number of state-of-the-art calibration methods are investigated in this work. Each method has been introduced previously in section 1.2.3, and these different methods are briefly discussed here with regard to their application to fast-scanning cantilevers.

Reference cantilever The reference cantilever calibration technique has been studied extensively and is well suited to fast-scanning probes; the technique provides a direct measurement and as such is unaffected by geometric, composition or size factors. Aside from the uncertainty on the reference cantilever, the method has several sources of uncertainty including the point of loading on the reference cantilever, how closely the spring constants match and the torque correction factor which is discussed below. As shown earlier in this chapter, uncertainty related to tip loading position can be substantially reduced by using spatial markers. The reference cantilevers used were type CLFC, supplied by Bruker. Aside from the torque correction factor addressed below, no significant modification of this technique is required in order to calibrate fast-scanning cantilevers.

The reference cantilever method requires a torque correction factor in the case where the height of the tip is comparable to the cantilevers' length; this is especially relevant for ultra-small fast-scanning cantilevers. The torque correction provided in equation 1.32 is applicable to beam-shaped cantilevers and has not been investigated for trapezoidal geometry.

Trapezoidal torque correction factor Here, the effect of trapezoidal cantilever geometry on the torque correction factor is considered. Equation 16 from the work of Edwards et al. defines the general expression for determining the torque correction factor, T_i, for a cantilever of arbitrary shape with a sharp tip where D is the height of the tip and θ is the cantilever approach angle [98]. The subscript z

denotes deflection of the cantilever in the normal direction.

$$T_z = 1 - \rho_z D \tan\theta \tag{3.26}$$

The term ρ_i is defined as follows, where subscript z is used instead [98]. Here, k_z and $k_{z\theta}$ are the normal and longitudinal spring constant of the cantilever respectively.

$$\rho_z = \frac{k_z}{k_{z\theta}} \tag{3.27}$$

For a rectangular cantilever, the normal and longitudinal spring constants are defined as follows, where E is the Young's modulus of the cantilever, w is the width, t is the thickness and L is the length [98].

$$k_z = \frac{Et^3w}{4L^3} \tag{3.28}$$

and

$$k_{z\theta} = \frac{Et^3w}{6L^3} \tag{3.29}$$

For convenience it is assumed that the imaging tip is located at the very end of the cantilever (ΔL=0), however in reality the tip is often set back a small distance ΔL, such that $\Delta L \ll L$. Dividing k_z by $k_{z\theta}$ the value of ρ_z for a beam-shaped cantilever results. Substituting this back into equation 3.26, the familiar torque correction factor for a beam-shaped cantilever is obtained.

$$T_{beam} = 1 - \frac{3D}{2L}\tan\theta \tag{3.30}$$

For a trapezoidal cantilever the situation is more complex. While equation 3.38 gives k_z for trapezoidal geometry, there is no trapezoidal expression for $k_{z\theta}$. It can be assumed, however, that $T_{trapezoidal}$ will lie somewhere between that for beam-shaped (T_{beam}) and cantilevers with triangular shape ($T_{triangle}$), where the triangular base width (w_0) and rectangular width (w) are identical as shown in 3.24. If $T_{triangle}$ can be determined, an upper and lower limit can be obtained for $T_{trapezoidal}$.

Firstly, k_z is required for a triangular cantilever. Equations A2a and A2b from Sader and White provide k_z for a triangular-shaped cantilever [99].

$$k_z = \frac{Et^3w_0}{6L^3} \tag{3.31}$$

The term w_0 is now the width of the triangular cantilevers' base. There is no simple expression for $k_{z\theta}$ in the literature for triangular geometry, however Sader et al. derived an expression (shown below) for $k_{z\theta}$ with V-shaped geometry, which is equation 3b in the original publication [100].

$$k_{z\theta} = \frac{Et^3w_0}{12L^2}\left[\frac{2w}{w_0} - \frac{\Delta L}{L}\left(1 + log\left(\frac{2w}{w_0}\frac{\Delta L}{L}\right)\right) + \Pi\left(\frac{w_0}{2w-1}\right)\left(\frac{1}{2} + \frac{w_0}{2w} - \frac{\Delta L}{L}\right)\right] \tag{3.32}$$

Where, as shown in figure 3.25 w is the width of the V-shaped cantilever arms, w_0 is the overall base width and Π is the Poisson's ratio of the cantilever material which is defined below:

$$\Pi = \frac{1+\nu}{\Gamma^2\left(2 - \Gamma^2\left[1-\nu\right]\right)} \tag{3.33}$$

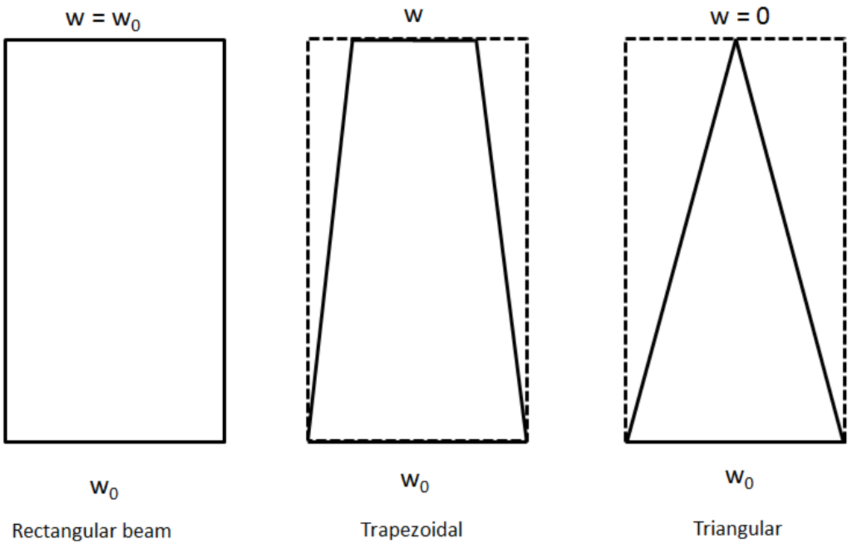

Figure 3.24: Schematic showing the variation of plan-view geometry from beam, through trapezoidal to triangular-shaped cantilever geometry.

The term Γ is then given by:

$$\Gamma = \frac{2L}{\sqrt{1+w^2}} \tag{3.34}$$

Assuming that $\Delta L = 0$, equation 3.32 can be simplified to:

$$k_{z\theta} = \frac{Et^3 w_0}{12L^2}\left[\frac{2w}{w_0} + \Pi\frac{w_0}{2w-1}\left(\frac{1}{2}+\frac{1}{w_0}\right)\right] \tag{3.35}$$

As the width of the cantilever arms (w) approaches $\frac{w_0}{2}$, the V-shaped cantilever approaches a closed triangular geometry as shown in figure 3.25.

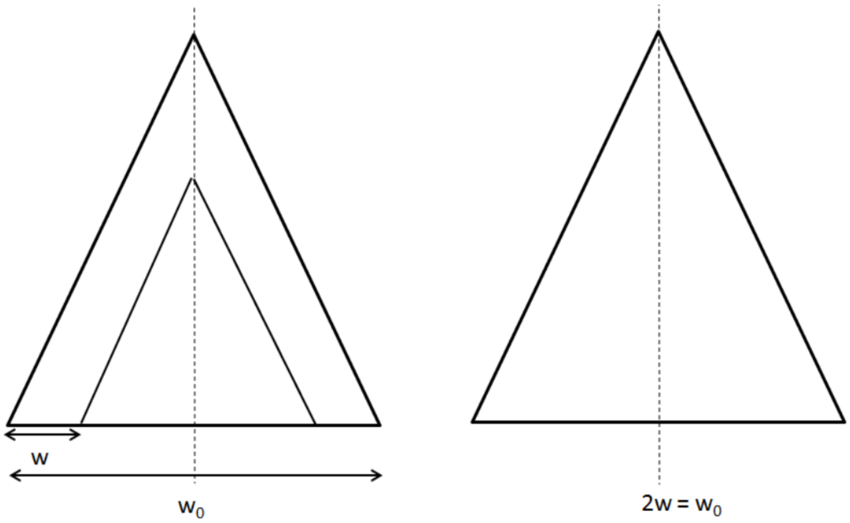

Figure 3.25: Schematic showing the geometry of V-shaped and triangular plate type cantilevers.

Setting $w = \frac{w_0}{2}$ and substituting this into equation 3.35, the following expression is obtained:

$$k_{z\theta} = \frac{Et^3 w_0}{12L^2} \tag{3.36}$$

The expressions for k_z and $k_{z\theta}$ with triangular geometry allow ρ_z to be determined for a triangular cantilever using equation 3.27. This value can then be used to determine $T_{triangle}$ using equation 3.26, which results in the following torque correction factor for a triangular cantilever.

$$T_{triangle} = 1 - \frac{2D}{L}\tan\theta \tag{3.37}$$

If $\frac{D}{L}$ and $\tan\theta$ are small ($\ll 1$), then equations 3.30 and 3.37 will be similar. Using typical values for FastScan cantilevers ($\theta = 12^o$, $\frac{D}{L} \approx 0.15$) and substituting them into equations 3.30 and 3.37, T_{beam}=0.952 and $T_{triangle}$=0.936 are obtained.

Trapezoidal geometry resides somewhere between beam and triangular geometry, and so the value for $T_{trapezoidal}$ will also lie between the values of $T_{rectangle}$ and $T_{triangle}$. Taking $T_{trapezoidal}$ to be the average of T_{beam} and $T_{triangle}$ gives $T_{trapezoidal}$=0.944, and the total range spanned by the limiting values is 1.6%. For the cantilevers studied in this work, the value for $T_{trapzoidal}$ is taken to be 0.94 with a conservative uncertainty estimate of ±1%.

FIB milling The FIB milling method has been demonstrated to provide high accuracy with conventional silicon cantilevers but struggles when applied to silicon nitride probes; this is due to high uncertainty of silicon nitride density. Milling must cause a large frequency shift (∼2 kHz) to attain low uncertainty, however the mass removed should be as small as possible in order to avoid altering the mechanical properties of the cantilever.

Fast-scanning probes with ultra-high resonant frequency are ideal candidates for this method, as a small mass change should cause a large frequency shift. Unfortunately, many fast-scanning cantilevers are silicon nitride, but do incorporate a silicon tip. In this work, the FIB technique is modified to take advantage of this, whereby the silicon tip is milled instead of the cantilever.

Thermal noise The thermal noise method relates the amplitude of the cantilevers' thermal motion to its spring constant. This technique has been widely adopted as an inbuilt calibration method on many commercial instruments, due to its ease of use [16]. Although application of the method is simple, correction factors are required to account for the cantilever tilt, dynamic to static spring constant conversion [101], optical lever sensitivity [17] and laser spot position [18]. These have been introduced in section 1.2.3, but are briefly reviewed here with an emphasis on fast-scanning cantilevers.

These individual corrections are grouped together into a single χ correction factor. One of these corrections is the dynamic to static spring constant ratio which is also discussed in section 1.1.1.3 of the introduction. This value varies with geometry and can be determined either experimentally, or theoretically using finite element analysis [41, 102].

The correction for the optical cantilever system is the most significant, and results in a χ factor of 1.106 for rectangular geometry and 1.144 for V-shaped cantilevers [58]. There is currently no χ factor available for fast-scanning cantilevers with trapezoidal plate geometry, which will limit application of the thermal method. Uncertainty in this method is primarily due to uncertainty in the deflection sensitivity and the necessary correction factors, and so increased uncertainty is expected for fast-scanning cantilevers.

Sader hydrodynamic (arbitrary shapes) The Sader hydrodynamic method for arbitrary shapes was introduced previously, and allows the spring constant of a well-calibrated reference cantilever to be transferred to a test cantilever using equation 1.28 [41]. Uncertainty in the method depends upon the error on the reference cantilever, the geometric similarity between the standard and the test cantilever and any inherent uncertainty in the method.

The Sader arbitrary method was chosen as a comparison method since it should be relatively unaffected by the trapezoidal geometry. The technique is applied in this work by using the reference cantilever results as the "standard" and so the total uncertainty in this case is estimated to be ∼10%.

Sader resonance The Sader resonance method relates the spring constant to the cantilevers' mass and unloaded resonant frequency. A geometric mass correction factor (n) is required and depends on the cantilevers' geometry [13]. This shape factor is available for most standard cantilevers, however there is currently no shape factor available for fast-scanning cantilevers with trapezoidal plate geometry.

Uncertainty arises from measurement of cantilever dimensions (primarily thickness and metal coatings) and the density of silicon nitride. The corrections required for cantilevers with metallic coatings are discussed in section 3.4.1.2. Considering the uncertainty associated with metallic coatings on fast-scanning cantilevers, the error on this technique is estimated to be 25-35%.

Euler beam (trapezoidal) The standard Euler beam equation is derived for rectangular cantilevers. Here, the trapezoidal form of the Euler beam equation is applied to fast-scanning cantilevers with trapezoidal plate geometry [95, 99].

$$k = \frac{E_l t^3 w_0}{4L_{tip}^3 K} \tag{3.38}$$

E_l is the effective Young's modulus for the cantilever, w_0 is the width of the base of the cantilever, L_{tip} is the length from the base to the tip and K is a trapezoidal shape correction factor. K was determined for each cantilever using figure 6.4.3 from the work of Joerres [96]. For the cantilever geometries studied in this work, the shape factor used was compared to that provided by the analytical expressions derived by Sader and White [99], which is discussed below.

Much like the Sader resonance method, the cantilever dimensions, density of silicon nitride and presence of metallic films are the primary sources of uncertainty. Corrections required for cantilevers with metallic coatings are discussed in section 3.4.1.2. Uncertainty in the Young's modulus of silicon nitride is generally greater than that of density, and although this data was unavailable from the manufacturer recent work by Ohler places the uncertainty in Young's modulus at 30% which is used as a conservative value [58]. Including the uncertainty on the Young's modulus and combining with that on the cantilever dimensions, the total uncertainty is estimated to be 40-45%.

Trapezoidal shape correction factor In order to compare the analytical formula provided by Sader and White with the shape factor used from the work of Joerres, the analytical formula was re-arranged to the form shown below. This provides the K factor determined by Joerres (shape factor) and plotting this value over the same range in the notation of Sader and White allows the two to be compared directly [99].

$$K = \frac{3\frac{w}{w_0}}{\left(\frac{w}{w_0}-1\right)^3}\left(1-\frac{w}{w_0}-\frac{\left(1-\frac{w}{w_0}\right)^2}{2\frac{w}{w_0}}+\frac{w}{w_0}Log\left[\frac{w}{w_0}\right]\right) \tag{3.39}$$

Comparing the plots, a difference of 1-2% is observed over the range used for the cantilevers in this work (0.2-0.3).

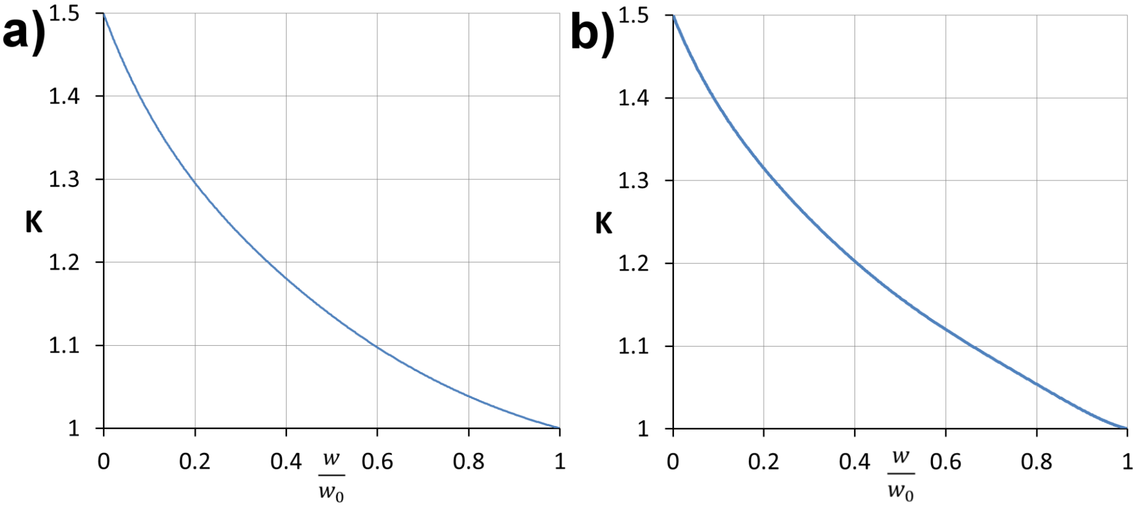

Figure 3.26: Comparison of the trapezoidal shape correction factor determined by a) Joerres and b) Sader and White. Figure a has been reprinted with permission from [96].

Euler-Sader resonance The Euler-Sader resonance formula is derived from the standard rectangular Euler beam and Sader resonance equations. These can be combined into a simple expression which eliminates the need to determine the thickness of the cantilever. This is known as the Cleveland formula [25] and has been extended to V-shaped cantilevers [20, 23].

Using equations 1.29 and 3.38, a new Euler-Sader resonance expression was derived for trapezoidal plate cantilevers, which is given below.

$$k_{end} = 496\nu^3\sqrt{\frac{\rho_l^3}{E_l}}\sqrt{\frac{K\left(nAL\right)^3}{w_o}} \tag{3.40}$$

The factor $\sqrt{\frac{\rho_l^3}{E_l}}$ was experimentally determined for each type of cantilever (FSA3, FSB2 and FSC2) by making this term the subject of the equation, and solving with a known spring constant in each case. The reference cantilever values were assumed to be accurate, and used for this purpose.

The primary advantage of this formula is that it requires only the resonant frequency and plan view dimensions of the cantilever, which can be determined using an SEM or optical microscope. The FastScan cantilevers were purchased in boxes of 10 with consecutive serial numbers, indicating they came from the same section of the batch or wafer and hence should have similar material properties between cantilevers.

This method can be considered indirect as it assumes uniformity of material properties for cantilevers located in close proximity in the same batch. The Sader and Gibson indirect methods also assume uniformity of material properties for cantilevers but use cantilevers from the same chip, which is expected to be a better assumption [14, 81]. The experimental determination of $\sqrt{\frac{\rho_l^3}{E_l}}$ introduces an error on this value of approximately 15 %; in combination with the other parameters in equation 3.40, the total uncertainty is estimated to be 20-30%.

3.4.2 Results and discussion

A total of 7 cantilevers were studied, and the spring constant determined by each technique is displayed in table 3.22 and figure 3.27 along with the associated uncertainty. The error reported is based on the propagation of uncertainty in measurements as well as that previously reported in other works [22, 26, 37, 40, 64].

Probe	Reference cantilever (±7-8%)	FIB milling (±10-25%)	Thermal noise (±20%)	Sader Hydrodynamic (±10%)	Sader resonance (±25-35%)	Euler beam (±40-45%)	Euler-Sader (±20-30%)
^{4}FSA-1	21.6	32.6	38.4	19.7	17.4	22.7	18.4
^{4}FSA-2	32.6	32.1	52	-a	33.2	33.7	41.2
^{4}FSA-3	18.7	-	30.8	18.8	17.4	20.4	-b
^{4}FSB-1	2.26	2.32	2.89	-a	1.78	2.11	2.07
^{4}FSB-2	2.07	1.75	2.86	2.18	1.59	2.18	-b
^{4}FSC-1	0.947	0.826	1.02	-a	0.819	0.891	0.939
^{4}FSC-2	0.836	0.783	1.02	0.852	0.713	0.893	-b

[a] The spring constant (ref. lever method) for these cantilevers were used to infer the spring constant for the other cantilevers of the same type.

[b] The spring constant (ref. lever method) for these cantilevers were used to calculate $\sqrt{\frac{\rho_l^3}{E_l}}$ for the other cantilevers of the same type.

Table 3.22: Spring constant of FastScan cantilevers measured by various techniques. Percentage uncertainties are quoted in brackets for each method, based on the factors discussed in the preceding section and reports in the literature.

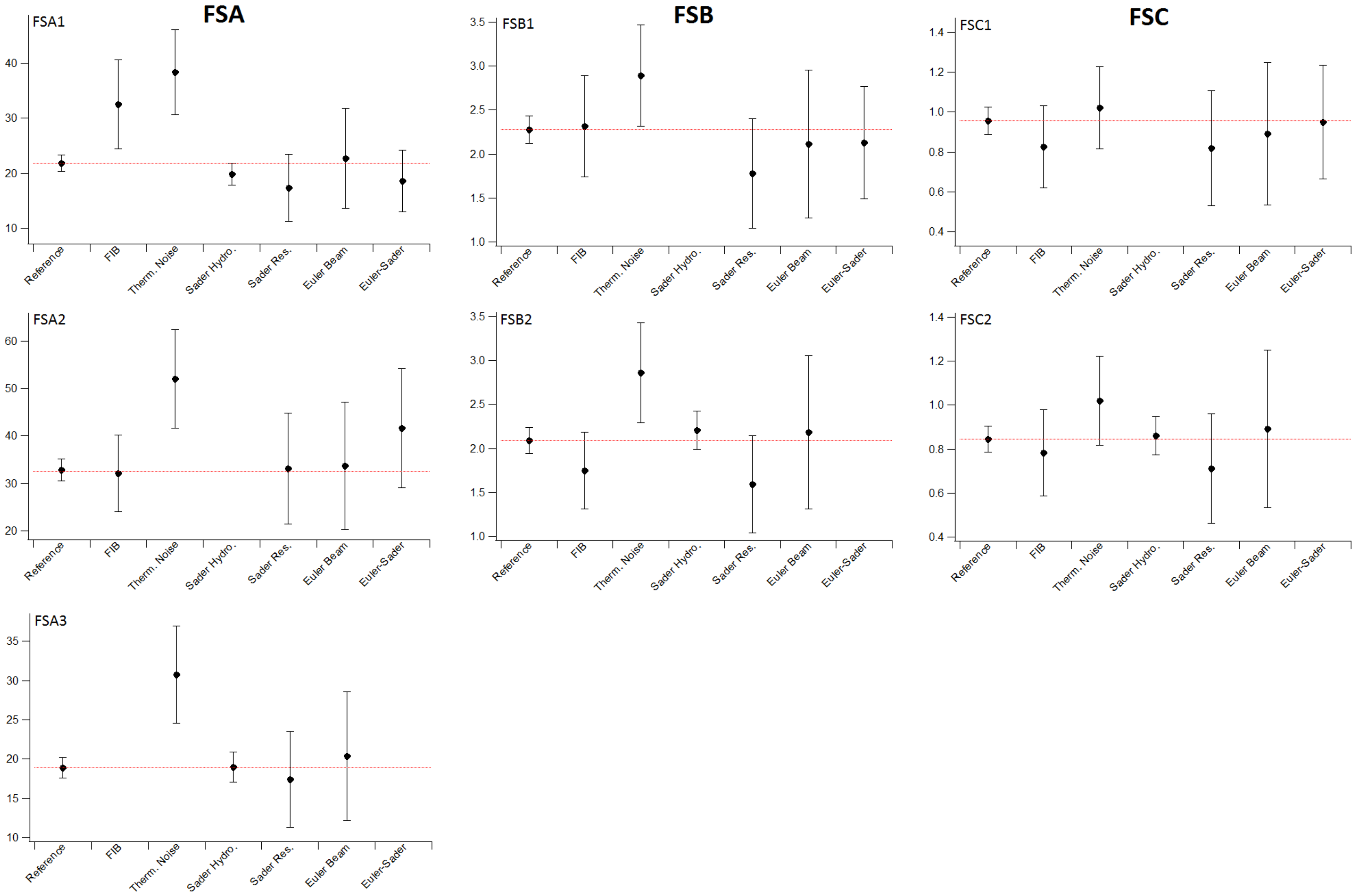

Figure 3.27: Spring constant results for each cantilever, compared to the reference cantilever benchmark method in each case. Reprinted with permission from [27].

3.4.2.1 Reference cantilever

This technique has the potential for very low uncertainty as demonstrated earlier in the chapter. Uncertainty in the technique will depend upon error on the reference cantilever (5%), the uncertainty of the technique (1-2%) and additional uncertainty related to the torque correction factor (1%). The total uncertainty of the method is hence, estimated to be 7-8%.

As a direct measurement technique, the reference cantilever method is unaffected by cantilever material properties, thus with the use of an accurately calibrated reference, this technique is considered to be a good benchmark for the other methods. The primary disadvantage of this technique is the requirement of tip-surface contact, which can be avoided by inverting the method (at the cost of small additional uncertainty) [9, 26].

3.4.2.2 FIB milling

The FIB milling method was applied to FastScan probes by milling the silicon tip instead of the silicon nitride cantilever, as can be seen in figure 3.28. This has the advantage that no mass is removed from the cantilever itself, which eliminates modification of the cantilever.

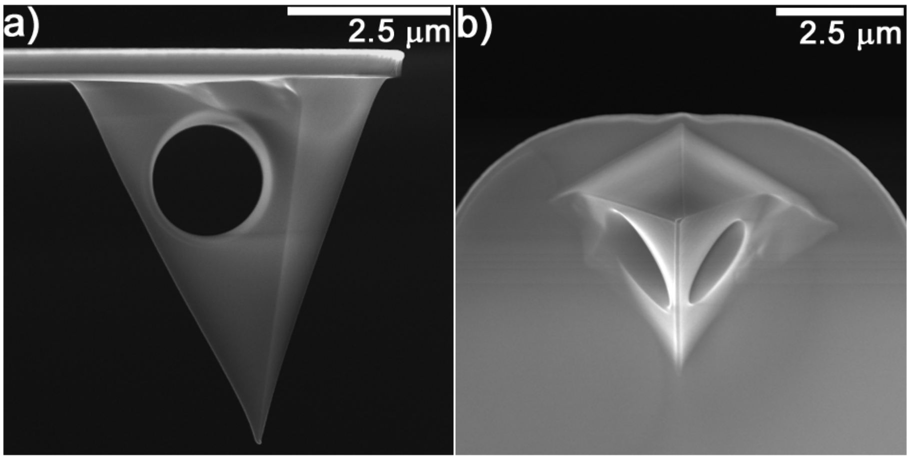

Figure 3.28: SEM images of FastScan probe tips after the milling process. Reprinted with permission from [27].

The FIB technique performs reasonably well for the larger FSB and FSC probes, while overestimating the spring constant for FSA1. This discrepancy is somewhat surprising since the high resonant frequency of the FSA probes provides improved sensitivity to the mass change. After the milling process, SEM inspection revealed material on the cantilever surfaces at the base of the imaging tips, shown in figure 3.29.

This material is expected to be silicon from the tip, redeposited during the FIB milling process. Re-deposition of milled silicon results in an overestimate of the removed mass, which then overestimates the spring constant as a result. This may explain the overestimation observed for FSA1, as the volume milled from this probe is 2.3-2.7 times smaller than that of the others. The proportion of redeposited material is thus, more significant for the FSA1 probe, resulting in a significant overestimation of the mass removed.

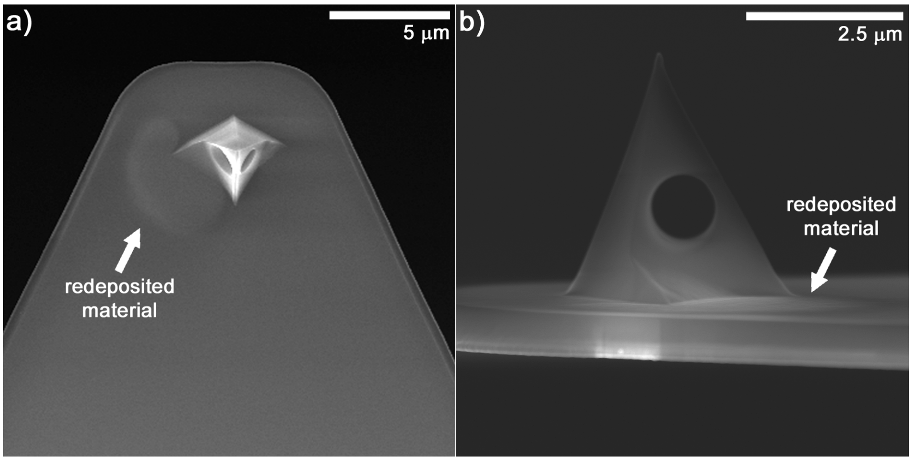

Figure 3.29: SEM images of a FSA probe after milling, the redeposited material is visible on the cantilever surface adjacent to the milled hole. Reprinted with permission from [27].

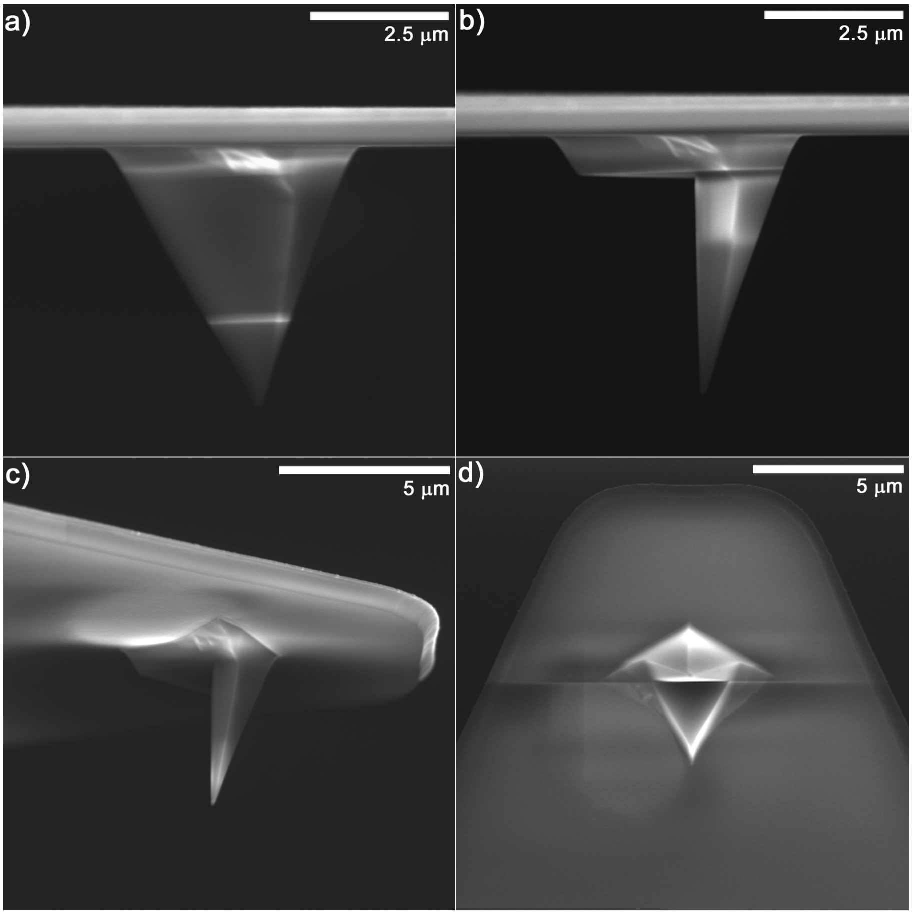

Figure 3.30: SEM images of FSA2 before a) and after b-d) milling of a pyramidal section from the tip. Reprinted with permission from [27].

This hypothesis was tested by removing a much larger volume of mass from a FSA probe, achieved by milling a pyramidal volume defined by the edges of the tip. The redeposited mass is expected to be similar for both circular and pyramidal shapes, in which case the amount of redeposition as a percentage of volume removed should be reduced, yielding better agreement with the other techniques. A pyramidal section was removed from the imaging tip on probe FSA2 and the result is shown in figure 3.30.

The milling appears to preserve the condition of the tip (already blunted by reference cantilever and thermal noise sensitivity measurements), and the cantilevers' imaging ability was also unaffected. This is demonstrated in figure 3.31, where the cantilever was used to image a CNT covered surface.

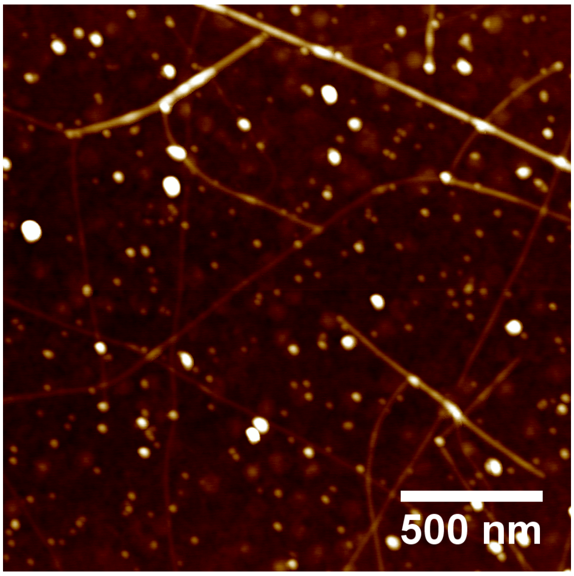

Figure 3.31: AFM image of a silicon surface with CVD grown CNTs obtained using the milled FSA2 cantilever. Reprinted with permission from [27].

The pyramidal volume removed was approximately 3.5 times that for FSA1 and very close agreement with the reference cantilever result was observed. Removing mass in this manner simplifies calculation of the volume removed, maximizes this quantity and reduces uncertainty in the volume calculation.

Given these advantages, removing a pyramidal section from the tip is the recommended approach for this method. For cantilevers FSA1, FSB1-2 and FSC1-2 uncertainty on the removed mass is estimated to be 10-15% due to modelling the complex hole shapes. Cantilever FSA2 however, is estimated to be closer to 10% or less.

Unfortunately the contribution due to re-deposited mass is unavoidable and difficult to characterise, which will raise the total uncertainty to approximately 10-25%. This uncertainty can be reduced by ensuring the removed mass is as large as possible. Details of the volume, centre of mass and uncertainty calculations can be found in section 2.2.4.

3.4.2.3 Thermal noise

The thermal noise method compares reasonably well to the reference cantilever results for the FSC cantilevers, however an overestimation of 30% is observed for the FSB cantilevers which increases to ~70% for the FSA type. The thermal method appears to break down for the smaller FastScan cantilevers, and there are a number of possible reasons for this.

There is currently no exact χ factor available for cantilevers with trapezoidal plate geometry. The χ factor used in this work was therefore assumed to be the same as for rectangular cantilevers with small adjustments depending on the dynamic to static spring constant ratio, which was calculated for each cantilever using finite element analysis (COMSOL) [103]. Using a significantly larger χ factor would reduce the calculated spring constant and improve agreement of these values. V-shaped cantilevers have a relatively high χ factor of 1.14 and an increase of 30-40% in this value would be required to account for the discrepancy. While an increase of this magnitude might seem unlikely, it has been shown recently that the χ factor for triangular cantilevers could extend to this range [65].

Another possible explanation for this discrepancy is related to the magnitude of the cantilevers' thermal noise. The thermal noise decreases with increasing cantilever stiffness, and a number of groups have reported that the thermal noise method tends to overestimate the spring constant for relatively stiff cantilevers ($k > 1$ Nm^{-1}) [40, 64]. Ohler attributed this to the reduced signal-to-noise ratio observed when measuring the thermal noise spectrum of these cantilevers [64].

Further adding to this effect is the fact that fast-scanning probes are designed to minimise their thermal noise. Manufacturers often achieve this by reducing the mass of the cantilever. The effect of reducing the cantilever size/mass for each type of FastScan probe, on their respective thermal noise spectrum is evident in figure 3.32.

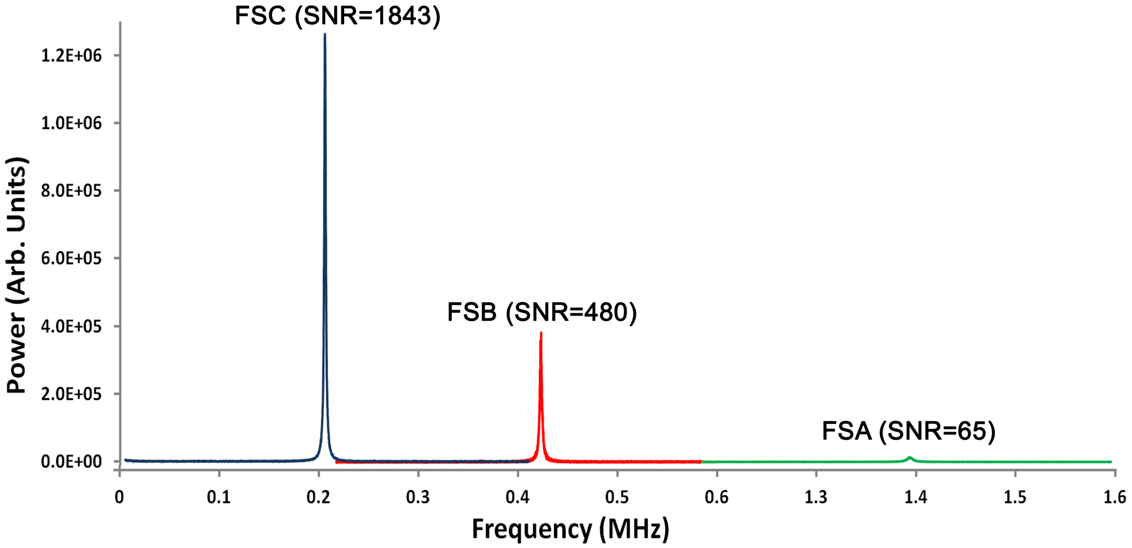

Figure 3.32: Thermal noise spectra and calculated signal-to-noise ratio for each type of FastScan probe (FSA2, FSB2 and FSC2). Reprinted with permission from [27].

It is obvious that the thermal noise is reduced significantly for the probes with lower mass (ie. FSA). The signal to noise ratio (SNR) is determined by taking the ratio of the signal peak magnitude to the standard deviation of the baseline noise. This is represented in equation 3.41, where μ is the mean value of the signal and σ is the standard deviation of the noise. In each case, a 400 kHz window around the resonance peak was used. The spectrum was background subtracted using a linear fit, and then the peak height and standard deviation of the baseline obtained.

$$SNR = \frac{\mu}{\sigma} \tag{3.41}$$

The SNR was measured to be lowest for the FSA type probe, almost 7.5 times smaller than the next larger FastScan cantilever. The FSC cantilever seemingly has a reasonable thermal noise profile, however the spring constant is still overestimated to a very small extent. With this consideration, it is most likely that the poor performance of the thermal noise method is due to a combination of the poor SNR and also the lack of appropriate χ factors.

A primary aim for cantilever manufacturers is to maintain the cantilever spring constant while minimizing the thermal noise, as this would otherwise limit the scan speed and force resolution. This poses a challenge for the thermal noise method, as one would expect the uncertainty to degrade further as cantilever thermal noise continues to be reduced.

This may be addressed by incorporating more sensitive methods of detecting cantilever deflection, which can be made available to AFM users. The use of interferometric methods to improve the detection of miniaturised cantilevers has been described previously, and may offer a convenient solution if incorporated into commercial instruments [104, 105]. If laser Doppler vibrometry is available (along with accurate χ factors) then the thermal noise method could be applied accurately to small cantilevers, although this is not a standard piece of equipment for many laboratories [64, 106].

3.4.2.4 Sader hydrodynamic (arbitrary shapes)

This method gives very good agreement for cantilevers FSA1, FSA3, FSB1 and FSC1. This is due to the method being applicable to all cantilever types, regardless of geometry and coatings [41, 107]. While accurate calibration of a reference cantilever is necessary, this method is subsequently very simple to apply. The primary source of error on the method is associated with the standard cantilever, which could be further minimised using LDV thermal calibration [41]. Given its ease of use, non-destructiveness and relatively low uncertainty, this technique is considered an excellent choice for FastScan cantilevers once accurate reference cantilevers are available.

3.4.2.5 Sader resonance

To ensure accurate application of this method, shape factors for the FastScan cantilever trapezoidal plate geometry were calculated using finite element analysis (COMSOL) [103]. The Sader resonance method performs reasonably well for all the cantilevers studied. Compared to the reference cantilever method, the FSA cantilevers vary by +5% to -20% while for the FSB and FSC cantilevers the technique consistently underestimates by -24% to -14%; however it should be noted that this variation is within the estimated experimental uncertainty.

There are several possible reasons for this discrepancy within the technique. The thickness of the FSB and FSC probes is approximately 400 nm, almost 50% smaller than the FSA cantilevers. Accurate thickness measurement becomes increasingly difficult as the cantilever gets thinner, while the gold coating significantly complicates calculation of the cantilevers' average density. An underestimation of the gold coating thickness could also account for lower spring constant values obtained for the FSB and FSC probes.

3.4.2.6 Euler beam (trapezoidal)

This technique gives very good agreement to other methods within experimental error. This suggests that the Young's modulus provided by the manufacturer is a good approximation for the cantilevers used. It is also important to note that the Young's modulus for the metal coatings on the cantilevers resulted in a decrease of 10-15% in the cantilevers' average Young's modulus. The Young's modulus for aluminium is 69 GPa and for gold is 79 GPa which is 2.5-3 times smaller than the Young's modulus quoted by the manufacturer for silicon nitride. Although still significant, this means that errors in the thickness of the metal coatings will not be as substantial as for the Sader resonance method, where density differences between gold and silicon nitride are much greater [13].

Despite the good agreement, the uncertainty on the Young's modulus is at least 30%, given that the manufacturer does not provide an uncertainty. The thickness can be determined to an uncertainty of 2-3% with an experienced SEM operator and a sufficiently advanced SEM; this contributes 6-10% error since the thickness is a cubed quantity in equation 3.38. Uncertainty in metal coating thickness and in the measurement of other dimensions will also contribute uncertainty. Therefore, despite the good agreement with the reference lever method, an uncertainty on the order of 40-45% at this time is a reasonable estimate for this technique when applied to FastScan cantilevers.

3.4.2.7 Euler-Sader resonance

This technique does not require the cantilever thickness, but instead the main uncertainty arises from the $\sqrt{\frac{\rho_l^3}{E_l}}$ term. Much like the Euler beam method, the agreement between this method and the other techniques is very good except for FSA2. The spring constant of cantilever FSA2 is somewhat larger in value when compared to the reference cantilever measurement, but still falls within experimental error. A reason for this discrepancy is that cantilever FSA2 was not from the same batch as FSA1 and FSA3 and therefore may have slightly different material properties. However, this method is still appropriate for users who do not have access to advanced FIB and SEM facilities, since this technique can still provide a good approximation for the spring constant.

3.4.2.8 Tip preservation

As discussed previously, an important consideration for each method is how potentially destructive the technique is to the imaging tip. As seen in preceding sections, for static and thermal methods such as the reference cantilever and thermal noise techniques, tip contact with a hard surface for deflection sensitivity measurement can cause significant damage. This is especially problematic for tips functionalised by specific molecules [73], antibodies [108, 109] or carbon nanotubes [110, 111]. Theoretical approaches such as the Euler beam method, and dynamic techniques like the thermal noise and Sader hydrodynamic methods require no tip-sample contact and therefore offer a clear advantage in this regard for many users.

3.4.3 Summary

The calibration of conventional AFM cantilevers has long been challenging and is an ongoing field of research. For the next generation of AFM probes, which are an order of magnitude smaller and with resonant frequencies in the MHz range, spring constant calibration continues to be a challenge. Several state-of-the-art techniques were tested, and advantages, disadvantages and limitations were identified for each method in relation to these new cantilevers.

Modifications to some existing techniques were developed and a variation of the FIB-milling method was introduced, where mass is removed from the tip instead of the cantilever; this extends the method to the increasingly prevalent hybrid Si/SiN probes. Accurate calibration of this new generation of probes was demonstrated, although a number of different methods should be in a researcher's repertoire in order to cover the various types of fast-scanning cantilevers - especially if maintaining tip quality is critical.

Reference cantilever methods offer very good accuracy, provided the technique is performed to minimise uncertainty. The reference cantilever method was used as the benchmark technique in this work.

The thermal noise method was found to generally overestimate the spring constant, with the effect worsening for smaller cantilevers. This was attributed to a combination of inaccurate knowledge of the Chi factor for trapezoidal cantilevers, and low SNR of the thermal noise spectrum, a consequence of their reduced mass and high resonant frequency.

The FIB method is found to be effective as long as the mass removed from the tip is accurately determined and as large as possible. The geometry of the hole is recommended to be pyramidal in shape, which simplifies volume calculation and minimises uncertainty associated with redeposited material. This method requires a sufficient quantity of material with accurately-known density, which may prove problematic for extremely small silicon nitride cantilevers incorporating diamond-like carbon tips (eg. NanoWorld USC). With careful application, the method has the potential to be limited only by the uncertainty of the mass removed. Further advances in this technique may allow the mass change to be monitored accurately and directly [106]. Accurate monitoring of the mass change, independent of material density could allow allow any cantilever to be calibrated with uncertainty well below 10%.

The Sader resonance, Euler beam and Euler-resonance methods all provided values in agreement with the reference cantilever method, but suffered from large uncertainty due to error on material properties and/or dimensions. The possibility still exists that these methods could be more effectively applied if accurate material properties are available.

The new Sader hydrodynamic expression for arbitrary shaped cantilevers gives very good agreement and this method overall shows a great deal of promise as the technique which possesses the most sought after attributes; these are low uncertainty (10% or less), no tip-sample contact, simple implementation, cost effectiveness and applicability to all types of cantilevers.

The technique relies on accurate spring constant calibration of a standard cantilever for each geometric type, which could be achieved using reference cantilever or LDV methods. Accurate and widespread application of this technique is contingent on a study which provides a systematic calibration of a standard for each type of specific cantilever geometry, which could be made available to all AFM users. Alternatively, manufacturers could provide a single low uncertainty spring constant value for each type of probe, with plan view images along with accurately determined resonant frequency and Q factor.

This research has demonstrated that accurate spring constant calibration of small fast-scan cantilevers is possible using a variety of techniques. For research groups which do not have access to sophisticated FIB and SEM facilities, then methods such as the Sader hydrodynamic (arbitrary shape) and Euler-Sader resonance techniques can yield accurate results provided manufacturers can keep the plan view dimensions of cantilevers consistent.

In response to the results presented here, Song et al. investigated the spring constant calibration of FastScan cantilevers using an electronic balance [112]. This technique provides a direct measurement in a similar manner to the reference cantilever method, and the uncertainty reported was very low at 2%. This technique is very effective for fast-scanning cantilevers, however it does suffer from the issue of potential tip damage and also the requirement of a dedicated calibration instrument.

The focus of this work has been primarily on FastScan cantilevers, which are larger than their video-rate counterparts. However, as instrumentation and cantilever design develops, it is likely that cantilevers will further reduce in size and video rate AFM will become routine. Cantilevers with size in the sub-10 μm region will continue to push the limits of current calibration techniques, in particular the thermal noise method will struggle as the mass of these cantilevers continues to reduce. In the case where material properties and shape factors are well defined, geometric methods can potentially provide acceptable uncertainty. Direct measurement techniques such as the reference cantilever method should continue to serve as a benchmark, which can provide low uncertainty regardless of cantilever dimensions, geometry or composition.

Bibliography - Chapter 3

[1] Christopher T Gibson, Gregory S Watson, and Sverre Myhra. *Nanotechnology* 7.3 (1999), pp. 259–262. DOI: `10.1088/0957-4484/7/3/014`.

[2] Charles A Clifford and Martin P Seah. *Measurement Science and Technology* 20.12 (2009), p. 125501. DOI: `10.1088/0957-0233/20/12/125501`.

[3] Peter J Cumpson, Charles a Clifford, and John Hedley. *Measurement Science and Technology* 15.7 (2004), pp. 1337–1346. DOI: `10.1088/0957-0233/15/7/016`.

[4] Peter J Cumpson and John Hedley. *Nanotechnology* 14.12 (2003), pp. 1279–88. DOI: `10.1088/0957-4484/14/12/009`.

[5] Peter J. Cumpson et al. *Journal of Vacuum Science & Technology A: Vacuum, Surfaces, and Films* 22.4 (2004), p. 1444. DOI: `10.1116/1.1763898`.

[6] Peter J Cumpson, John Hedley, and Peter Zhdan. *Nanotechnology* 14.8 (2003), pp. 918–924. DOI: `10.1088/0957-4484/14/8/314`.

[7] P J Peter J Cumpson, Peter Zhdan, and John Hedley. *Ultramicroscopy* 100.3-4 (2004), pp. 241–51. DOI: `10.1016/j.ultramic.2003.10.005`.

[8] Richard S Gates and Jon R Pratt. *Measurement Science and Technology* 17.10 (2006), pp. 2852–2860. DOI: `10.1088/0957-0233/17/10/041`.

[9] Richard S Gates and Mark G Reitsma. *The Review of scientific instruments* 78.8 (2007), p. 086101. DOI: `10.1063/1.2764372`.

[10] Akihiro Torii et al. *Measurement Science and Technology* 7.2 (1996), pp. 179–184. DOI: `10.1088/0957-0233/7/2/010`.

[11] C.J. Drummond and T.J. Senden. *Materials Science Forum* 189-190 (1995), pp. 107–114. DOI: `10.4028/www.scientific.net/MSF.189-190.107`.

[12] Christopher T. Gibson et al. *Review of Scientific Instruments* 72.5 (2001), p. 2340. DOI: `10.1063/1.1361080`.

[13] John E. Sader et al. *Review of Scientific Instruments* 66.7 (1995), p. 3789. DOI: `10.1063/1.1145439`.

[14] John E Sader, James W M Chon, and Paul Mulvaney. *Review of Scientific Instruments* 70.10 (1999), pp. 3967–3969. DOI: `10.1063/1.1150021`.

[15] Charles a Clifford and Martin P Seah. *Nanotechnology* 16.9 (2005), pp. 1666–1680. DOI: `10.1088/0957-4484/16/9/044`.

[16] Jeffrey L. Hutter and John Bechhoefer. *Review of Scientific Instruments* 64.7 (1993), p. 1868. DOI: `10.1063/1.1143970`.

[17] S M Cook et al. *Nanotechnology* 17.9 (2006), pp. 2135–2145. DOI: `10.1088/0957-4484/17/9/010`.

[18] R Proksch et al. *Nanotechnology* 15.9 (2004), pp. 1344–1350. DOI: `10.1088/0957-4484/15/9/039`.

[19] Robert W. Stark, Tanja Drobek, and Wolfgang M. Heckl. *Ultramicroscopy* 86.1-2 (2001), pp. 207–215. DOI: `10.1016/S0304-3991(00)00077-2`.

[20] John E Sader, James W M Chon, and Paul Mulvaney. *Review of Scientific Instruments* 70.10 (1999), pp. 3967–3969. DOI: `10.1063/1.1150021`.

[21] Ashley D. Slattery, Christopher. T. Gibson, and Jamie. S. Quinton. *2010 International Conference on Nanoscience and Nanotechnology*. 2010, pp. 407–410. DOI: `10.1109/ICONN.2010.6045265`.

[22] Ashley D Slattery, Jamie S Quinton, and Christopher T Gibson. *Nanotechnology* 23.28 (2012), p. 285704. DOI: `10.1088/0957-4484/23/28/285704`.

[23] John Elie Sader. *Review of Scientific Instruments* 66.9 (1995), pp. 4583–4587. DOI: `10.1063/1.1145292`.

[24] Mark a Poggi et al. *Analytical Chemistry* 77.4 (2005), pp. 1192–1195. DOI: `10.1021/ac048828h`.

[25] J. P. Cleveland et al. *Review of Scientific Instruments* 64.2 (1993), p. 403. DOI: `10.1063/1.1144209`.

[26] Ashley D Slattery et al. *Nanotechnology* 24.1 (2013), p. 015710. DOI: `10.1088/0957-4484/24/1/015710`.

[27] Ashley D. Slattery et al. *Nanotechnology* 25.33 (2014), p. 335705. DOI: `10.1088/0957-4484/25/33/335705`.

[28] Ashley D. Slattery et al. *Ultramicroscopy* 131 (2013), pp. 46–55. DOI: `10.1016/j.ultramic.2013.03.009`.

[29] Vinzenz Friedli et al. *Applied Physics Letters* 90.5 (2007), p. 053106. DOI: `10.1063/1.2435611`.

[30] M. Woszczyna et al. *Microelectronic Engineering* 86.4-6 (2009), pp. 1043–1045. DOI: `10.1016/j.mee.2009.01.082`.

[31] Wen-Hsien Chuang et al. *MRS Proceedings*. Vol. 782. 2011, A5.21. DOI: `10.1557/PROC-782-A5.21`.

[32] M A Lantz et al. *Science (New York, N.Y.)* 291.5513 (2001), pp. 2580–3. DOI: `10.1126/science.1057824`.

[33] Gursel Alici and Michael J Higgins. *Smart Materials and Structures* 18.6 (2009), p. 065013. DOI: `10.1088/0964-1726/18/6/065013`.

[34] Dorothee Almecija et al. *Carbon* 47.9 (2009), pp. 2253–2258. DOI: `10.1016/j.carbon.2009.04.022`.

[35] C. T. Gibson et al. *Textile Research Journal* 71.7 (2001), pp. 573–581. DOI: `10.1177/004051750107100702`.

[36] R Garcia. *Surface Science Reports* 47.6-8 (2002), pp. 197–301. DOI: `10.1016/S0167-5729(02)00077-8`.

[37] Joost te Riet et al. *Ultramicroscopy* 111.12 (2011), pp. 1659–69. DOI: `10.1016/j.ultramic.2011.09.012`.

[38] Richard S Gates et al. *Journal of Research of the National Institute of Standards and Technology* 116.4 (2011), p. 703. DOI: `10.6028/jres.116.015`.

[39] Christopher T. Gibson, Gregory S. Watson, and Sverre Myhra. *Wear* 213.1-2 (1997), pp. 72–79. DOI: `10.1016/S0043-1648(97)00175-0`.

[40] Manuel L. B. Palacio and Bharat Bhushan. *Critical Reviews in Solid State and Materials Sciences* 35.2 (2010), pp. 73–104. DOI: `10.1080/10408430903546691`.

[41] John E Sader et al. *The Review of scientific instruments* 83.10 (2012), p. 103705. DOI: `10.1063/1.4757398`.

[42] Hendrik Frentrup and Matthew S Allen. *Nanotechnology* 22.29 (2011), p. 295703. DOI: `10.1088/0957-4484/22/29/295703`.

[43] Christopher P. Green et al. *Review of Scientific Instruments* 75.6 (2004), p. 1988. DOI: `10.1063/1.1753100`.

[44] Dmytro S Golovko et al. *The Review of scientific instruments* 78.4 (2007), p. 043705. DOI: `10.1063/1.2720727`.

[45] Lingyan Li, Qiuming Yu, and Shaoyi Jiang. *The Journal of Physical Chemistry B* 103.39 (1999), pp. 8290–8295. DOI: `10.1021/jp990645p`.

[46] Sy-Hann Chen, Heh-Nan Lin, and Pang-Ming Ong. *Review of Scientific Instruments* 71.10 (2000), p. 3788. DOI: `10.1063/1.1290503`.

[47] Hui Xie et al. *Journal of Micro-Nano Mechatronics* 4.1-2 (2008), pp. 17–25. DOI: `10.1007/s12213-008-0005-y`.

[48] J. Sidles et al. *Reviews of Modern Physics* 67.1 (1995), pp. 249–265. DOI: `10.1103/RevModPhys.67.249`.

[49] J. Kokavecz and a. Mechler. *Physical Review B* 78.17 (2008), pp. 1–4. DOI: `10.1103/PhysRevB.78.172101`.

[50] John Melcher, Shuiqing Hu, and Arvind Raman. *Applied Physics Letters* 91.5 (2007), p. 053101. DOI: `10.1063/1.2767173`.

[51] Georg Hähner. *Ultramicroscopy* 110.7 (2010), pp. 801–6. DOI: `10.1016/j.ultramic.2010.02.008`.

[52] Paul R. Wilkinson et al. *Journal of Applied Physics* 104.10 (2008), p. 103527. DOI: `10.1063/1.3018944`.

[53] Alex R. Hodges, Konrad M. Bussmann, and Jan H. Hoh. *Review of Scientific Instruments* 72.10 (2001), p. 3880. DOI: `10.1063/1.1405799`.

[54] You Wang and Xinyong Chen. *Ultramicroscopy* 107.4-5 (2007), pp. 293–8. DOI: `10.1016/j.ultramic.2006.08.004`.

[55] JCGM. Tech. rep. JCGM 100, 2008.

[56] Kenichi Fujii, Atsushi Waseda, and Naoki Kuramoto. *Technology* 12 (2001), pp. 2031–2038. DOI: `10.1088/0957-0233/12/12/302`.

[57] A. Khan. *Journal of Applied Physics* 95.4 (2004), p. 1667. DOI: `10.1063/1.1638886`.

[58] Benjamin Ohler. Tech. rep. Bruker, 2007, pp. 1–12.

[59] Jeffrey L Hutter. *Langmuir* 21.6 (2005), pp. 2630–2632. DOI: `10.1021/la047670t`.

[60] Ferdinand Walther, Wolfgang M. Heckl, and Robert W. Stark. *Applied Surface Science* 254.22 (2008), pp. 7290–7295. DOI: `10.1016/j.apsusc.2008.05.323`.

[61] Martin Munz et al. *Surface and Interface Analysis* 43.11 (2011), pp. 1382–1391. DOI: `10.1002/sia.3727`.

[62] Zhongfan Liu et al. *Advanced Materials* 22.21 (2010), pp. 2285–2310. DOI: `10.1002/adma.200904167`.

[63] Mahdi Farshchi-Tabrizia, Michael Kappl, and Hans-Jürgen Butt. *Journal of Adhesion Science and Technology* 22.2 (2008), pp. 181–203. DOI: `10.1163/156856108X306948`.

[64] Benjamin Ohler. *The Review of scientific instruments* 78.6 (2007), p. 063701. DOI: `10.1063/1.2743272`.

[65] John E. Sader, Jianing Lu, and Paul Mulvaney. *Review of Scientific Instruments* 85.11 (2014), p. 113702. DOI: `10.1063/1.4900864`.

[66] Ivan U Vakarelski et al. *Langmuir : the ACS journal of surfaces and colloids* 23.22 (2007), pp. 10893–6. DOI: `10.1021/la701878n`.

[67] M. Wendel, H. Lorenz, and J. P. Kotthaus. *Applied Physics Letters* 67.25 (1995), p. 3732. DOI: `10.1063/1.115365`.

[68] I-Chen Chen et al. *Nanotechnology* 17.17 (2006), pp. 4322–4326. DOI: `10.1088/0957-4484/17/17/007`.

[69] J D Beard and S N Gordeev. *Nanotechnology* 21.47 (2010), p. 475702. DOI: `10.1088/0957-4484/21/47/475702`.

[70] H Butt, B Cappella, and M Kappl. *Surface Science Reports* 59.1-6 (2005), pp. 1–152. DOI: `10.1016/j.surfrep.2005.08.003`.

[71] J Liu et al. *Small (Weinheim an der Bergstrasse, Germany)* 6.10 (2010), pp. 1140–9. DOI: `10.1002/smll.200901673`.

[72] Christopher T Gibson, Stewart Carnally, and Clive J Roberts. *Ultramicroscopy* 107.10-11 (2007), pp. 1118–22. DOI: `10.1016/j.ultramic.2007.02.045`.

[73] Mrinal Mahapatro et al. *Ultramicroscopy* 97.1-4 (2003), pp. 297–301. DOI: `10.1016/S0304-3991(03)00055-X`.

[74] Christopher J Tourek and Sriram Sundararajan. *The Review of scientific instruments* 81.7 (2010), p. 073711. DOI: `10.1063/1.3459886`.

[75] Marco Tortonese and Michael Kirk. *SPIE 3009, Micromachining and Imaging.* 1997, pp. 53–60. DOI: `10.1117/12.271229`.

[76] M. J. Higgins et al. *Review of Scientific Instruments* 77.1 (2006), p. 013701. DOI: `10.1063/1.2162455`.

[77] John E. Sader, Morteza Yousefi, and James R. Friend. *Review of Scientific Instruments* 85.2 (2014), pp. 1–5. DOI: `10.1063/1.4864086`.

[78] Richard S Gates and Jon R Pratt. *Nanotechnology* 23.37 (2012), p. 375702. DOI: `10.1088/0957-4484/23/37/375702`.

[79] Neill P. DCosta and Jan H. Hoh. *Review of Scientific Instruments* 66.10 (1995), p. 5096. DOI: `10.1063/1.1146135`.

[80] Ivan U Vakarelski et al. *The Review of scientific instruments* 78.11 (2007), p. 116102. DOI: `10.1063/1.2805518`.

[81] Christopher T. Gibson et al. *Review of Scientific Instruments* 75 (2004), pp. 565–567. DOI: `10.1063/1.1642750`.

[82] F.M Battiston et al. *Sensors and Actuators B: Chemical* 77.1-2 (2001), pp. 122–131. DOI: `10.1016/S0925-4005(01)00683-9`.

[83] Bryan D. Huey. *Annual Review of Materials Research* 37.1 (2007), pp. 351–385. DOI: `10.1146/annurev.matsci.37.052506.084331`.

[84] Takayuki Uchihashi, Toshio Ando, and Hayato Yamashita. *Applied Physics Letters* 89.21 (2006), p. 213112. DOI: `10.1063/1.2387963`.

[85] Christoph Braunsmann et al. *Review of Scientific Instruments* 85.7 (2014), p. 073703. DOI: `10.1063/1.4885464`.

[86] D. a. Walters et al. *Review of Scientific Instruments* 67.10 (1996), p. 3583. DOI: `10.1063/1.1147177`.

[87] C. Richter et al. *Microsystem Technologies* 18.7-8 (2012), pp. 1119–1126. DOI: `10.1007/s00542-012-1454-8`.

[88] Johannes H Kindt et al. Tech. rep. Bruker Nano Surfaces Division, 2011, p. 10.

[89] Toshio Ando et al. *Pflügers Archiv : European journal of physiology* 456.1 (2008), pp. 211–25. DOI: `10.1007/s00424-007-0406-0`.

[90] Georg E Fantner et al. *Ultramicroscopy* 106.8-9 (2006), pp. 881–7. DOI: `10.1016/j.ultramic.2006.01.015`.

[91] Olympus. *Olympus Micro Cantilevers.* URL: `http://probe.olympus-global.com`.

[92] Nanoworld(AG). *High Speed Scanning with SPM.* URL: `www.highspeedscanning.com`.

[93] AppNano. *UHF Fast Scanning Series.* URL: `www.appnano.com/products/silicon/uhf`.

[94] S. Hosaka et al. *Journal of Vacuum Science & Technology B: Microelectronics and Nanometer Structures* 18.1 (2000), p. 94. DOI: `10.1116/1.591157`.

[95] Niels L. Pedersen. *Engineering Optimization* 32.3 (2000), pp. 373–392. DOI: `10.1080/03052150008941305`.

[96] Robert E Joerres. *Standard Handbook of Machine Design.* 3rd ed. 2004. Chap. 6.

[97] H. Kawakatsu et al. *Review of Scientific Instruments* 73.6 (2002), p. 2317. DOI: `10.1063/1.1480459`.

[98] Scott A. Edwards, William A. Ducker, and John E. Sader. *Journal of Applied Physics* 103.6 (2008), p. 064513. DOI: `10.1063/1.2885734`.

[99] John Elie Sader and Lee White. *Journal of Applied Physics* 74.1 (1993), pp. 1–9. DOI: `10.1063/1.354137`.

[100] John Elie Sader. *Review of Scientific Instruments* 74.4 (2003), p. 2438. DOI: `10.1063/1.1544421`.

[101] H J Butt and M Jaschke. *Nanotechnology* 6.1 (1999), pp. 1–7. DOI: `10.1088/0957-4484/6/1/001`.

[102] Richard S Gates, William A Osborn, and Jon R Pratt. *Nanotechnology* 24.25 (2013), p. 255706. DOI: `10.1088/0957-4484/24/25/255706`.

[103] John Elie Sader. *Personal communication.* 2014.

[104] B W Hoogenboom et al. *Nanotechnology* 19.38 (2008), p. 384019. DOI: `10.1088/0957-4484/19/38/384019`.

[105] B. W. Hoogenboom et al. *Applied Physics Letters* 86.7 (2005), p. 074101. DOI: `10.1063/1.1866229`.

[106] Peter J. Cumpson et al. *Journal of Applied Physics* 114.12 (2013), p. 124313. DOI: `10.1063/1.4823815`.

[107] O Ergincan, G Palasantzas, and B J Kooi. *The Review of scientific instruments* 85.2 (2014), p. 026118. DOI: `10.1063/1.4864195`.

[108] Rhiannon Creasey et al. *Biophysical journal* 99.5 (2010), pp. 1660–7. DOI: `10.1016/j.bpj.2010.06.044`.

[109] Rhiannon Creasey et al. *Ultramicroscopy* 111.8 (2011), pp. 1055–61. DOI: `10.1016/j.ultramic.2011.03.008`.

[110] Ashley D Slattery et al. *Nanotechnology* 24.23 (2013), p. 235705. DOI: `10.1088/0957-4484/24/23/235705`.

[111] C T Gibson et al. *Environmental Science and Technology* 41.4 (2007), pp. 1339–1344. DOI: `10.1021/es061726j`.

[112] Yun-Peng Song et al. *Measurement Science and Technology* 26.6 (2015), p. 065001. DOI: `10.1088/0957-0233/26/6/065001`.

Chapter 4

Fabrication of CNT AFM Probes

4.1 Chemical vapour deposition

CVD is one of the main methods by which CNTs are grown, and the direct growth of CNTs onto an AFM tip has been reported in the literature using various approaches [1, 2]. For the work presented in the following chapter, a plentiful supply of CNT probes was required and so batch production was investigated using the CVD growth method.

There has been much development in the CVD growth of CNTs, however there are still areas of the process which are not completely understood, the growth mechanism is complex and the optimal growth parameters vary between systems with many variables. The system used in this work is shown schematically in figure 4.1 and is comprised of a tube furnace containing a quartz tube, which holds the CNT growth substrate over which the reactant gases flow at high temperature. The density of CNTs on the surface is an important factor in maximising the chances of obtaining a useful CNT probe [3], and so growth was initially performed on flat silicon to determine the ideal growth conditions.

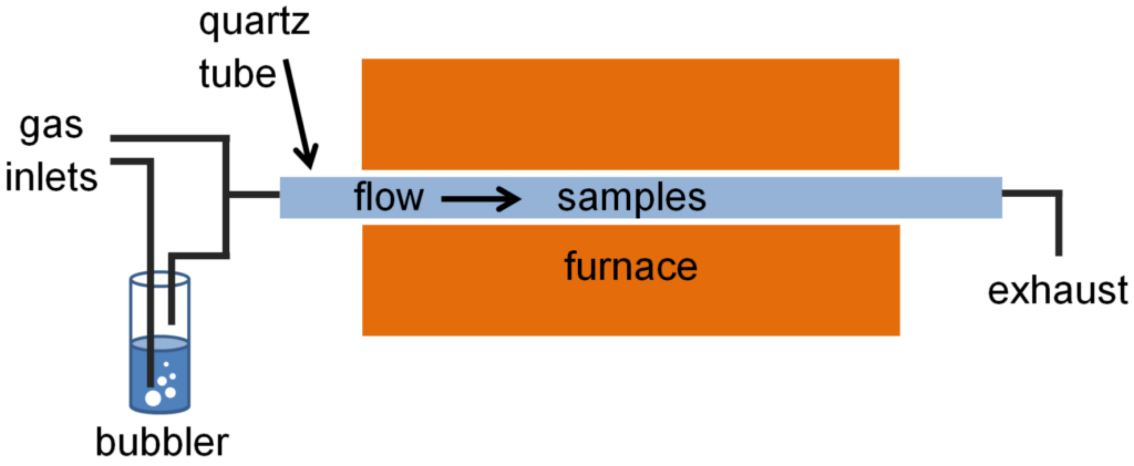

Figure 4.1: Schematic of the CVD system used in this work.

4.1.1 MWCNT growth

Many variables can be altered to affect the growth of the CNTs. In this study the primary variables were the carbon feedstock (acetylene, ethanol) and the catalyst deposition method (solution, sputtering). Acetylene was used initially along with a sputtered iron film catalyst, as this was an established process for MWCNT forest growth where a thick (5 nm) iron film was used with high acetylene content to promote rapid growth [4]. Water is introduced into the chamber using a bubbler as shown in figure 4.1; the concentration of water vapour is a key ingredient in obtaining successful growth [5]. This was found to be especially important when using acetylene as the carbon feedstock, as too much water would result in no CNT growth whilst too little would produce large quantities of carbonaceous soot.

MWCNT growth was readily achieved by this process, however the density of CNTs is far too high for application to AFM probes as shown in figure 4.2.

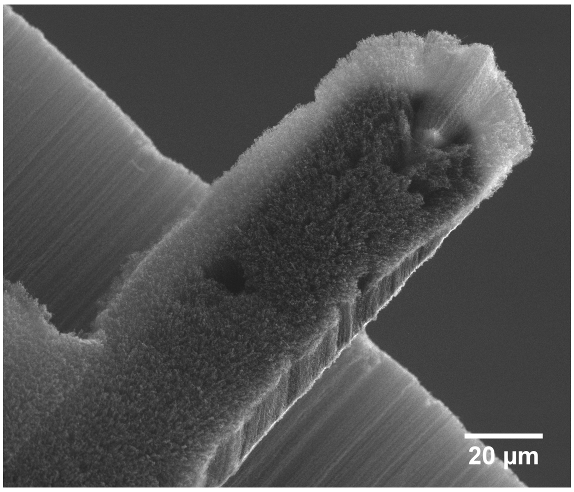

Figure 4.2: SEM image of a tapping mode cantilever with high-density MWNTs grown on the surface (the imaging tip is facing upwards).

4.1.2 SWCNT growth

In order to reduce CNT density, the size and density of the catalyst particles was reduced, and ethanol was used instead as the carbon feedstock. Reduction of the catalyst size should promote the growth of SWCNTs [6, 7], and lower catalyst density should avoid vertically-aligned forest growth. The catalyst was deposited from solution using the approach of Choi et al. where iron nanoparticles are grown directly onto the surface [8]. These nanoparticles are expected to have a narrower size distribution when compared to those in a sputtered film, and have much lower density than a complete film. AFM analysis of the surface after nanoparticle deposition is shown with a corresponding cross section in figures 4.3a and b, and the surface after CVD growth is shown in figure 4.3c.

The majority of the nanoparticles appear to have sizes from 1-2 nm and are not clustered together, which should reduce agglomeration at high temperature. After the growth process, the density of CNTs observed in figure 4.3c is acceptable for fabricating CNT probes. Several CNTs are observed over a 500 nm area, while a typical AFM tip is several microns in size. This should offer high enough density

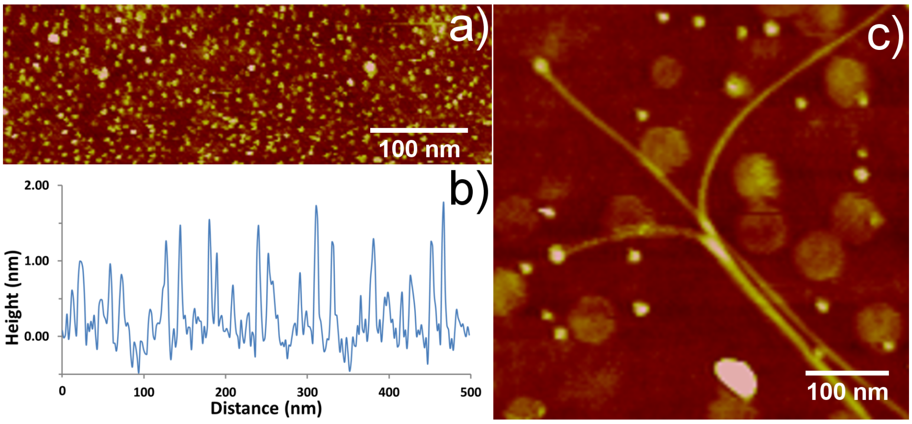

Figure 4.3: AFM images of the Si/SiO$_2$ surface after deposition of iron nanoparticle catalyst a) with the corresponding cross-section b) and the surface after CVD growth c).

such that CNTs are obtained at the tip apex, but low enough that the tip is not crowded.

Comparing the AFM images (which are at the same magnification), the density of nanoparticles certainly seems to have reduced after growth, suggesting that agglomeration has occurred to some extent. Additionally, some nanoparticles have not grown any CNTs which is expected as the catalytic efficiency for CNT growth is usually well below 100%. This is actually beneficial in this case, as growth from every nanoparticle seen in figure 4.3a would result in CNT density which is too high for successful growth on AFM probes.

4.1.3 Growth on AFM tips

Catalyst deposition was performed on AFM cantilevers by immersing the entire chip in the deposition solution; the cantilevers were then placed in the CVD furnace and CNT growth was performed using the same conditions established previously. CNT growth on the cantilevers was successful, as evidenced by SEM imaging, however the growth of a CNT specifically at the imaging tip was rarely observed. In most cases there were simply no CNTs observed at the tip, while in others a looped CNT was observed where the nanotube had presumably grown too long and reattached to the tip as shown in figure 4.4.

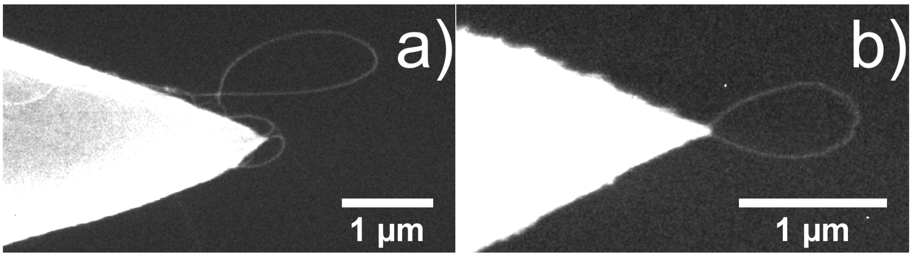

Figure 4.4: SEM image of an AFM tip after CVD growth, showing looped CNTs.

There were, however, some successful CNT tips obtained by this method which are shown in figure 4.5. These tips had CNTs protruding with good alignment and length, which should be ideal for imaging.

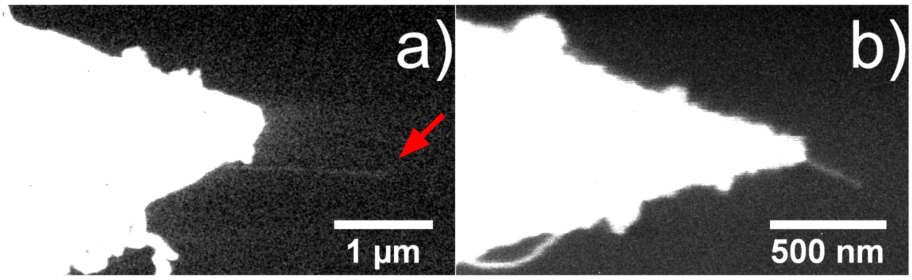

Figure 4.5: SEM image of an AFM tip after CVD growth, showing the presence of straight CNTs.

Despite the seemingly ideal orientation of the tips in figure 4.5, achieving stable imaging feedback with these probes proved to be very difficult. Image traces consistently showed sawtooth-shaped oscillations, suggesting that the tip was experiencing very large adhesion; this could be explained by buckling of the CNT such that it contacts along the sidewall. These probes were re-engaged softly several times in order to obtain stable feedback, but eventually reverted to stable, low-resolution images.

Figure 4.6 shows the AFM image obtained using the seemingly ideal CNT probe from figure 4.5b, but after several attempts at achieving stable feedback. The AFM image shown was eventually obtained, however SEM imaging confirmed that the CNT had detached. This was observed a number of times with other tips which were seemingly well-aligned, suggesting that the CNT is poorly adhered to the tip.

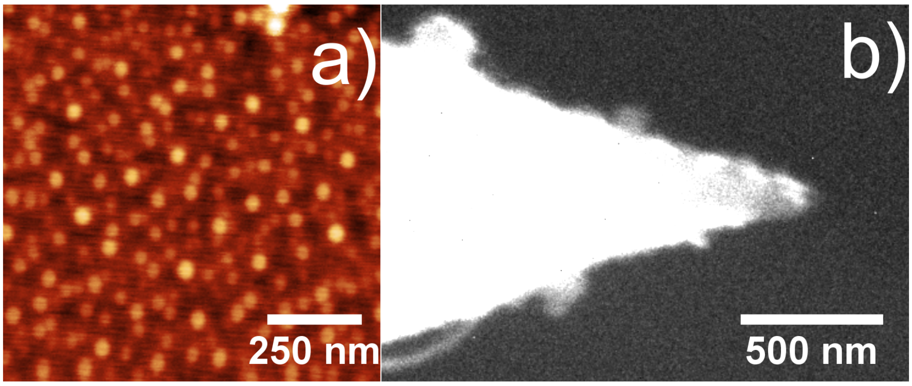

Figure 4.6: AFM image a) obtained using the CNT probe shown in figure 4.5b, after a number of unstable images. Figure b) shows an SEM image of the probe, confirming that the CNT had detached.

The CVD method, while holding great promise for extremely sharp single CNTs, proved to generate a very low yield of “ideal” CNT tips. Process optimisation such as that by Edgeworth et al. [3] can clearly improve the yield of well-aligned CNTs, however the usablility of these probes is a further challenge which hinders this fabrication process. Factors such as the length and adhesion of these CNTs serves to further reduce the number of usable probes.

4.2 Solution-based deposition

The attachment of single-walled carbon nanotube (SWCNT) fibres to AFM tips is demonstrated using two different solution-based deposition techniques. One of the techniques used is dielectrophoretic (DEP) assembly, and the basis of this approach is described in section 1.3.1.1. DEP assembly has been used by several groups to attach CNTs onto sharpened tungsten and AFM tips, as the application of a heterogeneous alternating current between two electrodes immersed in a CNT solution results in the growth of a long CNT fibre [9, 10].

The other approach used is a simple evaporation technique, which is yet to be reported for CNTs. Evaporation of the meniscus of a CNT solution over a sharp tip was found to deposit a CNT fibre, resembling that produced by DEP. This technique was used to attach short, well-aligned fibres to atomic force microscope (AFM) probes by utilising the snap-off effect observed when the meniscus recedes over the tip. A similar approach was used by Ondarcuhu and Joachim to draw gold nanoparticle fibres up to 1 mm in length and with diameter of 2-100 nm [11]. The work presented here builds on this by extending the technique to SWCNT solutions.

4.2.1 Dielectrophoresis

The AFM tip was aligned as shown in figure 4.7, where the tip is brought to within 50 μm of a silicon wafer using an optical microscope and a unidirectional microtranslator. A droplet of CNT solution was then placed to completely immerse the tip, and a bias voltage applied between the gap for a certain duration. The tip was then retracted from the solution and analysed using SEM.

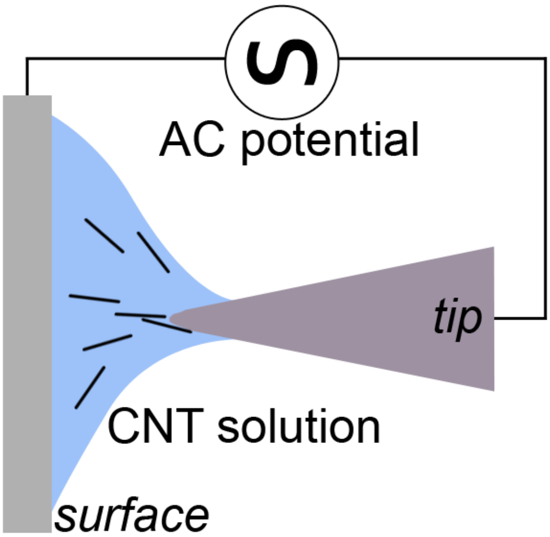

Figure 4.7: Schematic showing the assembly of CNTs from solution onto the AFM tip using dielectrophoresis.

This approach was found to deposit a long fibre on the AFM tip which tapered off to a sharp point. SEM imaging was used to inspect these probes, and the result on several tips can be seen in figure 4.8. Although the ideal scenario is a single, short CNT at the tip, the tapered structure of these thick fibres may offer enough stability to be usable.

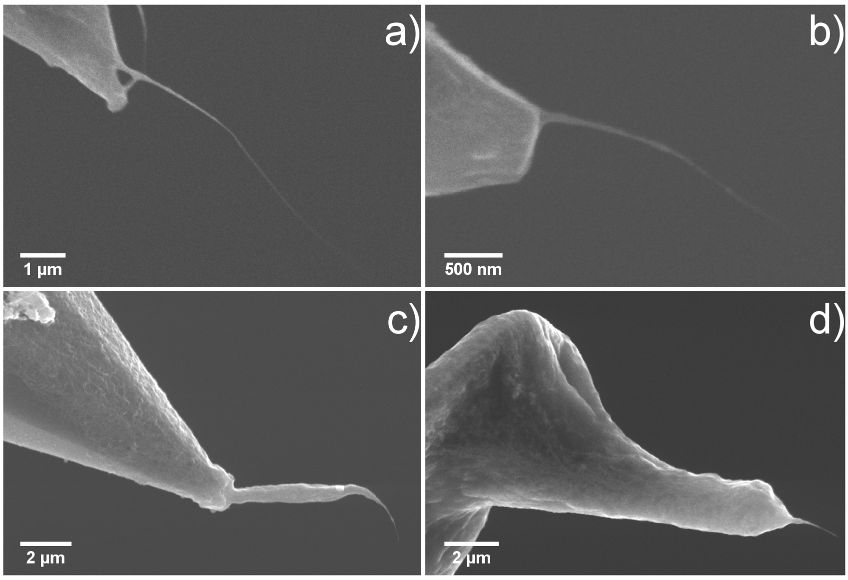

Figure 4.8: Various CNT tips fabricated by the DEP technique, a-c) are silicon tapping mode cantilevers and d) is a silicon nitride contact mode cantilever.

Unfortunately alignment of the fibre was often far from ideal, with many bending away from the tip orientation or exhibiting curvature near the end. This is likely due to a number of factors, including the alignment of the tip to the silicon surface, forces from the meniscus as the tip is removed from solution and internal stress on the fibre as the solvent dries. Occasionally, longer CNT fibres were observable by the optical microscope and these were observed to curl slightly after removal from the solution, presumably due to solvent evaporation from the fibre. Most of these factors would be difficult to avoid, although improvement of the tip alignment would be possible with a more powerful microscope and greater control over tilt and positioning.

Assessment of these probes for AFM imaging and feedback stability is reported in section 4.2.3

4.2.2 Solvent evaporation

Fibre formation was observed to occur during the DEP process, but without any applied bias. Further investigation was carried out to ensure that there was indeed no potential difference across the gap, by electrically connecting both the tip and the surface. Growth of the fibre was observed using an optical microscope as shown in figure 4.9. Etched tungsten wire was used as an ideal, sharp tip which was positioned some distance from the surface and a droplet of the SWCNT solution was applied to completely immerse the tip. Evaporation of the volatile THF solution occurred rapidly, resulting in the meniscus withdrawing over the tip and leaving a thin fibre attached.

A similar process was reported by Ondarcuhu and Joachim, where gold nanoparticle solution was used to form nanoparticle fibres [11]. This appears to be the only report of fibre formation at a sharp tip in the absence of any electrical bias, and is thus the first report of this technique being applied to CNT solutions.

There has been development in CNT fibre production by wet-spinning CNTs from superacid solutions (ie. sulfuric acid) or utilising polymer stabilisers through a

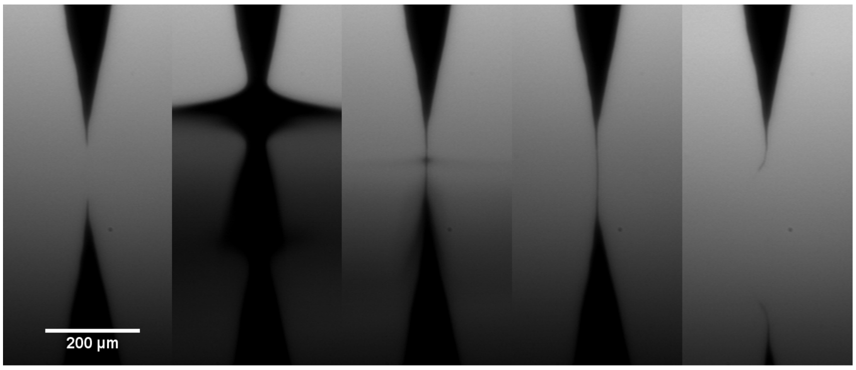

Figure 4.9: Sequential optical images (left to right) of the tungsten tip and silicon surface showing evaporation of the SWCNT solution and formation of a nanotube fibre with no applied bias.

narrow aperture for high throughput production [12–15]. The results presented here differ in that the solution used is not a hazardous superacid, and the fibre is formed at a sharp tip instead of through a nozzle. The closest report to this type of fibre formation is that by Zhang et al. who forced an etheylene glycol dispersed solution of MWCNTs through a syringe nozzle, into a solution of ether. This technique was used to form fibres 10-80 μm in diameter which were free from any surfactants, the main difference to the technique presented here is the usage of SWCNTs and that the formation mechanism (using evaporation at a sharp tip) is entirely different.

There has been much experimental and theoretical work on the alignment of nanomaterials (including CNTs) at receding solvent interfaces [16, 17]. These prior studies provide good understanding of the mechanisms underpinning formation of the fibre, which is often referred to as the "coffee stain" effect [18]. Preferential evaporation at the solid-liquid-air interface causes the CNTs to be transported via liquid flow to the edge of the solvent and the increase in concentration results in the CNTs ordering with nematic liquid crystal structure. As the droplet recedes over the tip apex, it is proposed that the CNTs order inside the capillary neck which then evaporates and leaves a highly-ordered fibre.

Several factors were observed to affect the properties of the nanotube fibre; these included the tip-sample separation, tip geometry and concentration of the CNT solution. This effect is attributed to the correlation between tip-sample separation and the withdraw rate of the tip from the solution. The receding rate of the droplet was observed to decelerate as evaporation proceeded, resulting in the withdraw speed of the tip being greater for increased tip-surface distances. One would also expect the concentration of the solution to increase as the droplet evaporated, which makes this factor difficult to control. The length of the fibre was observed to be inversely proportional to the tip-surface separation, resulting in shorter fibres forming for greater separations as shown in figure 4.10.

When the tip was placed close to the surface, the concentration of the solution was high enough that the fibre formed continuously until it reached the surface. Figure 4.11 shows the result of a tip placed 30 μm from the surface, where the fibre has formed across the gap and resulted in a branched structure of CNTs where it terminates at the surface.

It was also possible to draw fibres which were extremely long; figure 4.12 shows a CNT fibre almost half a millimetre in length. It is expected that with optimal

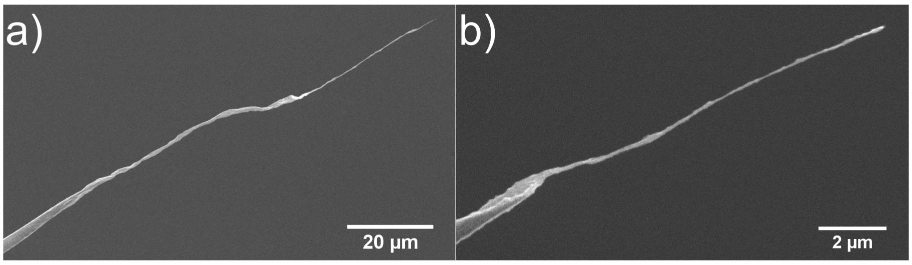

Figure 4.10: SEM images showing the variation in fibre length with increased tip-sample separation from a) 100 μm to b) 400 μm.

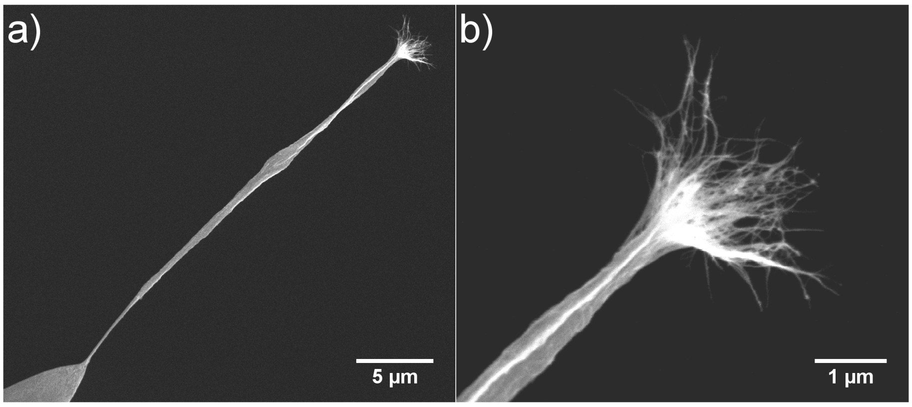

Figure 4.11: SEM images of a fibre which completely bridged the tip and the surface at a separation of 30μm.

drawing conditions and a large reservoir of fluid, the fibre could be drawn continuously. Macroscopic CNT fibres have many applications such as flexible conductors for textiles and batteries, and as mechanical actuators for muscles [19].

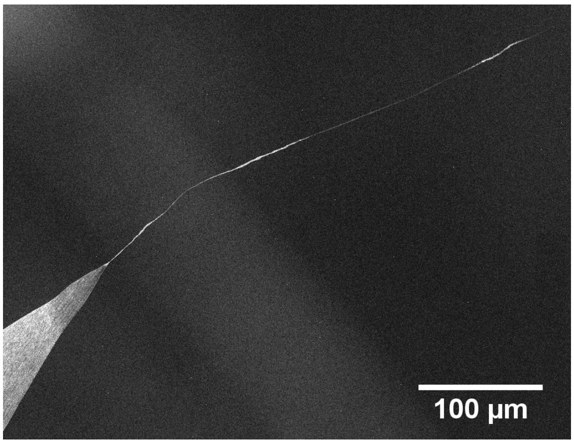

Figure 4.12: SEM image of a long CNT fibre, drawn by the solvent evaporation method.

The same process can be applied to an AFM tip, however the cantilever introduces some non-uniform geometry in comparison to the symmetrical etched tungsten tips. The cantilever is placed a certain distance from the silicon surface as shown in figure 4.13a and the droplet is then applied over the entire tip; figures 4.13b-d show gradual evaporation of the solvent and deposition of the fibre. The cantilever was generally flexible enough that the capillary force pulled the tip into contact with the surface, which would be expected to interfere with fibre formation. It can be seen, however, that the cantilever returns to its original position after the droplet has evaporated. Once the droplet has receded sufficiently, to the point that the meniscus force is lesser than the restoring force of the AFM cantilever, the tip will be pulled away from the surface and fibre formation should occur as expected.

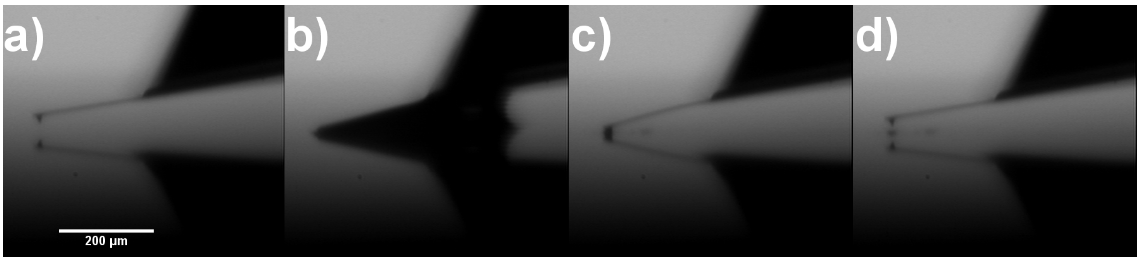

Figure 4.13: Optical images showing alignment of an AFM tip with a silicon surface a) and evaporation of the CNT solution over the cantilever b-d).

The SWCNT fibre deposited on the AFM probe is shown in figure 4.14a and is over 1 μm in length. The slightly curved geometry is commonly observed for fibres formed using solution-based methods as observed previously.

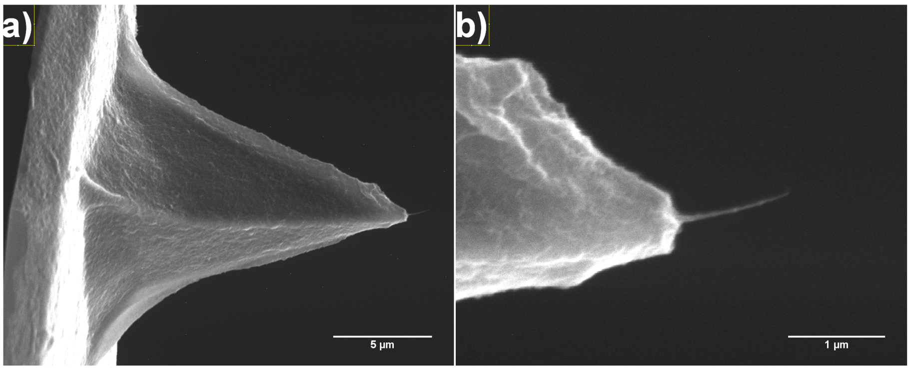

Figure 4.14: SEM images of a SWCNT fibre attached to the apex of an AFM probe.

4.2.3 Fibre processing

After attachment by either the DEP or evaporation method, the fibre is often curved and misaligned with the AFM probe. For all of the probes produced in this work, the fibres were too mechanically unstable to obtain images and required shortening and/or alignment with the axis of the AFM tip. This can be achieved using methods such as ion beam irradiation discussed in section 1.3.1.1, however it was found that imaging with very high force could also stabilise the fibre.

The tip was engaged in tapping mode and the set-point reduced to 10-30% of its free amplitude; this was continued until the probe started to track the surface properly, at which time the setpoint was increased to a normal operating value. This amplitude reduction approach is similar to a method used by Gibson et al. for attaching CNT's with the pick-up method [20].

SEM images for two probes in figure 4.15 support this observation, showing that the fibre has been shortened slightly and has aligned with the AFM tip. This behaviour was observed for 3 CNT fibre probes, and in each case produced a tip which was stable, sharp, high aspect ratio and wear resistant.

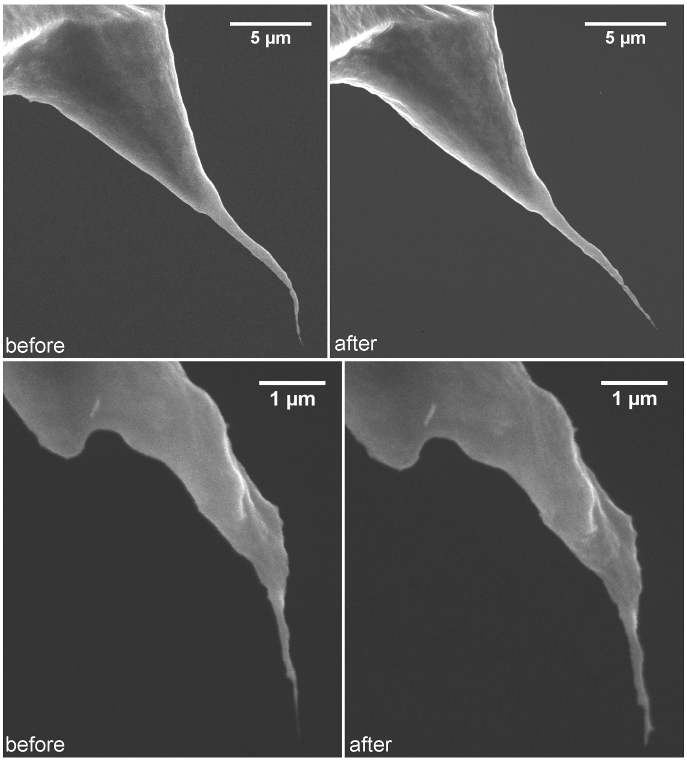

Figure 4.15: SEM images of two probes fabricated using the DEP method, the images show each tip before and after shortening/alignment using the high-force tapping method.

Amplitude versus distance curves also show this stabilisation process, with curves taken after fabrication exhibiting common instabilities observed for many of the CNT probes investigated [21, 22]. Figure 4.16a shows that as the tip approaches the surface, the amplitude drops by a very small amount before increasing again due to instability in the CNT fibre. This instability is present for over 500 nm of tip extension, and makes imaging effectively impossible. After the stabilisation process, the curve in figure 4.16b shows a stable, monotonic damping region over approximately 50 nm. The stability can be observed by the imaging achieved with this probe on a CNT surface, shown in figure 4.17.

The mechanism of the straightening effect is unclear, as one would expect a misaligned fibre to be bent further out of alignment by high force imaging. A possible explanation is that during the compression and relaxation of the nanotube fibre in the course of imaging; adhesion causes the tip of the fibre to stick to the surface to some degree. This would result in a “pulling” force that could stretch the fibre in the direction of the force exerted by the AFM probe, possibly causing alignment with the tip apex. The shortening effect observed for some tips is more simple than this and would either be caused by breakage of the fibre, or sliding and compression of the nanotubes within the fibre to produce a shorter, denser and hence more rigid structure.

As introduced in section 1.3.1.1, FIB irradiation can be used to align CNT fibres as reported by Shin et al. and Raghuveer et al. [23, 24]. This provides excellent

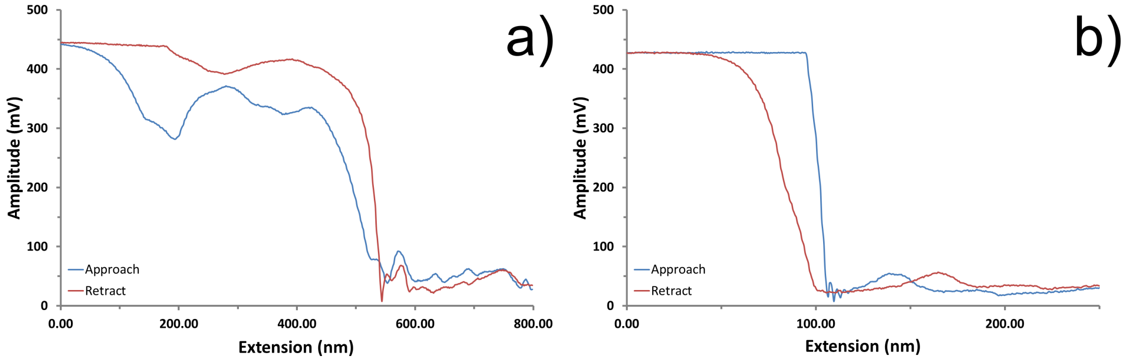

Figure 4.16: Amplitude versus distance curves for a CNT probe fabricated by the solvent evaporation method before a) and after b) the stabilisation procedure.

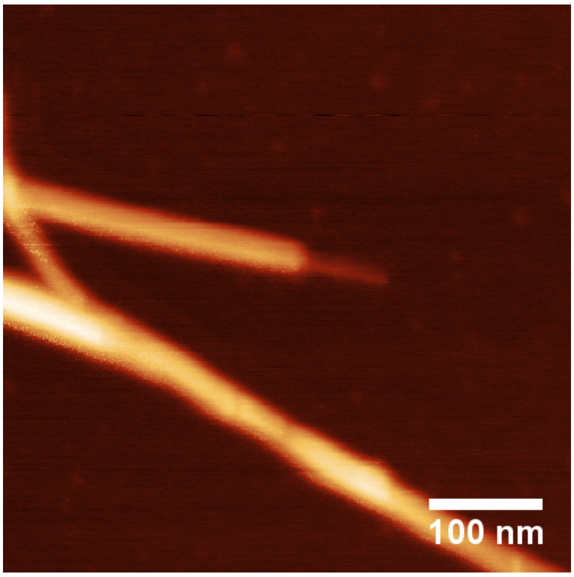

Figure 4.17: An AFM image of CNT's on a silicon surface, obtained with the CNT fibre probe after stabilisation.

control over the orientation of the fibre, but is quite destructive. Both Shin et al. and Raghuveer et al. observed that TEM images of the CNT after FIB irradiation showed significant damage to the graphitic structure and substantial implantation of metal ions. While the method described herein cannot afford the same precise control for orientation, it is far less destructive. This will be a significant advantage for applications where maintaining the graphitic structure of the CNTs is critical.

4.3 Manual attachment

The attachment methods reported thus far are simple to implement, but are difficult to control with regard to the properties of the attached CNT. In order to improve control over the attachment process, manual attachment was attempted using a micro-manipulator to place the CNTs directly inside a high-resolution SEM.

4.3.1 Attachment procedure

The process reported here builds on the work of Martinez et al. [25]. Several aspects of the technique are modified to improve the ease of attachment, the properties of the attached CNT and the precision with which the CNT can be manipulated. The key aspects of the attachment process and their advantages are described here.

4.3.1.1 CNT source and attachment

The quality of the CNT source affects the quality of nanotube probes fabricated and also the ease with which they can be assembled. Buckypaper was used as a source of aligned SWCNTs, which is essentially a mat of nanotubes removed from filter paper and then torn to to produce CNTs aligned at the edge. This source was found to be superior in many ways to others reported previously, and the preparation is described in detail in the experimental methods (section 2.3).

Most previous reports describe the use of a sharp electrode (often a razor blade) onto which CNTs are attached and aligned from solution using DEP [25–27]. There are several advantages to using buckypaper, primarily that the preparation is rapid, simple and highly reproducible, but also that the density, purity and alignment of the nanotubes along the edge is very high. Samples prepared by dielectrophoresis often feature aligned CNTs which are sparse and quite short, which is evident by comparison in figure 4.18.

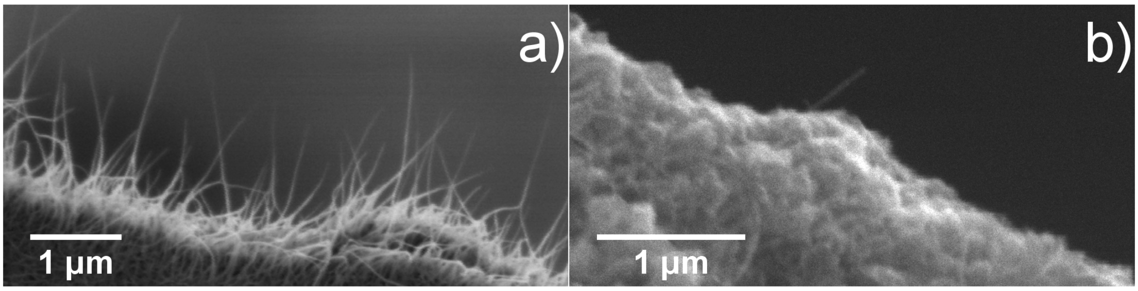

Figure 4.18: SEM images of a small section of the edge of the torn buckypaper a), and razor edge with SWCNTs attached and aligned using dielectrophoresis b). Reprinted with permission from [28].

Buckypaper has an additional advantage in that a very small piece can be attached to the end of a micro-manipulator needle. Placing the AFM probes on the SEM stage and the SWCNTs on the micromanipulator means that the instrument requires no modification. The use of larger CNT sources, such as aligned nanotubes on a razor blade is often applied using two independent micromanipulators placed on the SEM stage [27, 29, 30]. It is evident from figure 4.18a that there is no shortage of well-aligned SWCNTs present at the edge of the buckypaper, which allows many probes to be lined up in the SEM and attachment to be performed sequentially.

To facilitate attachment, a nanotube must firstly be selected from the buckypaper and then brought into contact with the tip of the AFM probe. This was achieved by bringing both objects into focus such that the nanotube was just above the probe tip, and then lowering the nanotube down until contact was observed. Contact between the nanotube and the probe was easily observed, as Van der Waals forces cause the nanotube to adhere strongly to the tip. For probes which exhibited slight charging, the portion of the nanotube in contact with the tip would become very bright, possibly as a result of charge dissipation from the probe through the nanotube in a similar process to that reported by Homma et al. [31].

4.3.1.2 Cutting procedure

Once placed on the tip, the nanotube must be cut; a significant improvement over previous techniques is the application of water-assisted electron beam cutting to sever and shorten the CNTs. Martinez et al. reported a method to precisely cut the nanotube using the electron beam, with cutting times on the order of 2 minutes [25]. During this time, the probe and nanotube can drift substantially which affects the contact point and the cutting location.

Yuzvinsky et al. reported that introduction of water vapour during the cutting process significantly increases the cutting rate [32]. In accordance with the results reported by Yuzvinsky et al., the introduction of water vapour with a low beam energy significantly increased the cutting rate. With beam energy of 1 kV, bundles of nanotubes were often completely severed in less than 5 seconds which is a ∼20 fold reduction in the cutting time compared to those reported previously. When higher beam energy was used, the cutting time was extended to approximately 30 seconds and it was found that cutting the CNT in a precise location was quite difficult.

The AFM probes were mounted on their side, and so there was slight drift in the tip position with time. When combined with drift of the electron beam and the manipulator itself, this was enough to make cutting the CNT challenging. The reduced cutting time afforded by the introduction of water vapour improves the accuracy with which cuts can be made and also minimizes the region of the nanotube damaged by the beam. The cutting process is shown in figure 4.19, where a nanotube bundle has been placed on the probe and the cut location is indicated by an arrow.

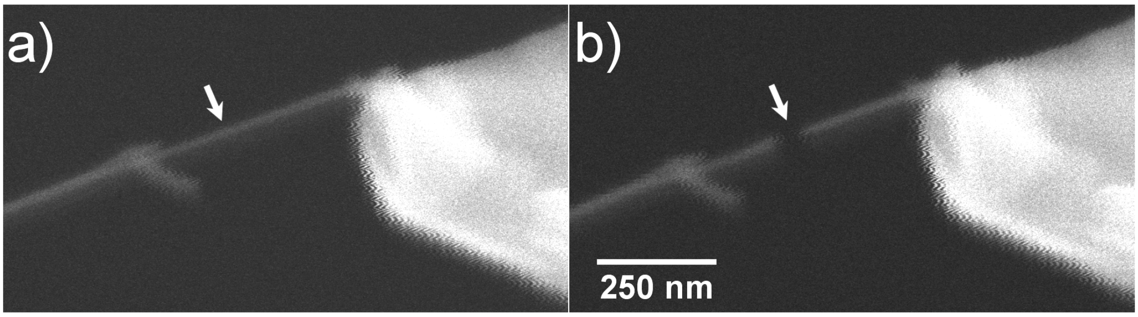

Figure 4.19: SEM images of the water-assisted electron beam cutting process showing the cutting position indicated by the white arrow before a) and after the cutting process b). Reprinted with permission from [28].

Heeres et al. used a similar method to produce MWCNT electron emitters, where water vapour was introduced into the chamber and cutting times were reported to be typically 1 min [33]. The nanotubes cut by Heeres et al. were reported to have open ends, which is expected to be case for those presented here. The cutting time reported in this method is again much lower than that reported by Heeres et al; this is likely due to the method of water vapour delivery. Heeres et al. used a leak valve to fill the entire SEM chamber whereas the gas injection system on the Helios Dualbeam places a delivery needle very close to the reaction site (∼200 μm). The close proximity of the delivery needle provides more localized reactants which are likely to be at a much higher concentration without compromising the pressure of the chamber.

4.3.1.3 CNT reinforcement

After cutting the nanotube, platinum was used to affix the CNT to the tip by electron beam induced deposition (EBID). This is necessary to prevent the nanotube from detaching during imaging, and also provides a chemically inert bond should the CNT need to be functionalised. A representative deposition is shown in figure 4.20 where a relatively large quantity of platinum was used to bond the CNT rigidly to the probe, ensuring long-term imaging stability. Smaller quantities of platinum were generally used for CNT attachment, as these still provided an effective bond and minimized the possibility of platinum deposition in undesired areas due to drift and other factors.

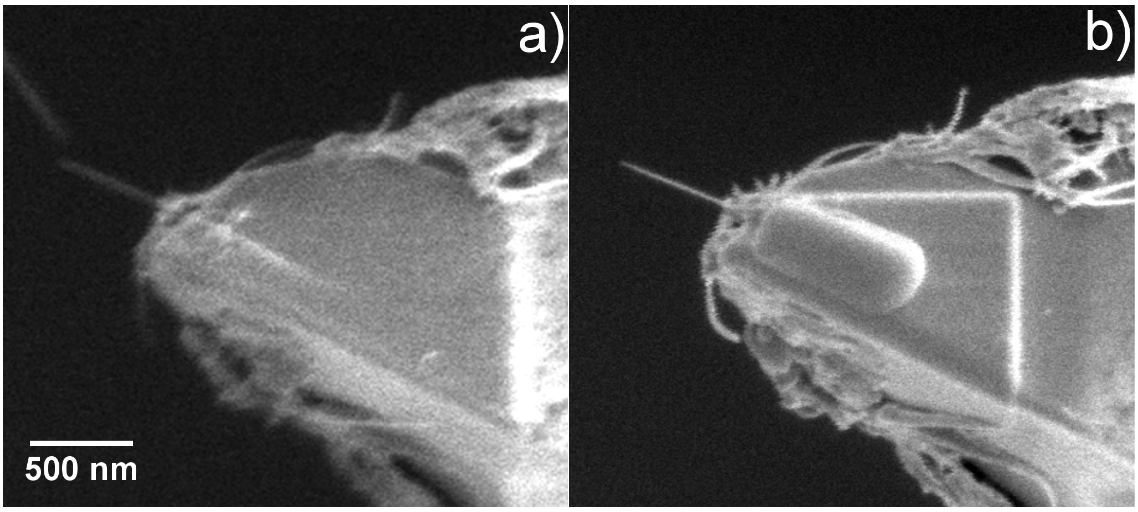

Figure 4.20: Deposition of a platinum film over the nanotube, forming a stable anchor point to the AFM probe. Reprinted with permission from [28].

The nanotube must be affixed to the AFM tip using EBID with either carbon or platinum, and this can be performed either before or after the nanotube is cut. The EBID process was initially applied before cutting the nanotube, however it was found that cutting the nanotube before EBID was preferable for two reasons. Firstly, switching between platinum deposition and water-assisted cutting requires the gas injection needles to be inserted/retracted, which results in some mechanical disturbance. If this process is performed whilst the nanotube is bridging the tip and the manipulator, the nanotube often detached, even when affixed with platinum.

The other reason that platinum deposition was performed as the final step is that the precursor adheres to the sample surface and remains for several minutes after deposition. Platinum deposition was confined to the contact area between the nanotube and the tip so as to avoid broadening the diameter of the CNT. Imaging with the electron beam after platinum deposition (or cutting nanotube) resulted in unwanted deposition of platinum if the precursor wasn't given time to evaporate. Consequently, it was found to be more efficient and simpler to cut the nanotube first and then perform the platinum deposition as the very last step in the attachment process.

4.3.2 Results

The complete attachment process is shown sequentially in figure 4.21; a thin bundle of SWCNTs is selected from the buckypaper, placed on the tip, cut to a length of 200 nm and then affixed with a thin layer of platinum.

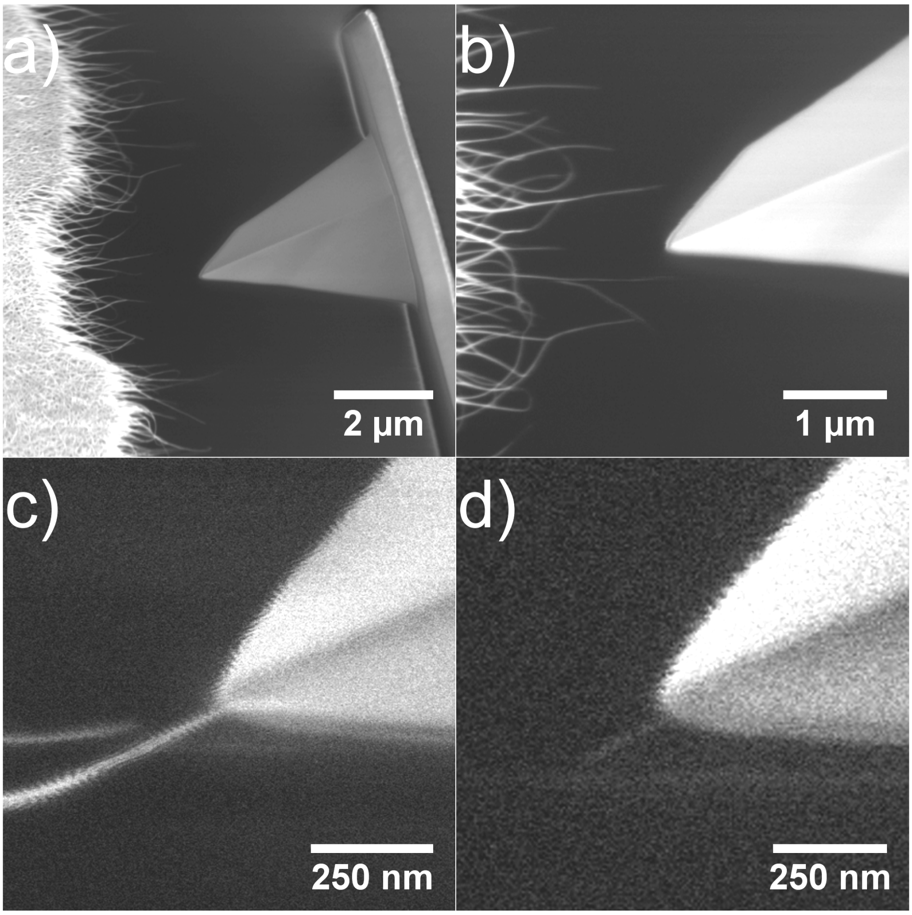

Figure 4.21: Sequential SEM images of the attachment steps used to attach the SWCNTs to the AFM probe. The approach to the buckypaper is shown in a) and b), the SWCNTs are then brought into contact with the tip c) and the nanotube is severed using water-assisted e-beam cutting d). Reprinted with permission from [28].

As the supply of nanotubes from the buckypaper is effectively unlimited, a number of AFM probes were mounted on the SEM stage in rows. Upon successful attachment, the next probe was simply moved to the nanotube sample and the process repeated.

This allowed CNT probes to be fabricated in rapid succession, producing up to 4 per hour. A number of CNT probes were fabricated using various types of cantilevers and a complete list of these is provided in table 4.1.

Cantilever	Figure	Cantilever model	CNT length (nm)	Spring constant (nominal) (Nm^{-1})	Resonant frequency (nominal) (kHz)	Si tip diameter (nominal) (nm)
CNT1	5.1a	Bruker FSA	270	18	1400	10
CNT2	5.1b		60			
CNT3	5.1c		80			
CNT4	4.21		200			
CNT5	4.22a		100			
CNT6	4.19	Bruker FMV	235	2.8	75	20
CNT7	4.20		525			
CNT8	4.22c		280			
CNT9	4.22b	Bruker SNL	100	0.35	65	4
CNT10	5.9b	Mikromasch NSC15	1200	40	325	-
CNT11	5.9a	Bruker OTR8	170	0.57	73	15

Table 4.1: Designations of AFM probes used in this work provided as a reference, along with important properties of the cantilever and tip.

SEM images for a number of the CNT probes are provided in figure 4.22, and also in the following chapter in figure 5.1. Results from the application of these CNT probes is reserved for the following chapter.

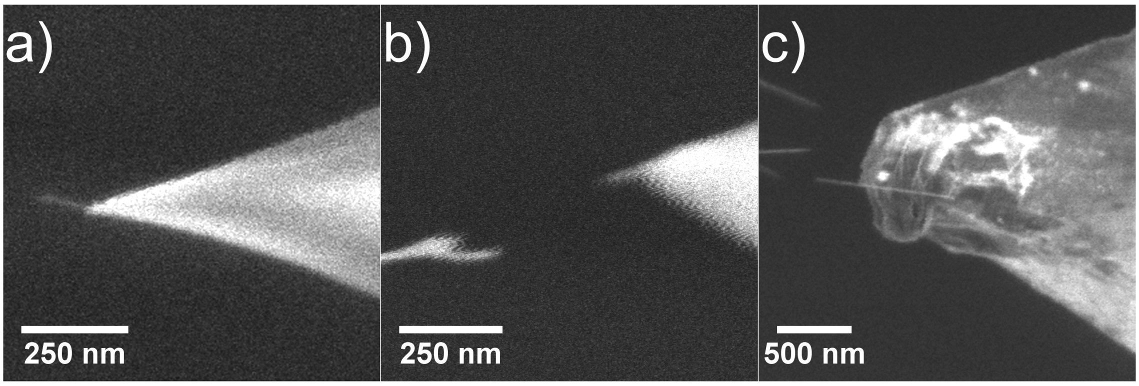

Figure 4.22: Several CNT probes fabricated by the manual attachment method. Reprinted with permission from [28].

4.4 Summary

There are many methods available for the production of CNT AFM probes, and this chapter has focused on the application of three different techniques in total. While all methods were found to be successful in producing CNT probes, the quality was found to vary substantially. The CVD method holds promise to produce extremely sharp tips with pristine CNTs, however the method was found to produce probes of inconsistent quality. In addition to a low success rate of CNT attachment, the probes that were fabricated were found to be highly unstable and difficult to apply.

Solution based methods proved to be fairly reliable, however the CNTs were frequently attached in large bundles. This was achieved both by applying existing DEP methods and also with the introduction of a simple evaporation technique. The CNT fibres attached by these methods proved to be initially unstable and required processing, which was achieved by tapping mode imaging with high force. SEM imaging revealed that the fibres straightened and the AFM imaging stabilised, allowing the probes to image, but with resolution only slightly better than that of standard probes. These probes still offer advantages due to their high aspect ratio and stability, even with very large tip lengths; there are applications in metrology for profiling high aspect ratio structures where probes such as these would be ideal.

The most effective method for CNT probe fabrication was found to be manual attachment. CNT's were attached using a micro-manipulator inside an SEM, which allowed the quality of the attached nanotube to be controlled directly. The attachment method developed enabled rapid fabrication of CNT probes, which were of very high quality and able to be applied without modification. The CNT probes used in the following chapter were all fabricated using the manual attachment method.

Bibliography - Chapter 4

[1] Jason H. Hafner, Chin Li Cheung, and Charles M. Lieber. *Journal of the American Chemical Society* 121.41 (1999), pp. 9750–9751. DOI: `10.1021/ja992761b`.

[2] Chin Li Cheung, Jason H Hafner, and Charles M Lieber. *Proceedings of the National Academy of Sciences of the United States of America* 97.8 (2000), pp. 3809–13. DOI: `10.1073/pnas.050498597`.

[3] J P Edgeworth et al. *Nanotechnology* 21.10 (2010), p. 105605. DOI: `10.1088/0957-4484/21/10/105605`.

[4] Mark Alexander Bissett. PhD thesis. Flinders University, 2011.

[5] Kenji Hata et al. *Science (New York, N.Y.)* 306 (2004), pp. 1362–1364. DOI: `10.1126/science.1104962`.

[6] Yiming Li et al. *Journal of Physical Chemistry B* 105 (2001), pp. 11424–11431. DOI: `10.1021/jp012085b`.

[7] E. F. Kukovitsky et al. *Chemical Physics Letters* 355 (2002), pp. 497–503. DOI: `10.1016/S0009-2614(02)00283-X`.

[8] Hee Cheul Choi et al. *Nano Letters* 3.2 (2003), pp. 157–161. DOI: `10.1021/nl025876d`.

[9] Haoyan Wei et al. *Nanotechnology* 19.45 (2008), p. 455303. DOI: `10.1088/0957-4484/19/45/455303`.

[10] J. Zhang et al. *Advanced Materials* 16.14 (2004), pp. 1219–1222. DOI: `10.1002/adma.200400124`.

[11] T Ondarçuhu and C Joachim. *Europhysics Letters (EPL)* 42.2 (1998), pp. 215–220. DOI: `10.1209/epl/i1998-00233-9`.

[12] Mikhail E. Kozlov et al. *Advanced Materials* 17.5 (2005), pp. 614–617. DOI: `10.1002/adma.200401130`.

[13] L. M. Ericson. *Science* 305 (2004), pp. 1447–1450. DOI: `10.1126/science.1101398`.

[14] Natnael Behabtu, Micah J. Green, and Matteo Pasquali. *Carbon nanotube-based neat fibers.* 2008. DOI: `10.1016/S1748-0132(08)70062-8`.

[15] Natnael Behabtu et al. *Science* 339 (2013), pp. 182–6. DOI: `10.1126/science.1228061`.

[16] Shanju Zhang et al. *Langmuir : the ACS journal of surfaces and colloids* 26.3 (2010), pp. 2107–12. DOI: `10.1021/la902642f`.

[17] Charlotte Bernard et al. *Nanoscale Research Letters* 2.7 (2007), pp. 309–318. DOI: `10.1007/s11671-007-9065-5`.

[18] R D Deegan et al. *Nature* 389.6653 (1997), pp. 827–829. DOI: `10.1038/39827`.

[19] Ken R. Atkinson et al. *Physica B: Condensed Matter* 394.2 (2007), pp. 339–343. DOI: `10.1016/j.physb.2006.12.061`.

[20] Christopher T Gibson, Stewart Carnally, and Clive J Roberts. *Ultramicroscopy* 107.10-11 (2007), pp. 1118–22. DOI: `10.1016/j.ultramic.2007.02.045`.

[21] a. N. Jiang et al. *Journal of Physical Chemistry C* 112.40 (2008), pp. 15631–15636. DOI: `10.1021/jp804481g`.

[22] A. Kutana et al. *Nano Letters* 6.8 (2006), pp. 1669–1673. DOI: `10.1021/nl060831o`.

[23] Y Shin et al. *Applied Surface Science* 253.16 (2007), pp. 6872–6877. DOI: `10.1016/j.apsusc.2007.01.135`.

[24] M. S. Raghuveer et al. *Applied Physics Letters* 84.22 (2004), p. 4484. DOI: `10.1063/1.1756191`.

[25] J Martinez et al. *Nanotechnology* 16.11 (2005), pp. 2493–2496. DOI: `10.1088/0957-4484/16/11/004`.

[26] Shu-Cheng Chin, Yuan-Chih Chang, and Chia-Seng Chang. *Nanotechnology* 20.28 (2009), p. 285307. DOI: `10.1088/0957-4484/20/28/285307`.

[27] Hidehiro Nishijima et al. *Applied Physics Letters* 74.26 (1999), p. 4061. DOI: `10.1063/1.123261`.

[28] Ashley D Slattery et al. *Nanotechnology* 24.23 (2013), p. 235705. DOI: `10.1088/0957-4484/24/23/235705`.

[29] Niels de Jonge, Yann Lamy, and Monja Kaiser. *Nano Letters* 3.12 (2003), pp. 1621–1624. DOI: `10.1021/nl034792h`.

[30] St. Fahlbusch et al. *Journal of Materials Processing Technology* 167.2-3 (2005), pp. 371–382. DOI: `10.1016/j.jmatprotec.2005.06.022`.

[31] Yoshikazu Homma et al. *Applied Physics Letters* 84.10 (2004), p. 1750. DOI: `10.1063/1.1667608`.

[32] T. D. Yuzvinsky et al. *Applied Physics Letters* 86.5 (2005), p. 053109. DOI: `10.1063/1.1857081`.

[33] Erwin C Heeres, Tjerk H Oosterkamp, and Niels de Jonge. *Nanotechnology* 22.23 (2011), p. 235308. DOI: `10.1088/0957-4484/22/23/235308`.

Chapter 5

Application and Performance of CNT AFM Probes

This chapter reports the application of SWCNT probes fabricated by the manual attachment method reported in section 4.3 of the previous chapter. A significant advantage of this attachment technique is that almost any type of cantilever can be used, which allowed SWCNTs to be attached to fast-scanning AFM probes for the first time. The scanning performance and wear properties of these probes were investigated on rough samples at scan rates of up to 30 Hz. Additionally, the PeakForce tapping (PFT) imaging mode was investigated as a technique which might offer improved imaging stability. Imaging using CNT probes in PFT mode is reported for the first time, with application to a range of samples and an investigation of CNT-related artifacts.

5.1 Fast-scanning and wear performance

5.1.1 Introduction

The excellent wear-resistant properties of CNT probes are widely known, and have been demonstrated to significantly improve the wear resistance of AFM probes [1–3]. There have however, been no reports of CNT attachment to high-frequency fast-scanning probes where wear resistance is of great importance. Attachment of SWCNTs to high frequency probes was achieved using the manual attachment method introduced in the preceding chapter, and the wear performance of these probes is investigated on tip shape calibration samples.

5.1.1.1 Tapping mode wear

The wear processes involved in tapping mode are not as intuitive as those associated with contact mode. There had been few studies of probe wear in tapping mode until a detailed investigation by Su et al., who observed wear as a function of operating set-point and found that wear in tapping mode is a function of the speed with which the tip impacts the surface [4].

To the authors' knowledge, there have been no direct investigations into how the resonant frequency of a probe affects the wear rate. It should be clearly stated that the reference is to the operation of different probes at their resonant frequency, and not variation of the tapping force due to off-resonance operation as investigated by Tamayo et al [5]. This effect may be important for the new generation of fast-scanning probes which are designed with resonant frequencies well above 1 MHz. One might expect that a greater rate of tapping would result in a greater rate of tip wear, because the tip is impacting the surface more frequently.

For the application of high speed AFM to soft biological material, Ando noted that the impulse (ie. the force multiplied by the probes' contact time) is the governing factor which determines the degree of damage to the sample [6]. This is simply reversed for the case where the sample is of comparable or higher modulus than the tip material, and so the impulse will largely determine the rate of tip wear. Interestingly, the total contact time is constant at a given set-point regardless of the resonant frequency of the probe, because for an increased rate of tapping the duration of each tap is reduced. Given that the total contact time is unchanged for higher resonant frequencies, the force applied to the surface must be considered.

Su et al. determined that the applied force is proportional to the impact speed of the tip, which is also proportional to the tapping frequency [4]. They provide the relationship between tip impact speed and tapping force, which is shown in equation 5.1. Here, V_r is the velocity immediately before the tip impacts the surface, f is the cantilevers' resonant frequency, A_S is the set-point of the feedback loop, R_S is the relative set-point and Q is the cantilevers' Q factor.

$$V_r = 2\pi f A_S \mathrm{sec}\left(\frac{R_S}{R_S + \frac{\pi}{Q}\left(1 - R_S\right)}\right) \tag{5.1}$$

This shows that probes with higher resonant frequencies will impact the surface with higher velocity and thus increased force, potentially resulting in an increased rate of wear. As the scanning rate of AFMs increases, probes with increasingly higher resonant frequencies will be required. For applications where high scan rates are sought to improve productivity in areas such as metrology, probe wear may prove to be a significant problem to which wear-resistant probes may be the solution.

An interesting point which is yet to be identified, is that the wear rate in tapping mode should be independent of scan speed. The assumptions are that the feedback parameters are optimized to ensure the probe tracks the sample effectively, such that wear is only due to the tip impacting the surface. In this case, increased scan rates would actually be beneficial for preserving the sharpness of high-frequency probes, as the governing factor for tip wear will be scanning time rather than the distance the probe travels. Increasing the scan rate results in an image being acquired faster and thus the tip performs fewer “taps” on the surface; this should result in less overall wear, again presuming that the tip tracks the surface effectively.

It is worth noting that although tip impact during tapping is likely to be the primary cause of tip wear, there are other factors which can cause damage to the tip and reduction in image resolution. These include, but are not limited to the modulus of the sample under investigation and the feedback parameters used (ie. setpoint). Contamination of the tip with material from the surface can also affect the tip shape, although it is not specifically a result of tip wear.

5.1.2 Results and discussion

The CNT probes used for the wear testing experiments were fabricated by the manual attachment method in section 4.3; these are listed in table 4.1, along with each probes' designation. Also included are the types of cantilever used and their general properties, along with the length of the attached CNT as measured by SEM. Probes used for the wear-testing studies are shown in figure 5.1, and are designated CNT 1-3 in table 4.1. Standard FSA cantilevers were used as comparisons against the CNT probes, these have a nominal spring constant of 18 Nm^{-1}, resonant frequency of 1.4 MHz and nominal tip diameter of 10 nm.

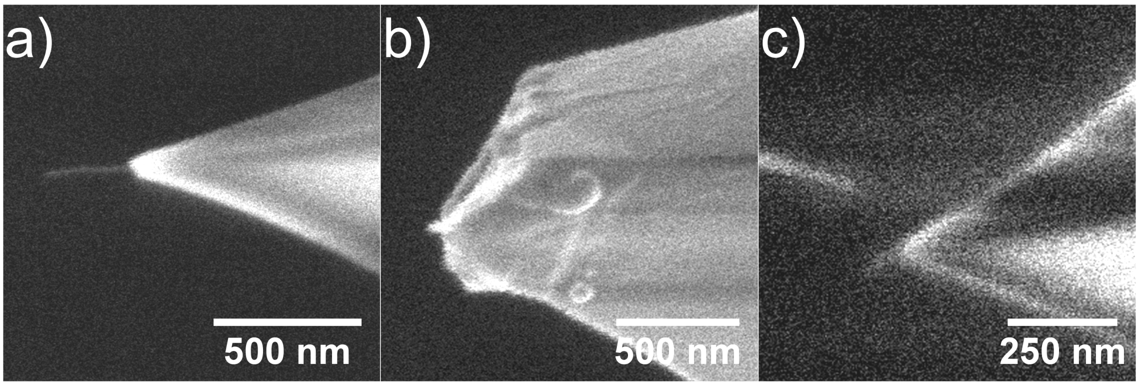

Figure 5.1: SEM images of the CNT probes used in the tip wear studies, a) is CNT 1 and has a long, thin nanotube bundle, b) is CNT2 and has a very short and thick nanotube bundle, while c) is CNT3 and has a very short nanotube bundle attached. Reprinted with permission from [7].

5.1.2.1 Wear testing

Wear testing was initially performed on a Nioprobe tip calibration sample, which is a Niobium thin film exhibiting many sharp peaks with random orientation (less than 5 nm peak diameter) designed for characterizing the very tip of the AFM probe. The combination of a material with high Young's modulus (104.9 GPa) and sharp surface features conveniently allows the probe to be worn while simultaneously characterizing the diameter of the tip.

An area 1x1 μm in size was imaged at 6 Hz, and 160 images were collected in sequence. Each image was then processed using blind tip reconstruction software (Nanoscope Analysis, Bruker) which analyses the shape and orientation of sharp features in the image, the software then uses algorithms developed by Villarrubia [8] to determine an estimated tip diameter (ETD) at a defined height above the tip apex. The wear testing was performed at reasonably low scan rates when considering the capabilities of the system, which were chosen to minimize the error signal such that the surface features were reproduced as accurately as possible. This helps to ensure that minimal probe damage occurs as a result of poor tracking, and that the wear data was as accurate as possible. This is expected to be particularly important for steep edges where the error is generally greatest, as this is where much of the tip analysis occurs.

Although the ETD gives a reasonable estimation of the tip diameter, there are a number of issues which limit the accuracy of the values produced. Accurate determination of the ETD is dependent on the features of the tip characterizer sample being sharper than those of the tip, and this is not necessarily the case for the probes used. Tranchida et al. determined that noise present in the images and the number of pixels chosen can also affect the ETD value obtained [9]. Accordingly, the ETD values presented here are intended to indicate the change in tip diameter rather than the absolute diameter of the tip.

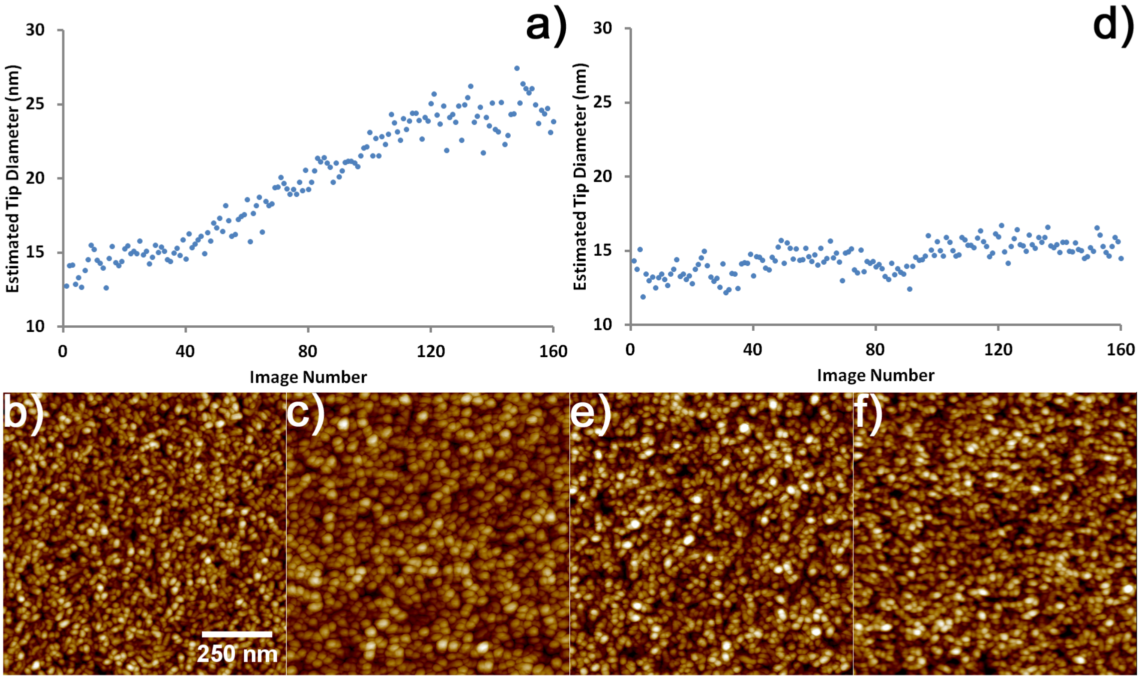

Figure 5.2: Wear testing results for successive images acquired of the Nioprobe sample using a standard FastScan A probe (FSA1) a-c), and a FastScan A probe modified with a CNT d-f) (CNT1). Each case shows the evolution of the ETD with image number at a height 3 nm above the tip apex (a,d), and the corresponding initial and final AFM images of the Nioprobe surface obtained with the standard (b,c) and nanotube (e,f) probes. The AFM image height scale is 18 nm. Reprinted with permission from [7].

The wear results are shown in figure 5.2 for a standard FastScan A probe (FSA1) in figure 5.2a-c, and a FastScan A probe with an attached CNT (CNT1) in figure 5.2d-f. The change in ETD with image number is shown, in addition to the corresponding initial and final frames obtained. It is immediately evident from figure 5.2 that the two probes exhibit very different wear rates; the standard silicon probe wears in a constant manner, while the CNT probe shows little or no wear. The quality of the final images obtained is also quite dissimilar, the CNT probe is able to clearly resolve the individual niobium particles after 160 images (approximately 7.5 hours of scanning) while the standard probe is no longer able to penetrate the gaps in between the grains.

Although the wear on the silicon probe is quite significant, the tip appears to have been very sharp initially. Bruker reports that the nominal tip diameter for these probes is 10 nm, making the resolution comparable to a small bundle of SWCNTs. While these silicon probes can be fabricated with extremely sharp tips, the pressure on a tip this small will be extremely high and as a result the wear is likely to be rapid.

The CNT probe exhibits very little change during the experiment, demonstrating the excellent wear properties of the nanotubes. There are some small fluctuations in the ETD however, which could be due to the image area drifting over the course of the measurements. A drift of approximately 500 nm was often observed over the duration of the measurement, and as the image position shifts, different topography is sampled which could cause slight changes in the ETD.

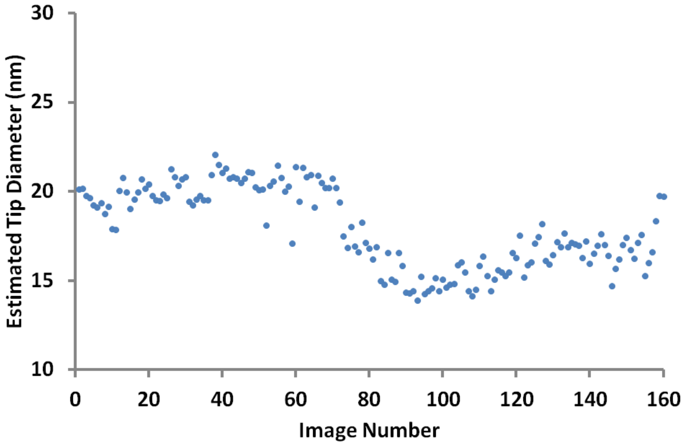

Figure 5.3: The CNT3 probe wear test performed on the Nioprobe sample, showing the reduction in probe diameter. Reprinted with permission from [7].

Although the wear observed for the CNT probes was less than 10%, a significant reduction in ETD was observed for the CNT3 probe whilst imaging the Nioprobe sample. This data is shown in figure 5.3, where the ETD drops from 20 nm to below 15 nm after approximately 70 images had been acquired. This was not accompanied by a significant drift to a different region of the sample, and a corresponding increase in image resolution was apparent.

Similar behavior was observed for several other CNT probes, but was always observed in the first few frames of imaging whereas in this case the probe acquired approximately 70 frames before the change occurred. It has been reported previously that commercial CNT probes can require 5-15 minutes of scanning before the CNT stabilizes [10]. Although the nanotubes are attached strongly to the probe tip, the attached CNTs may consist of nanotube bundles. It is possible that some imaging is required to allow the nanotubes to shift and stabilize. It is also possible that the cutting process leaves some carbonaceous impurities at the end of the nanotube, and examination of the TEM images of cut MWCNTs obtained by Yuzvinsky et al. shows small deposits to support this [11]. It is expected that repeated imaging would wear these impurities away, eventually exposing the sharper and more stable nanotubes beneath them, in a similar manner to the wear process observed for silicon tips. It is worth noting that of the CNT probes used, any changes in probe diameter always corresponded to a reduction in ETD rather than the blunting observed for standard silicon probes.

In addition to wear testing on the Nioprobe surface, a titanium “Tipcheck” sample was also used to characterize the wear properties of CNT and standard probes. This sample is a crystalline Titanium film (Young’s modulus 115.7 GPa) and the surface features are not as sharp as that of the Nioprobe but are much steeper, with average peak-to-valley distances of 150 nm. The image size was increased to provide a greater sampling area for the tip qualification procedure, and as a result the scan rate was lowered to 2 Hz to provide optimum tracking and thus precise ETD results.

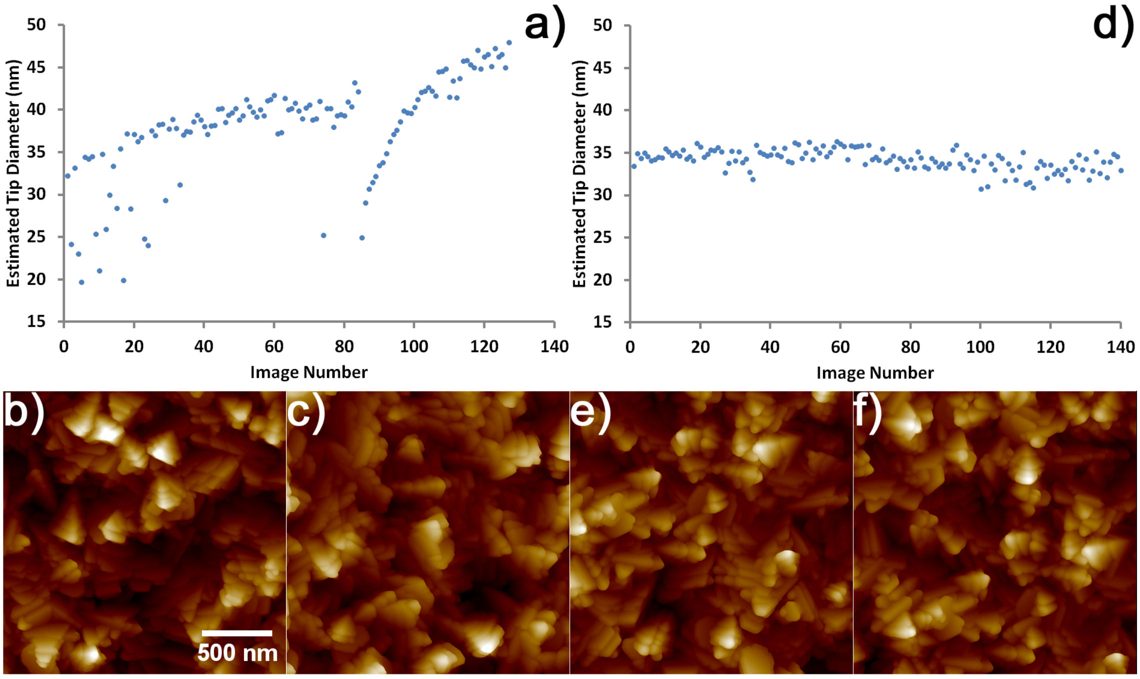

Figure 5.4: Wear testing results for successive images acquired of the Tipcheck sample using a standard FastScan A probe (FSA2) a-c), and a FastScan A probe modified with a CNT d-f) (CNT2). Each case shows the evolution of the ETD with image number at a height 10 nm above the tip apex (a,d), and the corresponding initial and final AFM images of the Tipcheck surface obtained with the standard (b,c) and nanotube (e,f) probes. The AFM image height scale is 270 nm. Reprinted with permission from [7].

The wear on the standard silicon probe is very similar to that observed on the Nioprobe sample, the ETD increases in a constant manner up until image number 84. A significant decrease in ETD is observed instantaneously in this image, and the reverse tip imaging data was used to determine the possible cause for the decrease in ETD. The tip analysis introduced earlier generates an image of the AFM tip, which is displayed as the tip orientated normally out of the image.

A sequence of reverse images of the tip is shown in figure 5.5, which shows gradual wear (increase in tip size) and then a significant change in the shape of the tip at image number 84. The reverse image of the tip at this frame appears to show that the tip has fractured, as evidenced by the sharp ridges which suddenly appear; the fractured tip appears to increase in size as it continues to wear. This provides a reasonable explanation for the observed decrease in ETD, as there have been several reports in the literature of silicon AFM tips fracturing as a result of imaging samples with high modulus [4, 12, 13].

Similar to imaging the Nioprobe sample, there is almost no wear observed for the CNT2 nanotube probe over the 140 images acquired on the Tipcheck sample. This result was expected as the Youngs' modulus of titanium is similar to that of niobium, however the larger features present on this sample provide a more challenging topography to image and also allow a larger region of the tip to be

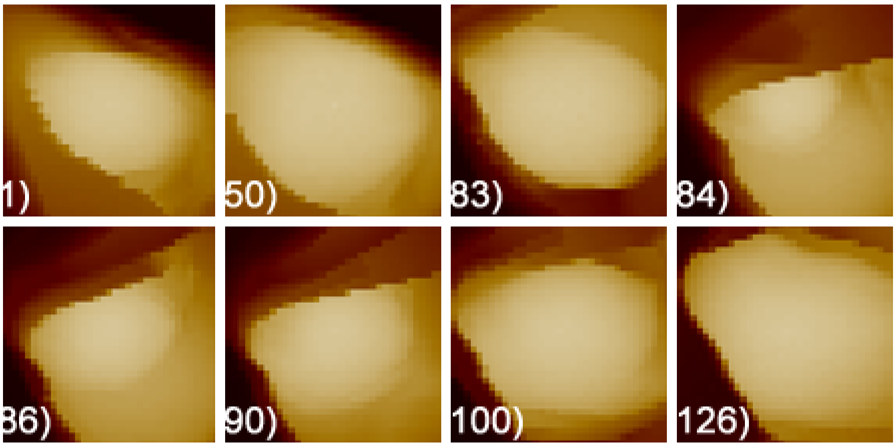

Figure 5.5: Image sequence of the reconstructed silicon tip shape while scanning the Tipcheck sample with a standard Fastscan A probe (FSA2), corresponding to the ETD data in figure 5.5a. This tip appears to fracture between images 83 and 84, as evidenced by the drastic change in the reconstructed tip image at this point. Reprinted with permission from [7].

characterised. The ability of carbon nanotube probes to image the steep features of the Tipcheck sample without tip degradation suggests that these probes could be well-applied to high-throughput characterization in metrological applications on samples with high Youngs' modulus. In addition, the cylindrical geometry of CNTs means that if wear does occur, it would have minimal effect on the diameter of the imaging nanotube tip. This is yet another advantage of using CNT probes for AFM imaging where stable tip geometry is critical.

Figure	Standard tip			CNT tip		
	Initial ETD (nm)	Final ETD (nm)	Percent change	Initial ETD (nm)	Final ETD (nm)	Percent change
5.2 Nioprobe	13.9±1.00	24.4±1.17	75±15	13.4±0.890	14.6±0.689	8.7±8.9
5.4 Tipcheck	28.3±6.06	46.3±1.04	64±35	34.5±0.552	33.5±1.03	-2.9±3.4

Table 5.1: Comparison of the ETD values for standard and CNT probes from the wear testing on Nioprobe and Tipcheck samples. The initial and final values represent an average of 10 data points, and are shown with their corresponding standard deviation.

Table 5.1 summarises the results of the wear testing presented in figures 5.2 and 5.4. The initial and final ETD values are shown which represent an average of the first and last 10 data points respectively, and the uncertainty quoted corresponds to one standard deviation. The percentage change is also given for each case, and the uncertainty is calculated using uncertainty propagation. The silicon tips in both cases show a significant increase in ETD of approximately 70%, while the CNT tips show minimal change in ETD which is within the uncertainty of the measurement. The ETD is observed to decrease by 2.9% for the CNT probe used on the Tipcheck sample (CNT2), however as is the case with both CNT probes, this is within the uncertainty of the measurement and is unlikely to represent any actual change in the probes' diameter.

5.1.2.2 "Ringing" artifact

The large features on the Tipcheck sample would generally be quite challenging to image with a long, thin nanotube due to the so-called ringing effect [14–16].Ringing artifacts are observed as a result of adhesion of the laterally-flexible CNT to a steep, vertical feature on the surface. The adhesion of CNTs to surfaces can be very strong in many cases, and results in the oscillation of the probe being damped significantly. The result is a strong adhesion to and subsequent snap-off of the CNT from the surface, which is observed as a large "ringing" oscillation at the edge of feature where the adhesion occurs. This is then exacerbated by the gains used to track the surface, and makes imaging of these structures very difficult with CNT probes [17].

Ringing was observed on a scanner calibration sample, which consists of parallel trenches with step height of 20 nm. A thin CNT was attached to a Bruker FMV probe (CNT6), and the trench edge was imaged in tapping mode. Substantial ringing was observed along the entire edge as shown in figure 5.6. An SEM image of the CNT probe used to obtain the image is shown in figure 4.19 in the previous chapter. The ringing effect would exert large forces on the nanotube, and the ability of the probe to acquire the image and remain stable demonstrates the strong attachment afforded by platinum deposition.

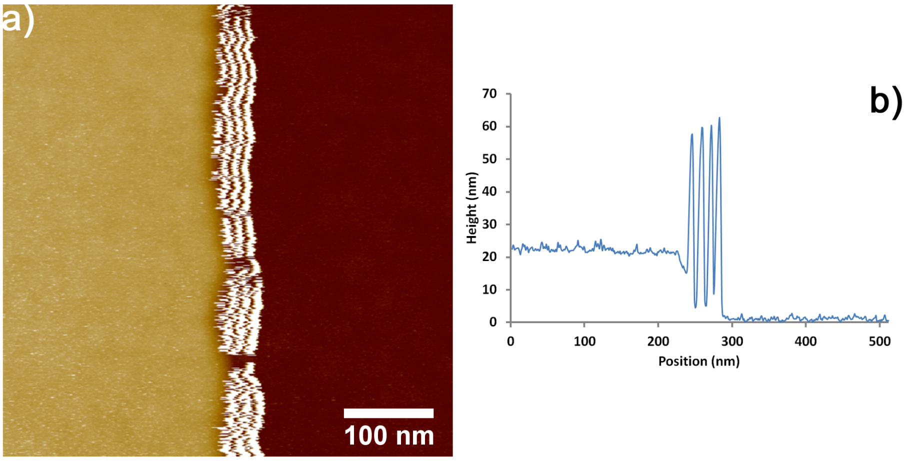

Figure 5.6: An AFM image and cross section of a 20 nm step on a calibration grid (TGZ01, Mikromasch). This image was acquired in tapping mode using CNT6, a FMV (Bruker) probe with a CNT attached as shown in figure 4.19. The height scale is 60 nm. Reprinted with permission from [7].

Given that the ringing artifact was observed on a step of only 20 nm, a slightly thicker nanotube bundle was used to improve the imaging stability for fast-scanning probes in the wear testing experiments. The shorter nanotube attached to the CNT2 FastScan A probe allows the steep, randomly-orientated features of the Tipcheck sample to be resolved clearly with a reduced rate of tip wear and without the ringing artifact. While the diameter of these particular CNT probes is comparable to the sharp, new silicon FastScan probe, the stable tip shape as a result of reduced wear is a significant advantage.

It should be noted that there are several methods which can be used to stabilize attached CNTs in order to reduce or remove the ringing artifact completely. Strus et al. found that the ringing artifact could be reduced somewhat by lowering the integral gain during imaging [17]. Gao et al. were able to avoid the ringing artifact by depositing platinum on the CNT using EBID, in order to increase the nanotubes lateral stiffness [18].

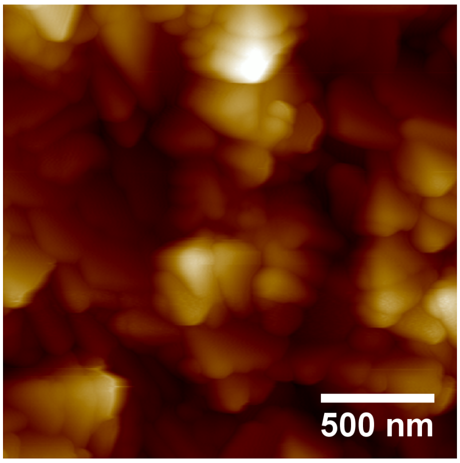

Figure 5.7: An AFM image of the Tipcheck sample at a scan rate of 30 Hz (tip velocity = 109 μms^{-1}) using the CNT2 probe, the height scale is 240 nm. Reprinted with permission from [7].

5.1.2.3 Fast scanning

Although the wear testing experiments (particularly on the Tipcheck sample) were performed at reasonably low scan rates, these CNT probes are capable of scanning much faster. After the completion of the wear testing in figure 5.4f), the scan rate was raised to 30 Hz with an image size of 1x1 μm and imaged for approximately 10 minutes. The image obtained is shown in figure 5.7, and shows the Tipcheck features clearly which demonstrates that the CNT is stable at these high scan rates, producing a 512x512 point image every ~17 seconds.

Provided that the CNT is attached firmly and is rigid, the scan rate is expected to be limited by the performance of the cantilever and the AFM. In this case, the scan rate of 30 Hz demonstrated with the CNT probe is similar to the maximum scan rate achievable with an unmodified Fastscan A probe on the same sample. The attachment of CNTs to high-frequency probes combines high wear resistance with fast scanning, making these probes ideal for high-throughput imaging of samples which would otherwise damage silicon tips.

The AFM is used extensively in industry as a tool for characterizing sample roughness and dimensions [19, 20], and the stability of the tip over long-term measurements can be critical in applications such as these [21]. CNT modified probes may prove ideal for these applications as well as for video-rate imaging at much higher scan rates.

5.1.3 Summary

The manual attachment process was used to attach CNTs to commercial high-frequency AFM probes designed for rapid scanning, which were then applied at scan rates up to 30 Hz. The wear rates of standard and CNT probes on Tipcheck and Nioprobe tip characterization samples were compared and CNT probes were observed to provide constant tip geometry over a large number of scans, demonstrating their exceptional wear-resistant properties. CNT probes such as those produced here may be useful for applications where high throughput imaging enabled by new-generation AFMs and cantilever design is desired, and constant tip geometry is critical during the measurement process.

5.2 Improved application using PeakForce tapping

5.2.1 Introduction

While CNT AFM probes can provide extremely high-resolution imaging, their application has unfortunately been hindered due to varied behaviour from that of standard silicon probes. CNTs are extremely rigid in their axial direction; however they are quite flexible in the lateral direction and buckle easily. There have been many papers investigating the dynamics of CNT probes during imaging, highlighting the challenge posed by using these specialised probes [22–25]. Improved understanding of CNT-sample interactions assists researchers to better apply these probes, however they remain difficult to fabricate and use. Efficient fabrication of CNT probes was demonstrated in the preceding chapter, addressing part of this issue, while here the reliable application of these probes is investigated.

5.2.1.1 Imaging with CNT probes

There are a number of important factors which must be controlled effectively when imaging with a CNT to ensure that the probe remains stable, but perhaps the most critical is the applied force. Excessive force can cause the nanotube to buckle, resulting in an unstable interaction [24, 26]. CNT buckling results in unstable imaging, produces artifacts and if the force applied is significant or the CNT is weakly attached, the CNT may break free from the tip. Buckling is a significant problem if the CNT is too long or not at an angle normal to the surface. The orientation and length of the CNT are critical factors in probe fabrication for these reasons, making the fabrication requirements of these probes highly demanding.

For the reasons described above, CNT probes are not well suited to imaging in contact mode, as the high lateral forces buckle the nanotube easily. In order to reduce lateral forces, CNT probes are most commonly applied in tapping mode.

5.2.1.2 Tapping mode

Tapping mode is widely used in AFM systems, primarily due to its ability to image samples with reduced lateral forces and thus reduced tip wear. For most applications the tapping amplitude is tens of nanometers and must be great enough such that the tip can tap the surface without becoming “stuck” due to adhesive forces such as those discussed in section 1.1.2. The tapping amplitude is directly related to tip velocity and thus the imaging force, as shown by equation 5.1 earlier in this chapter. In order to reduce the imaging force, the tapping amplitude can be reduced to values in the sub-5 nm range as long as tip adhesion can be avoided. This approach has been used to achieve extremely high resolution in fluid where capillary forces are not present, and in vacuum where the somewhat different “non-contact ” technique is used [27]. CNT probes are often applied using tapping mode, and require careful operation with very small amplitude, to reduce the imaging force and the possibility of destabilizing the nanotube.

While tapping mode is generally a very good imaging mode and is still used extensively, it has several inherent disadvantages. Operation at cantilever resonance produces a complicated interaction which can make imaging difficult, imaging forces vary with sample properties such as roughness and modulus, which can cause tip damage. The imaging setpoint force represents an average over the entire oscillation trajectory and a number of oscillation cycles; this makes it difficult to quantify and extract material properties, and also reduces sensitivity to the high-resolution forces at small tip-sample separation.

Figure 5.8 shows an image and amplitude-distance curve obtained in tapping mode with a very long CNT tip. A rigid silicon tip exhibits rapid, monotonic damping of the cantilever amplitude as the tip-sample distance decreases, which provides stable imaging feedback. Unstable CNT tips often show minimal damping over large extensions, as the CNT buckles against the surface.

The CNT probe used here shows the buckling feature almost immediately after contacting the surface; the CNT buckles and the amplitude remains relatively constant. The length of the CNT can be measured as the difference in extension between the onset of amplitude damping, and the point where the amplitude drops to its minimum. An ideal CNT tip should exhibit a large reduction in amplitude before buckling, providing a region in which stable feedback can be maintained.

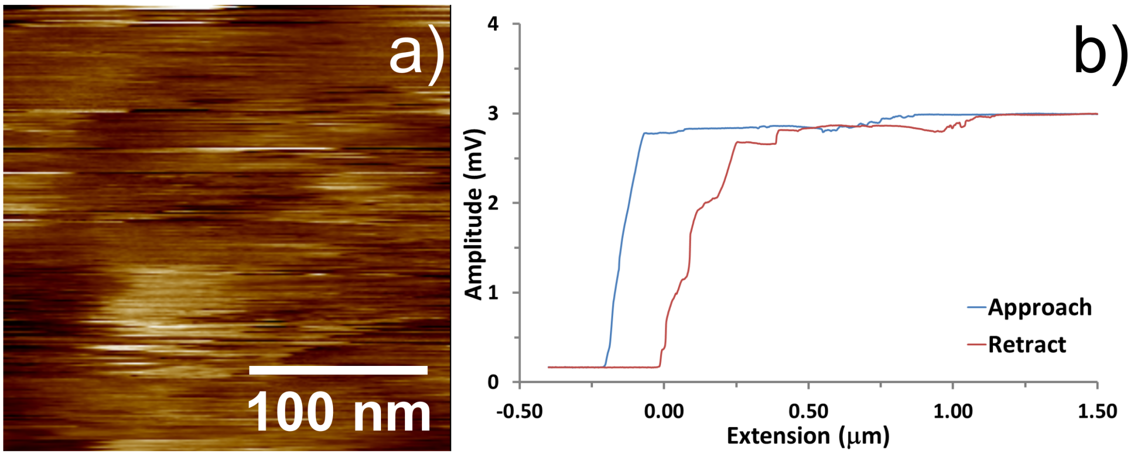

Figure 5.8: An AFM image obtained in tapping mode with a long CNT attached to a tapping mode cantilever. The instability in the image is clear, as is the large region of instability in the amplitude-distance curve, corresponding approximately to the length of the nanotube.

Another disadvantage of tapping mode imaging is that cantilevers with relatively high resonant frequencies are required, and hence the spring constant of these cantilevers is also quite high. If the cantilever is as soft as possible, then (in static operation) more deflection of the cantilever will occur before the CNT begins to buckle.

Due to their extremely high aspect ratio, CNT probes have also been proposed as excellent candidates for measurement of deep trenches with steep, vertical sidewalls. These features frequently require accurate measurement for quality control in the semiconductor industry; however this application has been hindered partially by the presence of the “ringing” artifact first reported by Park et al., which occurs when a CNT probe is in close proximity with steep sidewall [15]. Strus et al investigated this ringing artifact in detail, and this was demonstrated and discussed briefly in the previous section [17].

5.2.1.3 PeakForce tapping

The theme of this final section is the use of the PeakForce Tapping (PFT) imaging mode to improve the application of CNT probes. The PFT mode is offered by Bruker on many of their AFMs, and has been in use for over 5 years. It is important to note that while PFT is unique to Bruker and is the main focus of this work, there are other manufacturers who offer similar imaging modes. JPK instruments include their quantitative imaging (QI) mode with the family of NanoWizard 3 AFMs, which operates in a similar manner to PFT. The PFT mode has already been introduced thoroughly in section 1.1.3.2 of the introduction. Here, the benefits of the mode are reviewed with a focus on their application to imaging with CNT AFM probes.

Precise force control One of the key advantages of PFT is that the tip-sample interaction force is directly measured and used as the feedback for imaging. This allows constant imaging force to be maintained over the entire scan, which is critical for avoiding instabilities due to CNT buckling and also enables imaging forces in the piconewton range.

Simple application Optimisation of probe tracking in tapping mode is dependent on the dynamics of the probe, and requires the gains and setpoint to be carefully adjusted to achieve good feedback. This process is generally quite simple on basic surfaces with standard probes; however the introduction of a complex surface or probe (ie. CNT) often complicates the feedback and thus the required gain and setpoint optimization process significantly.

A substantial benefit of PFT is that the feedback interaction is greatly simplified, which makes the transition from standard silicon probes to CNT probes much easier to understand and apply. In addition to this, constant display/analysis of PFT's real-time force curve output allows the interaction of the CNT with the surface to be monitored for processes such as buckling, enabling subsequent correction of feedback parameters.

Mechanical property mapping Analysis of force curves using the PF-QNM mode introduced in section 1.1.3.2 can provide quantitative information about the interaction of the CNT with the sample. Wear resistance of the CNT results in a stable tip radius, which is highly desirable for quantitative analysis, allowing consistent measurement of interactions during imaging.

5.2.2 Results and discussion

CNT probes fabricated using the manual attachment method were used in this study, and these are shown in figure 5.9. CNTs were intentionally attached to cantilevers with relatively low spring constant and resonant frequency. Generally high resonant frequency is required for effective imaging in tapping mode (<100 kHz); PFT only requires a resonant frequency above the 1-8 kHz oscillation in order to avoid resonant effects.

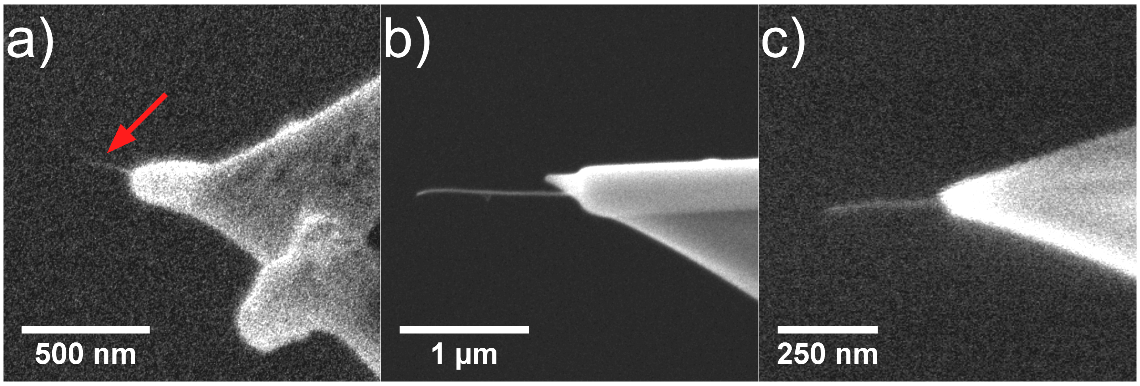

Figure 5.9: SEM images of the CNT probes used in this work, designated a) CNT11, b) CNT10, and c) CNT1. Figure c is reprinted with permission from [7].

Application of the CNT probes for routine imaging was found to be very simple when using PFT mode. To demonstrate the imaging capability and high resolution obtained, a Nioprobe tip calibration sample was imaged using CNT11 (figure 5.9a) and a standard new tapping mode probe (Bruker FMV type); the resulting AFM image is shown in figure 5.10. The sharp CNT probe clearly provides superior resolution, clearly resolving the niobium grains present on the Nioprobe sample. The high aspect ratio of the CNT also allows imaging deeper between the grains; as both images are displayed with the same height scale, the effect on image quality is dramatic.

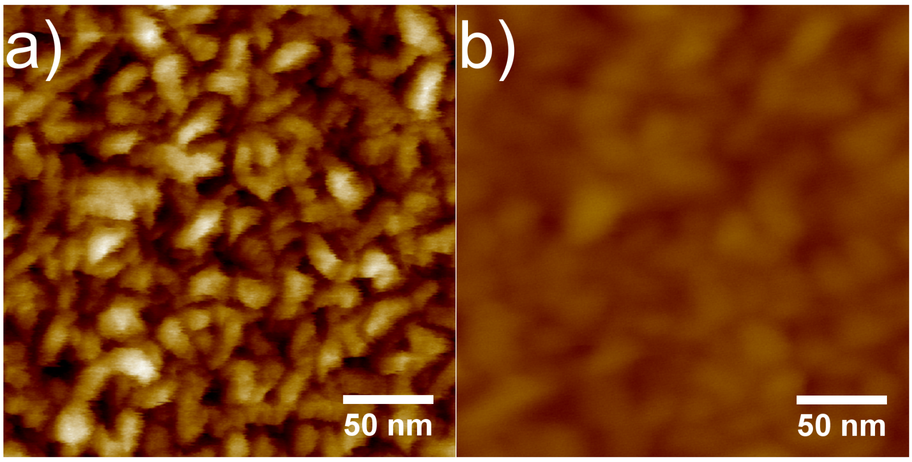

Figure 5.10: AFM images of the Nioprobe tip calibration sample in PFT mode using a) probe CNT11 and b) a new silicon FMV probe. The colour scale for both images is 20 nm.

5.2.2.1 Elimination of “ringing” artifact

One of the most commonly encountered artifacts when imaging in tapping mode with a CNT probe is the “ringing” artifact introduced previously in section 5.1.2.2.

A benefit of PFT is that feedback is based on the applied peak force, which is independent of adhesion during tip retraction; as a result, PFT should not suffer from the various adhesion-based artifacts observed with tapping mode. In order to test this and further demonstrate the application of PFT to CNT probes, a calibration sample consisting of parallel trenches 20 nm deep was imaged in both tapping and PFT with the same CNT probe. The probe used was CNT1 shown in figure 5.9c, a FastScan A type with resonant frequency 1400 kHz and spring constant 18 Nm^{-1} which was used in the previous wear testing study. A cantilever with lower spring constant would be more suited to imaging in PFT, however this cantilever was chosen such that it was able to image effectively in both Tapping and PFT modes.

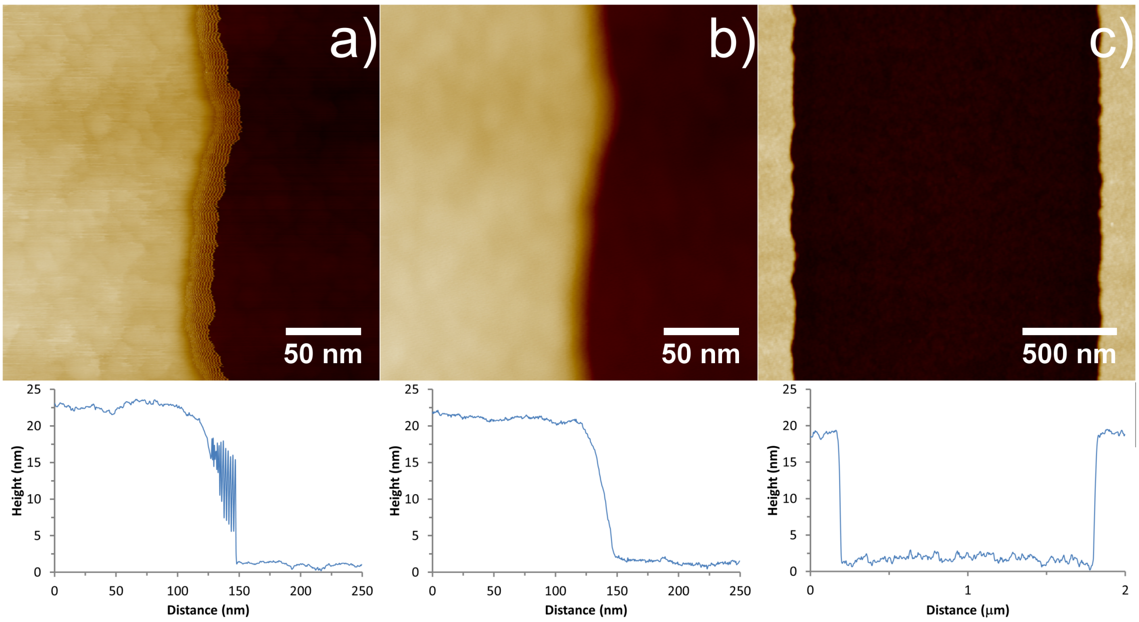

Figure 5.11: AFM images and corresponding cross sections of a Mikromasch TGZ01 calibration grid with 20 nm deep parallel trenches using the CNT1 probe. Image a) was acquired in tapping mode while images b) and c) were acquired using PFT.

The benefits of PFT in measurement of narrow trenches have been reported previously with standard probes [28]. Even when neglecting the geometry of a standard probe, in tapping mode the amplitude is damped by adhesion with the trench walls and does not allow the probe to reach the base of the trench. The use of peakforce tapping with CNT probes avoids the problem of low aspect ratio and neglects side-wall adhesion, providing an imaging mode well-suited to measuring deep, narrow trenches. This may prove to be an invaluable technique as the size of features in the semiconductor industry continue to decrease and characterisation becomes more and more challenging.

5.2.2.2 Pit artifact

A sample of gold nanoparticles (5-10 nm diameter) was used to characterize the diameter of the CNT probes. There have been several reports of nanoparticles (often gold or polystyrene) being used to determine tip diameter and also calibrate piezoelectric scanners [29–31]. The cross-section of ten gold nanoparticles from various images was used to determine the diameter of CNT11, with an image and cross section of the nanoparticles shown in figure 5.12. Using the approach taken by Vesenka et al. [31], equation 5.2 was applied to the nanoparticle cross sections where W and h are the measured width and height of the nanoparticle and R is the tips' radius of curvature. Equation 5.2 is determined from the contact geometry between two spheres representing the particle and the tip, as described by Vesenka et al.

$$W^2 = 8Rh \tag{5.2}$$

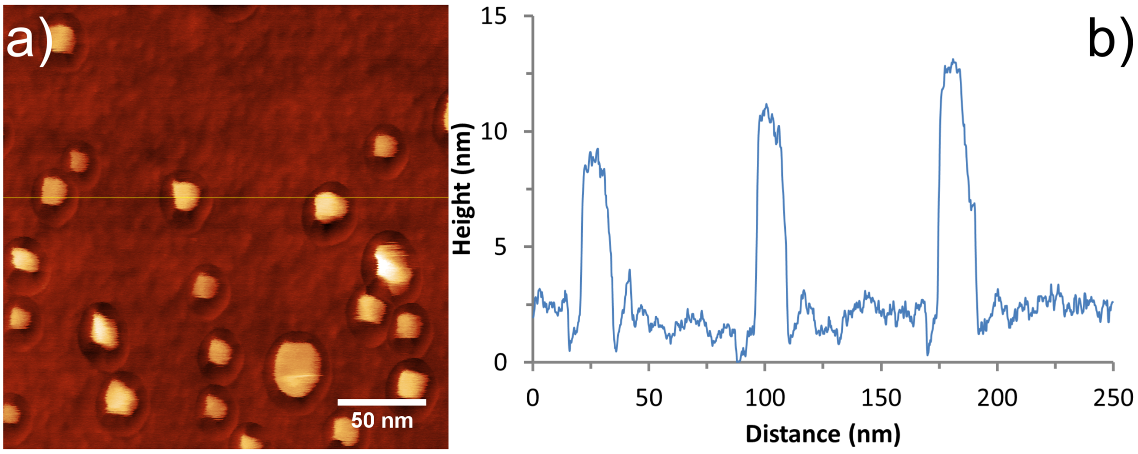

Figure 5.12: AFM image of gold nanoparticles using probe CNT11, with corresponding cross section.

The diameter of the CNT tip was determined to be 2.54±0.34 nm, through the measurement of 10 different nanoparticles. Although this tip estimation model isn't particularly suited to characterisation of sharp CNT tips, comparison with the "full width at half maximum" method used by Hafner et al. yielded a similar tip radius (within 2%) [32]. Use of this model may result in overestimation of the CNT tip diameter, and finding structures to characterise ultra-sharp tips such as these is likely to be a challenge.

It was found that when imaging these small features with a sharp CNT probe, an artifact resembling a "crater" or "pit" was observed around each of the nanoparticles. The pit was observed to extend a constant distance from the perimeter of the particle, independent of the particle size, and varied in depth to some extent between particles and around each individual particle. These features can be observed in figures 5.12 and 5.13, the pit artifact is clearly visible around all of the nanoparticles in the image.

In order to immobilize the nanoparticles on the silicon surface, a silane layer was employed; this was thought to be a possible source of the artifact, whereby the pit may actually be a real feature on the surface. In order to test this hypothesis, a droplet of solution containing the same gold nanoparticles was applied to a bare silicon surface. The nanoparticles formed were not as well adhered or ordered as those attached with the silane, but it was possible to find and image several individual particles. This result is shown in figure 5.14, and the pit artifact was clearly observed in the absence of the silane layer, albeit to a lesser extent.

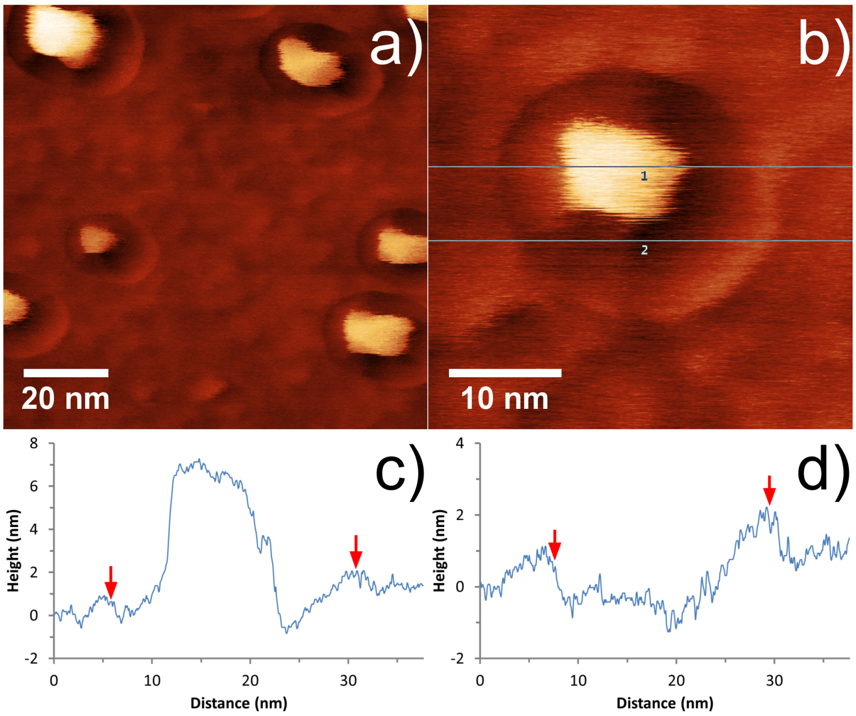

Figure 5.13: AFM images of gold nanoparticles on silicon using CNT11, clearly showing the pit artifact with corresponding cross sections through the nanoparticle and pit. The edge of the pit as observed by the AFM image is indicated by the red markers.

These observations indicate that the pit observed is a result of the probe interacting with the nanoparticle, and not a real feature on the surface. The CNT was immediately suspected as a possible source of the artifact, as these special tips give rise to various artifacts in other imaging modes. To test this, a very sharp (Bruker SNL, 2 nm nominal tip radius) silicon probe was applied to the sample under the same conditions as the CNT probe. The same artifact can be observed in figure 5.15. This suggests that the artifact is not a specific effect of the CNT probe, arising instead from the tip-sample interaction which interferes with the PFT feedback signal.

When operating in the standard PFT imaging mode, two channels report convoluted force interaction data in a similar manner to the phase channel in tapping mode. These are the “inphase” and “quadrature” channels, and are direct outputs from the lock-in amplifier used to monitor the cantilevers’ oscillation. While they cannot provide quantitative interaction data, to some extent they can indicate variation in the tip-sample interaction, or energy dissipation of the tip. During the scan in figure 5.15, both of these channels showed features in the pit region around the nanoparticle. The quadrature channel is shown in figure 5.15c, and an increase in this signal can be observed in the region of the pit, this prompted further investigation into the tip-sample interaction in this region.

An advantage of the PFT imaging mode is that the feedback signal can be easily extracted during a scan. The high-speed data capture function was used to capture the cantilevers’ deflection and height during a scan across a nanoparticle. Figure 5.16c shows the image of a nanoparticle and indicates the scanline captured, while a) and b) show the topography trace and sequential force curve tracking signal

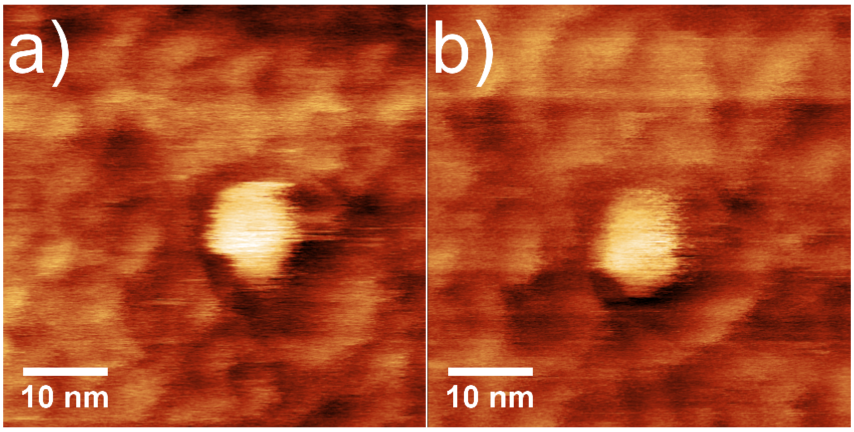

Figure 5.14: AFM images of gold nanoparticles on bare silicon, obtained with the CNT11 probe.

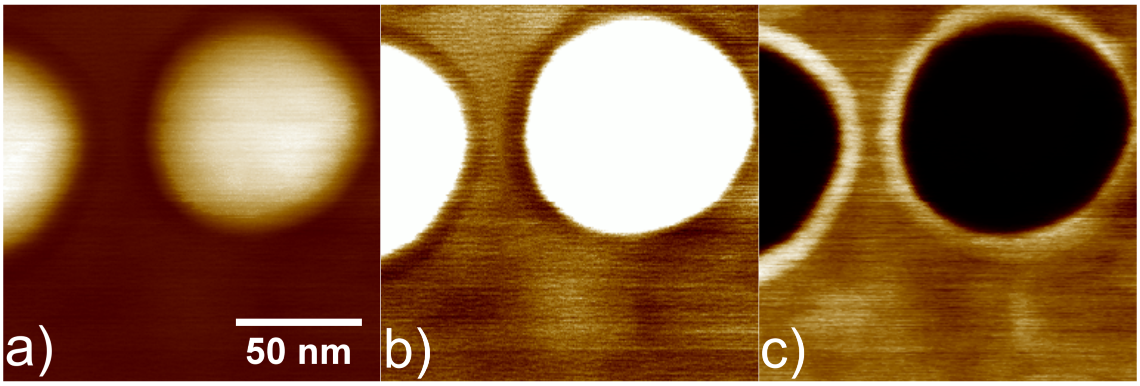

Figure 5.15: AFM images of silane-immobilised gold nanoparticles using an ultra-sharp silicon tip, figure a-b) are the height channel with different vertical scales while c) shows the “quadrature” channel. The colour scale for figure a is 22 nm, while figure b) is reduced to show the pit artifact clearly.

acquired. The inset shows a zoomed-in region of the force curve trace acquired over 0.5 ms, this shows the individual force curves which make up the overall shape of the data. These are a series of deflection versus time curves, resembling that introduced earlier in figure 1.8 of the introduction. The data observed in figure 5.16b exhibits a central baseline at zero deflection, with spikes above and below this central position. Spikes above represent deflection of the cantilever as it presses onto the surface, which is the peak force value that the system uses to track the surface and should remain relatively constant. Spikes below the baseline correspond to adhesion, and this is the value which appears to vary over the scan line.

Moving along the line, there is a slight increase in the peak force as the tip encounters the nanoparticle edge at 365 ms, this is due to the finite response of the feedback system and is to be expected. Looking at the adhesion in the region of the pit artifact, the value appears to increase significantly on both sides, with a greater increase on the approach side of the particle. Based on this, it is proposed that the pit artifact is a result of adhesion at the side of the nanoparticle, which somewhat contradicts the earlier assumption that PFT feedback is independent of adhesion.

In order to explain the appearance of the pit, PFT feedback is briefly revisited and the forces acting on a CNT tip during an oscillation cycle in close proximity to

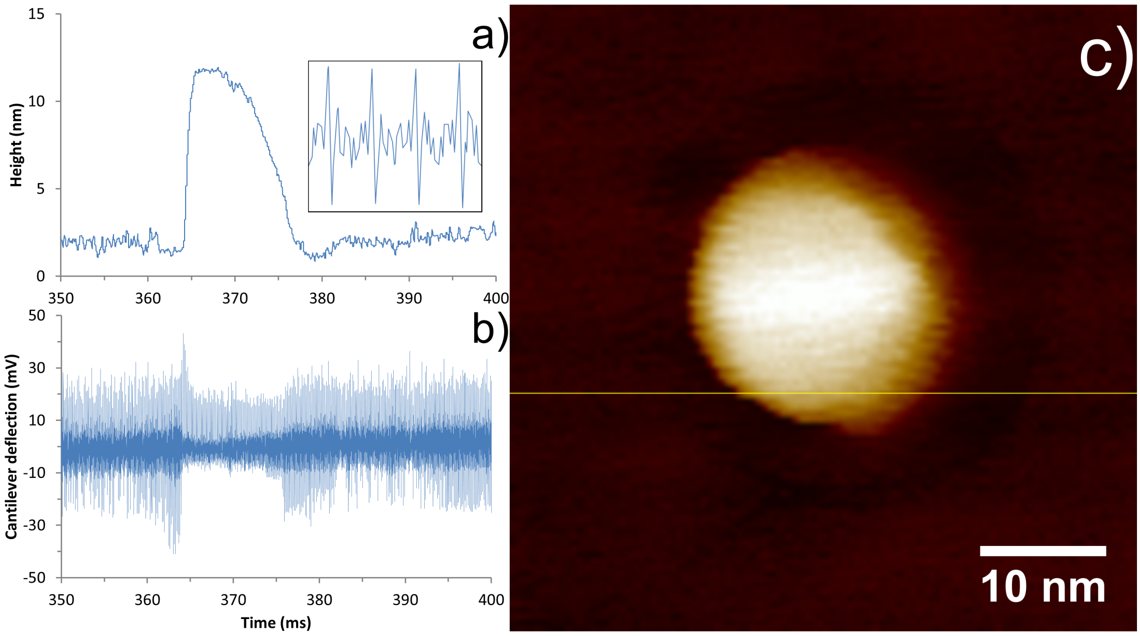

Figure 5.16: Height profile a) and corresponding force curve data capture b) for a sharp silicon Bruker SNL probe scanning over a gold nanoparticle shown in c). The inset shows a magnified portion of the deflection data, over a 0.5 ms time interval.

a nanoparticle are considered. The sample height in PFT mode is determined by the tip-sample distance at which the PeakForce setpoint is reached. The tip (or sample) oscillates, bringing the tip and sample into intermittent contact and resulting in a peak repulsive force for each tap. The system tracks this peak force and adjusts the tip-sample separation to maintain the desired setpoint.

Consider a CNT tip approaching the surface in the proximity of a nanoparticle, as shown in figure 5.17; on approach the CNT experiences attractive forces towards the nanoparticle. If the CNT is in close proximity it can make contact, if the CNT is a greater distance away then it will bend towards the nanoparticle before contacting the sample surface. In either case the CNT undergoes some degree of lateral bending before contacting the sample surface, which results in the effective length of the CNT decreasing. If the CNT effectively becomes slightly shorter in regions of high lateral adhesion, then the tip-sample separation must be decreased further to achieve the same cantilever deflection, thus resulting in the observation of a "pit" on the surface.

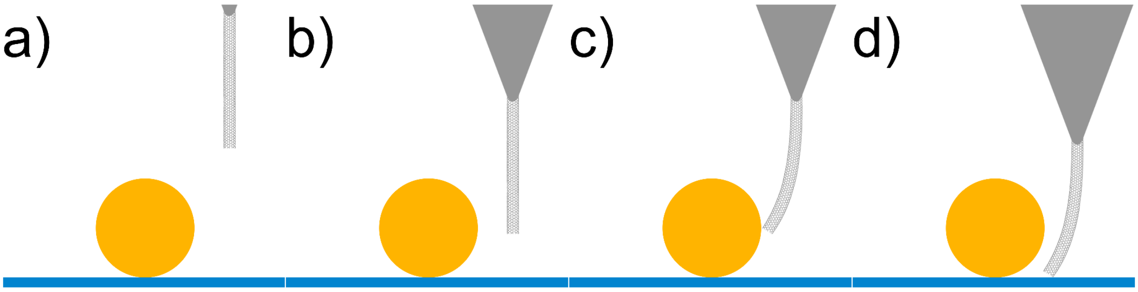

Figure 5.17: Schematic of a CNT tip during an oscillation cycle in the proximity of a nanoparticle, showing adhesion and buckling with the resulting height discrepancy.

Explanation of the artifact seems reasonable for the case of a CNT tip, however the same feature was observed for a very sharp silicon tip also. While there can be no flexing of the Si tip, it might be possible that the attractive forces cause lateral flexing of the cantilever and result in a similar effect. The pit artifact was only observed for sharp Si tips; one might expect that a blunt tip would experience significant attractive forces in directions other than towards the nanoparticle (ie. towards the substrate). For the case of a sharp tip, the tip-nanoparticle forces would likely be comparable to the tip-substrate forces and thus have a greater effect.

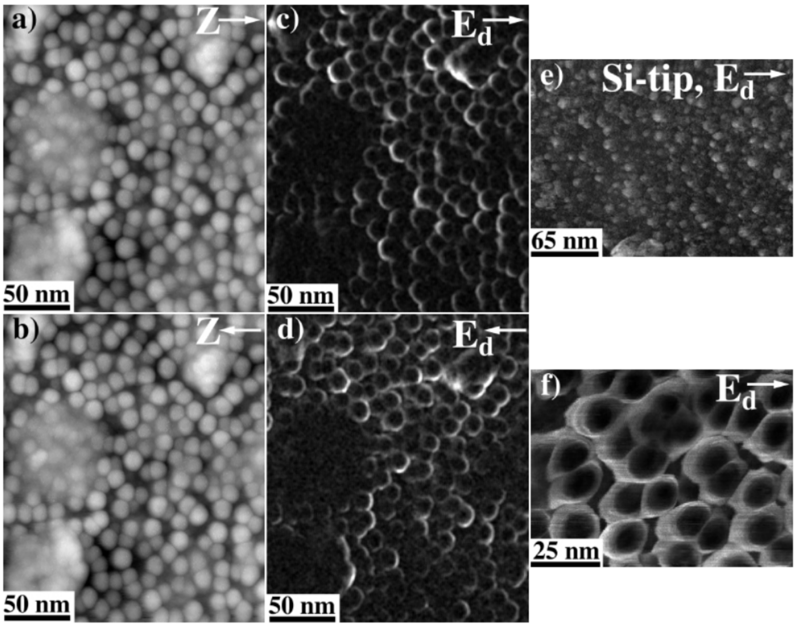

Figure 5.18: Topography images of Pt clusters on Al_2O_3 acquired in the (a) forward and (b) backward scan directions with CNT-tips, and their corresponding dissipation signals in (c) and (d), respectively. A strong dissipation signal, occurring around the perimeter of each cluster and approximately independent on the scanning direction, suggests that there is an inelastic interaction which depends strongly on the properties of the CNT and the clusters and not necessarily on the scanning parameters. The dissipation signal that occasionally could be seen while scanning with Si-tips is shown in (e), whereas (f) illustrates the dissipation from a CNT-tip at a higher magnification [27]. © IOP Publishing. Reproduced with permission. All rights reserved.

Meinander et al. reported an artifact of very similar origin for non-contact mode operation with CNT tips, which is shown in figure 5.18 [27]. CNT and ultrasharp Si tips were compared for their ability to image platinum nanoparticles and the CNT profiles were found to be much broader than expected. Analysis of the energy dissipation for CNT tips revealed similar features to the quadrature channel shown in figure 5.15c, where an interaction is observed around the entire perimeter of the particle. Meinander et al. attributed this to the same adhesion effect as described earlier, where the CNT is pulled onto the nanoparticle laterally by attractive forces. The broadening effect was not observed for the sharp Si tip, although a very faint energy dissipation was occasionally observed at the perimeter of the particles. The non-contact tip used in the study had a relatively high spring constant (42 Nm^{-1}), which would reduce lateral twisting of the cantilever, potentially explaining why this feature was not observed by Meinander et al.

5.2.3 Summary

With an efficient method to fabricate CNT probes developed in the previous chapter, this chapter has focused on their application. The wide applicability of the attachment method allowed CNTs to be attached to high-frequency fast-scanning AFM probes. Access to a fast-scanning AFM enabled investigation of their wear properties, along with demonstration of scanning speeds up to 30 Hz (109 $\mu m s^{-1}$).

Silicon fast-scanning tips were observed to wear as expected, while the CNT probes showed extremely high wear resistance with almost no wear over the duration of the study. This is the first report of a CNT tip being applied to fast-scanning, and the wear resistance demonstrated is very useful considering that the wear rate was shown to be greater for fast-scanning applications.

The application of CNT probes has proven to be as much a challenge as their fabrication, and the disadvantages of tapping mode were introduced. The PeakForce tapping technique was investigated as an alternative mode for CNT probe feedback. CNTs were attached to soft cantilevers ideal for PFT imaging, and applied to gold nanoparticle and calibration trench samples. Stable imaging was reported and the PFT mode was compared directly to tapping mode by imaging vertical steps 20 nm in height. Tapping mode exhibited the adhesion-based “ringing” artifact as expected, which was not present with images obtained by PFT. By considering only the peak interaction force for feedback, PFT is able to avoid certain artifacts caused by probe adhesion which are incorporated into the feedback signal for tapping mode.

The gold nanoparticle sample provided a good resolution test and allowed the CNT diameter to be estimated as 2.54±0.34 nm. While very high resolution was observed, the nanoparticles were surrounded by a pit which appeared to be an artifact. Varying the sample showed that the pit was indeed an artifact and not a real feature of the surface; observation of the artifact with an ultra-sharp Si tip also excluded the CNT as a specific cause.

The high-speed data capture mode was used to obtain the feeback signal of the sharp Si tip as it traversed the pit. The data showed increased adhesion in the pit region on both sides of the nanoparticle, and this information was used to formulate a possible mechanism for the artifact. Attractive forces acting on either the sharp Si tip or the CNT are proposed to pull the tip towards the nanoparticle when tapping in close proximity, this is in agreement with reports by Meinander et al. [27]. Lateral bending of the CNT or twisting of the cantilever (in the case of a sharp Si tip) will reduce the effective tip length, thus resulting in increased tip-sample separation and formation of a pit feature in close proximity to the nanoparticle. Although the pit artifact has a minimal effect on image resolution, it may be possible to reduce the effect by using shorter CNT’s which are less susceptible to lateral bending.

Bibliography - Chapter 5

[1] T. Larsen et al. *Applied Physics Letters* 80.11 (2002), p. 1996. DOI: `10.1063/1.1452782`.

[2] Chang-Soo Han, Young-Hyun Shin, and Yu-Hwan Yoon. *2nd IEEE International Conference on Nano/Micro Engineered and Molecular Systems.* 2007, pp. 290–293. DOI: `10.1109/NEMS.2007.352029`.

[3] M Yasutake et al. *Ultramicroscopy* 91.1-4 (2002), pp. 57–62. DOI: `10.1016/S0304-3991(02)00082-7`.

[4] Chanmin Su et al. *Ultramicroscopy* 97.1-4 (2003), pp. 135–144. DOI: `10.1016/S0304-3991(03)00038-X`.

[5] J Tamayo and R Garcia. *Langmuir* 12.18 (1996), pp. 4430–4435. DOI: `10.1021/la960189l`.

[6] T Ando. *2011 IEEE 24th International Conference on Micro Electro Mechanical Systems.* 2011, pp. 57–62. DOI: `10.1109/MEMSYS.2011.5734361`.

[7] Ashley D Slattery et al. *Nanotechnology* 24.23 (2013), p. 235705. DOI: `10.1088/0957-4484/24/23/235705`.

[8] J.S. Villarrubia. *Journal of Research of the National Institute of Standards and Technology* 102.4 (1997), p. 425. DOI: `10.6028/jres.102.030`.

[9] D Tranchida, S Piccarolo, and R a C Deblieck. *Measurement Science and Technology* 17.10 (2006), pp. 2630–2636. DOI: `10.1088/0957-0233/17/10/014`.

[10] Nanoworld(AG). Tech. rep. NanoWorld AG, p. 3.

[11] T. D. Yuzvinsky et al. *Applied Physics Letters* 86.5 (2005), p. 053109. DOI: `10.1063/1.1857081`.

[12] Björn Skårman et al. *Langmuir* 16.15 (2000), pp. 6267–6277. DOI: `10.1021/la000078t`.

[13] Koo-Hyun Chung, Yong-Ha Lee, and Dae-Eun Kim. *Ultramicroscopy* 102.2 (2005), pp. 161–71. DOI: `10.1016/j.ultramic.2004.09.009`.

[14] Erhan Yenilmez et al. *Applied Physics Letters* 80.12 (2002), p. 2225. DOI: `10.1063/1.1464227`.

[15] Byong Chon Park et al. *Proc. SPIE 5038, Metrology, Inspection, and Process Control for Microlithography XVII.* 2003, pp. 935–942. DOI: `10.1117/12.482816`.

[16] F Z Fang, Z W Xu, and S Dong. *Measurement Science and Technology* 19.5 (2008), p. 055501. DOI: `10.1088/0957-0233/19/5/055501`.

[17] M C Strus et al. *Nanotechnology* 16.11 (2005), pp. 2482–2492. DOI: `10.1088/0957-4484/16/11/003`.

[18] Haifeng Gao et al. *International Journal of Nanomanufacturing* 9.1 (2013), p. 87. DOI: `10.1504/IJNM.2013.052885`.

[19] A. Karbach and D. Drechsler. *Surface and Interface Analysis* 27.5-6 (1999), pp. 401–409. DOI: `10.1002/(SICI)1096-9918(199905/06)27:5/6<401::AID-SIA533>3.0.CO;2-A`.

[20] Higinio González-Jorge et al. *Sensors* 10.4 (2010), pp. 4002–9. DOI: `10.3390/s100404002`.

[21] Georg Schitter et al. *International Journal of Nanomanufacturing* 8.5/6 (2012), p. 392. DOI: `10.1504/IJNM.2012.051109`.

[22] Mark C. Strus and Arvind Raman. *Physical Review B* 80.22 (2009), pp. 1–9. DOI: `10.1103/PhysRevB.80.224105`.

[23] S I Lee et al. *Nanotechnology* 15.5 (2004), pp. 416–421. DOI: `10.1088/0957-4484/15/5/002`.

[24] S I Lee et al. *Ultramicroscopy* 103.2 (2005), pp. 95–102. DOI: `10.1016/j.ultramic.2004.09.012`.

[25] Charlotte Bernard et al. *Nanotechnology* 19.3 (2008), p. 035709. DOI: `10.1088/0957-4484/19/03/035709`.

[26] Cattien V Nguyen et al. *Nanotechnology* 12.3 (2001), pp. 363–367. DOI: `10.1088/0957-4484/12/3/326`.

[27] Kristoffer Meinander et al. *Nanotechnology* 23.40 (2012), p. 405705. DOI: `10.1088/0957-4484/23/40/405705`.

[28] Stefan B. Kaemmer. Tech. rep. 2011, pp. 1–12.

[29] Ch. Wong et al. *JOM* 59.1 (2007), pp. 12–16. DOI: `10.1007/s11837-007-0003-x`.

[30] M Van Cleef and SA Holt. *Journal of ...* 181.1 (1996), pp. 2–9. DOI: `10.1046/j.1365-2818.1996.74351.x`.

[31] J Vesenka et al. *Biophysical journal* 65.3 (1993), pp. 992–997. DOI: `10.1016/S0006-3495(93)81171-8`.

[32] Jason H. Hafner et al. *The Journal of Physical Chemistry B* 105.4 (2001), pp. 743–746. DOI: `10.1021/jp003948o`.

Chapter 6

Conclusion

The work presented here has focused on two main aspects of atomic force microscopy, that concerned with quantitative force measurement and imaging improvement through increased resolution, durability and elimination of artifacts.

Spring constant calibration of AFM cantilevers has been a challenging task from the very beginning; the tiny scale and variable geometry and composition of these devices poses a significant challenge to accurately determining their mechanical properties. The first work on AFM cantilever spring constant calibration began over 20 years ago and since then, there has been constant development in the field, highlighting the significant challenge it poses and also the importance of quantitative force measurement.

The work presented in chapter 3 offers improved calibration methods using several different approaches. FIB milling plays an integral role throughout this chapter, the ability to modify cantilevers with extremely high spatial precision allows cantilevers to be studied with accurate adjustment of their geometry.

FIB milling was initially incorporated into the Cleveland added mass method, where a hole was milled into cantilevers and the resonant frequency shift observed. This is in contrast to the original technique where the cantilever is loaded with a microsphere. FIB milling allows the mass and its location to be defined precisely, greatly improving the accuracy of the existing technique with uncertainty as low as 7% obtained.

A range of cantilevers were studied and the technique was found to be applicable to almost all types with low uncertainty. Poorly defined material properties appeared to be the greatest source of uncertainty, as the technique relies on accurate knowledge of the cantilever material density. This is specifically a challenge for silicon nitride cantilevers and those with poorly defined coatings, whereas single-crystal silicon has very well-defined material properties.

FIB milling was then applied to the reference cantilever method; the ion beam was used to mill spatial markers along the cantilevers' length. When pressing a test cantilever against a reference cantilever, a large degree of uncertainty arises from uncertainty in the exact loading position. Imaging the spatial markers with the test cantilever allowed the loading position to be determined precisely, essentially eliminating this source of uncertainty.

Building on the method, the reference cantilever technique was inverted, and markers were milled in the test cantilever instead. This allowed the calibration to be performed without the test cantilever's tip ever touching the surface, by using the reference cantilever tip to reverse image the spatial markers.

The reference cantilever method is very powerful, as is applicable to any type of cantilever, unaffected by factors such as material properties or geometry. Not only has the application of FIB-milled spatial markers greatly reduced uncertainty in this technique, but the ability to calibrate cantilevers without any tip-sample contact is a great advantage for delicate tips.

The previous statement (while true for the reference cantilever method) requires some clarification. Even though the spring constant can be determined, the test cantilever must have accurately calibrated deflection sensitivity in order to perform force measurements, which requires tip-sample contact. This introduces the work reported in section 3.3, which describes the use of FIB milling again to remove tip-sample contact from the deflection sensitivity calibration procedure. Rather than pressing the test cantilever against a hard surface it was instead pressed against another stiff, inverted cantilever. Spatial markers were milled into the underside of the test cantilever, and the underlying cantilevers' tip was used to image these markers, again allowing the contact position to be determined precisely.

The sensitivity measurement is then corrected to the test cantilevers' tip, and a wide range of cantilevers were calibrated using this approach which were then compared to the standard method. Comparison of the results showed extremely good agreement between the two techniques, providing an effective method to measure deflection sensitivity while eliminating tip-sample contact.

In the final section of the calibration chapter, spring constant calibration of the recently-commercialised fast-scanning cantilevers was investigated. These ultra-small cantilevers are vastly different from their standard counterparts, and until now there has been no assessment of whether existing calibration techniques are applicable.

The reference cantilever technique is unaffected by the properties of fast-scanning cantilevers, and so was chosen as a benchmark against which various existing techniques were compared. The Sader resonance, Euler beam and Euler-resonance methods showed good agreement with the reference cantilever results, but suffered from high uncertainty due to error on material properties. The thermal method was found to consistently overestimate the spring constant, attributed to poor knowledge of the Chi correction factor and low thermal noise signal inherent in fast-scanning cantilevers. The poor performance of the thermal noise method is expected to be a major problem as cantilever size continues to reduce.

The FIB mass removal method was modified, such that the silicon tip material was milled instead of the cantilever. Re-deposition of milled material resulted in over-estimation of the spring constant, this was avoided by milling a greater section of the tip which resulted in good agreement with the reference method. Of the techniques studied, the Sader hydrodynamic expression for cantilevers of arbitrary shape was the most promising due to the scalability of the method. This technique requires a reference spring constant, but was found to provide good values with low uncertainty when the reference cantilever value was used. Provided that reference spring constant values are available for the required geometry, this technique should prove very useful for fast-scanning cantilevers.

In chapter 4, the fabrication of CNT probes was reported using various methods. CVD growth was successful in producing CNT tips, however the yield of well-aligned probes was very low. In addition, the CNTs obtained by this method were poorly attached and unstable during imaging.

CNTs were also attached using dielectrophoresis, a large CNT fibre was routinely formed at the tip and the yield of usable probes was found to be much higher than that of CVD. These CNT fibres were not capable of imaging immediately; the interaction was initially unstable, but then improved over time. Imaging at high force was found to stabilise the tip, at which point the force was reduced and images obtained as usual. The CNTs were confirmed to have straightened using SEM, and a mechanism related to tip adhesion was proposed. Tips made by this method had similar resolution to that of standard probes, although the aspect ratio and wear resistance was very high, making these probes suitable for metrology applications.

The final method for CNT attachment was chosen for superior control over the attachment process and properties of the CNT. The CNTs were physically placed onto AFM tips using a micromanipulator in a SEM, platinum was then deposited for good adhesion and water-assisted electron beam cutting was used to cut the nanotube to an ideal length. This approach proved to be both highly effective and efficient, producing a CNT tip of very high quality in 15-30 minutes.

The CNT probes fabricated by the manual attachment method were then used for several applications in chapter 5. Attachment of CNTs to fast-scanning probes was reported for the first time, and these were used to image a number of challenging surfaces with a focus on wear resistance. Comparison between standard and CNT fast-scanning probes on nioprobe and tipcheck calibration samples showed a significant difference in the wear rates. Standard probes were observed to wear steadily as expected, while CNT probes showed almost no change in image resolution over approximately 7.5 hours of scanning.

CNT probe application was also investigated using the novel “PeakForce Tapping” imaging mode. In contrast to tapping mode, PFT offers direct control over the imaging force which should provide more stable imaging with CNTs. CNTs were attached to the soft cantilevers used for PFT imaging (nominal spring constant 0.4 $\mathrm{Nm^{-1}}$), and high resolution imaging was demonstrated on a sample of gold nanoparticles.

A pit-shaped artifact was observed around the perimeter of the gold nanoparticles, for both CNT and sharp silicon tips. Deflection data was acquired as the tip traversed a nanoparticle, which indicated that the pit artifact was related to high adhesion at the nanoparticles’ perimeter. This was attributed to to tip adhering to the side of the nanoparticle, either by lateral bending of the CNT or by lateral twisting of the cantilever in the case of a sharp silicon tip.

In addition to the pit artifact, the ringing artifact was also investigated; this feature is commonly observed with CNT probes in tapping mode and is also adhesion-related. PFT is not susceptible to adhesion-related aritfacts in the same way that tapping mode is, and should be avoidable using the PFT mode. The CNT tip was sequentially scanned over a 20 nm step in tapping and then PFT mode; the artifact was observed clearly in tapping mode, but was absent in PFT mode. Due to the occurrence of the artifact at steep edges, it greatly hinders analysis of steep features which would otherwise be ideal to characterises with high aspect ratio CNT probes. Removal of the ringing artifact by PFT mode will be useful for characterisation of vertical steps with very high resolution, such as process monitoring in the semiconductor industry.